

21 July 2006 | \$10

Science



 AAAS



Don Kennedy is the Editor-in-Chief of *Science*.

News on Women's Health

A PIECE OF IMPORTANT AND ENCOURAGING NEWS FOR THE WORLD'S WOMEN AND THEIR HEALTH has recently arrived from the world of clinical trials. The results of a carefully structured controlled trial have persuaded the U.S. Food and Drug Administration (FDA), with strong endorsement from an advisory committee, to approve a vaccine that is effective against the two forms of human papilloma virus (HPV) that are most likely to lead to cervical cancer. 3700 women die of this disease annually in the United States, but the mortality is far, far greater in the developing world, where this vaccine could provide a major public health benefit. Thus there is strong international interest in this result, and approval processes are under way in a number of countries. Here in the United States, which individuals receive immunization, when they get it, and where, are problems that await resolution in potentially heavy ethical weather.

The new vaccine, developed as a result of research done in the United States and other countries, has resulted in the development of competing products by Merck & Co. and Glaxo-Smith-Kline (GSK). The Merck entry, which was the subject of the recent FDA approval for vaccination of girls and young women between the ages of 9 and 26, is called Gardasil. It is effective, but it is not cheap; the manufacturer says it will cost about \$360 for the three doses that will be required over 6 months. HPV is a high-prevalence sexually transmitted disease: In fact, about half of adult Americans who are sexually active will become infected at some time in their lives. Because the new vaccine is far less effective against already-established infections, immunization is plainly indicated for young girls before they become sexually active; and, after additional testing, probably for boys as well. Already, Merck and GSK are applying to market products in Europe and South America and are conducting additional trials to test for long-range efficacy and possible effects on pregnancy.

Scientific advice on immunization issues in the United States is the responsibility of the Advisory Committee on Immunization Practices, which advises the Centers for Disease Control and Prevention and various other units of the U.S. Public Health Service. On 29 June, that group met in Atlanta, recommended that females between the ages of 12 and 26 receive the vaccine, and suggested that it be made available for girls aged 9 and older on the advice of a physician. But major challenges remain in the wake of that decision. The first is to determine how it will be paid for. The total treatment costs for an immunization project of this magnitude would outrun the economic capacity of most cities and school systems, and of public health agencies in poor countries, where the needs are greatest.

The other problem, perhaps more serious, is that conservative religious groups in the United States, such as Focus on the Family, politically oppose a mandatory program on the grounds that it might encourage promiscuity. They deliver pro-forma praise for the vaccine (after all, who likes cancer?), but they then advise young women candidates that abstinence is a preferable alternative. That is bad advice.

If there is to be significant progress in reducing the incidence of cervical cancer, the HPV vaccine should be made part of a mandatory preschool immunization package. In the present situation, in which participation is voluntary, the girl who says no to vaccination and yes to Focus on the Family's advice to elect abstinence creates two risks. One is to herself: Numerous studies have shown that abstinence often fails; and even if it succeeds, it will eventually be displaced by either marriage or romance—with a partner who may have HPV. The second risk is to society: By declining vaccination, the refusenik becomes a free rider. The objective of vaccination programs is to reduce the overall probability of infection by creating herd immunity—that is, by making a large majority of the population immune. Those who won't participate in the vaccination program are thereby spreading a small risk to the rest of society. "Freedom of choice" is an argument favored by the abstinence advocates. But that slogan ignores a serious ethical consequence: If the choice entails spreading harm to other people, can it really be called "free"?

— Donald Kennedy

10.1126/science.1132381





2007 U.S. BUDGET

Senate Panel Backs Integrated Ocean Observation System

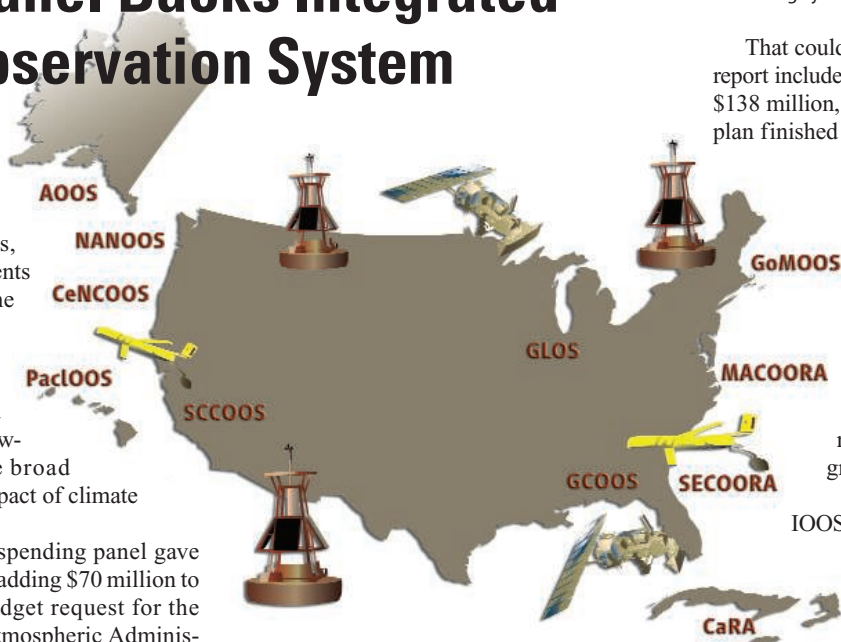
From the Gulf of Maine to the Alaska Peninsula, the U.S. coastline is dotted with idiosyncratic networks of buoys, radar, and other instruments that keep their eyes on the seas. For years, marine scientists have wanted to expand and update this network so that all the data would be compatible, allowing them to investigate broad questions, such as the impact of climate change on the coasts.

Last week, a Senate spending panel gave that effort a major boost, adding \$70 million to the Administration's budget request for the National Oceanic and Atmospheric Administration (NOAA) to start up the Integrated Ocean Observation System (IOOS). Although thrilled about the news, lobbyists for ocean science are worried that NOAA may not be in it for the long haul.

In a 2004 report, the U.S. Commission on Ocean Policy described IOOS as a "system of systems" for increasing maritime safety, mitigating the danger of tsunamis and other natural hazards, and improving coastal ecosystems. New buoys and other types of platforms would provide local information, and larger-scale questions could be addressed by standardizing and linking the sensors and data. "IOOS could fundamentally change our understanding of the ocean," says Philip Bogden, who directs the Gulf of Maine Ocean Observing System.

The commission recommended \$138 million to get IOOS rolling, ramping up to \$500 million a year in 5 years. NOAA would lead a consortium of 10 agencies already involved in ocean monitoring. Although the White House hasn't asked Congress to fund IOOS, Congress appropriated about \$68 million for it in each of the past 2 years.

This year, the Senate appropriations panel embraced the commission's recommendation. It designated \$10 million to start a data center at the Stennis Space Center in Mississippi and \$60 million more for start-up funding. In addition, it earmarked \$31 million for 13 existing regional networks and \$37 million for a vari-



ety of existing programs related to IOOS. But there are strings attached: Before NOAA can spend the start-up money, it must provide Congress next spring with "realistic cost estimates" and a strategic plan.

2007 U.S. BUDGET

NASA Budget Soars as Shuttle Lands

With NASA celebrating the safe return this week of the space shuttle, space and earth scientists have their own reasons to put some champagne on ice. A Senate panel last week added a cool \$1 billion to the space agency's 2007 budget. The money would ease the financial



On a roll. Discovery's safe landing this week coincides with congressional support for a bigger NASA budget.

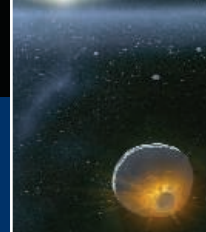
Buoyed hopes. The Senate is backing a long-planned program to expand and link regional ocean observing systems.

That could be a tall order. The commission report included only a rough breakdown for the \$138 million, however, and an implementation plan finished last year by Ocean.US, a federal entity, doesn't contain a budget. "It will be a real push" for NOAA to cobble together all the details in time, predicts John Orcutt of the Scripps Institution of Oceanography in San Diego, California, director of the southern California network. The Senate also directs NOAA to start funding regional centers with competitive grants by 2008.

The panel's healthy funding for IOOS is part of its \$536 million boost to NOAA's current \$3.9 billion budget. That figure must be reconciled with a \$506 million cut by the House of Representatives. Still, IOOS supporters are optimistic that the project will move forward in 2007. The bigger challenge, they say, is persuading the Bush Administration to request more money in subsequent years. —ERIK STOKSTAD

crunch threatening to cancel and delay a host of science missions—if the measure wins the backing of the full Senate and the House of Representatives later this year.

Senators Barbara Mikulski (D-MD) and Kay Bailey Hutchison (R-TX) argued successfully at a 13 July meeting of the Senate Appropriations Committee that the space agency deserved \$1 billion in emergency funding to cover the huge costs of getting the shuttle flying again as well as \$40 million to repair damage to its Gulf Coast facilities from Hurricane Katrina. Although Senator Pete Domenici (R-NM) insisted that calling the situation an emergency "is a stretch of the word," the committee approved the measure by voice vote. NASA chief Michael Griffin would decide how to allocate the money, but the intention ▶



is to spread it among the science, aeronautics, and human exploration efforts that took a hit to cover shuttle expenses. “I will not let NASA back down from its commitment to science,” Mikulski said in a 17 July statement.

The bill would give NASA \$17.8 billion in 2007—a 7% increase rather than the 1% hike proposed by President George W. Bush in February. (The panel also included millions of dollars in controversial earmarks for projects for which NASA has not requested funds.) The additional funding could provide relief to missions such as the James Webb Space Telescope, which remains behind schedule and over

budget. A Government Accountability Office report released last week warns that, under current planning, “the program will not have sufficient funding resources to ensure [its] success.” NASA asked for \$443 million for the project in 2007; agency officials estimate they need an additional \$1 billion over the next few years to solve difficult technical challenges.

Even if the measure passes the full Senate later this year, it’s expected to face tough sledding in the House, which on 29 June approved only \$16.7 billion for NASA. “The odds that this will work are less than 50–50,” says one space agency official. The two senators met

earlier this month with Vice President Dick Cheney, but so far the White House has remained silent on whether it supports the additional spending.

Meanwhile, with the shuttle back on Earth, Griffin is expected to decide by this fall whether to give the green light to a servicing mission to the Hubble Space Telescope. NASA officials last year said that safety issues ruled out a shuttle flight to install new instruments and refurbish the satellite. Griffin, however, is likely to approve the idea now that the shuttle fleet is back in action.

—ANDREW LAWLER

INTELLECTUAL PROPERTY

Groups Challenge Key Stem Cell Patents

Three patents that cover most U.S. research using embryonic stem (ES) cells should not have been granted because the work was obvious and not new, a nonprofit organization argues in a filing with the U.S. Patent and Trademark Office (PTO) this week. “All they really did here was follow what a number of stem cell scientists were showing,” says John Simpson of the Santa Monica, California–based Foundation for Taxpayer and Consumer Rights (FTCR), which is leading the effort with patent watchdog Public Patent Foundation. A successful challenge to the patents, held by the Wisconsin Alumni Research Foundation (WARF), could allow more companies to exploit the technology for basic research or marketed treatments.

WARF’s patents, the first of which was granted in 1998, cover the use, sales, or research on stem cells obtained from primates—regardless of who makes them or how. Experts say the patents are broad because they cover both actual cell lines and general descriptions of making them. WARF requires that university researchers and those at other nonprofit institutions obtain licenses before they use the cell lines. But it only charges them licensing fees if a commercial product resulting from the research is made with stem cells. Companies must pay as much as \$250,000. Harvard University pancreatic cell researcher Douglas Melton calls Warf’s licensing terms “onerous, restrictive, and uncooperative” barriers to cures.

WARF Managing Director Carl Gulbrandsen says the challenge is “politically and financially motivated.” The foundation’s patents are legitimate and “do not inhibit research,” he adds.

James Thomson, a University of Wisconsin, Madison, developmental biologist, applied for the patents in 1995. The first patent was issued in 1998, followed by very similar ones in 2001 and 2006. In 1999, WARF signed



Under scrutiny. This colony of human embryonic stem cells (*inset*) comes from the lab of University of Wisconsin patent holder James Thomson.

a licensing agreement with Geron, now the main licensee.

In its 18 July petition to reexamine the patents, FTCR charges that the first two patents are invalid because they cover a technique that was published before 1995. They cite a patent granted in 1992 to Australian Robert Williams, who described a method of deriving the mammalian stem cells in culture that, like Thomson’s, required feeder cells and could turn into all manner of adult cells. FTCR also says that Thomson’s efforts to isolate primate ES cells mimicked existing approaches to isolate ES cells from mice and

other organisms. In an attached declaration to PTO, molecular biologist Jeanne Loring of the Burnham Institute in San Diego, California, says that the techniques mentioned in a 1990 paper and scientific books render Thomson’s work “obvious to someone skilled in the art,” a condition that should disqualify a patent application.

“If it were so obvious, it would have been done [before],” says WARF attorney Elizabeth Donley, who plans to review the Williams patent. “What worked in mice didn’t work in humans.”

Experts say the challenges touch on fundamental difficulties about obviousness and novelty claims. “On one hand, you can say the technology was almost identical to what they did in mouse [cells], so you could argue it was obvious,” says Allan Robins, a molecular biologist with Irvine, California–based stem cell start-up Novocell. “On the other hand, there had been failures in rats and pigs; therefore, you could argue that it wasn’t obvious.”

Bill Warren, an attorney with Sutherland Asbill & Brennan LLP in Atlanta, Georgia, says that PTO could decide not to review the patents because two of four key references FTCR cites were previously reviewed by PTO when it issued the original patents. But “if the Patent Office takes the case, then there are some very close questions of patentability” at issue, he says.

PTO can take up to a year to decide whether to do a full reexamination and 2 years or more to rule.

—ELI KINTISCH

HIV/AIDS

Gates Foundation Doubles Support For AIDS Vaccine Research

The Bill and Melinda Gates Foundation announced grants this week that will more than double its already substantial investment in AIDS vaccine research and development. The \$287 million commitment is the largest non-governmental contribution ever made to this struggling field.

The Gates Foundation in 2005 sought proposals to develop consortia to work on a variety of HIV vaccine approaches. After receiving some 65 letters of intent, the foundation tapped a panel of outside experts to help select 16 groups, which will receive the money over the next 5 years if they meet specific milestones. "After working 20 years on an HIV vaccine and not finding a clear path forward, this is a really elemental step," says José

Fred Hutchinson Cancer Research Center in Seattle that won a \$30.1 million grant to explore ways to boost vaccines using additives called adjuvants. Institutions in particular will have to work out difficult intellectual property issues, says David Ho, head of the Aaron Diamond AIDS Research Center in New York City. "The ideals are all good, but there are issues to work out," says Ho, whose lab will receive \$24.7 million to make vaccines that use a novel family of immune cells to help boost immunity.

The other vaccine-discovery grants will either focus on antibodies, which prevent cells from becoming infected, or the cellular arm of the immune system that clears already-infected cells. Projects include exotic ideas such as studying llama antibodies, exploring skin patches as delivery devices, and evaluating unusual vectors such as the virus that causes Newcastle disease. "It should be great for the field," says Bruce Walker, an HIV immunologist at Massachusetts General Hospital in Boston, who did not apply for one of the grants. "It's clear that answers are going to come from incorporating research in multiple different fields, and that's what these grants are really designed to do."

About 25% of the money is going to three consortia led by principal investigators who are also the recipients of a separate, similar award from the National Institutes of Health (NIH) that's called the Center for HIV/AIDS Vaccine Immunology (CHAVI). Esparza says the foundation worked closely with NIH to make sure that people were not double-funded for the same work. "CHAVI is working on a different part of the Enterprise Strategic Plan," stresses Barton Haynes, who heads CHAVI and received a Gates grant.

The new commitment brings the Gates Foundation's investment in HIV/AIDS vaccine research and development to more than \$500 million. "I'm excited by the amount of money being pumped into the field," says Seth Berkley, head of the New York City-based International AIDS Vaccine Initiative, which received one of the new grants to do a large-scale comparison in monkeys of little-studied viral vectors. The challenge now, Berkley says, is to make sure the money is well spent.

—JON COHEN



Upping the ante. Bill and Melinda Gates have awarded \$287 million to 16 new consortia that will work together to find an AIDS vaccine.

Esparza, senior adviser on HIV vaccines for the foundation, which is based in Seattle, Washington.

The foundation has united the grantees into what it calls the Collaboration for AIDS Vaccine Discovery. In all, the collaboration involves 165 researchers from 19 countries who are divided into 11 consortia that will develop vaccines and five others that will run central facilities for immunology, storing specimens, and managing data. The initiative is part of a loosely coordinated international effort on HIV vaccine research development, called the Global HIV Vaccine Enterprise, first proposed in *Science* 3 years ago (27 June 2003, p. 2039).

The principal investigators, who met in Seattle last week, have agreed to share data and specimens. "That's going to take a lot of time to get used to, but everyone embraces it in spirit," says Julie McElrath, who heads a group at the

Harvard Reloaded

Science and engineering schools at Harvard University are too autonomous to cope with the interdisciplinary fervor sweeping areas such as biomedical research. That's the conclusion of a 97-page draft report by a 24-member committee of Harvard University faculty led by a molecular biologist, physicist, and chemist.

The committee, created in January by former President Lawrence Summers at the behest of senior scientists, recommends a central coordinating body to promote collaboration and respond more quickly to emerging research issues. The organization would have the authority to allocate research space and recruit and promote faculty. Those may be fighting words for Harvard's department chairs, who are notoriously protective of their turf. But one Harvard official insists that "this is not pie-in-the-sky stuff." Interim President Derek Bok and Harvard's governing board have already seen the preliminary results and are open to the committee's ideas, he adds. They will get a final report in December. —ANDREW LAWLER

House Wants U.S. Shore Survey

In a move that surprised and pleased climate scientists, the House of Representatives has approved a \$1 million National Academy of Sciences (NAS) study of how U.S. coastal areas would be affected by a rise in sea levels due to global warming. It's the first legislation of its kind by the Republican-controlled House, which has traditionally discounted the risks of climate change.

The \$1 million study, passed 29 June after Representative Frank Pallone (D-NJ) introduced it, was an amendment tacked in a \$62 billion spending bill. Over the last decade, world seas have risen roughly 3 mm per year; the Intergovernmental Panel on Climate Change predicted in 2001 that seas could rise between 9 and 88 cm over the next century. Although a few regional and coastal studies, some federally funded, have laid out scenarios including increased storm surge and lost beaches, researchers complain that the message to coastal citizens from the government has been muddled, despite a Bush Administration report on the mid-Atlantic coast due out next year.

"Pallone should already have something like [the NAS study] on his desk," says Rick Piltz, a former program manager at the U.S. Climate Change Science Program who now runs an advocacy organization called Climate Science Watch. The spending bill that includes the study still faces months of legislative negotiations, but observers don't expect that politicking to affect plans for the study.

—ELI KINTISCH

WOMEN IN SCIENCE

MIT Hiring Controversy Sparks Faculty Fracas

Faculty members at the Massachusetts Institute of Technology and neurobiologists elsewhere are in an uproar over a decision last month by an up-and-coming scientist to decline a position at MIT. Some scientists claim the incident reflects gender bias by a prominent faculty member, whereas others see it as simply a nasty case of academic politics. MIT's president has apologized for the incident, which points to ongoing tensions among MIT's fractious neuroscience teams and the university's struggle to hire accomplished women.

Alla Karpova, a postdoctoral fellow at Cold Spring Harbor Laboratory in New York, was offered a job this spring as an assistant professor at MIT's McGovern Institute, which specializes in brain and cognitive sciences. She declined the position on 24 June. A week later, 11 senior women faculty members wrote MIT President Susan Hockfield complaining that Susumu Tonegawa, head of the rival Picower Institute of Learning and Memory and a 1987 Nobel Prize recipient, "strongly opposed her recruitment" and that other professors and administrators could not assure her "that she was wanted and welcome at MIT." Karpova has since accepted a post as an independent investigator at the new Howard Hughes Medical Institute Janelia Farm research campus in northern Virginia.

The letter goes on to warn that the incident has "damaged MIT's reputation as an institute that supports academic fairness for young

faculty and jeopardized our ability to attract the best scientists to MIT." The authors urged Hockfield to apologize to Karpova and investigate the incident. "At stake are the career of a brilliant young scientist and the reputation of a great institution," the letter concludes.

A separate letter to Hockfield and MIT Provost Rafael Reif from Stanford University neurobiologist Ben Barres, an MIT alumnus, made more explicit charges. "I'm tired of seeing women treated poorly at MIT," he told *Science*. Describing conversations he says he had with Karpova and with MIT officials, Barres wrote that Tonegawa and science dean Robert Silbey "in essence advised her not to accept the offer." Tonegawa and Silbey, who has said he's "not happy" with the rate of hiring women science faculty members since he became dean, did not return phone calls and e-mails (*Science*, 21 April, p. 347, and 14 July, p. 171).

Tonegawa's supporters at MIT, however, say that any suggestion of gender bias is

absurd. "To portray it as such sets back the cause for women scientists," states a 7 July letter to Hockfield from a half-dozen Picower Institute faculty members. Tonegawa is under no obligation to collaborate with anyone, they write, adding that he contacted Karpova "at her instigation." But other sources familiar with the content of e-mails sent by the 68-year-old Tonegawa to the postdoc say his words went beyond the issue of collaboration and conveyed hostility.

Reif says that he will chair a committee to investigate both the Karpova affair and how neuroscience is organized at the university, adding that "a bit of tension seems to be underlying this set of events." And on 17 July, Hockfield wrote the women faculty members that MIT apologizes to Karpova "for any misunderstanding." The gender issue may be beside the point, says MIT biologist Nancy Hopkins, who chaired a 1999 committee on gender bias and who signed the 30 June letter. "Regardless of the specifics of this case, this shows exactly why it is challenging to hire outstanding women at MIT," says Hopkins.

Karpova says she is "very much upset" over the publicity. "I am trying to move on with my life, to get back to doing science," she says.

—ANDREW LAWLER



Close quarters. MIT's new home for both the Picower and McGovern institutes.

BIOSECURITY

U.S. Panel Calls for Extra Review of Dual-Use Research

A panel set up to help the U.S. government prevent terrorists from misusing life sciences research has recommended that institutions and journals adopt formal procedures to pre-screen the publication of findings from such dual-use projects.

At a meeting last week, the 25-member National Science Advisory Board for Biosecurity (NSABB) unanimously approved recommendations from one of its working groups asking authors, institutional reviewers, and journal editors to carry out a risk-benefit analysis before deciding whether to publish results of dual-use research and in how much detail. "If you accept the fact that there is potential for science to be misused, then you could envision a situation where it might be necessary to withhold certain information from a paper," says board chair Dennis Kasper, a microbiologist at Harvard University. Other points to consider would be whether to defer

publication until a time when the benefits might outweigh the risks, and whether to limit access to the published material.

The board has yet to specify how campus officials might implement this approach or how federal agencies funding dual-use projects might ensure compliance with guidelines for prepublication review. More detailed recommendations will not be ready before NSABB's next meeting in October, but several panelists suggested that the primary responsibility for oversight will likely fall upon institutional biosafety committees (IBCs), "which might need to be modified to include biosecurity experts," Kasper says.

The process would likely involve the following: An institutional oversight committee, either the IBC itself or another body appointed by the university administration, would first review proposals from researchers to determine, based on answers to specific questions, whether their

projects have potential for misuse. If a project were to meet the standard for dual use—which the board has defined in broad terms as research leading to knowledge that could be misapplied to threaten "public health, agriculture, plants, animals, the environment, or materiel"—the proposal would be flagged accordingly before being submitted to a federal agency for funding. Papers and presentations arising from the work would need to undergo review by the same oversight body or a different one. In addition, journal editors accepting such submissions would be encouraged to conduct similar reviews of their own. Authors would have the option of appealing institutional decisions to modify their papers or prevent publication.

Even so, says toxicologist Gary Miller, chair of the IBC at Emory University in Atlanta, Georgia, scientists are likely to balk at "prepublication screening" by institutional officials.

—YUDHIJIT BHATTACHARJEE

CREDIT: ANDREW THOMAS RYAN

SCIENCE FACILITIES

NSF Reopens Competition for Site To Build Underground Lab

The long, strange quest to build a U.S. underground lab has taken another unexpected turn. A year ago, the National Science Foundation (NSF) announced that only two locations remained in the running to house the proposed Deep Underground Science and Engineering Laboratory (DUSEL)—which would conduct experiments in particle physics, geology, microbiology, and other fields (*Science*, 29 July 2005, p. 682). But last month, NSF reopened the site competition to all comers. The reversal was prompted by an appeal from a losing group, but that group has now decided not to reapply.

“There had been concerns raised that, in going with two awardees, we may have cut things off at too early a stage,” says Judith Sunley, acting assistant director for math and physical sciences at NSF, about last year’s decision to award \$500,000 each for conceptual designs at the abandoned Homestake gold mine in Lead, South Dakota, and the active Henderson molybdenum mine near Empire, Colorado. NSF said it would choose three to five finalists from among the eight candidates, and many researchers grumbled when it didn’t.

The about-face has failed to appease critics, who say the Homestake and Henderson groups, which have already submitted their conceptual designs, have an insurmountable advantage. “For all practical purposes, it’s not open to anyone beyond Henderson and Homestake,” says Robert Bodnar, a geochemist at Virginia Polytechnic Institute and State University in Blacksburg.

The push for a deep underground lab began with a campaign to persuade federal lawmakers to take advantage of Homestake before the mine was abandoned and began flooding in 2003 (*Science*, 15 February 2002, p. 1213). That lobbying effort failed, however, allowing NSF to take the more traditional route of engaging the broader scientific community. When the agency chose the finalists last summer, NSF officials said that the depth of the two mines and their geologic characteristics and existing infrastructure set them apart from the other candidates, four of which would have required massive excavation.

Researchers from the University of Washington, Seattle, who had proposed a site at Icicle Creek in the nearby Cascade Mountains, appealed NSF’s decision. They argued that NSF considered factors beyond the intended scope of its assessment, such as opposition from a local citizens’ group. Last month, NSF granted the appeal, and in a 12 June letter offered the team \$500,000 and extra time to prepare a conceptual design.

That’s when things took a bizarre turn. On 14 June, the group accepted the offer but told NSF that it wanted to focus on a second site in nearby Pioneer Tunnel. The group changed its plans in large measure because it would be far easier to get permission to use the privately owned tunnel, says John Wilkerson, a physicist at the University of Washington, Seattle. Eight days later, NSF withdrew its offer. “We can only grant a reconsideration request on a project as originally proposed,” says NSF’s Sunley.

Sunley’s 12 June letter also announced NSF’s decision to mount an open competition. Ironically, the Washington group doesn’t plan to enter. “We were disheartened by the [appeal] process,” Wilkerson says. “That certainly factored into our thinking about the



Figure. Researchers who had planned to tunnel under Washington state’s Cashmere Mountain say they won’t enter the new NSF competition for a lab site.

probability of a successful proposal.”

Meanwhile, the Henderson and Homestake groups worry that a delay will sap their momentum. A new solicitation will go out in September, Sunley says, with proposals due in December and a final decision next spring, 6 months later than the original timetable. But even with an agreed-upon site, DUSEL is hardly a sure bet. NSF would have to find room in its budget for such a lab, which could cost as much as \$300 million to build and an unknown amount to outfit. **—ADRIAN CHO**

Biodiversity Experts Unite

Scientists from 13 nations want to carry out a new global assessment initiative to help warn policymakers of the world’s coming “biodiversity crisis.” In a statement published this week in *Nature*, the scientists say the assessment is needed because “biodiversity is still consistently undervalued” by governments and current efforts are insufficient. The group envisions a body with the authoritative voice of the Intergovernmental Panel on Climate Change; the Convention on Biological Diversity and other current efforts, it says, are not sufficiently interdisciplinary. “The biodiversity science community has to create a way to get organized,” says World Bank Chief Scientist Robert Watson. The French government recently funded a series of consultations to sketch out organizational plans.

—ELI KINTISCH

To the Shores of Tripoli

Last week, the U.S. government put a down payment on its plans to build scientific ties with Libya. At a meeting in Tripoli, the U.S. Department of Health and Human Services announced a \$1 million grant for Libya to strengthen pandemic flu preparedness, disease surveillance, and lab capacity. The high-level Tripoli discussions also explored potential collaborations in areas such as water, education, health, and the environment. Given Libya’s oil wealth, “money is not the issue,” says delegate William Colglazier, executive officer of the U.S. National Academy of Sciences. Both sides also pledged to improve passage for scientists and students traveling between the two countries.

—RICHARD STONE

Mano a Nano

U.S. federal agencies should better coordinate and increase funds to investigate health and environmental effects of nano-sized particles, according to a report released this week by Andrew Maynard, chief scientist for the Woodrow Wilson Center for International Scholars Project on Emerging Nanotechnologies in Washington, D.C. The report called for more than tripling the \$30 million a year the U.S. National Nanotechnology Initiative currently spends on work the report labels as “generally relevant” to nano risk research. The report also says those efforts are not well synchronized; risk research is “all over the place,” says DuPont toxicologist David Warheit.

—ROBERT F. SERVICE

ECOLOGY

Pollinator Diversity Declining in Europe

Several studies have suggested that particular pollinating insects might be in trouble—the domesticated honeybee in the United States, for example—but there has been little evidence for a large-scale problem. That is about to change: On page 351, a team led by Jacobus Biesmeijer and William Kunin of the University of Leeds, U.K., report a significant decline in pollinator diversity across the U.K. and the Netherlands since 1980. “They’re going down, absolutely,” says ecologist Jane Memmott of the University of Bristol, U.K. The study found that insect-pollinated plants in the two countries have also run into trouble, but the authors and others acknowledge that it’s difficult to prove that the loss of pollinating species is to blame.

Establishing a widespread trend for pollinators was a massive task. As part of a European Union biodiversity research program called ALARM, Biesmeijer helped gather nearly 1 million records of when and where various bees and hoverflies had been collected. Many records came from amateur naturalists, including Victorian vicars, whereas others came from scientists. After applying techniques to make all the data comparable, the team divided the countries into squares 10 kilometers on a side and compared pollinator diversity before and after 1980.

Bees have been stung by the biggest losses. There were statistically significant declines in bee diversity in 52% of the U.K.’s cells and in 67% of the Netherlands’. Only a small fraction of the cells displayed increases in bee diversity. The extent of the decline is “worse than I had feared,” says entomologist Peter Kevan of the University of Guelph in Canada. Others note that experiments have shown that a diversity of pollinators can help maintain the diversity of plant communities, and vice versa.

The situation is far less grim for hoverflies. British hoverflies declined in 33% of cells but increased in 25%. In the Netherlands, hoverfly diversity has actually increased in more cells than it has decreased. It’s not entirely clear why, but hoverflies seem to do better in farm fields than bees do, and they do not depend entirely on nectar for food.

Specialist hoverflies and bees—those that live in a narrow range of habitats or pollinate

only a few species of plants—were particularly hard hit. They experienced greater declines in distribution than less choosy pollinators in both countries. “Many of the rare species are now so rare that they will probably go extinct [in these regions] in the next decades,” Biesmeijer predicts. The declines are probably due to destruction of habitat or agricultural changes; the team is analyzing the ALARM database for clues.

To see whether plants have been affected on a national scale by declines in pollinator diversity, Biesmeijer and his colleagues pored over botani-

cal atlases. In the U.K., 75 wild plants that need insects for pollination had declined in distribution, whereas 30 that are pollinated by wind or water increased overall. In the Netherlands, where just the bees have declined, only bee-pollinated plants lost ground. “It seems too cozy to be coincidence,” says Kunin.

Biesmeijer and Kunin suspect that there is a causal relationship between the pollinator and plant declines, although it’s not clear which is driving the trend. Ecologist Jaboury Ghazoul of the Swiss Federal Institute of Technology in Zurich is skeptical that recent pollinator declines have affected plant populations; he thinks it’s more likely that human disturbances, for example, favor weedy, wind-pollinated plants. Others fear that the loss of bees and other pollinators will have a clear agricultural impact. Says pollination ecologist Juliet Osborne of Rothamsted Research in Harpenden, U.K., “There is an economic reason to be worried.”

—ERIK STOKSTAD



Rarer. In Britain and the Netherlands, wild bees, such as *Andrena gravida* (above), are declining.

PARTICLE PHYSICS

Europe Draws Up Road Map, With Added CLICs

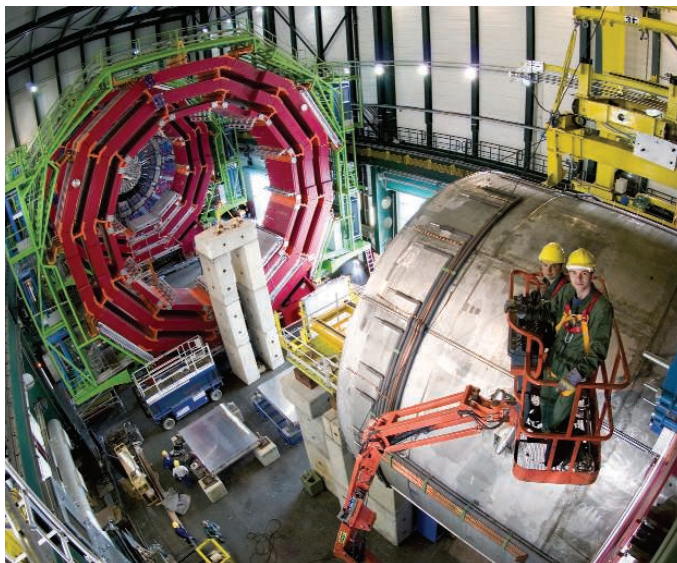
European particle physicists last week laid out their priorities for the future in a document that gives top billing to the nearly completed Large Hadron Collider (LHC) at CERN, the European particle physics lab near Geneva, Switzerland. Commissioned by the CERN Council, the adopted road map runs parallel to

a recently released U.S. strategy but differs slightly about future machines—a nuance that has raised some eyebrows.

When CERN was founded 52 years ago, it was tasked with both running its central laboratory on the French-Swiss border and coordinating European particle physics. For the first

half-century, the lab took precedence. But with the increasing cost and globalization of particle physics experiments, the CERN Council, made up of one government representative and one scientist from each of the 20 member states, last year appointed a committee to draw up an European strategy, says Council President Enzo Iarocci.

At a meeting last week in Lisbon, Portugal, the council voted unanimously to accept the committee’s recommendations. The report’s main focus is ▶



Top priority. European particle physicists’ main goal is to complete the Large Hadron Collider, whose CMS detector is shown during assembly.

CREDITS (TOP TO BOTTOM): ROY KLEUKERS/EIS NATURALIS; CERN GENEVA

the LHC, which is scheduled to start smashing protons together sometime next year. With its unprecedented energy, physicists expect to discover new particles—including the Higgs boson, which according to theory endows everything from quarks to freight trains with mass, as well as shadowy partners predicted by supersymmetry theory which correspond to all the known particles.

“But once you have made the discovery, then you have to understand what you have found,” Iarocci says. To do this, physicists agree, instead of large, messy hadrons, you need to collide pointlike electrons and anti-electrons in a linear collider. Hence the strategy endorses the International Linear Collider (ILC), a project that many consider to be the next big particle physics machine. A global design effort is currently working out details, and a final blueprint is scheduled for 2008.

Besides LHC and ILC, the strategy makes broad recommendations on how European research should be carried out—giving special attention to advanced accelerator R&D and a possible future neutrino factory. Many of the same points are included in EPP2010, a report commissioned by the U.S. National Academies and released in April. “It’s a great relief that they say the same things,” says EPP2010 committee member Jonathan Bagger of Johns Hopkins University in Baltimore, Maryland. He thinks the coherent messages will help efforts to resuscitate the flagging U.S. particle physics program.

The European strategy differs from EPP2010 in one main respect: Between the LHC and ILC, it inserts another type of linear collider, dubbed CLIC, which is currently under development at CERN. CLIC would use a low-energy particle beam to drive the adjacent main beam to energies five times as high as the ILC can achieve in the same length. Most researchers consider this two-beam acceleration scheme a promising but still unproven technique for the future, but the fact that CLIC is listed before ILC has turned some heads. “It’s the only real issue I have with the strategy,” says Brian Foster of Oxford University, who leads the ILC design effort in Europe.

But Iarocci says that the ordering is not meant to be a prioritization. And committee member Albrecht Wagner, director of Germany’s DESY particle physics lab, notes that the European strategy includes CLIC in a broad recommendation for accelerator R&D, whereas it describes the ILC as “fundamental”—which in its predefined vocabulary means it is “absolutely necessary for advancement.” Foster is satisfied with that: “The wording overrides the positioning.”

—MICHAEL SCHIRBER

Michael Schirber is a writer in Lyon, France.

ASTRONOMY

Result Rattles Dark-Matter Machismo

WIMPs versus MACHOs has turned into EROS versus MACHO.

An astronomical collaboration looking for signs of the mysterious dark matter surrounding the Milky Way reported in 2000 that it had evidence of relatively large numbers of massive compact objects in the galactic halo (MACHOs). The team, known as the MACHO collaboration, said its observations show that such objects—possibly ancient, burnt-out dwarf stars about half as massive as the sun—make up roughly 20% of the Milky Way’s dark matter, an amount comparable to the mass of all the galaxy’s stars. That would imply that the other leading dark-matter candidate—weakly interacting massive particles (WIMPs)—accounts for most of the galaxy’s unseen mass.

Now a new analysis from a competing team suggests that MACHOs may not even exist in substantial numbers. This collaboration, known as EROS-2, concludes that MACHOs contribute at most 7% of the halo mass and probably much less. “This is in clear conflict with the MACHO result,” the EROS-2 team declared in a paper posted online last week (11 July) at arXiv.org.

“It’s an important paper,” says Kim Griest of the University of California, San Diego, a member of the MACHO team. But he says it’s too soon to be sure of its implications.

Andrew Gould, an astronomer at Ohio State University in Columbus and a member of the EROS-2 group, says the new analysis does not definitively disprove the MACHO team’s conclusions, but “it argues that there are basically no contributions to dark matter from compact objects.” If so, WIMPs would likely account for almost all the halo dark matter.

Both teams sought MACHOs using a technique known as microlensing. The gravity of a MACHO passing in front of a distant star distorts its light, causing the star to temporarily brighten for a period of days, weeks, or longer.

MACHO and EROS searched for such lensing signals from stars in the Magellanic Clouds, small satellite galaxies to the Milky Way. A brightening of a Magellanic star could indicate the presence of an intervening MACHO in the Milky Way’s halo.

In almost 6 years at the Mount Stromlo Observatory in Australia, the MACHO team observed nearly 12 million stars in the

Large Magellanic Cloud and reported 17 possible MACHO sightings. The EROS-2 project (and its predecessor, EROS-1), using European Southern Observatory telescopes at La Silla, Chile, also reported several lensing events.

But after reanalyzing its data, EROS-2 has now ruled out all but one of its MACHO candidates from observations of nearly 60 million stars. That result is statistically irreconcilable with the MACHO estimate of a halo hiding 20% of its mass in dark compact objects. “The weight of the evidence is ... that the mysterious dark population is not really there,” Gould says.

Unlike the MACHO collaboration, the EROS team considered only the brightest stars, fewer than 7 million. Changes in the brightness of such stars caused by lensing are supposedly less susceptible to confusion with natural variations, and analyzing bright stars avoids the complications caused by the blended light of faint stars.

But choosing the wrong threshold for selecting the brightest stars could skew the lensing data, says a member of the MACHO team, David Bennett of the University of Notre Dame in Indiana—especially in the central region of the Large Magellanic Cloud, where stars are densely packed. Bennett also notes that the new EROS-2 paper has been submitted for publication but not yet refereed and accepted. “We think there are probably some things that need to be changed,” he says.

—TOM SIEGFRIED

Tom Siegfried is a writer in Los Angeles, California.



Big question. Light from the Large Magellanic Cloud should reveal mysterious dark objects within our galaxy—but are they there?

With an unprecedented countrywide survey of human-rights abuses, statisticians have calculated the tragic numbers from Sierra Leone's decade of civil war—and pointed out who may be most to blame

Grim Statistics

TO MANY, FORMER LIBERIAN PRESIDENT

Charles Taylor personifies Sierra Leone's decade of conflict. The Special Court of Sierra Leone has indicted him for numerous war crimes, including supporting rebels seeking to destabilize the country, and he was arrested in Nigeria in March. Last month, after the United Kingdom agreed to imprison Taylor if he is convicted, he was transferred to The Hague, where his trial will finally take place. But Taylor is not the only target of the Special Court. It has handed down a dozen other indictments, more than half of them for leaders of various rebel groups, including the Revolutionary United Front (RUF) that Taylor backed. Some of those trials are already under way.

Yet prosecutors, human-rights activists, and researchers are still uncovering the enormity of what happened in Sierra Leone during its 1991–2000 civil war. In a soon-to-be-released statistical analysis funded by the U.S. State Department, scientists have put together the most credible figures yet on the tragedies that unfolded. After conducting an unprecedented survey involving face-to-face interviews with 3633 randomly selected households from across all of Sierra Leone's 150 chiefdoms, the authors of the analysis conclude that more than 25% of the country's 5 million people were forced from their homes and approximately a quarter-million saw their property destroyed during the conflict.

The survey's results, which were incorporated into a draft report to the State Department—a public version with additional analysis will be available later this year—include estimates of the prevalence of more violent crimes as well: Approximately 140,000 civilians suffered assaults and beatings, 95,000 were arbitrarily detained, and several thousand suffered amputations. In addition, about 25,000 were raped, and nearly 10,000 were forced into sexual slavery. The researchers expect to release an estimate of the total death toll this fall. In a new project cosponsored by AAAS (the publisher of



Science), they also hope to use the survey's results to guide humanitarian efforts in the still-devastated country (see sidebar, p. 289).

Some familiar with the ambitious effort, known as the Sierra Leone War Crimes Documentation survey, see part of its value as a proof of concept. "The real novelty is that this experience shows that you can have a survey-based approach for measuring massive human violations in a dangerous country with sensitive respondents raising very sensitive issues. It was argued before that this kind of exercise was impossible because you couldn't get people to answer, or data wouldn't be good enough for robust statistical analysis," explains Raul Suarez de Miguel, who runs a project on documentation of human-rights violations for the Organisation for Economic Co-operation and Development. "Thanks to the Sierra Leone survey, we can now imagine replicating this kind of survey in other parts of the world."

Perhaps as important, the survey indicates which of the warring rebel and government groups in Sierra Leone were most responsible for atrocities. The new statistical analysis could be entered into evidence at the Special Court, but it's not clear by whom. Some who have seen the data say it could actually help certain defendants by shifting the blame for a large share of atrocities to other factions, such as the group affiliated with Taylor.

Witness to horror. Thousands of people lost limbs in the gruesome amputations perpetrated during Sierra Leone's civil war. Researchers are now revealing the magnitude of human-rights violations in the country.

From Yugoslavia to Sierra Leone

Reducing 10 years of civil war in a largely illiterate country populated by more than 20 different tribal groups to numbers wasn't easy, especially because many crimes happened in the countryside, far from any communications infrastructure. The new effort, from a team led by statistician Jana Asher, a Ph.D. candidate at Carnegie Mellon University in Pittsburgh, Pennsylvania, was a joint project of the American Bar Association (ABA) and Benetech, a California company that produces technology for social good.

In some ways, the Sierra Leone survey is the outgrowth of an earlier statistical analysis that Asher and Patrick Ball, director of Human Rights Programs at Benetech, did for the trial of Slobodan Milosevic, the former president of Serbia and later Yugoslavia who was accused of war crimes and human-rights violations. Ball, who was with the AAAS Science and Human Rights Program at the time, presented those results to the United Nations International Criminal Tribunal for the former Yugoslavia, although Milosevic died of a heart attack before his trial ended (*Science*, 22 March 2002, p. 2188).

For that study, Ball and Asher analyzed data collected by other groups, including nongovernmental organizations (NGOs), such as Human Rights Watch, and border-crossing guards. They used a technique called multiple systems estimation (MSE), which was originally developed to count wildlife and has been adapted for epidemiology work and human-rights data analysis. Most data sets available to human-rights researchers document just a piece of a greater conflict. Even when researchers collect their own data, they frequently rely on what statisticians call convenience samples—for example, responses to a call for testimony from anyone who suffered a human-rights violation.

MSE's strength is that it can use two or more separately collected but incomplete lists of a population, such as displaced people, to determine a total population size. However, its formula relies on assumptions that are virtually never true in the context of human-rights data collection, namely that each individual in a population is equally likely to be captured on a list and that there are no dependencies between the lists. As a result, researchers have expended a great deal of effort on statistical modeling to account for dependencies.

Through a combination of luck and timing, Sierra Leone became the testing ground for a different approach, a randomly sampled household survey of human-rights violations.

A prosecutor for the Special Court for Sierra Leone who had seen the Milosevic work approached an ABA representative who coordinated that study to ask whether data analysis could help the court better understand the Sierra Leone conflict. Ball, who was leaving AAAS for Benetech, saw the chance to try a random-sample survey on a larger scale than had been done before. Benetech and ABA decided to collaborate on a new project on Sierra Leone, and ABA hired Asher to lead the survey component of it.

Random-sample household surveys are "always hard to do ... in the underdeveloped world, and [they are] incredibly hard to do in an unsettled community," says David Banks, a professor of statistics at Duke University in Durham, North Carolina. "It's certainly novel

to do it from a rights standpoint, and [this survey] is certainly a big deal."

On the ground

In January 2004, Asher touched down in Freetown to start her survey. Other groups had already questioned many people about the conflict; the Sierra Leone Truth and Reconciliation Commission (TRC) interviewed 7706 people, and an NGO called the Campaign for Good Governance had talked to more than 1000. However, because both groups used convenience samples, neither set of data could be used to independently estimate the total prevalence of war crimes across the country. And it seemed likely that both groups, which collected testimony primarily in the cities, would have missed crimes in the countryside.



Finding the crimes. Jana Asher (far right) and her partners spent 9 months visiting all of Sierra Leone's 150 chiefdoms for a war-crimes survey.

From Accountability to Rebuilding

The conflict in Sierra Leone is officially over, but the country is still recovering. Life expectancy there is only 40; in the 2005 United Nations Human Development Index, Sierra Leone ranked second to last out of 177 countries.

Having surveyed more remote regions in Sierra Leone than anyone since the conflict ended, Jana Asher and her colleagues got a close view of the damage (see main text). Asher recently took a position with the Science and Human Rights Program at AAAS (the publisher of *Science*), where she is now reanalyzing the data she gathered on human-rights violations to document humanitarian needs. For example, although rape and dismemberment were some of the most visible crimes, many more people lost homes and had their property destroyed or stolen during the fighting. Asher and the American Bar Association plan to release a "needs map" for Sierra Leone by year's end, which they'll make available to nongovernmental organizations.

"Reparations need to include helping people rebuild," says Asher. Her current work shows that 63% of the violations reported to her team during the survey were forced displacements. This is far more than other groups had found. Only about 20% of the violations recorded by the country's Truth and Reconciliation Commission, which took statements from more victims but didn't go out into the countryside, were displacement. Asher doesn't discount the severity of other crimes—in fact, she hopes to document the geographic distribution of sex crimes, to show where clinics are needed—but she notes that for people already living on the edge, the loss of a home and livestock can prove fatal.

—R.M.



Legal review. The Special Court of Sierra Leone (above) is judging the fate of those accused of human-rights violations and war crimes during the country's civil war. One defendant is the recently arrested Charles Taylor, former president of Liberia (right).

Asher talked to about half as many people as TRC did, but her staff of 32 was the first to cover the whole country, a feat that took 9 months. Although Sierra Leone is slightly smaller than South Carolina, many regions are almost inaccessible to outsiders. One survey team hiked for 16 kilometers to get to a site—after a 16-hour boat ride.

The members of Asher's local staff, whom she calls her "partners" to emphasize their importance, were key to obtaining cooperation from respondents. They suggested, for example, that team leaders visit with the many Sierra Leone chiefs before interviewing households in each one's territory. That encouraged otherwise reluctant villagers to talk, says Asher. Local staff also helped her figure out the best way to get people to discuss touchy subjects such as rape and worked with her on the innovation she's most proud of: a method of determining dates for the survey.

In illiterate societies, victims frequently cannot give calendar dates for when crimes occurred. For the Sierra Leone survey, the team developed a list of seven landmark events that virtually everyone would remember from the civil war, such as "the invasion from Liberia" and "the attack on Freetown." Using these landmarks as reference points in combination with questions about seasons and ages of family members, interviewers were able to determine the age of a victim and the date of a crime to within a year in more than 99% of the interviews.

Asher's team also did four rounds of field tests for the survey, ensuring that its questions were conceptually equivalent in each of the six languages the interviewers used. During this



testing, she discovered that the idea of human-rights abuses didn't exist in all of the languages, so the surveys were reworded around the concept of "suffering."

Asher "sets an example for us," says Fritz Scheuren, vice president of statistics and methodology at the National Opinion Research Center and past president of the American Statistical Association, who calls her work "the best I've ever seen of understanding the difficulties of working across cultures."

Asher's estimates still have good-sized confidence intervals—for example, the figure of approximately 96,000 who were arbitrarily detained is plus or minus 14,000—but the numbers are more precise than what is normally available after a decade of civil fighting in a developing country. Suarez characterizes the result as "the difference between having an idea that something occurred and having data structured" so that you can analyze it to determine the magnitude of abuses, the geographic distribution, and whether conditions are improving or deteriorating over time. "This is where science can really contribute to human rights," he says.

For example, it was widely believed that the RUF was responsible for the worst violations. The survey puts numbers to the claim, finding that the RUF committed 40% of the nonfatal war crimes, and "rebels" whose affiliations aren't completely understood committed another 30%. The Civil Defense Force (CDF) and Sierra Leone Army, whose alleged leaders have also been indicted by the Special Court for Sierra Leone, perpetrated 4% and 3% of the crimes, respectively.

On trial

The survey wasn't without problems. Several of the interviewers came down with malaria or typhoid severe enough to require medical evacuations. Since the interviews in Sierra Leone have ended, the research team also has fractured. Asher and Ball both signed off on the report to the State Department, but they are no longer speaking. Both independently plan to analyze deaths as a function of other violations, such as forced migrations and amputations, to show how each contributes to death during conflict.

Ball is now using the Sierra Leone survey, along with data sets collected by TRC and Campaign for Good Governance, to develop software that automates part of the MSE work. He expects to focus primarily on MSE in future Benetech projects. "Surveys cost a lot more than MSE," he says, particularly when there are already-existing data sets.

At this point, it's unclear whether the Special Court for Sierra Leone will use Asher's survey in legal proceedings. "The idea was always that the information would be available to them if they need it," says Wendy Betts, the original ABA lead on the project. (She is now program director at the National Center for State Courts International Division.) "It depends on ... the prosecution's strategy. It happened in Kosovo that the data helped show that the attacks were widespread, which was key to the case."

Yet Asher's results could be exploited by some defendants, notes Ball. Out of the Special Court's 13 indictments, five were for alleged RUF leaders, one for Charles Taylor, and the rest, including three for CDF leaders, are for others. That distribution bothers him: "Even the most casual observer of the statistics can see that the CDF is not responsible for the majority of crimes. ... That's false moral equivalence."

Betts considers the documentation of proportional responsibility more in the context of future human-rights tribunals. "It could have implications as to how courts use their resources next time," she says. Unfortunately, when it comes to human-rights violations and war crimes, there always seems to be a next time.

—ROBIN MEJIA

Robin Mejia is a freelance writer in Santa Cruz, California.

CREDITS (TOP TO BOTTOM): THE SPECIAL COURT FOR SIERRA LEONE; GUIDO BENSCHOP/AFP/GETTY IMAGES

PARTICLE PHYSICS

Neutrino Hunters Go Nuclear to Tackle Antimatter Deficit

A team in China and others around the globe hope an obscure property of neutrinos may answer the question of why the universe isn't full of antimatter

HONG KONG—It's nearly 1:30 a.m. when three unmarked cars ease into a deserted tunnel linking Hong Kong's central business district and Aberdeen, a residential community in the island's southwest corner. About halfway through the mountain passage, which is closed for maintenance, the cavalcade rolls to a halt beside a cavernous service hall. A young man leaps out and unlocks a steel door, and his colleagues swarm into a tiny, humid room hewn from granite. After a couple of hours of fiddling with electronics and scintillation counters, the group huddles around a computer. "We have a signal," says a young physicist, beaming with pride.


This is no spy operation. The physicists in the Aberdeen Tunnel are testing their scintillation counters by spotting muons, particles produced when cosmic rays slam into the upper atmosphere. The setup is a prelude to an ambitious attempt to slay one of physics's most obdurate dragons: Why is there so much more matter than antimatter in the universe? Construction is planned to begin in 2007 on the main attraction 55 kilometers northeast on the mainland: the Daya Bay Neutrino Experiment—a set of detectors up close and personal with a nuclear power plant. Last month, the Chinese government pledged \$6.25 million to the effort.

Daya Bay and four similar efforts worldwide are vying to measure a fundamental property of neutrinos, ghostly particles that rarely interact with normal matter. Only in the past decade have physicists confirmed that neutrinos have mass, albeit minuscule, and oscillate between three flavors: electron, muon, and tau neutrinos. Physicists have enumerated four measurable oscillation properties: three "mixing angles" and the charge-conjugate parity (CP) value. Two angles are known from studies of neutrinos from the sun, the atmosphere, reactors, and accelerators. Only an upper limit has been reached for the third mixing angle, θ_{13} , while the CP value remains an enigma.

CP is of supreme significance: If neutrinos violate CP, that could explain why antimatter is now so scarce. Quarks are proven CP violators, but that's "not enough" to explain the matter-antimatter imbalance, says Ming-Chung Chu, a theoretical physicist at the Chinese University of Hong Kong. "CP violation in neutrinos is what we really need to go after," adds physicist Kam-Biu Luk of the University of California, Berkeley, and Lawrence Berkeley National Laboratory. The only way to

solve the riddle is to first measure θ_{13} .

Enter Daya Bay and its brethren. They will use nuclear power plants to study θ_{13} . The nuclear chain reaction produces a flood of electron antineutrinos, which are assumed to have the same fundamental properties as neutrinos. All five experiments will install a detector near a reactor to measure antineutrino flux and then place an identical detector a certain distance away. The few antineutrinos that might oscillate as they travel that distance will evade the second detector because it can register only electron antineutrinos. This dip in antineutrino



Limbering up. Kam-Biu Luk examines a scintillation counter in the Aberdeen Tunnel.

The Race for θ_{13}

Project	Location	Present power (gigawatts)	Start-up (projected)	Maximum sensitivity* (est. after 2 yrs)
Angra	Brazil	6	2013	0.007
Daya Bay	China	11.6	2010	0.008
Double Chooz	France	8.7	2007	0.02
KASKA	Japan	24.3	2009	0.015
RENO	South Korea	17.3	2009	0.03

* $\sin^2 2\theta_{13}$

Sources: Kam-Biu Luk; Maury Goodman; Argonne National Laboratory; Fumihiko Suekane; Institut National de Physique Nucléaire et de Physique des Particules.

flux would yield θ_{13} . Most theorists believe that the target value— $\sin^2 2\theta_{13}$ —lies between its present limit of 0.19 and 0.01, says Maury Goodman, a neutrino physicist at Argonne National Laboratory in Illinois.

Physicists need as large a supply of antineutrinos as possible, because few will actually interact with the detectors, and even fewer will oscillate and show up as a deficit. The detectors must be shielded from background radiation that can mimic the antineutrino signature. The teams plan to cocoon their detectors—in all five cases, massive tanks filled with a gadolinium-

doped scintillator solution—inside a mountain or in an underground shaft and sheathe them in water or metal to absorb particles other than antineutrinos. However, cosmic-ray muons can barrel through these defenses. And that's why Aberdeen Tunnel is a good warm-up: Physicists hope to learn how to differentiate between the flashes caused by muons and antineutrinos.

Daya Bay won't be the first out of the gate. The French-led Double Chooz group aims to start taking data next year. Nor will Daya Bay have access to the biggest antineutrino source: The Japanese KASKA team intends to track the particles from the world's most powerful assemblage of reactors, the Kashiwazaki Kariwa Nuclear Power Plant near Niigata. "It's a healthy competition," says KASKA physicist Fumihiko Suekane of Tohoku University. But thanks in part to favorable positions right up close to the Daya Bay Nuclear Power Plant and its neighboring Ling Ao plant, the Daya Bay experiment is poised to be the first to reach the 0.01 benchmark within 3 years of start-up.

Whether that will be good enough to snare θ_{13} is an open question. "It's unknown exactly how sensitive these experiments will be," cautions Goodman, the U.S. spokesperson for Double Chooz. He says that initial measurements "will be steps along the way to more precise experiments."

The Daya Bay collaboration is headed by Luk and Wang Yifang of the Institute of High Energy Physics in Beijing, who have assembled a 100-strong team from 24 institutions in four countries. The group has cash in hand from the Chinese Academy of Sciences, and commitments are expected this fall from China's Ministry of Science and Technology and other agencies. The U.S. Department of Energy is also backing Daya Bay with \$800,000 for R&D this year and is expected to add more. "It's groundbreaking for us. Hong Kong has never been involved in a physics project of this kind," says Chun-Shing Jason Pun of the Uni-

versity of Hong Kong. And it is strengthening scientific links across the Taiwan Strait, with three Taiwanese and seven mainland institutions taking part.

There's always a chance that the predictions are wrong and that the θ_{13} value will be much smaller than 0.01, perhaps even 0—and frustratingly out of reach. That would leave experimentalists and theoreticians alike scratching their heads. Chu, for one, is not perturbed by that prospect. "That would mean new physics," he says. "Either way, we can't lose."

—RICHARD STONE



SCIENCE IN IRAN

Picking a Path Among the Fatwas

Scientists in Iran find themselves challenged by true believers; some are trying to negotiate a peaceful compromise

TEHRAN—Scientists and philosophers mingled with clerics in robes and turbans here at a recent gathering in Iran’s cavernous new international conference center. They had come to discuss science and religion—specifically, to seek common ground between Western science and the tenets of Islam. The Iranian intellectuals who helped organize the meeting* are hoping for a kind of détente that will help Iranian scholarship blossom. They were encouraged at the outset by Gholam Ali Haddad-Adel, president of the Iranian parliament, who offered the contingent of foreign academics a warm welcome.

But 2 days into the meeting, a chill filtered through the halls. Iran’s government-controlled newspapers announced that a prominent Iranian sociologist, Ramin Jahanbegloo, had been arrested at the airport on his way to a conference in Belgium. His crime, according to the reported comments of Iranian Minister of Information Mohsen Ejei, amounted to “contacts with foreigners.” Another state-controlled paper described Jahanbegloo as “an element of the United States who is part of the plot to overthrow the regime under the guise of intellectual work by peaceful means.” No other charges have been cited. As *Science* went to press, Jahanbegloo was still being held without legal council in a prison notorious for torture. Hundreds of academics around the world have signed a letter to the Iranian government calling for his release.

* First International Congress on the Dialogue Between Science and Religion, sponsored by Tehran University of Medical Sciences, 1–4 May.

The foreigners who were aware of the arrest left the meeting uncertain about the government’s intentions for Iranian academia. Iranians are often confused, too. Interpreting the leadership’s signals can be difficult in a country where scientific achievement is revered but where the Koran—and a small group of clerics who interpret it—has the final say in all matters. And it can be disastrous to read the signals incorrectly.



Iran is investing heavily in science now, after decades of neglect (*Science*, 16 September 2005, p. 1802). Even the Iranian supreme leader Ayatollah Ali Khamenei has issued a fatwa, or edict, calling on researchers to

Open encounter. Clerics met with scientists and philosophers in Tehran in search of common ground.

secure Iran’s position as the “leader in science” in the Middle East over the next 20 years. But at the same time, discussing ideas that displease the religious elite can land you in jail. As Haddad-Adel told *Science*, “We do not allow our scientists to make propaganda against Islam.” Exactly what might constitute such propaganda is unclear, and Haddad-Adel declined to specify.

Many Iranian academics argue that science and Islam are compatible and that the challenge for each is to adapt to the other. “Iran is the world’s only laboratory for bringing science and religion together,” says Haddad-Adel, who was an academic philosopher before becoming one of Iran’s most powerful politicians. But what this might mean in practical terms for Iran’s scientists is uncertain. Some see any dialogue with the ruling clerics as helpful. “Most of the conflicts [between science and religion] are due to misunderstanding,” says Jamshid Darvish, an evolutionary biologist at Ferdowsi University in Mashhad. But others are wary; they fear that more entanglement with Iran’s religious conservatives will only lead to tighter controls over academia.

Dangerous questions

A glance at the evolution exhibit at Tehran’s museum of natural history reveals the tension below the surface. Wave after wave of schoolgirls in matching headscarves file past a row of glass cases containing meticulously arranged

“We do not allow our scientists to make propaganda against Islam.”

—Gholam Ali Haddad-Adel
President, Iranian Parliament

fossils. A label next to a trilobite, for example, says that the specimen, discovered in the nearby Alborz mountains, came from the Devonian, a period 400 million years ago when those sediments were submerged in a shallow sea. Along the opposite wall, a diorama chronicles the evolution of life on earth. Painted scenes of ancient life look as if they’ve been copied directly from the latest biology textbooks. But the exhibit takes a sharp detour from science in the final display case where evolution is summed up. In an open tome representing the Koran, phrases in calligraphy proclaim that “God willed an atmosphere created from gases” and “God created man from water.” Above that is a poster—published by the Creation Evidence Museum in Glen Rose, Texas—describing how Earth was created in a few days by an omnipotent being.

If this exhibit leaves you wondering what the curator actually believes, then that is probably by design. Under today's Iranian theocracy, "you are forbidden to deny the existence of god," explains Eghbal Taheri, a pharmacologist at the Tehran University of Medical Sciences. "You can do your science," she says, "but in the end you must choose your words carefully." For example, "you cannot say that the amazing cells in the eye are nothing more than a product of evolution over millions of years."

Religious constraints have consequences for academia, says an Iranian philosopher of science who spoke on condition of anonymity. "Censorship, and especially self-censorship, is everywhere," he says. "In my papers and presentations, I must often change the ending to include some religious aspects, even though I am agnostic, which of course I can never admit." The clerics ignore most of the sciences, he says. But potential hotspots in addition to evolutionary biology include psychology and neuroscience; researchers in these fields often take care to leave room for the existence of a soul, he says. "But most of all," he adds, "there's sociology," where the benefits of theocracy are questioned at a researcher's peril. This is the widely assumed motivation for arresting Jahanbegloo, although the Sorbonne-trained sociologist is not known for activism.

There is no consensus among Iranian scientists, however, on whether religious constraints are doing harm. Taheri acknowledges that censorship exists but says, "I do not think it inhibits our work." The chancellor of the Tehran University of Medical Sciences, Bagher Larijani, brother of Iran's nuclear negotiator, disagrees. "It is a problem," he says. "We scientists must approach [the religious leaders] very quietly and humbly to explain ourselves." Larijani, an endocrinologist and Iran's chief medical and research ethicist, says that such dialogues have already encouraged Iran to embrace research tools banned in other Muslim countries, including human embryonic stem cells and transgenic plants and animals. To meet Iran's 20-year science goal, he says, scientific and religious experts must come together to work out their differences. Or, as Shiva Khalili, a psychologist at the National Research Center of Medical Sciences in Tehran puts it, "science and Islam must be harmonized."

Science in the balance

The conference in Tehran—organized by Khalili and a diverse team of Iranian academics—was supposed to get the scientists and ayatollahs talking, but the discussions revealed as much discord as harmony. Speakers did not even agree on whether it made sense to bring religion and science together.

"Science is secular," says Reza Davari Ardakani, a philosopher at Tehran University and the current president of the Iranian Academy of Sciences. "We are pitting these two things against each other, but there is no reason to do so. Science and religion occupy different positions." Nonetheless, says Haddad-Adel, the "harmonization" will proceed, starting with the construction of a bricks and mortar institution in Tehran "to give a permanent home for the dialogue."



Mixed message. Visitors to Tehran's natural history museum can view standard displays on geology and evolution as well as a "creation evidence" poster from Texas.

The diverse menu of conference lectures gave a flavor of the dialogue to come. Some theologians brought Islamic ethics to bear on scientific issues such as human cloning and climate change. Their conclusions were similar to those of the Western mainstream: Reproductive human cloning should be banned, and the risks of climate change call for immediate action. Others wrestled with issues raised by science-oriented theologians in the West—such as whether the physical constants of the universe are fine-tuned to make life possible. With something less than scientific rigor, they cited the health benefits of prayer and belief in god while warning against the dangers of atheism. In the midst of this, Iranian academics gave lectures on everything from cosmology to evolutionary psychology.

Many Iranian scientists say that more interaction with the clerics is badly needed. Although applied science such as medical biotechnology receives the government's blessing, "we lack funding for basic research," especially evolutionary biology, says Darvish. Religious leaders need help understanding that embracing evolution "is necessary to solve problems in many fields, including medicine and the environment," he says. "We need today's biology to stay up to date."

Darvish is adamant that religion should stay out of the science classroom and laboratory. "In my classes, I only teach evolution and the mountain of evidence that supports it," he says. But science in Iran may not emerge from harmonization unaffected. Discussions at the conference touched on possible plans ranging from a voluntary science and religion seminar series, which Darvish supports, to a revision of science textbooks to include theology, which he rejects.

Which way this dialogue tips could determine how many of Iran's best researchers remain in the country or drain away to the West. "Science students are required to take a number of religious classes," says Hazineh Rahmandad, an Iranian engineer at the Massachusetts Institute of Technology in Cambridge. "But right now the burden does not prevent you from getting a proper scientific education," he says. "What worries me is that there seems to be a new push to change this equilibrium." Student protests erupted last year when Iran's ultra-conservative president, Mahmoud Ahmadinejad, appointed a cleric as chancellor of Tehran University. Critics say that the new chancellor's "forced retirement" of 40 members of the university faculty last month is part of an effort to eliminate dissent.

But optimists say the conservative trend will be short-lived. "I don't think there will be any Islamicization of science," says Saba Valadkhan, an Iranian molecular biologist at Case Western Reserve University in Cleveland, Ohio. "There is a new generation of pragmatic reformers in Iran, and they are the ones pushing for this dialogue between science and religion," she says. "That is the way to make science functional in a highly dysfunctional atmosphere."

—JOHN BOHANNON

Twinkling Stars May Reveal Stuff of Early Solar System

Australian researchers say dips in the brightness of stars may tell of a vast array of objects beyond the planets, but others aren't so sure

CATANIA, ITALY—The Kuiper Belt, resting place of much of the detritus left over from the creation of the solar system, may contain many more small objects than previously thought. Australian astronomers scanned the outer reaches of the solar system by looking for a brief dimming of the light of distant stars as subkilometer-sized bodies passed in front of them. Preliminary results presented at a workshop here earlier this month* suggest that huge numbers of such objects lurk beyond the orbit of Neptune. Although most Kuiper Belt researchers are cautious, studies by some other teams suggest the Australians may be onto something. “If this is true, it would be fantastic,” says Alessandro Morbidelli of the Observatoire de la Côte d’Azur in Nice, France, because information about the smaller denizens of the Kuiper Belt cannot be found any other way.

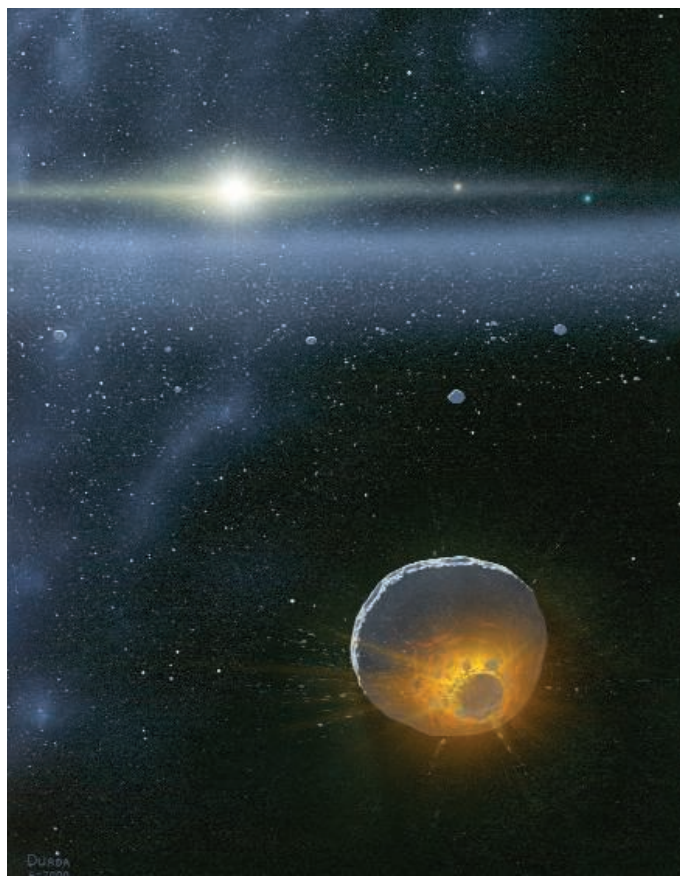
Astronomers have found more than 1000 bodies in the Kuiper Belt, including an object known as 2003 UB₃₁₃ (nicknamed Xena) that is slightly larger than Pluto. But because they are several billion kilometers away, even the most powerful telescopes can't see Kuiper Belt objects smaller than about a hundred kilometers across. Researchers are keen to know more about their size distribution, as it would shed light on the early youth of the solar system.

An effort to fill that gap has been going on since last year. The Taiwanese-American Occultation Survey (TAOS) operates three automated 50-centimeter telescopes at Lu-Lin Observatory, Taiwan, which scan starlight for telltale dimming that signals a Kuiper Belt object passing in front of, or “occulting,” the star. So far, the survey has drawn a blank. Team member Federica Bianco of the Harvard-Smithsonian Center for Astrophysics (CfA) in Cambridge, Massachusetts, says TAOS can't observe very brief dips in brightness, so it is capable of spotting only the relatively rare objects larger than a few kilometers in diameter.

* Trans Neptunian Objects: Dynamical and Physical Properties, Catania, Italy, 3–7 July.

But George Georgevits and Michael Ashley of the University of New South Wales in Sydney and Will Saunders of the Anglo-Australian Observatory in Siding Spring say the Kuiper Belt may team with objects too small for TAOS to see. Using a fast detector at the 1.2-meter U.K. Schmidt Telescope in Siding Spring, they saw well over a thousand brief brightness dips, each lasting for a tenth of a second or less, while monitoring dozens of stars for about 2 weeks.

“It's very important work, and they should certainly continue,” Morbidelli says. “But the



When worlds collide. Two icy bodies crash in the Kuiper Belt in this artist's depiction. Could such collisions have populated the belt with tiny objects?

results so far are very strange,” because current theories of the evolution of the solar system do not predict huge numbers of small Kuiper Belt objects. Michael Brown of the California Institute of Technology in Pasadena, who discovered 2003 UB₃₁₃, adds that “the believability factor [of these results] isn't very high. Unfortunately, you can never go back

and check.” But Georgevits counters that he has checked and ruled out every other possible cause of the stellar winks.

So are the results real? “Well, it seems they are observing *something*,” says David O’Brien of the Planetary Science Institute in Tucson, Arizona, although he adds that no one has yet carried out a detailed statistical analysis of the Australian results. According to O’Brien, collisions in the Kuiper Belt may have produced hordes of small objects. “If confirmed, these results could tell us something about the strength properties of Kuiper Belt objects,” he says.

Some other studies support the Australian results. Taiwanese astronomers have uncovered similar brief occultations of the well-known x-ray source Scorpius X-1 in data from NASA's Rossi X-ray Timing Explorer satellite. A team led by astronomer Ping-Shien Wu of the National Tsing Hua University in Hsinchu presented the finding in April at the Chinese Astronomical Society Taiwan's meeting in Taichung and is due to publish it in *Nature* next month. And at the Catania workshop, Françoise Roques of the Paris Observatory described three brief occultations detected with the 2-meter Bernard Lyot Telescope in the French Pyrenees, which Roques says may also represent small Kuiper Belt objects.

Not everyone is convinced. “They have to do more checks on possible false alarms,” says Matthew Lehner of CfA. For instance, the dips might be caused by unknown effects in Earth's atmosphere. To avoid these, you need to observe from space, says Lehner, who is part of a team that has pitched to NASA a \$425 million occultation mission called Whipple, which would detect Kuiper Belt objects as well as comets in the much more distant Oort Cloud.

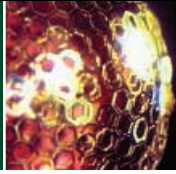
Meanwhile, Georgevits hopes to raise half a million dollars for a purpose-built ground-based telescope equipped with a very fast video camera. Such a device could survey the whole Kuiper Belt for a fraction of the cost of a space mission, he says. And although his team's preliminary results raised some eyebrows, everyone agrees on the need for a more comprehensive search. Says O'Brien: “Small Kuiper Belt objects will never be observed directly. Occultation surveys have a lot of potential to fill in this gap.”

—GOVERT SCHILLING

Govert Schilling is an astronomy writer in Amersfoort, the Netherlands.

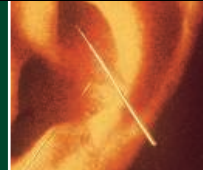
Self-assembly of
small materials

300



Studying alternative
medicine

303



LETTERS | BOOKS | POLICY FORUM | EDUCATION FORUM | PERSPECTIVES

LETTERS

edited by Etta Kavanagh

How and When Was Wild Wheat Domesticated?

ESTIMATING THE TIME SPAN OF PLANT DOMESTICATION IS FUNDAMENTAL TO UNDERSTANDING AND reconstructing the cultural processes underlying the “Neolithic Revolution.” In their Brevia “How fast was wild wheat domesticated?” (31 Mar., p. 1886), K. Tanno and G. Willcox argue for a gradualist model for wheat domestication in the ancient Near East and suggest that the domestication of cereals took over a millennium. Their biological explanation includes the difficulty of isolating nonbrittle spike genotypes and occasional collection from the wild at times of crop failure. This model is an important advance; however, several points require clarification.

First, spike disarticulation in wheat and barley is governed by major genes on chromosome group 3 (1), and therefore it is unlikely that the incipient farmers would have faced difficulties had they tried to select for such a phenotype once they noticed it in their cultivated fields.

Second, following Kislev *et al.*, it appears that considerable amounts of wheat and barley spikelets/grains may be gathered from the ground, after spike shattering (2). This may provide a possible mechanism underlying the gradual emergence of domesticated wheat, which is missing from the Tanno and Willcox model. If such practice persisted in early cultivated fields, it follows that the establishment of nonbrittle types would have been considerably delayed. This would probably be more significant than the effect of occasional gathering from wild stands, as suggested by Tanno and Willcox.

Third, in the context of the emergence of Near Eastern farming, the description of domestication as a series of events occurring at different places does not automatically follow from the data presented, nor is it in line with genetic evidence concerning chickpea, lentil, einkorn, and emmer wheat domestication, suggesting a localized event (3, 4).

SIMCHA LEV-YADUN,¹ AVI GOPHER,² SHAHAL ABBO³

¹Department of Biology, Faculty of Science and Science Education, University of Haifa, Oranim, Tivon 36006, Israel. ²Sonia and Marco Nadler Institute of Archaeology, Tel-Aviv University, Ramat Aviv, Israel. ³The Levi Eshkol School of Agriculture, The Hebrew University of Jerusalem, Rehovot 76100, Israel.

References

1. V. J. Nalam, M. I. Vales, C. J. W. Watson, S. F. Kianian, O. Riera-Lizarazu, *Theor. Appl. Genet.* **112**, 373 (2006), and citations therein.
2. M. Kislev, E. Weiss, A. Hartmann, *Proc. Natl. Acad. Sci. U.S.A.* **101**, 2692 (2004).
3. S. Lev-Yadun, A. Gopher, S. Abbo, *Science* **288**, 1602 (2000).
4. F. Salamini, H. Özkan, A. Brandolini, R. Schäfer-Pregl, W. Martin, *Nat. Rev. Genet.* **3**, 429 (2002).

IN THEIR BREVIA “HOW FAST WAS WILD WHEAT domesticated?” (31 Mar., p. 1886), K. Tanno and G. Willcox provide an interesting viewpoint regarding the possible rate of wheat and barley domestication during the Neolithic period. The authors wrongly assume that jagged broken nodes appear only on domesticated threshed cereals. Wild species produce jagged broken nodes on up to 10% of their spikelets, namely, those coming from the lower part of the ear (1). In addition, presenting the

domestication of barley, einkorn, and emmer as proceeding with comparable rates seems inappropriate in view of their different anatomies, ecologies, and geographical distributions.

The authors did not fully consider the harvesting possibilities that would have affected the concentration of domesticated mutants with disarticulated ears in the plant population. Their suggestion of harvesting before full maturation helps us to understand how domestication occurred for short-awned einkorn. All

wild cereal fields host early- and late-ripening plants. Therefore, when a field was harvested before full maturation and the disarticulation mutation occurred in early-ripening plants, these plants would experience a significant selective advantage. The harvested early-ripening plants produced larger grains with a higher germination capability than the later-ripening plants gathered with them. Consequently, sowing these grains would have automatically increased their percentage of germination and favored mutation accumulation in the population.



This accumulation mechanism can be applied to the short-awned einkorn, which was harvested by sickle. In contrast, long-awned emmer and barley can also be collected from the ground (2). The cereals growing in the south of the Fertile Crescent mature and disarticulate more quickly than those growing in the north, where einkorn was domesticated (3). Therefore, it is much more likely that early farmers collected fallen emmer or barley from the

ground. Because only a fraction of the southern crops would have been harvested by sickle before full maturation, emmer and barley domestication would be expected to require an even longer period for domestication to take hold.

ANAT HARTMANN,¹ MORDECHAI E. KISLEV,² EHUD WEISS^{1*}

¹Land of Israel Studies and Archaeology Department, ²Faculty of Life Sciences, Bar-Ilan University, Ramat-Gan 52900, Israel.

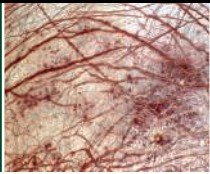
*To whom correspondence should be addressed. E-mail: eweiss@mail.biu.ac.il

References

1. M. E. Kislev, in *People and Culture in Change*, I. Hershkovitz, Ed. (British Archaeological Reports, International Series 508, Oxford, 1989), pp. 147–151.
2. M. E. Kislev, E. Weiss, A. Hartmann, *Proc. Natl. Acad. Sci. U.S.A.* **101**, 2692 (2004).
3. M. Heun *et al.*, *Science* **278**, 1312 (1997).

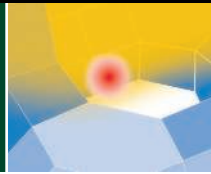
Response

LEV-YADUN *ET AL.* RAISE THREE IMPORTANT points concerning wheat domestication. First, they are correct that selection for a phenotype that had lost its ability to disarticulate could be easy (1). However, it is not clear whether early farmers would have recognized rare nonshattering plants, and if they did, whether they



Darwinian thinking
for the 21st century

306



Zeolites to
the rescue

309

would have considered them advantageous. Isolation of nonshattering plants from shattering ones would have been difficult to achieve. If farmers succeeded in isolating nonshattering plants, they would create a homologous single-lined nonshattering population (these are predominantly self-pollinating plants) at the expense of a population consisting of diverse landraces. This would drastically decrease crop diversity, but may have increased its vulnerability (2) and hence would not have been so advantageous.

Second, we consider harvesting fallen spikelets from the ground in cultivated fields (also mentioned by Hartmann *et al.* in their Letter) to be improbable, particularly in light of archaeological evidence that farmers used sickles to harvest cereals. Micro-wear analysis of flint blades recovered from archaeological sites for the period indicates that they were used for harvesting cereal stems (3, 4). A disadvantage of harvesting fallen spikelets is that the products become contaminated with soil.

Third, the genetic evidence (5) may identify the locality where ancestral populations grow today, but this does not rule out a series of events occurring at different places and different times. For example, a population of wild einkorn was identified and localized as the wild ancestor of domestic einkorn (6). This population may still have been domesticated more than once either in or outside its present-day habitat. Some domestication events may not be on the genetic record because cultivars have disappeared, and present-day populations represent a fraction of those in the past (7, 8). Wild progenitor habitats have been reduced through human impact. These impoverishments were particularly strong in the area where agriculture arose.

Hartmann *et al.* are correct that a wild population can produce up to 10% of domestic type disarticulation scars, which come from the base of the ear (9, 10), but this does not affect our interpretation. Their second point, that we present barley, emmer, and einkorn domestication as proceeding with comparable rates, is not the case. We are aware that our data are too fragmentary for such a conclusion; we observed that wild types persist alongside domestic types on the sites mentioned and indeed at other sites (11, 12), which suggests that domestication was slow to become established.

GEORGE WILLCOX¹ AND KEN-ICHI TANNO²

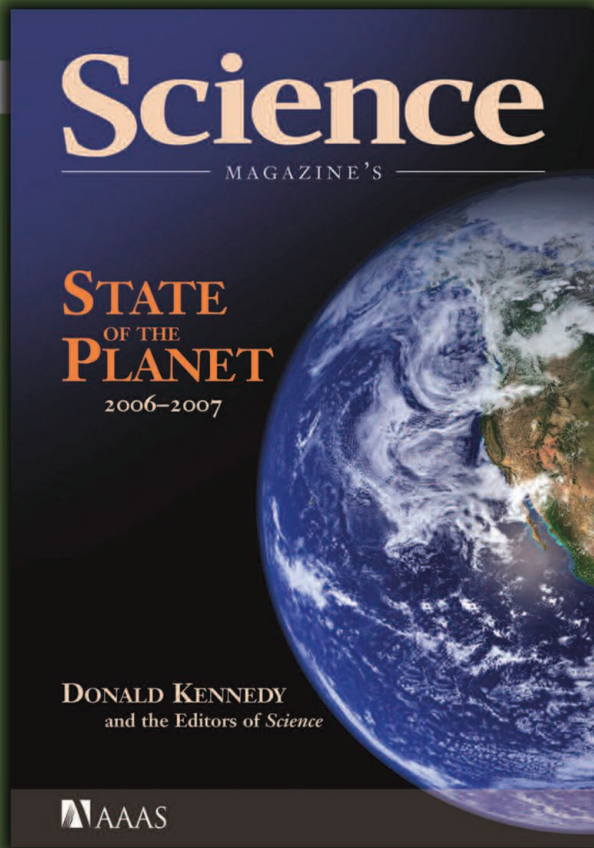
¹National Centre for Scientific Research (CNRS), Unité Mixte de Recherche 5133, Jalès, Berrias 07460, France. ²Research Institute for Humanity and Nature, Takashima 335, Kamigyo, 602-0878 Kyoto, Japan.

References and Notes

1. G. Hillman, S. Davies, *J. World Prehist.* **4**, 157 (1990).
2. M. Kislev, *Isr. J. Plant Sci.* **50**, 85 (2002).
3. P. Anderson, in *Prehistory of Agriculture*, P. Anderson, Ed. (Monograph 40, Institute of Archaeology, University of California, Los Angeles, 1999), pp. 118–144.
4. R. Unger-Hamilton, in (3), pp. 145–152.
5. F. Salamini, H. Özkan, A. Brandolini, R. Schäfer-Pregl, W. Martin, *Nat. Rev. Genet.* **3**, 429 (2002).
6. M. Heun *et al.*, *Science* **278**, 1312 (1997).
7. G. Jones, S. Valamoti, M. Charles, *Veget. Hist. Archaeobot.* **9**, 133 (2000).
8. M. Kislev, *Isr. J. Bot.* **28**, 95 (1980).
9. M. Kislev, in *People and Culture in Change*, I. Hershkovitz, Ed. (British Archaeological Reports, International Series 508, Oxford, 1989), pp. 147–151.
10. G. Willcox, in *The Prehistory of Food*, J. Hather, C. Gosden, Eds. (Routledge, London, 1999), pp. 479–500.
11. D. de Moulins, *Agricultural Changes at Euphrates and Steppe Sites in the Mid-8th to the 6th Millennium B.C.* (British Archaeological Reports, International Series 683, Oxford, 1997).
12. W. van Zeist, G. J. de Roller, *Palaeohistoria* **33/34**, 65 (1994).

Maintaining the Foundations of Science

I APPLAUD THE RECENT EDITORIAL (“SCIENCE AS smoke screen,” S. C. Trombulak *et al.*, 19 May, p. 973) decrying changes to the U.S. Endangered Species Act of 1973 outlined in the bill H.R. 3824. I attended the mark-up of H.R. 3824 in the House of Representatives Resources Committee and witnessed firsthand the contentious nature of the bill, as well as the influence of strong political will on the success of this legislation. I am concerned that given the current political direction and climate in the United States, the suggestion that an independent scientific advisory panel be assembled to advise the U.S. Secretary of the Interior on relevant scientific issues misses an important point. Although such a panel could be a step in the right direction, unless an entirely new framework for federal advisory committees is established, this panel ultimately would be at the discretion of political appointees. Thus, a new panel would likely be prone to the same fate as the Department of Energy’s Scientific Advisory board: disbanded after a closed-door meeting (1). The abolishment of this independent board, reportedly because it was being deemed unnecessary (2) after nearly 16 years of service, demonstrates the lack of value ascribed to scientific input by the current administration and their subordinates. We need to emphasize creative solutions that provide an avenue for science in relevant policy-making and to protect this channel from the whims of changing political pressures or personalities.



Science Magazine's
State of the Planet
2006-2007

Donald Kennedy, Editor-in-Chief,
and the Editors of *Science*

The American Association for
the Advancement of Science

The most authoritative voice in American
science, *Science* magazine, brings you current
knowledge on the most pressing environmental
challenges, from population growth to
climate change to biodiversity loss.

COMPREHENSIVE • CLEAR • ACCESSIBLE



islandpress.org

LETTERS

In addition, all scientists must recognize these as attacks not only on science in policy-making, but on the scientific process more generally. If people no longer respect the scientific method as a valuable means for pursuing answers, as is the growing trend, we might not only see the disbanding of scientific advisory boards, but the disappearance of the foundations that support science in this country.

JUDSEN BRUZGUL

Department of Biological Sciences, Stanford University,
334 Serra Mall, Stanford, CA 94305, USA. E-mail:
bruzgul@stanford.edu

References

1. G. Brumfiel, *Nature* **440**, 725 (2006).
2. M. Janofsky, "Science Advisory Board Is Abolished," *N.Y. Times*, 7 April 2006 (available at <http://query.nytimes.com/gst/fullpage.html?res=980DE1DB1130F934A35757C0A9609C8B63>).

TECHNICAL COMMENT ABSTRACTS

COMMENT ON "Opposing Effects of Native and Exotic Herbivores on Plant Invasions"

Anthony Ricciardi and Jessica M. Ward

Parker *et al.* (Reports, 10 March 2006, p. 1459) showed that native herbivores suppress exotic plants more than native plants. Further analysis reveals that the effect of native herbivores is reduced on exotic plant species that are closely related to native species in the invaded region. Exotic plants may share traits with native congeners that confer similar resistance to resident herbivores.

Full text at www.sciencemag.org/cgi/content/full/313/5785/298a

RESPONSE TO COMMENT ON "Opposing Effects of Native and Exotic Herbivores on Plant Invasions"

John D. Parker, Deron E. Burkepile, Mark E. Hay

Our investigation found that non-native plants were more susceptible to native generalist herbivores than were native plants. Ricciardi and Ward's finding that non-native plants without native congeners are more susceptible to native herbivores than are non-natives with coexisting native congeners supports our hypothesis that evolutionary naiveté leaves plants at greater risk of attack by newly encountered generalist herbivores.

Full text at www.sciencemag.org/cgi/content/full/313/5785/298b

Letters to the Editor

Letters (~300 words) discuss material published in *Science* in the previous 6 months or issues of general interest. They can be submitted through the Web (www.submit2science.org) or by regular mail (1200 New York Ave., NW, Washington, DC 20005, USA). Letters are not acknowledged upon receipt, nor are authors generally consulted before publication. Whether published in full or in part, letters are subject to editing for clarity and space.

HISTORY OF SCIENCE

The Camera Never Lies?

Donna C. Mehos

Science and engineering's most powerful statements are not made from words alone. (1)

The annual Science and Engineering Visualization Challenge (2) demonstrates that photographs (among other images) provide critical evidence in today's scientific practice, a fact that can be seen in every issue of *Science*. Yet this was not always the case. When photography was invented in 1839 and throughout the 19th century, its evidentiary authority was highly contested. In *Nature Exposed: Photography as Eyewitness in Victorian Science*, Jennifer Tucker explores the history of scientific photography. Tucker (a historian of science at Wesleyan University, Connecticut) shows adeptly that photographs were not always received in the world of science as realistic representations of nature. Through a series of well-researched case studies, she discusses such topics as the character of debates over the objectivity of photographs, the roles of individuals and institutions in reaching a consensus about these images, the sources of the different meanings people attached to photography and photographs, and the influences of gender and social class on the development of scientific photography.

The strength of the book lies in Tucker's analysis of the broad historical context in which scientific photography emerged in Victorian Britain. By looking further than academic science, she unveils a story in which complex social relations influenced the acceptance of photographs as serious scientific evidence. In its first decades, photography was an expensive pursuit pioneered by elite members of British society, who also practiced amateur natural history. These gentlemen and gentlewomen naturalists combed the countryside in pursuit of natural knowledge, collecting specimens of plants, insects, and other naturalia. They also photographed nature in their efforts to record it realistically. However, as the cost of the technology decreased in the 1860s, photography emerged as both a popular hobby and a profitable commercial occupation practiced by Britons of all classes. This change led many genteel and highly skilled photographers not only to abandon pho-

tography but also to bring into question the technical skills and truthfulness of photographs produced by their social "inferiors." It also led those interested in the uses of photography as a scientific tool to develop a specialized language to distinguish their work from that of the lower classes.

The credibility of photographs soon came to depend on the reputations of the photographers rather than on their images. Hence, when the subscribers of the widespread spiritualist movement began to photograph spirits or ghosts in studios and séances, both their honesty and technical skills were suspect. In support of the photographs, well-respected scientist-spiritualists, such as Alfred Russell Wallace—the co-discoverer of natural selection—lent their scientific authority to the contested practice of spiritualist photography. Whether or not these images were produced fraudulently or due to sloppy methods is not relevant here. Rather, these debates illustrate how the reputation (and often social class) of photographers determined the integrity of their photographs.

Drawing on a rich variety of sources, Tucker's nuanced analysis demonstrates how scientific photography became defined as it moved between popular and elite culture. In the rise of meteorology, when meteorologists struggled to create accurate visual representations—drawings, paintings, photographs—of weather phenomena such as clouds and lightning, scientists drew on artistic renditions of nature. They studied landscape paintings in museums to ascertain whether they were unrealistic representations or realistic depictions suitable as models for meteorological photography. Because early weather data

Nature Exposed
Photography as
Eyewitness in
Victorian Science

by Jennifer Tucker

Johns Hopkins University
Press, Baltimore, MD,
2005. 306 pp. \$55, £36.50.
ISBN 0-8018-7991-4.



Visual expression of atmospheric electricity. Lightning striking the Eiffel Tower, Paris (ca. 1900).

were collected by a legion of amateur field naturalists across the country, meteorologists trained these volunteers in photographic technique to ensure they produced images valuable as weather observations. Meteorology photographers, therefore, had to demonstrate their photographic and observational skills before their photographs were seen as reliable objective scientific evidence.

Early photomicrography of bacteria, even if produced by respected scientists such as Robert Koch, was received with skepticism and viewed as inferior to traditional drawings. Therefore, drawings were often made to highlight or idealize the significant characteristics of these scientific photographs—a practice still seen today. Tucker explores photographs and illustrations of microbes not only in the laboratory and medical education but also in the popular press during the microbe craze. Similarly, in astronomy, scientists supplemented early fuzzy planetary photographs with drawings. The interpretation of

The Perfect Medium. Photography and the Occult. Clément Chéroux, Andreas Fischer, Pierre Apraxine, Denis Canguilhem, and Sophie Schmit. Yale University Press, New Haven, CT, 2005. 288 pp. \$65. ISBN 0-300-11136-3.

Beautifully produced, this catalog of a 2005 exhibition held at New York's Metropolitan Museum of Art (after appearing at la Maison Européenne de la Photographie in Paris) documents the fascinating history of occult photography with scores of captivating images from the heyday of the spiritualist movements in the United States and Europe, circa 1870 to 1930. Intriguing essays illuminate the practices and beliefs of occultists who used photography to visualize the invisible, such as spirits, auras, feelings, and dreams. Photographers also portrayed supernatural events purported to occur during séances when mediums were at work (for example, levitation, telekinesis, and transfiguration). Though addressing a seemingly bizarre subject, the volume explores seriously the intersections of the history of photography with that of the occult. Readers may find it a refreshing escape from rationalist daily practices of 21st-century science.

—Donna C. Mehos

The reviewer is in the Faculty of Technology Management, Eindhoven University of Technology, Post Office Box 513, 5600 MB Eindhoven, Netherlands. E-mail: d.c.mehos@tm.tue.nl

Mars photographs as providing evidence of canals—and the suggestion of extraterrestrial life—sparked debates among scientists and the public as speculation about Martians raged in the popular press. In this case, Tucker demonstrates convincingly that scientific institutions, such as the Royal Society, played crucial roles in establishing the evidentiary authority of photography.

Nature Exposed provides a timely historical perspective on the disputed authority of scientific photographs still relevant today—when, for example, the Microscopy Society of America maintains ongoing discussions to develop ethical guidelines for the manipulation of digital images. Tucker shows us that scientific photographs were not always accepted at face value and, more significantly, that the truth or falsity of images is not simply a matter of honesty or deceit. Rather, how we view images, and whether or not we accept them as accurate representations of nature, are the results of social negotiations. Photographs, like all forms of scientific data, constitute contested terrain.

References and Notes

1. "Science and Engineering Visualization Challenge Call for Entries," *Science* **311**, 948 (2006).
2. The challenge is sponsored by the National Science Foundation and *Science*. For the 2005 winners, see *Science* **309**, 1989 (2005).

10.1126/science.1126852

MATERIALS SCIENCE

There's Still Plenty of Room at the Bottom

Michael W. Pitter

It would not be an understatement to say that anything that has the prefix "nano" is currently considered a hot topic in science. Nano courses are being developed at the undergraduate and graduate levels, entire nano programs are being implemented at a variety of institutions around the globe, nanoscience papers are a staple of many top journals, and the popular scientific and general media present nanotechnology as the answer to everything from a cure for cancer to advancing space exploration. Amidst all of the excitement, it might be tempting to dismiss *Nanochemistry: A Chemical Approach to Nanomaterials* as another attempt to cash in on the hype. Doing so, however, would lead you to miss a gem in the scientific literature.

The reviewer is at the Department of Chemistry, Middle East Technical University, Ankara 06531, Turkey. E-mail: pitter@metu.edu.tr

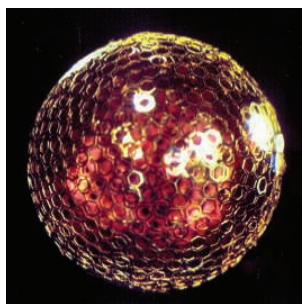
Geoffrey Ozin and his graduate student André Arsenault (chemists at the University of Toronto) have produced a beautifully written and richly illustrated book that is unlike any other. Although designed primarily as a textbook for teaching nanochemistry (the first of its kind), it should appeal to a broad range of readers—from those involved in cutting-edge nanomaterials research to those with only a casual interest in the field, who may simply marvel at what scientists are currently able to achieve in the laboratory. Before guiding us through the material in a clear and logical progression, the authors distinguish among nanoscience, nanotechnology, and their topic:

In its broadest terms, the defining feature of nanochemistry is the utilization of synthetic chemistry to make nanoscale building blocks of different size and shape, composition and surface structure, charge and functionality. These building blocks may be useful in their own right. Or in a self-assembly construction process, spontaneous, directed by templates or guided by chemically or lithographically defined surface patterns, they may form architectures that perform an intelligent function and portend a particular use.

This quote accurately summarizes the power of the authors' approach and of the concepts they present.

In their introductory chapter ("Nanochemistry Basics"), Ozin and Arsenault stress the importance of materials self-assembly. The production of a targeted structure by self-assembly chemistry requires finding ways to synthesize or fabricate building blocks with the correct size, shape, and composition. The authors note that nature meets this challenge every day, as in biomineralization (where "form is function"). In subsequent chapters, they expand on the materials self-assembly theme by considering the various nanoscale building blocks currently available and the new architectures developed from these.

Two of the longest chapters in the book cover nanowires (plus nanotubes and nanorods) and nanoclusters. Their lengths reflect the high intensity of current research on these nanostructures. Some of these materials have already found practical applications, and others are likely to in the near future. Both chapters convey the importance of quantum size effects (the tunability of properties by controlling size in the nano regime).



Dome on a drop. This geodesic structure of gold hexagons self-assembled on a drop of water in hexane (3).

Living organisms have solved the formation of complex three-dimensional assemblies over many millions of years of evolution. In the chapter "Biomaterials and Bioinspiration," the authors tackle the issue of transferring these organic technologies to the laboratory by either mimicking the features found in nature or taking the self-assembled biological constructions and using them in synthetic systems (and perhaps for

novel purposes).

Throughout the book, Ozin and Arsenault mention how particular self-assembled structures might be used in a broad selection of next-generation devices (solar cells, computers, batteries, sensors, catalysts, ceramics, composites, fuel cells, etc.). In their penultimate chapter, "Nano and Beyond," the authors sketch their vision of how the field of nanochemistry will evolve over the next few years with short discussions of a couple dozen specific examples such as microfluidic computing, crystallographic control, and self-assembled electronics.

In all of the chapters, the material is up to date and thoroughly referenced and covers contributions to the field of nanochemistry by many key scientists, including George Whitesides, Charles Lieber, Paul Alivisatos, Chad Mirkin, and, of course, Ozin himself. For those planning to teach a course based on the book, each chapter ends with a section titled "nanofood for thought." These offer a series of questions (some without clear-cut answers) designed to make students both think about and develop a deeper understanding of the material. And the final chapter outlines a set of 20 experiments for labs in a nanochemistry course. (The authors plan to publish the corresponding set of detailed procedures in the future.)

Ozin and Arsenault should be congratulated for their groundbreaking book. Reading it will reward students in chemistry and materials science as well as researchers from many different disciplines (1). In December 1959, Richard Feynman delivered a classic, innovative talk on nanotechnology titled "There's plenty of room at the bottom" (2); *Nanochemistry* shows us that there is still plenty of room at the bottom.

References and Notes

1. Those desiring a taste of the book can download the first chapter (free of charge) at the Royal Society of Chemistry's Web site (www.rsc.org/Publishing/Books/085404664X.asp).
2. A transcript of this talk is available online (www.zyex.com/nanotech/feynman.html).
3. W. T. S. Huck, J. Tien, G. M. Whitesides, *J. Am. Chem. Soc.* **120**, 8267 (1998).

10.1126/science.1130965

CREDIT: PHOTO COURTESY OF JOE TIEN/REPRINTED WITH PERMISSION FROM (3)/© AMERICAN CHEMICAL SOCIETY

SCIENCE AND GOVERNMENT

Review for NCCAM Is Overdue

Donald M. Marcus^{1*} and Arthur P. Grollman²

The U.S. National Institutes of Health (NIH) were created by Congress to conduct research on the causes and treatment of common diseases. In contrast, the National Center for Complementary and Alternative Medicine (NCCAM) was created by pressure from a few advocates in Congress (1–3). The NCCAM budget for 2005 was \$123.1 million. At a time when NIH support of biomedical research is decreasing (4) and many excellent grant proposals are not being funded, NCCAM's expenditure of funds deserves scrutiny.

History of OAM and NCCAM

NCCAM began as the Office of Alternative Medicine (OAM) in 1992 (1–3). It was created within the office of the NIH director with a budget of \$2 million by a directive from the Senate Appropriations Committee. The driving force behind the directive was Senator Tom Harkin (D-IA), chairman of the Appropriations Committee, a long-time supporter of NIH research and advocate for alternative medicine.

In 1997, Senator Harkin proposed that OAM become an independent center with direct authority to appoint peer-review panels and to award grants. Despite opposition to this proposal from prominent scientists, including former presidential science adviser D. Allen Bromley and Nobel laureates Paul Berg and Jerome Friedman (5, 6), NCCAM was created in 1998 with an initial budget of \$50 million. In response to Harkin's complaints that alternative medicine specialists were excluded from previous review panels, the new NCCAM charter stipulated that 12 of the 18 members of the NCCAM Advisory Council "shall be selected from among the leading representatives of the health and scientific disciplines ... in the area of complementary and alternative medicine. Nine of the members shall be practitioners licensed in one or more of the major systems with which the Center is involved" (7).

In 1999, Stephen Straus, a respected virologist and immunologist, and chief of the Laboratory of Clinical Investigation of the National Institute of Allergy and Infectious Diseases, was appointed director of NCCAM. He has stated frequently that alternative therapies can and should be evaluated by the same methodology used in clinical trials of conventional treatments (8). What kinds of studies has NCCAM funded?

"We believe that NCCAM funds proposals of dubious merit; its research agenda is shaped more by politics than by science; and it is structured by its charter in a manner that precludes an independent review of its performance."

**Clinical Trials Funded by NCCAM**

A major emphasis of NCCAM's first 5-year strategic plan was to perform phase III clinical trials of popular herbal medicines and other supplements to inform the public about their efficacy (9). Accordingly, the fraction of funds allocated to clinical research by NCCAM has been high, ranging from 80% in fiscal 2000 to 68% in 2004, compared with ~33% by the rest of NIH. The results of clinical trials of St. John's wort, echinacea, and saw palmetto have

been published (10–12), and none of these herbal medicines was more effective than the placebo controls. Although Straus has commented that "he for one is satisfied that echinacea is not an effective cold remedy" (13), spokesmen for the herbal and nutraceutical industries predictably responded that the studies were flawed and that more research is needed. It appears doubtful that these negative trials will change the practices of many people who use herbal remedies, given their belief in the healing power of natural products and their distrust of physicians, scientists, and the pharmaceutical industry. When regular users of dietary supplements were asked, "If a government agency said that the dietary supplement is ineffective, what would you do?," 71% responded that they would keep using the supplement (14).

NCCAM's strategic plan for 2005–09 (9) recognizes the lack of quality control of commercial herbal products, a problem that is a consequence of the Dietary Supplement Health and Education Act of 1994 (DSHEA), which markedly restricts the Food and Drug Administration's (FDA's) authority to regulate dietary supplements. As Berman and Straus stated (8), "Herbal medicines are plagued by contamination with heavy metals and filth, by adulteration with prescription drugs, wide divergence from labeled content, interference with the pharmacokinetics of life-saving drugs, and even some inherent toxicities," an assessment that is supported by many reviews (15, 16).

To improve the quality of natural products used in clinical trials, NCCAM recommended chromatographic analysis of extracts and of their putative active ingredients (17). However, the number and identity of the active ingredients of most herbal remedies are unknown, and chromatographic standardization would not ensure standardization of biological activity or stability. Moreover, because there are few regulations governing herbals manufacture, products bought by the public will differ from the research materials. We see little reason, therefore, for NCCAM to continue to finance expensive clinical trials of plant extracts (18).

Two clinical trials supported by NCCAM deserve comment. In collaboration with the National Heart, Lung, and Blood Institute,

Two clinical trials supported by NCCAM deserve comment. In collaboration with the National Heart, Lung, and Blood Institute,

¹Department of Medicine, Baylor College of Medicine, Houston, TX 77030; ²Department of Pharmacological Sciences, State University of New York at Stony Brook, Stony Brook, NY 11794, USA.

*Author for correspondence. E-mail: dmarcus@bcm.tmc.edu

NCCAM is funding a 5-year \$30 million trial of EDTA (ethylenediaminetetraacetic acid) chelation therapy for coronary artery disease (19). It is being carried out at more than 100 sites and involves over 2300 patients. The justification for this study is that many patients are receiving chelation therapy, although it is not approved by the FDA and off-label use for treating heart disease is currently illegal. The American Heart Association and other national medical organizations have issued statements concerning the lack of evidence for its benefit (20), and smaller controlled trials (21–24) have found chelation therapy to be ineffective. Will another negative trial modify the practice of individuals who choose to ignore existing negative evidence and risk legal sanctions?

Another clinical trial compares the use of the chemotherapeutic agent gemcitabine with the Gonzalez regimen in patients with stages II to IV pancreatic cancer (25). The beliefs that underlie this regimen are that cancer is caused by a deficiency of pancreatic proteolytic enzymes that would normally eliminate cancer cells and their toxic products, and that environmental toxins cause imbalances in the body that lead to cancer (26). Patients are treated with porcine pancreatic enzymes, coffee enemas twice daily, and nutritional supplementation that includes Papaya Plus, vitamins, minerals, “animal glandular products,” and other products four times daily. Severe adverse effects have been associated with the Gonzalez regimen (26, 27).

Two important criteria used by scientific review groups to evaluate grant proposals are scientific plausibility and promising preliminary data. No evidence in peer-reviewed journals supports either the plausibility or the efficacy of chelation therapy or the Gonzalez protocol. We believe that funding these projects confers undeserved legitimacy on alternative practices and reflects poorly on the NIH review process.

Review Groups and Advisory Panels

Because of its charter, NCCAM review groups include individuals whose primary training is in alternative therapies, as well as representatives of the botanical industry. In terms of training and publications in medical and scientific journals, their scientific credentials are limited; also, some have potential conflicts of interest. Well-qualified scientists also serve on NCCAM review panels, but their influence is constrained by the narrow NCCAM agenda that emphasizes trials of alternative therapies.

Another problem is that a handful of individuals have been influential in shaping the agendas of OAM and NCCAM. Since the inception of OAM in 1992, those who have written policy papers (28) also have served on review panels and advisory groups and have received numerous grants for research and education.

Evaluation of NCCAM

Oversight of extramural programs is the responsibility of the advisory councils of institutes and centers. The extramural program of NCCAM has escaped critical evaluation because its charter requires a preponderance of proponents of alternative medicine on its council.

In 2002, the Institute of Medicine (IOM) was commissioned by NIH and the Agency for Healthcare Research and Quality (29) to “explore scientific, policy and practice questions that arise from the significant and increasing use of CAM [complementary and alternative medicine] therapies by the American public.” One of three tasks assigned to the IOM Committee was to “Identify major scientific, policy and practice issues related to CAM research.” Seven of the 17 committee members were CAM practitioners or directed CAM and integrative medicine centers. The IOM report identified problems in CAM research, such as the variable composition of herbal medicines and limited number of individuals with research training in the CAM community. Unfortunately, the IOM committee did not evaluate the quality of NCCAM-funded trials or the value of spending hundreds of millions of dollars on CAM research.

Conclusions

We believe that NCCAM funds proposals of dubious merit; its research agenda is shaped more by politics than by science; and it is structured by its charter in a manner that precludes an independent review of its performance. The central issue is not whether research into alternative therapies should be supported by NIH. In view of the popularity of alternative therapies, it is appropriate to evaluate the efficacy and safety of selected treatments. The issue is that the administration of research by NCCAM falls below the standards of other NIH institutes and that the evaluation of alternative therapies could be performed by mechanisms that are already in place at NIH. We do not question the qualifications or integrity of Stephen Straus and his staff. However, because of the constraints under which it operates, NCCAM is unable to implement a research agenda that addresses legitimate scientific opportunities or health-care needs (30). Applicants for NCCAM grants must follow the center’s guidelines that stipulate which therapies are eligible for study. In contrast, applicants to NIH institutes can propose any project that may provide new insights into human biology or the pathogenesis or treatment of disease.

Recommendations

We propose that the IOM appoint an independent panel of scientists to review NCCAM. The panel should evaluate the center’s unique charter as well as its research portfolio, and its members should not include NIH or NCCAM staff, NCCAM grantees, and other stakeholders. An

independent review is likely to be strongly opposed by members of Congress whose beliefs led to the creation of NCCAM and the passage of the DSHEA. Therefore, scientists and professional organizations should communicate to Congress and to Elias Zerhouni, the director of NIH, their strong support for an external assessment of NCCAM.

References and Notes

1. J. H. Young, *Bull. Hist. Med.* **72**, 279 (1998).
2. E. Marshall, *Science* **265**, 2000 (1994).
3. S. Budiansky, *U.S. News World Rep.*, 17 July 1995, p. 48; (www.usnews.com/usnews/culture/articles/950717/archive_032434.htm).
4. J. Mervis, *Science* **311**, 28 (2006).
5. G. Vogel, *Science* **278**, 378 (1997).
6. J. Couzin, *Science* **282**, 2175 (1998).
7. National Advisory Council for Complementary and Alternative Medicine (NACCAM) (<http://nccam.nih.gov/about/advisory/naccam/charter.htm>).
8. J. D. Berman, S. E. Straus, *Annu. Rev. Med.* **55**, 239 (2004).
9. “Expanding horizons of health care: Strategic plan 2005–2009” [National Center for Complementary and Alternative Medicine (NCCAM), U.S. Department of Health and Human Services, National Institutes of Health, Bethesda, MD, 2005].
10. J. S. Markowitz *et al.*, *JAMA* **290**, 1500 (2003).
11. R. B. Turner *et al.*, *N. Engl. J. Med.* **353**, 341 (2005).
12. S. Bent *et al.*, *N. Engl. J. Med.* **354**, 557 (2006).
13. G. Kolata, *New York Times*, 28 July 2005.
14. R. J. Blendon, C. M. DesRoches, J. M. Benson, M. Brodie, D. E. Altman, *Arch. Intern. Med.* **161**, 805 (2001).
15. P. A. G. M. De Smet, *Clin. Pharmacol. Ther.* **76**, 1 (2004).
16. M. Elvin-Lewis, *Adv. Food Nutr. Res.* **50**, 219 (2005).
17. NCCAM, Policy announcement on the quality of natural products, 2003; (<http://nccam.nih.gov/research/policies/bioactive.htm>).
18. W. Sampson, *N. Engl. J. Med.* **353**, 337 (2005).
19. “NIH launches large clinical trial on EDTA chelation therapy for coronary artery disease,” press release, 30 August 2002; (<http://nccam.nih.gov/news/2002/chelation/presrelease.htm>).
20. “Questions and answers about chelation therapy,” American Heart Association (www.americanheart.org/presenter.jhtml?identifier=3000843).
21. E. Ernst, *Am. Heart J.* **140**, 139 (2000).
22. M. L. Knudtson *et al.*, *JAMA* **287**, 481 (2002).
23. M. V. Villaruz, A. Dans, F. Tan, *Cochrane Database Syst. Rev.* **2002**(4), CD002785 (2002).
24. D. M. R. Seely, P. Wu, E. J. Mills, *BMC Cardiovasc. Disord.* **5**, 32 (2005).
25. Gemcitabine compared with pancreatic enzyme therapy plus specialized diet (Gonzalez regimen) in treating patients who have stage II, stage III, or stage IV pancreatic cancer (<http://clinicaltrials.gov>).
26. Metabolic therapy, American Cancer Society (www.cancer.org).
27. S. Green (www.quackwatch.org/01QuackeryRelatedTopics/Cancer/kg.html).
28. “Alternative medicine: Expanding medical horizons: A report to the National Institutes of Health on alternative medical systems and practices in the United States,” Workshop on Alternative Medicine, Chantilly, VA, 14 to 16 September 1992 (Government Printing Office, Washington, DC, 1995).
29. Committee on the Use of Complementary and Alternative Medicine by the American Public, *Complementary and Alternative Medicine in the United States* (Institute of Medicine, The National Academies Press, Washington, DC, 2005), chap. 9.
30. E. Stokstad, *Science* **288**, 1568 (2000).

SCIENCE AND GOVERNMENT

In Defense of NCCAM

Stephen E. Straus and Margaret A. Chesney*

The National Center for Complementary and Alternative Medicine (NCCAM) is one of the 27 institutes and centers that constitute the National Institutes of Health (NIH). Its mission is to investigate complementary and alternative medicine (CAM) in the context of rigorous science, to train CAM researchers, and to disseminate authoritative information to the public and professional communities. From its beginning, NCCAM has encountered controversy and strong sentiments for and against the scientific study of CAM, such as that appearing in this issue of *Science* (1) and elsewhere (2). Some criticisms have been valid and have led to more stringent policies on product quality and safety, for example. Others are misinformed. Our goal is to bring fact and clarity to this discussion, just as we seek to bring science to the assessment of CAM.

History of Establishing NCCAM

The U.S. Congress established NCCAM in 1998 to bring scientific rigor to studies of CAM by the same legislative process used to establish other NIH institutes and centers. This is a challenging mandate, one that required establishing a new CAM research enterprise that met the high standards of biomedical research for which NIH is known. NCCAM has outlined its approach to studying CAM in its 5-year strategic plans, the most recent of which was published in 2005 (3). These plans were developed with balanced debate and advice from a wide range of individuals representing the scientific community, conventional and CAM practitioners, and the public.

The criticism that only a handful of individuals have shaped the NCCAM agenda is not accurate. In creating our second strategic plan (3), NCCAM embarked on a year-long process of agenda-setting dialog. The center held a think tank of leading scholars, including three current and past NIH institute directors; convened stakeholder forums on the East and West coasts; assembled a strategic planning workshop with more than 80 individuals from mainstream medicine and CAM communities; and sought input from over 1500 individuals and professional organizations. We specifically included distinguished conventional scientists (without experience in CAM) to lend their expertise to discussions of CAM-related research challenges.

National Center for Complementary and Alternative Medicine, NIH, Bethesda, MD 20892, USA.

*Author for correspondence. E-mail: chesneym@mail.nih.gov

Counterpoint: The National Center for Complementary and Alternative Medicine has successfully met the challenge of conducting difficult and controversial research.



“NCCAM is applying the same scientific standards to the conduct of research and its review as used by other NIH institutes.”

NCCAM Advisory Council and Peer Review

As with other institutes at NIH, the composition of the NCCAM Advisory Council was specified in congressional language. The council includes individuals with conventional scientific and medical training, such as M.D.'s and Ph.D.'s, and others with CAM expertise, as well as representatives from the lay public [see (4) for the current roster]. NCCAM's Advisory Council has scientists with exemplary records of accomplishment in a variety of disciplines. This balanced composition reflects NIH's interdisciplinary approach to today's complex scientific questions. The 17 current council members have published 414 peer-reviewed articles and received 35 NIH grants in the period from 2001 to 2006 (23 of which were awarded by other NIH institutes).

NCCAM's peer-review process is the same as other NIH institutes, i.e., content experts review applications in their area of expertise. Cardiologists review applications on ischemic

heart disease, and pharmacologists, including pharmacognosists, review applications on botanical products. NCCAM's investigator-initiated R01 grant applications are reviewed by study sections convened by the NIH Center for Scientific Review; thus, they compete on an even playing field with all other applications to NIH. All members of NIH peer-review panels and advisory councils, including those at NCCAM, adhere to NIH policies concerning conflict of interest. The NCCAM Advisory Council acts as a second level of review.

Product Quality and Patient Safety

One of the most challenging issues in studying CAM has been the quality of dietary supplement products available for research and the variability of quality and content of products in the marketplace. Unlike pharmaceutical firms, dietary supplement manufacturers do not have to establish efficacy before marketing their products to the public. The Food and Drug Administration (FDA) regulates dietary supplements as foods, not drugs. Therefore, FDA does not analyze the content of dietary supplements. Moreover, U.S. law does not define the term “standardized.” Thus, product quality and consistency can vary. This is a challenge for both researchers and the public.

NCCAM has developed a multifaceted strategy to ensure the quality of biologically active agents used in NCCAM-supported research.

Now, before NCCAM funds a project, a Product Quality Working Group, composed of pharmacologists, pharmacognosists, and other scientists, reviews information to determine whether the product is of the quality required to replicate research findings. Information is collected on more than 20 factors, including product characterization, standardization, contamination, consistency, and stability, that could affect the quality of research data. NCCAM also carries out quality-control assessments of random samples of biologically active products that are being used in the studies it funds. The selected samples are sent to independent laboratories for analysis, thus providing information on stability, quality, and characterization.

In addition to these product-quality measures, NCCAM has also established an independent phase I resource center to conduct preclinical pharmacology research on dietary supplements. In selecting candidate supplements for study, NCCAM places a priority on products that are widely used by the public, yet have insufficient data on factors such as dose range, bioequivalence, pharmacokinetics, bioavailability, and botanical-drug interaction—information that is currently lacking for many botanical products.

The safety of individuals participating in NCCAM-supported clinical studies is of paramount importance to the center. In addition to NIH-required safeguards for human subject protection, NCCAM has an Office of Clinical and Regulatory Affairs to provide oversight of NCCAM studies involving human subjects. This office oversees the Data and Safety Monitoring Boards for NCCAM's clinical trials and ensures compliance with Institutional Review Boards' guidance and FDA regulations. Other NIH institutes have similar offices. This research infrastructure has been created to ensure that the research that NCCAM funds will be reproducible and meet the rigorous standards expected by NIH-funded research.

NCCAM Research

In the early years of NCCAM, there was a sense of urgency to scientifically assess a range of CAM therapies that had been in long use by the public in the absence of proof of safety or efficacy. Thus, NCCAM undertook a number of clinical trials in its first years, many with support from other NIH institutes. In doing so, we have gained valuable experience that has informed our thinking about challenging issues in CAM research such as dosing, methodology, and other experimental factors.

When early trials of botanical products, such as saw palmetto, did not show efficacy, NCCAM focused attention on the doses used in these studies, which were based on those widely used by the public. NCCAM now has a policy of requiring dose-range studies and

other preclinical research before conducting clinical trials. The NCCAM research portfolio now includes more basic research focused on mechanisms of action, pharmacokinetics of herbal products, drug-herb interactions, and dose optimization, as well as clinical effects. This shift is reflected in the decline of the NCCAM clinical research portfolio from 80% in 2000 to 68% in 2005. The balance of basic and clinical research continues to serve the specific public health issues that NCCAM was created to address.

Contrary to the criticism that NCCAM prescribes areas of study to investigators, the center, like other NIH institutes, accepts unsolicited, investigator-initiated applications that are based on ideas formulated by the applicant, not NCCAM. The percentage of solicited grants funded by year varies, but in the last three fiscal years, about 87% of NCCAM-funded grants are unsolicited. NCCAM welcomes well-designed research applications on a wide range of CAM therapies.

Research Findings

In 2002, the National Health Interview Survey of more than 31,000 people found that 62% of Americans use some form of CAM (5). The public is using CAM without proof of efficacy or safety, which is the very reason that NCCAM-funded research is so important.

NCCAM's research has provided valuable information on the physiologic pathway of the placebo effect using state-of-the-art brain imaging technologies (6), the efficacy of acupuncture to relieve pain associated with osteoarthritis of the knee (7), and a potential role for glucosamine-chondroitin for patients with moderate-to-severe osteoarthritis pain (8). NCCAM's research is in the forefront of understanding the interactions of prescription drugs and dietary supplements (9). NCCAM's scrutiny of product safety informed the FDA's decision to withdraw ephedra from the marketplace (10).

These are a few examples of the more than 1000 peer-reviewed publications that have resulted from the first 7 years of basic and clinical research supported by NCCAM. NCCAM's research results will help build a fuller understanding of what CAM can offer. We not only expand our knowledge about the tested therapy but also learn more about the condition it is meant to treat. Overall, we should regard each study's results in the same way—as yet another crucial piece of the research puzzle.

Conclusion

After only 7 years, NCCAM has made important contributions in a field that is fraught with controversy and challenges. NCCAM is applying the same scientific standards to the conduct of research and its review as used by other NIH institutes. We have raised the bar on the

study design and methods used in CAM research, including the quality of products under investigation. Our portfolio of basic research will inform subsequent clinical studies to ensure that we are testing a high-quality product, at the optimal dose, and in the appropriate population.

Before the establishment of NCCAM, there was no central source of CAM information. NCCAM brings evidence-based information on CAM to the public, practitioners, and researchers. NCCAM disseminates research findings and provides reliable information about commonly used CAM practices through numerous channels, including its information clearinghouse and its award-winning Web site (11). NCCAM's communications program deals with a field that is controversial, that has many critics, and that reaches a public that wants reliable information.

We fully support the Institute of Medicine's (12) recommendation that the same principles and standards of evidence apply to all treatments, whether labeled as conventional medicine or CAM. We believe that we have succeeded in establishing a research enterprise that will achieve this standard. While challenges remain, we are confident that knowledge gained from NCCAM-supported studies will continue to inform the public, health-care providers, and policy-makers about how and when evidence-based CAM therapies should be used and effectively integrated into conventional medical care.

References

1. D. M. Marcus, A. P. Grollman. *Science* **313**, 301 (2006).
2. W. Sampson, *N. Engl. J. Med.* **353**, 337 (2005).
3. "Expanding horizons of health care: Strategic plan 2005–2009" [National Center for Complementary and Alternative Medicine (NCCAM), U.S. Department of Health and Human Services, National Institutes of Health, Bethesda, MD, 2005]; (<http://nccam.nih.gov/about/plans/2005/>).
4. NCCAM Advisory Committee roster (<http://nccam.nih.gov/about/advisory/nccam/roster.htm>).
5. P. Barnes *et al.*, *Complementary and Alternative Medicine Use Among Adults: United States, 2002* [Centers for Disease Control and Prevention (CDC) advance data report no. 343, CDC, Atlanta, GA, 2004].
6. J. Zubieta, J. W. Yau, D. J. Scott, C. S. Stohler, *Brain Behav. Immun.* **20**, 15 (2006).
7. B. M. Berman *et al.*, *Ann. Intern. Med.* **141**, 901 (2004).
8. D. O. Clegg *et al.*, *N. Engl. J. Med.* **354**, 795 (2006).
9. J. S. Markowitz *et al.*, *JAMA* **290**, 1500 (2003).
10. P. Shekelle *et al.*, "Ephedra and ephedrine for weight loss and athletic performance enhancement: Clinical efficacy and side effects" (Evidence report/technology assessment no. 76, prepared by Southern California Evidence-Based Practice Center, RAND, under contract no. 290-97-0001, task order no. 9, AHRQ Publication No. 03-E022, Agency for Healthcare Research and Quality, Rockville, MD, 2003).
11. NCCAM (<http://nccam.nih.gov>).
12. Committee on the Use of Complementary and Alternative Medicine by the American Public, *Complementary and Alternative Medicine in the United States* (Institute of Medicine, National Academy Press, Washington, DC, 2005).

MOLECULAR BIOLOGY

A New RNA Dimension to Genome Control

Richard W. Carthew

MicroRNAs (miRNAs) and small interfering RNAs (siRNAs) are 21- to 25-nucleotide RNA molecules that influence their much bigger relatives, the messenger RNAs (mRNAs). Over the past few years, these small RNA species have captivated the study of gene regulation and modified our notions about how gene expression is controlled. A recent clutch of papers describe for the first time a class of small RNA cousins that are distinct from miRNAs and siRNAs (1–6). They promise to yield fascinating new insights into genome control.

The genesis of the discovery of a third type of small RNAs is linked to the Argonaute family of proteins. Certain Argonaute proteins such as Ago1 and Ago2 associate with miRNAs and siRNAs to form ribonucleoprotein complexes that associate and repress the expression of target mRNAs. Sometimes, mRNA targets are cleaved by a mechanism that is catalyzed by the particular associated Ago protein. However, a subclade of Argonaute proteins are phylogenetically distinct from the Ago1/Ago2 subclade and do not appear to associate with siRNAs or miRNAs (7). Led by its founding member, the Piwi protein of *Drosophila melanogaster*, this subfamily appears to play an important role in germline development. For example, genetic analysis of Piwi and its mouse orthologs (Miwi, Mili, Miwi2) indicates that they are essential for spermatogenesis (7–9). How the Piwi subfamily regulates the germline has remained for the most part elusive.

A recent breakthrough regarding this question has emerged from the identification of the small RNA partners that associate with Piwi proteins. In research reported on page 363 of this issue, Lau *et al.* (1) partially purified a ribonucleoprotein complex from extracts of rat testis and found testis-specific RNAs of 25 to 31 nucleotides, with a dominant subpopulation of 29- to 30-nucleotide RNAs. These RNAs are distinct in size from miRNAs and are associated with distinct protein complexes. Lau *et al.* purified the RNA-protein complex by conventional chromatography and identified the rat homologs to Piwi (Riwi) and the human RecQ1 protein as subunits of the complex. On this basis, the RNAs have been named Piwi-interacting RNAs (piRNAs) and the complex is called the Piwi-interacting RNA complex (piRC).

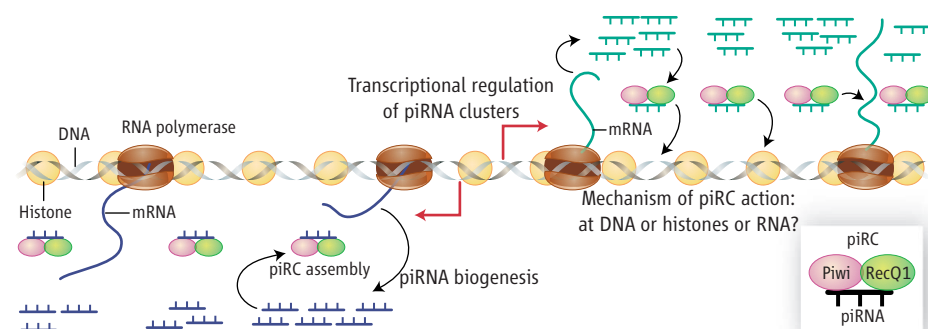
The author is in the Department of Biochemistry, Molecular Biology, and Cell Biology, Northwestern University, Evanston, IL 60208, USA. E-mail: r-carthew@northwestern.edu

piRC exhibits adenosine triphosphate-dependent DNA helicase activity, which is likely attributable to RecQ1. Interestingly, the RecQ1 homolog in *Neurospora crassa* has been implicated in gene silencing (10). Lau *et al.* (1) also found that piRC will cleave RNA targets in a manner dependent on piRNA complementarity, much like Ago2 cleavage of siRNA targets. This might imply that piRC has some posttranscriptional role in gene silencing. Indeed, piRNAs are associated with polysomes fractionated from mouse testis extract (4). However, genetic studies have implicated Piwi proteins in transcriptional gene silencing by altering chromatin conforma-

The discovery of small RNAs, microRNA and siRNA, has revolutionized thinking about the control of gene expression. Now a third new species of small RNA is shown to control gene expression in germline cells.

erates piRNAs from both strands, but plus-strand piRNAs are segregated from minus-strand piRNAs into distinct regions that are separated by a gap of a few hundred base pairs (see the figure). The paucity of evidence for overlapping complementary RNAs or potential foldback RNA precursors suggests that piRNAs are not derived from double-stranded RNA precursors. This would suggest a biogenesis mechanism distinct from that of siRNA and miRNA, both of which are derived from dsRNA through enzymatic cleavage by Dicer.

piRNAs and piRC complexes are not restricted to rats; they have been detected in testes



The known and unknown features of piRNAs. Shown is a genomic region that generates a cluster of piRNAs. The left side of the region generates antisense RNA transcripts (blue) and the right side generates sense transcripts (green); a short gap in between likely acts as the promoter for transcription of both sides (divergent red arrows). An RNA polymerase of unknown identity is shown in active transcription. These transcripts are processed into 25- to 31-nucleotide piRNAs by an unknown mechanism. piRNAs then associate with Piwi and RecQ1 homologs to form piRC complexes. These complexes might regulate the genome at the level of DNA or histones, or at a posttranscriptional level. The events that are under direct control of the piRC mechanism within developing sperm cells are currently unknown.

tion (7). Consistent with the idea that piRC plays a role in transcriptional silencing, RNAs that are longer than 24 nucleotides (such as piRNAs) have been associated with this mode of gene silencing in a wide variety of species (11).

One of the real surprises has been the nature of piRNAs themselves. Deep sequencing of complementary DNAs derived from piRNAs revealed that they correspond to regions of the genome previously thought not to be transcribed (1–3). These regions are limited in number to about 100 clusters ranging in size from 1 to 100 kilobases and are distributed across the genome. Very few clusters contain repetitive DNA; in fact, repetitive DNA is underrepresented. A greater surprise is that piRNAs in a typical cluster exclusively map to either one or the other strand of genomic DNA (1–5). A minority of clusters gen-

erates piRNAs from both strands, but plus-strand piRNAs are segregated from minus-strand piRNAs into distinct regions that are separated by a gap of a few hundred base pairs (see the figure). The organization of piRNA genomic clusters is conserved in other mammalian species as well. Most clusters in the rat, mouse, and human are homologous or syntenic, even extending to strand specificity. Nonetheless, piRNA sequences are not conserved between species. Sequence heterogeneity is consistent with the idea that the genomic clusters are subject to neutral selection pressure.

What testis cells express piRNAs? In the mouse, Mili is expressed in male germ cells from primordial to pachytene stages, whereas Miwi is expressed from pachytene to spermatid stages (8, 9). Both Mili and Miwi associate with piRNAs, which suggests that piRNAs are produced within the developing male germ cells. Consistent with a germline-specific expression

pattern, piRNAs are not detectable in *W^V* mutant mice, which are missing differentiating germ cells (2, 5), and piRNAs are reduced in *Miwi* mutants (4). piRNAs are detected throughout sperm development but appear to peak in abundance at the round-spermatid stage (1–5). The abundance of piRNAs in spermatids is staggering; about 1 million molecules are estimated per round-spermatid cell (3).

Although mammalian piRNAs are not associated with repetitive DNA, the situation might be different in *Drosophila*. On page 320 of this issue, Vagin *et al.* (6) describe repeat-associated siRNAs (rasiRNAs) in the fly germline as 24- to 29-nucleotide species that arise primarily from the antisense strand of repetitive sequences such as retrotransposons. These RNAs are associated with Piwi and another member of the Piwi subclade, and mutations in the Piwi class of genes cause derepressed retrotransposon silencing coupled with altered levels of rasiRNA abun-

dance. Interestingly, these effects are not restricted to the male germline but also apply to the female germline. Perhaps rasiRNAs in *Drosophila* use a molecular mechanism similar to that of mammalian piRNAs to silence portions of the genome.

Many questions ensue from these studies. Are testis-specific piRNAs found in species other than mammals? Does piRC regulate male meiosis by regulating genome organization, or is it a surveillance mechanism to ensure genome integrity during germ cell maturation, including suppression of selfish elements? Is piRC male-specific, or are other classes of RNAs associated with Piwi in the female germline? How are piRNAs produced? Their structures might suggest a ribonuclease III-independent origin. Indeed, neither of the two Dicers from *Drosophila* is essential for rasiRNA biogenesis and repeat DNA silencing (6), although it is possible that each is redundant for the other or that a third enzyme, Drosha, carries

out processing. Further investigation should reveal how piRCs regulate the genome.

References

1. N. C. Lau *et al.*, *Science* **313**, 363 (2006); published online 15 June 2006 (10.1126/science.1130164).
2. A. Girard, R. Sachidanandam, G. J. Hannon, M. A. Carmell, *Nature* 10.1038/nature04917 (4 June 2006).
3. A. Aravin *et al.*, *Nature* 10.1038/nature04916 (4 June 2006).
4. S. T. Grivna, E. Beyret, Z. Wang, H. Lin, *Genes Dev.* 10.1101/gad.1434406 (9 June 2006).
5. T. Watanabe *et al.*, *Genes Dev.* 10.1101/gad.1425706 (9 June 2006).
6. V. V. Vagin *et al.*, *Science* **313**, 320 (2006); published online 29 June 2006 (10.1126/science.1129333).
7. M. A. Carmell, Z. Xuan, M. Q. Zhang, G. J. Hannon, *Genes Dev.* **16**, 2733 (2002).
8. W. Deng, H. Lin, *Dev. Cell* **2**, 819 (2002).
9. S. Kuramochi-Miyagawa *et al.*, *Development* **131**, 839 (2004).
10. C. Cogoni, G. Macino, *Science* **286**, 2342 (1999).
11. M. A. Matzke, J. A. Birchler, *Nat. Rev. Genet.* **6**, 24 (2005).

10.1126/science.1131186

EVOLUTION

Darwin for All Seasons

Eörs Szathmáry

Many regard the Darwinian theory of evolution by natural selection as one of the most important and powerful theories of our times, in the good company of the general theory of relativity and quantum theory. What will be Darwin's legacy in the 21st century? Will new work be mainly confirmatory, or can we expect new breakthroughs? What constitutes a Darwinian way of thinking in biology, or more broadly in science? Is it still timely to think in a genuine Darwinian way, or should we resort only to some basic Darwinian principles? These questions were discussed by researchers at a recent conference at Trinity College, Cambridge, UK (1), which was hosted by the president of the Royal Society, Martin Rees.

There was fair agreement among the participants that Darwin's way of approaching problems remains valid and should be encouraged if possible. A feel for the organism, theoretical ideas guiding and aided by keen observations of meticulous details, excellent knowledge of natural history: These traits were characteristic of Darwin (as discussed by Randal Keynes), and there is little hope for biology in this century if at least some people will not walk in Darwin's footsteps. It seems mandatory that "professional generalists," when they rarely surface,

should be cultivated and encouraged. Presumably such individuals arise by nature rather than nurture, but a mechanism to identify and support such rare people is badly needed. As Darwin said: "My mind seems to have become a kind of machine for grinding general laws out of large collections of facts" (2). We should facilitate the emergence of this mindset in able people.

At the beginning of the 21st century, we are well equipped with the knowledge of two disciplines that were practically closed books to Darwin: classical and molecular genetics, and mathematical modeling. Units of evolution must multiply, have heredity, and possess variability; and among the heritable traits, some must affect survival and/or reproduction. If these criteria are met, evolution by natural selection is possible in a population of such entities. There are at least three remarkable features of this short description. First, it is extremely short, but very powerful [this is why philosopher Daniel Dennett speaks about "Darwin's dangerous idea" (3)]. Second, it is not restricted to living organisms, and if the criteria are met, Darwinian evolution may unfold in the realm of chemistry and culture as well. Third, although we have learned a lot since Darwin's times, Darwin would have presumably agreed with this telegraphic description.

There are still enormous challenges ahead of us in areas where a Darwinian way of thinking could turn out to be fruitful. The origin of evolu-

A recent conference featured discussions of Darwin's approach to science in the 19th century and how his methods may apply to 21st-century research.

ability lies in chemistry, and the origin of replicators and life may be (one of) the greatest challenges for that field. We do not know how RNA originated. We do not know how the first cells got organized, and there is no full scenario for the origin of the genetic code either. Chemistry has helped biology enormously: The development of biochemistry and molecular biology, and their contributions to our understanding of some fundamental features of life, have been profound. This may be the era when biology pays back its debt: Many fields within chemistry are more and more adopting evolutionary approaches. The triumph of in vitro genetics in producing catalytic RNA molecules (ribozymes) is a success story beyond doubt. An evolutionary approach toward nanotechnology may bear further fruits.

Mathematical modeling has contributed considerably to the foundations of modern evolutionary theory. Sometimes even the questions cannot be properly formulated without at least some elementary algebra or population dynamics. The problem of the evolutionary maintenance of sex in eukaryotes (consisting of cells much more complex than bacteria) is a good case in point. If an asexual female produces, on average, twice as many female progeny as a sexual one, then other things being equal, it is a miracle why the latter (with the necessary males) are still around. Many models have been put forward to solve this conundrum; some people would say far too many. What we need is more data. But relevant data are hard to arrive at. There is the

The author is at the Institute of Biology, Eötvös University Budapest, and Collegium Budapest (Institute for Advanced Study), 2 Szentháromság utca, H-1014 Budapest, Hungary. E-mail: szathmarty@colbud.hu

Darwinian way: Field work related to the problem of sex is not the easiest. In this century we have a powerful tool about which Darwin could not have dreamed: bioinformatics. Its application to the problems mentioned here rests on genetics, statistics, and molecular biology, among others—disciplines Darwin knew little or nothing about. It seems that the emerging field of comparative/Darwinian genomics is a gold mine for testing old evolutionary ideas (as

example, was also unique in the sense that all eukaryotes today share the same common ancestor. This did not prohibit us from insights into the origin of, say, mitochondria, which seem to be closely related to some free-living bacteria. In fact, the endosymbiotic theory for the origin of mitochondria (our energy-producing cell organelles) and plastids (the photosynthetic factories in plant cells), envisaging the gradual evolutionary transformation of particular bacteria

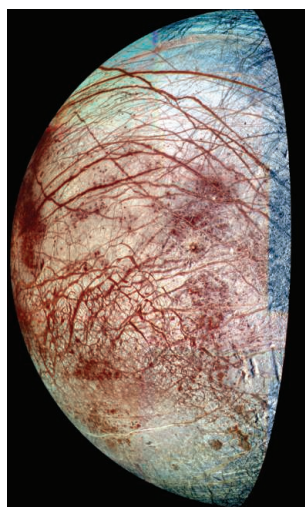
to the substantial exchange of geological material from there to here more than 3 billion years ago. In contrast, life on Jupiter's moon Europa could be an "independent experiment." If so, we may well know the answer before the end of the 21st century (not many of us will be around then, though). Must life have a "digital" way of storing genetic information? Probably yes. Will the genetic material of Europeans resemble DNA? It could be. If they have a genetic alphabet like DNA, will it have four letters (cytosine, thymine, adenine, and guanine in our case), or fewer, or more? There are theories around that discuss the evolutionary optimality of genetic alphabets, but a natural answer would be best. What is more or less contingent about life? We will know more about this in this century.

All this hinges, of course, on the assumption that we do not ruin the planet and its biota. It would be difficult to get rid of cyanobacteria, but it would be relatively easy to get rid of ourselves. This in turn depends on the ability of the "Earth system" to regulate itself. Part of this regulation is due to our lucky planetary constitution (including recycling of key materials through plate tectonic movements); other aspects may be selected products or unselected by-products of biological evolution. There are justified objections to simplistic approaches to what has become known as the Gaian view of the Earth system, but presumably a lot needs to be discovered about coevolution on the planetary scale (as discussed by Tim Lenton). Once again, at least one comparative case would be welcome.

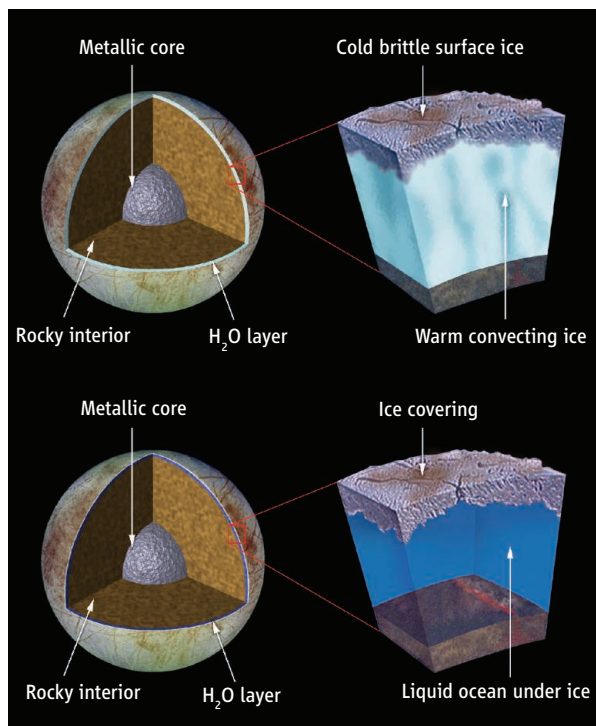
Darwin was a peculiar combination of keen observer, experimenter, and calm revolutionary. Whereas details matter enormously (we believe in the testability of scientific ideas), it is healthy to keep a balance: Among some of the half-baked ideas today may lurk a few outstanding theories of the future. As Einstein explained to Paul Valéry (5), one does not need a notebook for brilliant ideas since they are exceptionally rare. I do not believe in the end of science: Brilliant theories of the highest rank are yet to come. But I hold it unlikely that the Darwinian approach will be overturned in the way Aristotelian physics had been: We firmly remain on Darwin's side in the 21st century.

References

1. *Darwin and the 21st Century Science Seminar*, 23 to 24 March 2006, Cambridge, UK; organized by the Charles Darwin Trust.
2. C. Darwin, *The Autobiography of Charles Darwin 1809–1882*, N. Barlow, Ed. (Norton, New York, 1969), p. 139.
3. D. Dennett, *Darwin's Dangerous Idea* (Simon and Schuster, New York, 1996).
4. M. Christiansen, S. Kirby, in *Language Evolution*, M. Christiansen, S. Kirby, eds. (Oxford University Press, Oxford, UK, 2003), pp. 1–15.
5. B. Bryson, *A Short History of Nearly Everything* (Random House, New York, 2003).



Independent experiment. Jupiter's moon Europa may harbor life and provide a test bench for Darwinian thinking in the 21st century. (Left) Image of Europa's surface taken by NASA's Galileo spacecraft. (Right) Two proposed models of Europa's structure.



discussed by Laurence Hurst). Some regard this opportunity as the most rewarding by-product of the genome projects. Yet, this approach is very Darwinian in the sense that it is based on the comparative anatomy of genes, biochemical networks, and so on. This is going to be, without doubt, a very productive field.

Remote from questions about the origin of life there is the formidable set of problems that include the origin of human cooperation and the emergence of natural language. Some regard the latter as "the hardest problem of science" (4). This may be an exaggeration, but certainly a problem where processes of biological evolution, individual learning, and cultural transmission become intertwined cannot be considered trivial. It is perhaps no accident that cooperation in large non-kin groups, a developed theory of mind, tool use, teaching (different from learning), and natural language go together in our species. The uniqueness of language raises special problems. Some see this as a fundamental impediment to a successful Darwinian approach. I disagree. Uniqueness presents special methodological challenges, but we should bear in mind that the origin of the eukaryotic cell, as one

(living inside the host cell) into these organelles, is one of the great successes of 20th-century science. It could well be that explaining in at least broad but rigorous terms how the human condition has come about will be a success of the present century (as discussed by Stephen Mithen). Certainly, developments in comparative genomics, proteomics, and linguistics, as well as in neuroscience, hold promise that this endeavor may not be hopeless. It is again a safe bet that apt mathematical models of (cultural) group selection will be an indispensable ingredient of the explanation.

It was emphasized repeatedly at the meeting that Darwin's thinking was extremely integrative. This tradition must be kept up. The present century may cast a shadow on many previous ones if one of our old hopes comes true: finding extraterrestrial life. Astrobiology, a modern successor to exobiology, is regarded by some as the designated field to deal with this issue. Setting terminology aside, the potential implications are formidable. But one should be not overly optimistic, either. Even if there is some small biomass remaining on Mars, it is not unlikely that the Martians will turn out to be our relatives, due

Considering Therapeutic Antibodies

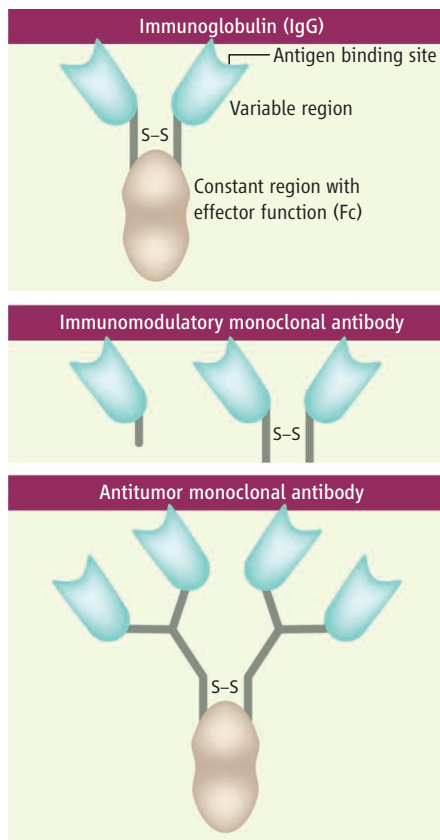
Ellen S. Vitetta and Victor F. Ghetie

In March 2006, the general public was stunned when six healthy individuals injected with an antibody targeting a small subset of T cells suffered immediate and profound side effects including severe pain and extreme swelling (1). All were admitted to the intensive care unit of a London hospital.

One individual remained in a coma for 3 weeks with heart, liver and kidney failure, septicemia, pneumonia, and gangrene. What went wrong? The published research leading up to this clinical trial was novel and provocative, showing that the antibody preferentially activated suppressor regulatory T cells from rodents even though the molecule that it recognizes is expressed on virtually all T cells. The antibody was also claimed to be entirely safe in monkeys and had clear efficacy in mice with autoimmune disease. Regardless, the fate of the volunteers might have been predicted by considering the “big picture” of the immune system. The important question confronting us now is what can be done in this field to prevent future mishaps and to optimize new antibody-based therapies? A significant challenge will be to better understand an antibody’s target as well as the spectrum of effects that occur when an antibody binds to its target. Meeting this challenge will have a critical impact on antibody design and the conduct of sound clinical trials.

The monoclonal antibody (mAb) used in the clinical trial in question is anti-CD28 (TGN1412), a “superagonist” designed to bind to the CD28 molecule on the surface of regulatory T cells. Together with the T cell receptor, CD28 normally promotes T cell proliferation and cytokine production. This superagonist antibody bypasses the need for T cell receptor specificity and can therefore activate T cells of all specificities. Most T cells are designed to eliminate infected cells and under normal circumstances, they are only activated when an infection or “danger” is present. Other T cells are self-reactive and are thought to be held in check by regulatory T cells that prevent their activation. It was hoped that activation of regulatory T cells by TGN1412 would further suppress the immune system and, thus, eventually be developed to treat patients with autoimmune diseases. However, CD28 is expressed on the vast

majority of T cells as well as eosinophils, all of which secrete cytokines or chemokines following activation. Even though TGN1412 did “preferentially” activate regulatory T cells, it also activated nonregulatory T cells, albeit much less effectively and at a higher dose (2, 3). The same was true in monkeys (according to the patent application for the antibody), even though this activation was claimed to have no systemic side effects. Activation of these other T cells in humans, however, would result in the damage of one’s own tissues, as well as the secretion of cytokines that cause inflammation—a cytokine storm. Such a storm can cause multisystem organ failure, as seen in the TGN1412 trial. Because nonregulatory T cells outnumber regulatory T cells by at least 10 to 1, the assumption that only the latter would be activated following injection of TGN1412 should not have been made. Furthermore, regulatory and non-regulated T cells might not be strictly separate lineages. TGN1412 would likely bind to and activate the first T cells that it encountered. Activation of even a small percentage of the



Antibody design. A schematic of a prototype monoclonal antibody and proposed structures for immunomodulatory and antitumor antibodies are shown.

majority of T cells as well as eosinophils, all of which secrete cytokines or chemokines following activation. Even though TGN1412 did “preferentially” activate regulatory T cells, it also activated nonregulatory T cells, albeit much less effectively and at a higher dose (2, 3). The same was true in monkeys (according to the patent application for the antibody), even though this activation was claimed to have no systemic side effects.

Activation of these other T cells in humans, however, would result in the damage of one’s own tissues, as well as the secretion of cytokines that cause inflammation—a cytokine storm. Such a storm can cause multisystem organ failure, as seen in the TGN1412 trial. Because nonregulatory T cells outnumber regulatory T cells by at least 10 to 1, the assumption that only the latter would be activated following injection of TGN1412 should not have been made. Furthermore, regulatory and non-regulated T cells might not be strictly separate lineages. TGN1412 would likely bind to and activate the first T cells that it encountered. Activation of even a small percentage of the

Unexpected dangerous side effects of antibody-based therapies may be prevented with improved design of monoclonal antibodies and of clinical testing protocols.

total T cells (self-reactive and otherwise) by TGN1412 could have dire consequences.

mAbs constitute a multibillion dollar industry. There are currently 15 mAbs that are used worldwide to treat conditions including cancer, autoimmune disease, allergy, cardiovascular disease, and transplant rejection (table S1). Notably, all the successful clinical mAbs kill cells, inhibit cellular interactions, or prevent effector molecules from binding to their targets. None are agonists. At least 100 other mAbs are in the pipeline (4). Scientists have done a stellar job in turning mouse mAbs into humanlike or human forms so that patients do not generate an immune response to them. This has been accomplished by genetically engineering mouse mAbs so that more than 80% of their structure is the human form. Other techniques to produce human antibodies include immortalizing human cells, immunizing mice endowed with a human immune system, and expressing human antibody genes in high-producer cell lines (4). Scientists have also developed screening platforms for new mAbs, and have genetically engineered mAbs for improved effector functions and pharmacokinetic behavior in vivo (5).

How can the design of mAbs and clinical trials be improved to enhance their use as therapeutic agents? Given their complex structure, there are different issues to consider when designing mAbs to either kill cells or modulate the immune response.

At the amino terminus of an immunoglobulin G (IgG) type mAb are two identical target-binding variable regions (Fv portions), each of which forms a pocket where two polypeptide chains—the heavy and light chain—come together (see the figure) (5). Two heavy chains are linked to two light chains by disulfide bonds, and the two heavy chains are linked to each other by disulfide bonds in a flexible hinge region. Each IgG has a single constant region (Fc portion) composed of the carboxyl termini of both heavy chains. The Fc portion determines the half-life and biodistribution of the IgG in the body. Moreover, the Fc region recruits effector molecules and specialized cells that kill the cell to which the variable regions of the IgG are bound.

To more effectively kill tumor cells in vivo, one could design an IgG with more target binding sites so that it could hypercrosslink its target molecule. Hypercrosslinking particular cell surface molecules can often arrest cell growth or deliver a death signal to the target cell (6). In addition, the Fc region should be preserved and even engineered to have a longer half-life and the desired effector functions (4, 5). It has been argued that smaller IgG fragments that lack an Fc portion can penetrate

Enhanced online at
www.sciencemag.org/cgi/
content/full/313/5785/308

The authors are at the Cancer Immunobiology Center, University of Texas Southwestern Medical Center, 6000 Harry Hines Boulevard, Dallas, TX 75235–8576, USA. E-mail: ellen.vitetta@utsouthwestern.edu

tumors more effectively (7). However, such molecules are rapidly cleared and lack effector functions. Hence, they can only kill tumor cells if they bind to target molecules that deliver death signals. Alternatively, they can be coupled to toxins or drugs for delivery to tumor targets.

It is unlikely that even optimized mAbs will be curative as monotherapy because some tumor cells will be inaccessible and others will lack the target antigen. Hence, chemo- or radiotherapy should be given with mAb treatment. It is also unlikely that mAbs that recognize single epitopes or molecules will be curative, suggesting that cocktails of such mAbs should be used.

In contrast to using mAbs to kill tumor cells or inhibit cell growth, their use as immunomodulatory agonists is an entirely different issue both with regard to structural design and clinical trials. Such an antibody should either be devoid of its Fc portion or contain an Fc region that lacks effector functions so that target cells will not be killed and such that the mAb will have a shorter half-life. A shorter half-life might prevent chronic activation of cell signaling networks that trigger the release of mediators or activation of self-reactive cells. Repeated treatment with very low doses might be a safer choice. In addition, if a mAb does not bind to its target in experimental animals and humans with identical affinity, extremely low doses should be used in the first human exposed to the mAb. Finally, surrogate endpoints indicating that the antibody is reaching its targets and is having the desired effect

should be built into the clinical trial protocol and analyzed before doses are increased. The design of clinical trials must focus first and foremost on safety and acknowledge possible differences in results of preclinical testing of any mAb in rodents or monkeys compared to humans.

Activation of cells such as lymphocytes *in vivo* is not a trivial matter, given the risk of side effects. Although preclinical data claimed to show that TGN1412 was safe when administered to two species of monkey, T cells from monkeys and humans do not have identical CD28 molecules. They likely differ at critical residues recognized by TGN1412. There were no reports of how well TGN1412 bound to human versus monkey T cells, so it is possible that the affinity of the mAb for the former was much greater and that there was no “dose window” for activating regulatory T cells versus all cells in humans. More in-depth studies on cultured human T cells should have addressed these issues. Cytokine storm also might be less prevalent in nonhuman primates. To our knowledge, this was not investigated. Given these concerns, the first volunteer should have been injected with a dose far lower than that which was active in mice. This individual should have been observed for a week or more for side effects and for the presence of activated T cells and cytokines in the blood. Only then should the next individual at that dose have been injected. Instead, all the volunteers in the TGN1412 trial were injected within 20 to 30 minutes. One might even question whether it is ethical (although it might be scientific

sound) to test an agonistic mAb for the first time in normal individuals.

Because the development of therapeutic mAbs has shifted largely from academia to the industrial sector, most information has become proprietary. There are too few peer-reviewed publications concerning preclinical safety and adverse effects in clinical trials. These practices can lead to misjudgments, repeated mistakes, and consequently, higher costs. None of these serves the interests of patients or the future development of drugs. Considering the great promise of mAbs to treat a myriad of diseases, we hope that the design and conduct of clinical trials will become more academic in nature, with open access to results and data.

References and Notes

1. E. Marshall, *Science* **311**, 1685 (2006).
2. N. Beyersdorf, T. Hanke, T. Kerkau, T. Hunig, *Ann. Rheum. Dis.* **64** (suppl 4), 91 (2005).
3. R. Lühder *et al.*, *J. Exp. Med.* **197**, 955 (2003).
4. O. H. Brekke, I. Sandlie, *Nat. Rev. Drug Discov.* **2**, 52 (2003).
5. T. A. Waldmann, J. C. Morris, *Adv. Immunol.* **90**, 83 (2006).
6. X. Liu, L. M. Pop, D. C. Roopenian, V. Ghetie, E. S. Vitetta, J. E. Smallshaw, *Int. Immunopharmacol.* **6**, 791 (2006).
7. P. Holliger, P. J. Hudson, *Nat. Biotechnol.* **23**, 1126 (2005).
8. We thank N. VanOers, J. Niederkorn, D. Farrar, N. Karandikar, J. Uhr, and H. W. Corley for their insightful discussion.

Supporting Online Material

www.sciencemag.org/cgi/content/full/313/5785/308/DC1
Table S1

10.1126/science.1130482

CHEMISTRY

Selective Hydrocarbon Oxidation in Zeolites

Heinz Frei

Partially oxidized hydrocarbons are the most important building blocks of plastics and synthetic fibers; they play an equally dominant role as intermediates for the manufacture of everyday chemicals. These molecules are prepared from natural gas and volatile fractions of petroleum by partial oxidation. Zeolites—crystalline aluminosilicates featuring a network of molecule-size pores and cages—may have important advantages over currently used processes to prepare partially oxidized hydrocarbons, although catalytic rates must be improved.

Existing partial oxidation processes involve gas- or liquid-phase reactions using homoge-

neous catalysts, or catalysis on solid surfaces. Because of the very large scale of these processes, molecular oxygen is the only economically viable oxidant. However, most hydrocarbons form a range of products when they react with oxygen molecules in solution or gas phase, or with activated oxygen species on solid catalysts. Achieving product selectivity thus remains a serious challenge. The large amounts of energy needed to separate the desired product from unwanted side products, the resulting waste, and the inefficient use of starting materials all cause a substantial environmental burden.

The main reasons for the lack of selectivity include the often very high temperatures required, the free-radical nature of gas- and liquid-phase reactions, and the tendency to cause runaway oxidation, which often leads to the formation of carbon oxides (1, 2). There is thus an

Zeolites are highly selective catalysts for partial oxidation of hydrocarbons, but practical applications require faster release of the products.

urgent need for alternate routes for hydrocarbon oxidation that are milder and avoid the formation of highly reactive oxy radicals.

Dioxygen and hydrocarbon molecules can be activated by shining visible light on a gas mixture of oxygen and small saturated or unsaturated hydrocarbons loaded into the nanometer-sized cages of a zeolite (3, 4). The conversion to aldehyde or ketone products is highly selective, with minimal loss of selectivity even after conversion of most of the reactants. In some cases, mild heating in the absence of light also induces the reaction. This route may allow partial oxidation of small saturated and unsaturated hydrocarbons to important industrial chemicals with much improved selectivity compared to that of existing processes. The key ingredients responsible for this oxidation route are the largely unshielded alkali or alkaline-earth ions in the

The author is in the Physical Biosciences Division, Lawrence Berkeley National Laboratory, University of California, Berkeley, CA 94720, USA. E-mail: hmfrei@lbl.gov

large zeolite cages. The positive charge of these cations balances the negative charge introduced into the framework by the aluminum centers (5). The unusually high electrostatic fields in the vicinity of the cations dramatically reduce the energy needed to excite hydrocarbon-oxygen charge transfer (see the figure).

Existing methods of hydrocarbon oxidation typically start off by hydrogen abstraction from the hydrocarbon. These paths invariably lead to runaway, unselective oxidation because hydrogen abstraction from the initial products occurs much more easily than from the starting hydrocarbon. The charge-transfer path does not have this problem, because it is an extremely mild way of activating hydrocarbon and oxygen, and the first products formed are inherently stable against further reaction with oxygen. Also, the very mild reaction conditions avoid the formation of high-energy intermediates.

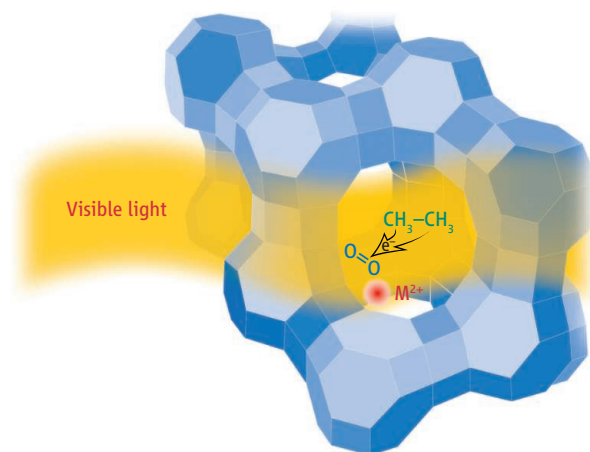
Colliding hydrocarbon-oxygen pairs in the gas or liquid phase have charge-transfer states that absorb at high energy, deep in the ultraviolet region (6, 7). Extremely large electrostatic fields—like those in the vicinity of the zeolite cations—stabilize charge-transfer states of properly oriented pairs. As a result, reaction can be initiated at the much lower energies of visible photons, or even thermally by mild heating. The ionization potential of the hydrocarbon and the charge density of the zeolite cation can influence reaction rates (3, 4, 8, 9). Highly detailed insights into the charge-transfer path are now emerging from several laboratories.

In zeolite Y containing Ca^{2+} ions, Berg *et al.* have observed very similar rates of light-induced oxidation for propane molecules that have virtually the same ionization potential but have deuterium (D) substituted in different positions ($\text{CD}_3\text{CH}_2\text{CD}_3$ and $\text{CH}_3\text{CD}_2\text{CH}_3$). By contrast, for propane isotopes with very different ionization potentials, such as C_3H_8 (11.22 eV) and C_3D_8 (11.40 eV), the reaction rates differ by a factor of more than 20 in favor of the molecule with the lower potential (10). The large influence of the hydrocarbon ionization potential on the one hand, and the absence of a kinetic-isotope effect for the reacting CH bonds on the other, are clear manifestations of the charge-transfer nature of the reaction path.

Xu *et al.* have prepared zeolite materials with varying Ca^{2+} content and used mild heating instead of light to activate propane oxidation. The rate of propane oxidation to acetone increased sharply when Ca^{2+} ions began to

occupy the large zeolite cages and the windows between them (11). This is a beautiful demonstration that the reaction requires hydrocarbon-oxygen encounters in locations of high electrostatic fields (that is, near Ca^{2+}). Once launched onto the charge-transfer path, the highly acidic hydrocarbon radical cation readily transfers a proton to an O_2^- partner, followed by coupling of the alkyl and HOO radicals to form a hydroperoxide molecule. Spontaneous elimination of a water molecule yields the desired carbonyl product. For selective ethane oxidation (see the figure), a reaction that is particularly attractive for mild C-H bond activation, the intermediate is ethyl hydroperoxide, and the commodity chemical acetaldehyde is the final product.

Photochemical quantum efficiencies (the number of product molecules per absorbed pho-



Selectivity at low energy. Visible light induces charge transfer between ethane and oxygen molecules to form a transient ethane radical cation and a superoxide species (O_2^-).

ton) can reach up to 50% depending on the hydrocarbon used. These high efficiencies, combined with achievable light intensities of visible lamps, give catalytic rates suitable for practical applications (4). However, the polar reaction products are strongly bound to the ionic zeolite environment, preventing rapid desorption from the catalyst. Fast removal of the final products from the zeolite is essential if conversion of hydrocarbon to gas-phase product is to be accomplished at practical rates.

To address this challenge, a more detailed understanding is required of how hydrocarbon and oxygen molecules arrange themselves around the high-field cations to access the low-energy charge-transfer path. Distinct infrared features have revealed the simultaneous interaction of an oxygen and a propane molecule with a single alkaline-earth cation inside the zeolite cage at room temperature (12). Such insights into the location and precise geometry of the reactant pair before charge transfer may guide the design of modified or new zeolite materials that accomplish product desorption with sufficient speed without diminishing the oxidation rate.

A density functional theory study of a small unsaturated hydrocarbon molecule interacting with O_2 suggests that the electrostatic field locks the reactant pair in a pretransition state that lowers the charge-transfer excitation energy but only influences the position of the excited state in a minor way (13). This result suggests that it may be possible to create confined spaces for hydrocarbon-oxygen charge-transfer pairs in less ionic environments that might facilitate the desorption of the polar carbonyl products.

Insights into the origin of the high product selectivity, even as substantial amounts of reactants get converted to products, have been gained with time-resolved spectroscopy. By monitoring small transient radicals with step-scan Fourier-transform infrared spectroscopy on time scales from nanoseconds to milliseconds, we have been able to distinguish between reaction of radicals originating from the same reactant pair (geminate encounters) and reaction of radicals emerging from different pairs, which may lead to side products (nongeminate encounters). The results show that the constrained zeolite environment minimizes the occurrence of nongeminate encounters (14, 15).

Charge transfer-induced oxidation in zeolites offers opportunities for converting abundant hydrocarbon resources to important industrial chemicals with high selectivity. The main challenge will be to improve product desorption rates while preserving access to a low-energy charge-transfer path. The further development of spectroscopic and computational methods for elucidating the dynamics and energetics of colliding hydrocarbon and oxygen molecules within the zeolite will be particularly important. Insights from these mechanistic studies will accelerate the development of zeolite environments suitable for practical use.

References and Notes

- R. A. Sheldon, J. K. Kochi, *Metal-Catalyzed Oxidation of Organic Compounds* (Academic Press, New York, 1981).
- G. Centi, M. Misono, *Catal. Today* **41**, 287 (1998).
- F. Blatter, H. Frei, *J. Am. Chem. Soc.* **115**, 7501 (1993).
- F. Blatter *et al.*, *Catal. Today* **41**, 297 (1998).
- D. W. Breck, *Zeolite Molecular Sieves: Structure, Chemistry, and Use* (Wiley, New York, 1974).
- D. F. Evans, *J. Chem. Soc.* **1953**, 345 (1953).
- H. Tsubomura, R. S. Mulliken, *J. Am. Chem. Soc.* **82**, 5966 (1960).
- D. L. Vanoppen, D. E. De Vos, P. A. Jacobs, *Stud. Surf. Sci. Catal.* **105**, 1045 (1997).
- Y. Xiang, S. C. Larsen, V. H. Grassian, *J. Am. Chem. Soc.* **121**, 5063 (1999).
- O. Berg, M. Bonn, A. W. Kleyn, *van Marum Colloquium* (Leiden, the Netherlands, May 2005).
- J. Xu *et al.*, *J. Phys. Chem. B* **108**, 15728 (2004).
- J. Xu *et al.*, *J. Phys. Chem. B* **109**, 18361 (2005).
- E. A. Pidko, R. A. van Santen, *J. Phys. Chem. B* **110**, 2963 (2006).
- Y. H. Yeom, H. Frei, *J. Phys. Chem. B* **107**, 6286 (2003).
- Y. H. Yeom, H. Frei, in *In-Situ Spectroscopy of Catalysts*, B. M. Weckhuysen, Ed. (American Scientific, Stevenson Ranch, CA, 2004), pp. 32–46.
- The author is supported by the U.S. Department of Energy, Office of Basic Energy Sciences.

10.1126/science.1128981

ASTRONOMY

Near-Field Cosmology

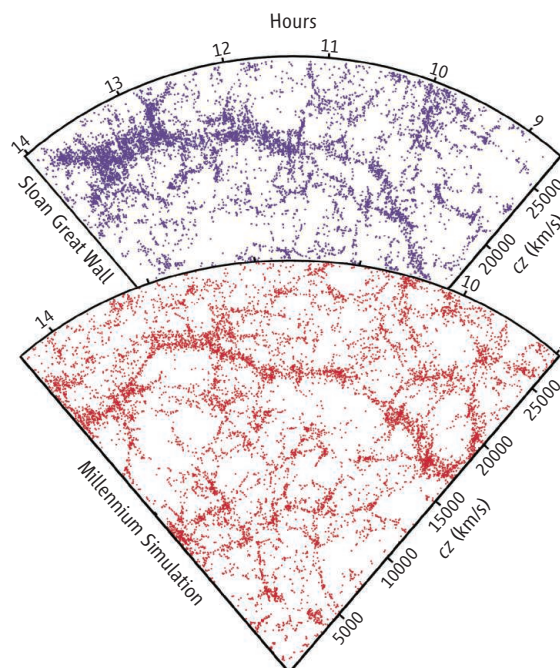
Joss Bland-Hawthorn and P. J. E. Peebles

These are exciting times for astronomy and cosmology. On the one hand, we find that the main predictions of Big Bang inflationary cosmology are confirmed by observations of distant objects. On the other hand, nearby galaxies continue to surprise and inform us. In February 2006, a group of 50 scientists convened in Aspen, Colorado, to discuss what we are learning about cosmology from detailed observations of the nearest galaxies (1).

Approximately 380,000 years after the Big Bang, the expanding universe became cool enough to allow ions and electrons to combine to form a gas of atomic hydrogen and helium. The free electrons had scattered and trapped the thermal radiation from the hot Big Bang; the abrupt elimination of these free electrons allowed the thermal radiation to move nearly without scattering. Precision measurements of the distribution of this radiation, most recently by the Wilkinson Microwave Anisotropy Probe (WMAP) satellite (2), are in beautiful agreement with the relativistic theory of how the present concentrations of mass in and around galaxies grew out of the distribution of mass at the time of release of the radiation.

But the story does not end there. The universe was ionized again in a process that is thought to have commenced some 100 million years after the Big Bang and is observed to be complete by the time the universe was 10 times that age. The study of this reionization is a topic for current research, but we do know that the first generations of massive stars likely played a major role. Observations of distant galaxies, seen as they were in the past because of the light travel time, show that many young galaxies were strong sources of ionizing radiation, but observations must reach still greater distances to show us the earliest generations of stars. This is a key science goal of the next generation of large telescopes, including the James Webb Space Telescope due to launch in the next decade.

A notable issue for Big Bang cosmology is that it requires only 4% of the mass of the universe to be in the form of baryons (particles such as protons and neutrons) of which stars and people are made. The rest is in “dark matter,” which acts like a gas of particles that are not baryons, and “dark energy,” which is the new name for Einstein’s cosmological constant or something that acts like it. The evidence for the existence of



Simulated structures. Comparison of the galaxy distribution obtained from spectroscopic redshift surveys and theoretical mock catalogs. (Top) Galaxy distribution in a small section of the Sloan Digital Sky Survey, in which one of the largest observed structures in the universe has been detected. This “Sloan Great Wall” contains more than 10,000 galaxies and stretches over more than 1.3 billion light-years. (where c is the speed of light and z is the redshift). (Bottom) Mock galaxy survey with matching survey geometries and magnitude limits, constructed with semianalytic techniques to simulate the formation and evolution of galaxies within the evolving dark matter distribution of the Millennium Simulation (8).

these dark components is strong, but their properties are only loosely understood.

Fossil evidence available in nearby galaxies is an important part of the research on such open issues. The Local Group contains two large spiral galaxies, our Milky Way and Andromeda, and about 40 dwarf galaxies. Halo stars—the stars outside the discs and luminous central bulges of the two spirals—have relatively low abundances of elements heavier than helium. These stars likely formed at early times, because nuclear burning in stars is forever increasing the amount of mass in heavy elements (3). Two stars in the halo of the Milky Way have very low heavy element content, with mass fractions in iron relative to hydrogen less than 1/200,000 the mass fraction in iron in the Sun (4). It is plausible that these stars are ancient, and if so, their very unusual mix of chemical elements provides vital information about the nature of the earliest generations of stars. This would include the elusive

Cosmological puzzles are usually tackled by studying distant objects. A recent meeting considered the ways in which observations of nearby galaxies can add to the picture.

population that ionized almost all the neutral matter and produced the first heavy elements (as discussed at the meeting by Jason Tumlinson and Takuji Tsujimoto).

Other ancient stars may be hiding in the centers of galaxies, where the mass density is high and conditions likely first favored star formation (in presentations by Jon Fulbright and Rosie Wyse). It would be fascinating to search for ancient stars with unusual heavy element abundances in the center of the Milky Way, but dealing with the crowds of stars and the obscuration by dust will require an extremely large ground-based telescope (20 to 40 m diameter) working at high angular and spectral resolution. This is a project for the future.

Modern computer simulations of how the Big Bang unfolded over 13.7 billion years to yield present-day galaxies can involve up to 10 billion particles (as presented by Simon White). These computations yield structures that look a good deal like real galaxies and clusters of galaxies, adding to the evidence that our picture for the evolution of the universe is on the right track. But close examination of the nearby galaxies shows discrepancies with what the simulations might lead one to expect. For example,

our Local Group is expected to have a thousand small mass concentrations (5), but we infer the presence of fewer than 50 from the number of visible galaxies. It is plausible that when the universe was ionized, the heating of the gas in the smallest of the dark matter concentrations was sufficient to prevent the formation of any stars, leaving dark galaxies. But dwarf galaxies are observed. Consistent with that knowledge, the simulations indicate that some stars formed in small mass concentrations before or shortly after the disruption by ionization (as discussed by Andrey Kravtsov and Oleg Gnedin), producing almost dark galaxies. The challenge is to reconcile the large number of low-mass dark matter concentrations with the smaller number of observed dwarf galaxies. Ideas are being tested by ongoing searches for the faintest nearby galaxies and the study of their properties.

The simulations also indicate that a vast hierarchy of merging of the dark matter concentra-

J. Bland-Hawthorn is at the Anglo-Australian Observatory, Epping, NSW 2121, Australia. P. J. E. Peebles is in the Department of Physics, Princeton University, Princeton, NJ 08544, USA. E-mail: jbh@ao.ao.gov.au

tions continues to the present day. As discussed at the meeting, such merging does happen: Dwarf galaxies spiral into larger ones, where they are torn apart to produce the star streams observed in the Milky Way and Andromeda galaxies (work presented by Amina Helmi; Mike Irwin; Heidi Newberg). But the patterns of heavy element abundances indicate that no major component of the Milky Way could have been assembled largely by accretion of dwarfs of the kind observed today (discussed by Eline Tolstoy). The two large galaxies in the Local Group certainly could have formed by merging of dwarfs in the early universe; the curious thing is that the dwarfs that were left behind have to be substantially different (6).

Another aspect of the merging issue concerns the tight concentrations of stars known as globular clusters. The color of a globular cluster—and likely its heavy element abundance—correlates with the luminosity of the host galaxy. Because globular clusters generally are old, this indicates either that the globulars became attached to the present host galaxy a long time ago—which does not naturally agree with the substantial recent merging in the simulations—or that the globulars were recently attached to the host galaxy but “knew” the luminosity of the host, which seems strange (discussed by Jean Brodie).

Another issue emerges from the Millennium

Simulation, one of the largest such studies ever carried out (see the figure) (7). In this simulation there are satisfactory analogs of the Local Group (as presented by Simon White). A study of the local universe reveals that groups dominated by a few large galaxies, such as the Local Group, are common (discussed by Brent Tully). The issue debated at the meeting is whether such groups are common in the simulation. Related to this is the abundance of spiral galaxies like the Milky Way that have a modest bulge of quite old stars and a prominent disk of stars with a broad range of ages. Elegant examples form in simulations (presented by Matthias Steinmetz). But because the theory predicts substantial merging and accretion in nearby galaxies, which tend to destroy thin disks, a pressing issue is whether disk-dominated systems that contain old stars as well as young are as common in the simulations as they are observed to be nearby.

In short, present-day cosmological simulations do not give a very complete account of the finer details of the nearby universe. This is in part a result of the extreme difficulty of understanding the gas dynamics that determines how matter settles into galaxies and collapses from there to form much denser stars, and how stellar winds and explosions stir up the remaining gas and control the rate at which new stars form. Dealing with all this in full detail is far beyond the capabilities of modern computers. But we have observations of

forming stars to teach us what happens, and what we are learning is being applied to increasingly detailed simulations of this complex process.

Also to be borne in mind is that the problems with the simulations may be highlighting the need for improved physics. After all, the simulations invoke many parameters to describe the 4% of the universe that is made of baryonic matter, while using only a few to describe the remaining 96% in dark matter and dark energy. It was surprising to find that we must postulate dark matter. Dark energy was another surprise, and the dark sector may surprise us yet again.

References and Notes

1. Aspen Center for Physics workshop on Local Group Cosmology, Aspen, CO, 5 to 11 February 2006.
2. D. N. Spergel *et al.*, <http://arxiv.org/abs/astro-ph/0603449> (2006).
3. The Big Bang produced mostly hydrogen and helium, whereas most of the heavier elements were produced in stars and returned to the interstellar medium by supernovae and winds, in a process that cycled through generations of stars.
4. T. Beers, N. Christlieb, *Annu. Rev. Astron. Astrophys.* **43**, 531 (2005).
5. A. R. Zentner, J. S. Bullock, *Astrophys. J.* **598**, 49 (2003) and references therein.
6. B. Robertson *et al.*, *Astrophys. J.* **632**, 872 (2005).
7. German Astrophysical Virtual Observatory simulation query page (www.g-vo.org/mpasims).
8. V. Springel *et al.*, *Nature* **435**, 629 (2005).

10.1126/science.1127183

CHEMISTRY

A Golden Boost to an Old Reaction

Hans-Ulrich Blaser

Functionalized aminobenzenes [anilines (see the figure)] are important intermediates for the manufacture of many agrochemicals, pharmaceuticals, dyes, and pigments. To yield anilines, aromatic nitro compounds must be reduced in a hydrogen-addition or hydrogenation reaction. The hydrogenation of simple aromatic nitro compounds poses few problems and is carried out catalytically on very large scales. But when other reducible groups are present in the molecule, it is difficult to reduce the nitro group selectively in a catalytic process. In such cases, the use of older, noncatalytic manufacturing processes prevails despite the large amounts of waste produced by these processes. On page 332 of this issue, Corma and Serna (1) report a promising new, highly chemoselective catalyst to make anilines.

There are few generally applicable catalytic systems for the selective reduction of a

nitro group in the presence of C=C, C≡C, C=O, C=N, or C≡N groups. In light of the industrial importance of functionalized anilines, it is surprising that in the past decade, relatively little research has been carried out to develop new catalysts for this task. Today's state of the art was mainly established in the mid-1990s (2). Corma and Serna now show that gold particles supported on TiO₂ or Fe₂O₃ catalyze the reduction of various functionalized aromatic nitro compounds without hydroxylamine accumulation (a common problem in such reactions) and with high chemoselectivity. The work should give a strong impulse to new research efforts for this important transformation.

Why it is so difficult to selectively reduce a nitro group in preference to other groups present in the molecule? More than 100 years ago, Haber (3) proposed the reaction network shown in the figure to explain the electrochemical reduction of aromatic nitro compounds. Obviously, the sequence of reactions

Gold catalysts promote selective reduction of aromatic nitro compounds to anilines, providing a new way to synthesize industrially important products.

is complex. Furthermore, the intermediates formed in this process are very reactive species that can react with each other as well as with other chemicals.

The intermediates proposed by Haber have all been verified, and it has been generally accepted that catalytic hydrogenation reactions in principle proceed via the same routes. The major difference to the electrochemical variant is that the catalyzed reaction steps—especially the splitting of the H-H bond and the addition of H to the various intermediates—occur while the molecule is adsorbed on the catalytic surface.

The reduction to anilines occurs in several steps, either by the direct route via nitroso and hydroxylamine intermediates (see the figure, left) or via a condensation route (see the figure, right); the latter route is favored under basic conditions. The first two reduction steps in the direct route tend to be fast, and the nitro and nitroso compounds are strongly adsorbed on the catalyst surface. In

The author is at Solvias AG, 4002 Basel, Switzerland.
E-mail: hans-ulrich.blaser@solvias.com

contrast, hydroxylamine reduction, which requires the cleavage of an O-N bond, is slow; aniline may even be formed via a disproportionation pathway. The slowness of this step leads to accumulation of hydroxylamine intermediates, the formation of unwanted by-products, and possible runaway reactions due to decomposition (with accompanying health and safety issues).

If an additional functional group R is present that can also be reduced or cleaved by hydrogen, this unwanted reduction can occur in any of the intermediates or after the functionalized aniline has been formed. For chlorinated aromatic nitro

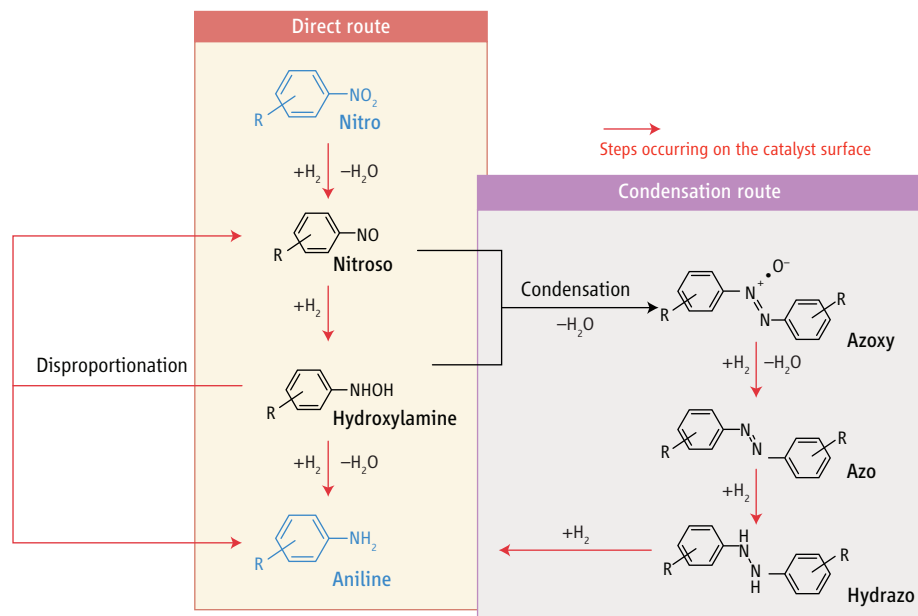
inimum, and nickel as the active metal—and have improved chemoselectivity by modification. This led to a plethora of catalysts modified by the addition of sulfur-, phosphorus-, nitrogen-, or halogen-containing compounds that showed better chemoselectivity, especially for chlorinated aromatic nitro compounds (4). However, chemoselectivity was often achieved at the price of lower catalytic activity and the accumulation of hydroxylamines. A common view is that these modifiers preferentially adsorb on the most active sites (thought to be least selective), thereby hindering adsorption and unselective hydrogenation. Other possible

As pointed out above, large amounts of hydroxylamines can accumulate, because the catalyst is not active enough (for example, because a modifier is present) and/or because the hydroxylamine intermediate is particularly stable. This problem can be avoided through the addition of promoters, especially of vanadium compounds. On the basis of this finding, a series of very selective Pt/C catalysts modified with hypophosphorous acid and promoted by vanadium compounds have been developed (5).

Corma and Serna chose a different approach. They did not start with a known active catalyst, but rather tried gold as the active metal. In contrast to silver (6), no precedent for nitro group reduction exists for gold. However, several cases of gold-catalyzed hydrogenation of C=C and C=O groups have been published (7). It is thus surprising that the authors achieved high chemoselectivities for the hydrogenation of 4-nitrostyrene, 4-nitrobenzaldehyde, 4-nitrobenzotrile, and 1-nitrocyclohexene. It is even more remarkable that—with the exception of the aldehyde substrate—very little hydroxylamine accumulation or by-product formation was observed.

The gold catalysts achieve good chemoselectivity without any additives and require only very small amounts of vanadium promoter. The selectivities are comparable to those of the Pt/C-H₃PO₂ and Pb-Pt/CaCO₃ catalysts. Catalyst recycling is possible, but recycling strategies are always much more cumbersome than a once-through approach. Furthermore, the problems with the aldehyde substrate indicate that more stable hydroxylamines might accumulate more readily.

The newly discovered gold catalysts are a welcome addition to the toolbox for the chemoselective catalytic reduction of nitro compounds with hydrogenation-sensitive substituents. The scope of the new catalysts and their mode of action remain to be established, but the promising results should give a strong stimulus to this area of catalytic chemistry.



How to make anilines. Starting from a functionalized aromatic nitro compound, several reduction steps are required to form the corresponding aniline via either the direct route (left) or the condensation route (right) (modified Haber scheme).

compounds, dehalogenation occurs mostly after the strongly adsorbing nitro group has been reduced. This may be one reason why several effective catalysts for the chemoselective hydrogenation of chlorinated aromatic nitro compounds have been developed (4).

The situation is different for nitro compounds in which R is an unsaturated group. Such groups also adsorb quite strongly on the catalyst, and at least some reduction of the R group is likely to occur at the same time as the nitro group is reduced. However, little concrete structural or kinetic information is available on this point. The basic problem is to find a catalyst that can catalyze all different steps in the reduction cascade from NO₂ to NH₂—where each step might require different catalytic properties—without touching a C=C or C=O bond attached to the same molecule.

The most successful strategies to achieve this task have started from active but unselective catalysts—mostly with palladium, plat-

consequences of adsorbed modifiers are the formation of isolated or electronically altered sites. These explanations are difficult to confirm experimentally.

Another way to modify the properties of a catalyst is the formation of an overlayer of irreversible adsorbed species. For example, the Pb-Pt/CaCO₃ catalyst achieves high chemoselectivity for the hydrogenation of various functionalized aromatic nitro compounds in polar solvents (5). Best results are observed when a thin but complete layer of lead is deposited on the platinum. This layer prevents adsorption of the nitro and other reducible groups on platinum active sites. However, the smaller hydrogen molecule can still reach the platinum surface, dissociate, and reduce the strongly oxidizing nitro group via an electrochemical mechanism. The hydrogenation of other reducible groups can only proceed via a classical mechanism that requires adsorption on the active platinum site and is therefore inhibited.

References and Notes

1. A. Corma, P. Serna, *Science* **313**, 332 (2006).
2. H. U. Blaser, U. Siegrist, H. Steiner, M. Studer, in *Fine Chemicals Through Heterogeneous Catalysis*, R. A. Sheldon, H. van Bekkum, Eds. (Wiley-VCH, Weinheim, Germany, 2001), pp. 389–406.
3. F. Haber, *Z. Elektrochem.* **22**, 506 (1898).
4. P. Baumeister, M. Studer, F. Roessler, in *Handbook of Heterogeneous Catalysis*, G. Ertl, H. Knözinger, J. Weitkamp, Eds. (Wiley-VCH, Weinheim, Germany, 1997), pp. 2186–2209.
5. P. Baumeister, H. U. Blaser, U. Siegrist, M. Studer, *Catal. Org. React.* **75**, 207 (1998).
6. Y. Chen, C. Wang, H. Liu, J. Qiu, X. Bao, *Chem. Commun.* **2005**, 5298 (2005).
7. P. Claus, *Appl. Catal. A* **291**, 222 (2005).
8. I thank U. Siegrist, H. Steiner, and M. Studer for their critical comments.

10.1126/science.1131574

Evolution of the Molecular Machines for Protein Import into Mitochondria

Pavel Dolezal,^{1,2} Vladimir Likic,² Jan Tachezy,³ Trevor Lithgow^{1,2*}

In creating mitochondria some 2 billion years ago, the first eukaryotes needed to establish protein import machinery in the membranes of what was a bacterial endosymbiont. Some of the preexisting protein translocation apparatus of the endosymbiont appears to have been commandeered, including molecular chaperones, the signal peptidase, and some components of the protein-targeting machinery. However, the protein translocases that drive protein import into mitochondria have no obvious counterparts in bacteria, making it likely that these machines were created de novo. The presence of similar translocase subunits in all eukaryotic genomes sequenced to date suggests that all eukaryotes can be considered descendants of a single ancestor species that carried an ancestral "protomitochondria."

Eukaryotic cells have two distinguishing features: an endomembrane system that provides the nuclear envelope and mitochondria. Both the nucleus and mitochondria house and protect DNA; the nuclear genome carries the vast majority of genes, with the mitochondrial genome coding for 0.1 to 1% of the cellular proteome (Fig. 1). The sequence of the first mitochondrial genome gave vital support to the endosymbiotic origin of mitochondrion (*J*). Mitochondria represent a relic of an ancient species of alphaproteobacteria that inhabited the cytosol of the first eukaryotes (*2*), with phylogenetic studies suggesting that this early bacterial symbiont had a proteome coded from more than 630 distinct genes (*3*).

According to the endosymbiotic theory, the bacterial symbiont transferred much of its genome in a gradual process such that the bacterial genes were integrated into the nuclear chromosomes. It remains difficult to gauge the metabolic nature of the original symbiosis and, therefore, difficult to know what factors might have driven the ancient bacterial symbiont to surrender its genome and become a mere organelle of the host cell (*4*). Whatever the metabolic advantages, the majority of proteins functioning in mitochondria are now coded on nuclear genes. In a classic "chicken and egg" scenario, it remains equally possible that the susceptibility of the endosymbiont to lose genes provided the selective pressure to create machinery to promote protein import, or that installing a protein import machinery enabled the productive transfer of endosymbiont genes to the nucleus. Either way, the molecular machines created to drive protein import into mitochon-

dria were established in the last common ancestor to all eukaryotes. Recent studies suggest that the central components of the machines are present in all eukaryotes.

Here, we look at how protein import pathways were established to create mitochondria. The protein import pathway is driven by a set

of molecular machines, and these machines are of modular design (Table 1). Each machine has a core module that seems to be common to all eukaryotes. Additional modules have been added to each machine over time, with these add-ons being common only to particular eukaryotic lineage. The evolution and comparative aspects of the function of these mitochondrial machines provides a blueprint for understanding the evolution of cellular machinery in general and a rich means of determining the precise function of these sophisticated machines. That most of the machinery was created de novo and established in the mitochondrial membranes of the first eukaryote supports the idea that all eukaryotes are descendants of a single ancestor species.

The Protein Import Machinery in Mitochondria

Most mitochondrial proteins are encoded in the nucleus and carry a targeting signal that ensures their proper delivery into the organelle. Mitochondrial targeting sequences are recognized sequentially by a series of protein translocases (*5, 6*); most of the functional studies to date have focused on the protein import machinery in the yeast *Saccharomyces cerevisiae* (Fig. 2). The protein translocases have a core

Table 1. Modules of the protein translocases of mitochondria. For each of the protein translocases summarized in Fig. 2, the modular design is indicated and the function of each module shown. The subunit proteins from yeast are indicated for each module. Some modules have evolved independently so that the subunit composition in other eukaryotes might differ from that seen in yeast. Where not referenced in detail in the text, references are noted in the table. OXA, required for cytochrome oxidase activity; IMP, inner membrane peptidase; MPP, matrix-located processing peptidase.

	Modules	Subunits in module (yeast)	Function of module
TOM complex	Core translocase	Tom40, Tom22, Tom7	Translocation channel
	Small subunits Receptors	Tom6, Tom5 Tom70, Tom20	Assists substrate transfer Promotes substrate binding
SAM complex	Core translocase	Sam50	Membrane protein assembly
	Metaxins	Sam35, Sam37	Assists protein assembly? (<i>24, 26</i>)
	Mdm10	Mdm10 (others?)	Assists protein assembly? (<i>32</i>)
Tiny TIMs	Core complexes	Tim9, Tim10 and Tim8, Tim13	Transfer of substrates to TIM22 or SAM complexes
TIM22 complex	Core translocase	Tim22	Assembly of proteins into inner membrane
	Peripheral Tim	Tim12	Docking of tiny TIMs
	Accessory subunits	Tim54, Tim18	Assists protein assembly? (<i>9</i>)
TIM23 complex	Core translocase	Tim23, Tim17	Translocation channel
	Tim50	Tim50	Regulates channel opening
	PAM complex	Pam18, Pam16, Tim44, mHsp70	Transfer of substrates into the matrix
	Tim21	Tim21	Regulates module docking
OXA complex	Core chaperone	Oxa1	Assembly of proteins into inner membrane
	Ribosome receptors	Mba1, Mdm38, Ylh47	Docking of mitochondrial ribosomes (<i>55, 56</i>)
IMP complex	Core peptidase	Imp1, Imp2	Processes transfer-type sequences (<i>18</i>)
	Substrate binding	Som1	Modulates recognition (<i>18</i>)
MPP	Core peptidase	Mas1, Mas2	Processes N-terminal presequences in matrix (<i>18</i>)

¹Department of Biochemistry & Molecular Biology, University of Melbourne, Parkville 3010, Australia. ²Bio21 Molecular Science and Biotechnology Institute, Parkville 3010, Australia. ³Department of Parasitology, Charles University, Vinicna 7, 128 44 Prague 2, Czech Republic.

*To whom correspondence should be addressed. E-mail: t.lithgow@unimelb.edu.au

translocation unit enhanced by one or more modules of distinct function (Table 1).

The molecular machine translocating proteins across the mitochondrial outer membrane is the TOM complex (translocase of the outer membrane of mitochondria). The TOM complex is composed of several integral membrane protein components: Tom70 and Tom20 are receptor subunits (7) that recognize substrate proteins destined for import, with mitochondrial proteins bound by these receptor subunits subsequently released into a translocation channel composed of the core translocase components Tom40, Tom22, and Tom7 and two small proteins, Tom6 and Tom5. Tom40 is probably a β -barrel protein, whereas Tom22, Tom5, Tom6, and Tom7 each have a single α -helical transmembrane segment that locks them tightly into position on Tom40 (8). Electron microscopy, electrophysiology, and functional assays have been used to investigate the import mechanism and the nature of the translocation channel formed by Tom40 in the outer membrane. Tom22 assists the transfer of substrate proteins from the receptors to the pore and subsequently assists their transfer out into the intermembrane space (6, 9–11). The other small proteins appear to function in regulating the stability of interactions within the complex, thereby assisting substrate protein transfer to and through the core translocase.

After passing through the channel of the TOM complex, substrate proteins can interact with one of the two distinct machines in the inner membrane (Fig. 2). One of these, the TIM22 complex (translocase of the inner membrane of mitochondria, built around the Tim22 subunit), binds only protein substrates destined for integration into the inner membrane. The TIM22 machine is composed of four subunits embedded in the inner membrane and a peripheral set of “tiny Tim” subunits that shuttle to and from the TOM complex to collect substrates (5, 6, 9). The translocation and insertion of inner membrane proteins by the TIM22 complex does not require adenosine triphosphate but depends on the electrochemical potential across the inner membrane (9). Electrophysiological measurements demonstrate that the TIM22 complex contains pores that can flicker between different conformation states (12), which might reflect the movements the TIM22 subunit makes to assist substrate protein integration into the inner membrane.

The TIM23 complex is a distinct TIM complex built around a channel formed from Tim23, with this channel allowing for substrate entry to the mitochondrial matrix. Associated with the TIM23 complex, Tim50 is a receptor that guides protein substrates to bind the translocation channel (9) and thereby serves to regulate the opening and closing of the channel (13). According to recent findings, Tim21 interacts with the Tim17 subunit of the core translocase to assist in determining whether a bound substrate should be integrated into the inner membrane or translocated through into the matrix (14, 15). Translocation through the TIM23 complex is driven by a motor complex built around a mitochondrial Hsp70. The molecular chaperone Hsp70 is

black represent bacterial protein translocation machines that must have been present. There are cases of these present even today on the mitochondrial DNA of some eukaryotes: For example, SecY is encoded in the mitochondrial genome of the freshwater protist *Reclinomonas americana* (16); TatC is encoded in the mitochondrial genomes of a number of plants, algae, and protists (17). Furthermore, some proteins of bacterial ancestry are found commonly in mitochondria: The ubiquitous Imp proteases are clearly derived from bacterial signal peptidases (18), Oxa1 is a member of the YidC family of bacterial membrane protein chaperones (19), and the mitochondrial Hsp70s are derived from bacterial DnaK-type Hsp70s (20). Homologs of the inner membrane protein Tim44 are also present in alphaproteobacteria, although their function remains to be determined.

One of the major protein translocases in the outer membrane, the mitochondrial SAM (sorting and assembly machinery) complex, is closely related in sequence and function to the bacterial Omp85 protein translocase. In all bacteria with outer membranes, Omp85 assembles integral proteins into the outer membrane (21–23). The SAM complex was first identified in the mitochondrial outer membrane in yeast (24) and shown to integrate and assemble outer membrane protein complexes, including the TOM complex (21–23, 25, 26). Phylogenetic analysis provides a strong case for the evolution of Sam50 from the Omp85 that would have been present in the original endosymbiont (22). Related sequences have been identified in a range of animal and plant species (22), and functional analyses verify that Sam50 in the mitochondria of humans is equivalent to the yeast protein (27).

In bacteria, substrate proteins are assisted through the periplasmic space to Omp85 by the molecular chaperones Skp and SurA, whereas distinct chaperones, the tiny TIMs, assist substrates through the mitochondrial intermembrane space to the SAM complex (26) (Fig. 4A).

Although the two are unrelated in sequence, recent structural analyses of Skp from *Escherichia coli* (28, 29) and the tiny TIMs from human mitochondria (30) suggest structural and functional similarities (26, 31). The tiny TIMs can be considered a module of the SAM complex, functioning to transfer substrates from the TOM to SAM complex. Two further modules of the SAM complex are the metaxins (Sam37 and Sam35 in yeast) that sit on the cytosolic face of

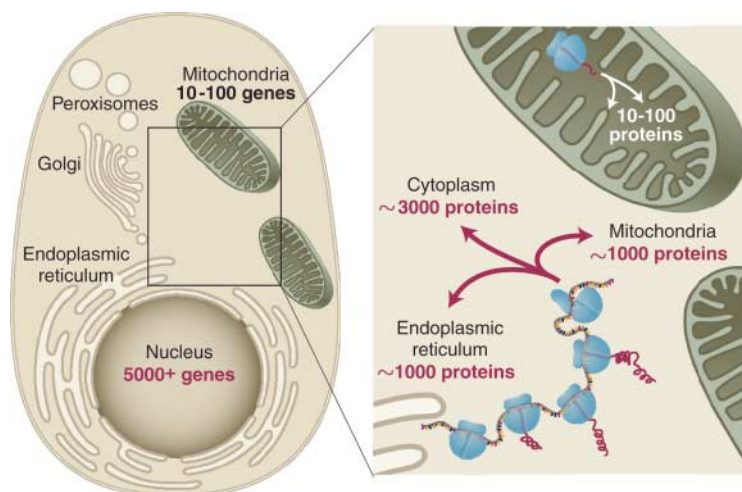


Fig. 1. Cellular genome and subcellular proteomes. A representation of a eukaryote with ~ 5000 protein-coding genes in its nuclear genome is shown. Based on work from the yeast *S. cerevisiae*, the nuclear genes might code for ~ 1000 proteins that are targeted to the endoplasmic reticulum to be distributed through the endomembrane system, ~ 3000 proteins that would fold in the cytoplasm (although they might then be redistributed to the peroxisomes or nuclear compartment), and ~ 1000 proteins that would be directed to mitochondria by virtue of the specific targeting sequences they carry (53, 54). A further set of proteins are coded in the mitochondrial genome and synthesized on mitochondrial ribosomes.

anchored to the membrane by J proteins Pam16 and Pam18 (6, 9) and the peripheral inner membrane protein Tim44; this module of subunits tethers Hsp70 to the translocation channel, thereby harnessing its activity to drive substrate proteins into the matrix.

Evolution of a Mitochondrial Protein Import Machinery

The multisubunit protein import machinery provides the means to import and sort the many hundreds of proteins needed in mitochondria. The complexity of the molecular machinery raises the question of how it was created. Evolution has made very selective use of the protein translocation machinery that would have been present in the endosymbiont ancestor of mitochondria. A model illustrates a reconstructed protein import machinery of the “protomitochondrion” of the ancestral eukaryote (Fig. 3). The components in

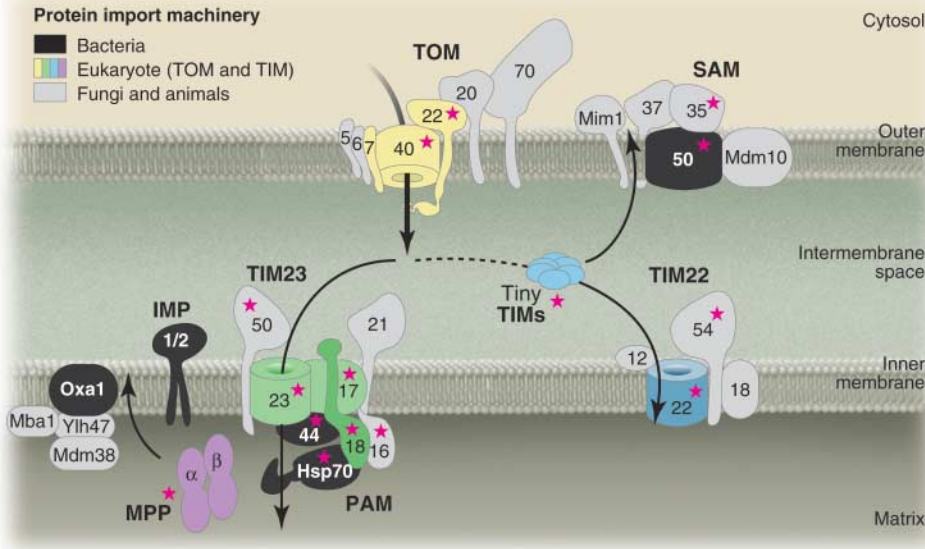


Fig. 2. The protein import machinery in mitochondria of the yeast *S. cerevisiae*. Arrows indicate the directional flow of protein substrates from their site of synthesis in the cytosol to each of the submitochondrial compartments. Subunits of the protein import machinery have been color-coded: Those with functional homologs in bacteria are in black, and the eukaryote-specific core components of the TOM and TIM machinery are in color. Shaded gray are components of the import machinery that are only found in fungi and animals, which suggests that they might be modules added to the machinery relatively recently. Stars depict the essential yeast proteins.

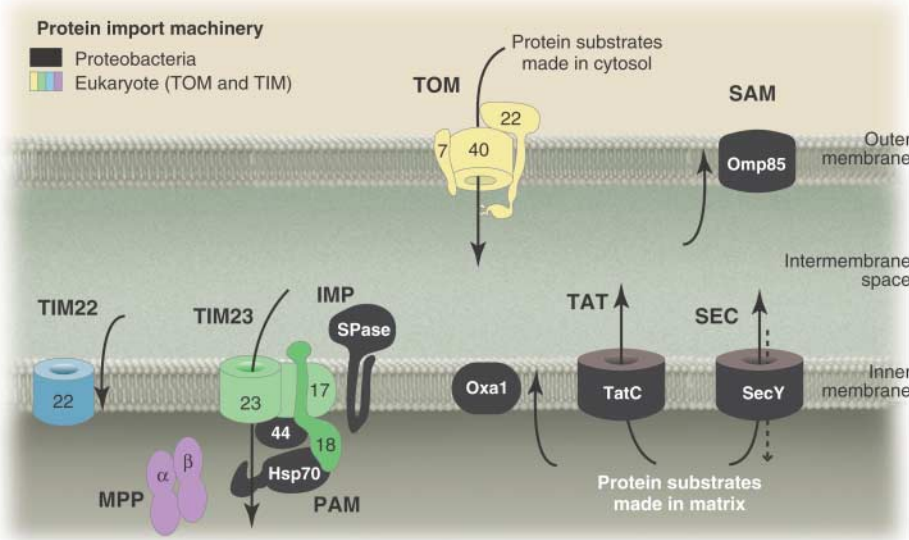


Fig. 3. A proposal for the protein import machinery of protomitochondria. In proteobacteria, the ancestor to the protomitochondrion, Omp85 drives protein assembly into the outer membrane, the YidC/Oxa1 complex chaperones protein assembly into the inner membrane, the SecYEG complex drives protein translocation across the inner membrane, the TAT complex drives protein translocation across the inner membrane, and the signal peptidase (SPase/IMP) cleaves signal sequences from translocated proteins. In the protomitochondrion, most protein synthesis would have occurred in the “matrix” (equivalent to the bacterial cytoplasm). In the course of evolution, as copies of the endosymbiont’s genes were transferred to the nucleus, protein substrates made in the cytosol would require a TOM complex for import across the outer membrane. The assembly of the TOM complex, even today, is driven by the Omp85/SAM complex that was preexisting in the endosymbiont.

been shown to assist the process of outer membrane protein assembly (33, 34) and might therefore represent a dynamically associating module of the SAM complex.

Hidden Markov models and other pattern-searching approaches represent powerful and sensitive tools to screen for diverse members of protein families (35). Hidden Markov model analysis shows that only in the case of the Sam50 subunit of the SAM complex are there sequences in the genomes of all eukaryotes for which complete data are available (Fig. 4B). This includes a number of organisms previously considered “amitochondriate,” such as *Trichomonas vaginalis*, the microsporidian *Encephalitozoon cuniculi*, and the apicomplexan *Cryptosporidium parvum*. These sequences have all the hallmarks of the Sam50 protein family: They are all ~50 kD, with a C-terminal domain of ~30 kD that corresponds to the Pfam “bacterial surface antigen domain” (PF01103) characteristic of the Omp85 family (36, 37) (Fig. 4B). The N-terminal extension in each protein has sequences that conform to features of the polypeptide translocase (POTRA) domain, and as a group the N-terminal extensions on these proteins are considerably shorter than the 40- to 50-kD extensions found in the bacterial Omp85 proteins.

Core Complexes Without Bacterial Ancestors?

Similar comparative genomics confirms the ubiquitous nature of other components of the protein import machinery (38–41). Some components of the TOM, TIM22, and TIM23 machines are common in enough diverse eukaryotes to believe that all mitochondria import proteins with the use of machinery built around common cores. Whereas the SAM complex is derived from a bacterial translocase, the TOM, TIM22, and TIM23 machines are apparently not related to bacterial protein transport machinery and seem to have been installed by evolution in the course of converting the endosymbiont to an organelle (Fig. 3).

Only three subunits of the TOM complex, Tom40, Tom7, and Tom22, are found commonly in eukaryotes (38). This includes plants, animals, and fungi, as well as diatoms and at least some amoebae and parasitic protists like *Plasmodium*. It has therefore been hypothesized that the small, primitive TOM complex (Fig. 3) was operational in the mitochondrial outer membrane of the last common ancestor for all eukaryotes (38, 42). According to this model, additional components for the TOM complex, such as Tom6, Tom70, and Tom20, were derived subsequently to increase the efficiency of protein import. In the case of both Tom20 and Tom70, there is good evidence that these receptor subunits are found only in animals and fungi (43, 44), which supports the idea that they were not present in earlier eukaryotes.

the complex and Mdm10. The integral protein Mdm10 is a striking example of a modular component, given its dual participation in the

complexes containing subunits that regulate mitochondrial morphology as well as the SAM complex (32). In addition, the protein Mim1 has

A stepwise evolution of the component parts of the TOM complex is most strongly evidenced in the case of Tom20. A common Tom20 is found in animals and fungi, and the protein has been analyzed in detail (44, 45). Although sequence analyses show that no related protein exists in plants or in protists (44, 46, 47), there is a 20-kD protein that functions as an import receptor in the TOM complex of mitochondria from *Arabidopsis thaliana* (47). Structural analysis of this “plant Tom20” showed it to be equivalent to the animal and fungal Tom20, but only if the sequence is considered in reverse (46). The convergent evolution of these two types of Tom20 proteins is best explained if they arose from distinct ancestral genes after the split of the animal and plant lineages.

A few components of the translocation machinery in the mitochondrial inner membrane might also be ubiquitous in eukaryotes, although a more complete analysis remains to be done. The Tim17 and Tim23 subunits of the TIM23 complex are related to each other and to the central subunit of the TIM22 complex (39, 41). Each of these TIM protein families in turn shares some similarity to a family of bacterial amino acid transporters (41). However, there are clear distinguishing features in the sequences and function of each of these protein families. If Tim17, Tim22, and Tim23 were derived from bacterial amino acid transporters, they have since been highly modified to serve as components of protein translocases.

The sequence relationship between the mitochondrial protein Tim44 and proteins found in alphaproteobacteria is clearer. According to the Pfam database, the Tim44 family of proteins (PF04280) includes members in all eukaryotes and alphaproteobacteria for which the complete genome sequence is available (29). The function of the protein in bacteria is not known, but its presence presumably reflects the fact that the endosymbiont ancestor to mitochondria had an Hsp70-binding protein available to be coopted into the evolving TIM23 machinery.

Sequences representing members of the Tim23, Tim17, Tim44, and Pam18 subunits of the TIM23/PAM complex are found in a wide range of eukaryotes, including the genome of *Trichomonas vaginalis*. Like many other unicellular eukaryotes living anaerobically, *Trichomonas* has hydrogenosomes instead of mitochondria. Mitochondria, hydrogenosomes, and other double membrane-bounded organelles called mitosomes have previously been considered to be distinct organelles, but very recent data suggests that hydrogenosomes and mitosomes represent highly evolved mitochondria (4). The Pam18 identified in *Trichomonas* has been studied in detail and

is located in the hydrogenosomes, and a homolog of Pam18 is also found in the mitochondria of *Giardia intestinalis* (48). Homologs of mitochondrial-type Hsp70 have also been detected in *Trichomonas* hydrogenosomes (49) and in *Giardia* mitosomes (50). It is reasonable to anticipate that the Hsp70 in hydrogenosomes could be kept in contact with the trichomonad

otes contain mitochondria that are atypical in terms of organellar biochemistry or morphology, they all contain organelles with a double membrane, whether they be called mitochondria, hydrogenosomes, or mitosomes. Most of the proteins that function in mitochondria carry short N-terminal targeting sequences. The targeting information in these sequences is conserved:

Hydrogenosomal and mitosomal proteins are recognized and delivered to mitochondria when expressed in yeast or mammalian cells (50, 51). A number of very recent reports suggest that the molecular machines, installed in protomitochondria to provide for protein import, are present in mitochondria of all eukaryotes, including hydrogenosomes and mitosomes. (48, 50).

In the course of transforming from endosymbiont to mitochondria, most of the genes encoding bacterial proteins were transferred into the host nucleus. To ensure the delivery and the assembly of these proteins in the newly established organelle, protein import machinery was needed. Some of the preexisting protein translocation apparatus of the endosymbiont appears to have been commandeered, with molecular chaperones such as mHsp70 and Oxal1 derived from the bacterial chaperones DnaK and YidC, respectively. The SecYEG machinery in the inner membrane is known to transport bacterial proteins across or into the inner membrane. This complex is theoretically capable of a retrograde mode of transport [observed for the related Sec61 complex (52)] and might at least partially have enabled protein translocation across the inner membrane, perhaps at a time when copies of some of the endosymbiont's genes had been transferred to the host nucleus but few had been deleted altogether from the symbiont's genome. At this early protomitochondrial stage, protein import would not have been an essential requirement for cell viability.

The TOM, TIM23, and TIM22 complexes have no obvious protein translocation counterparts in bacteria, making it likely that these machines were created de novo during the coevolution of the host and endosymbiont. The core modules of the TOM and the TIM23 and TIM22 machines function independently so that the function or dysfunction of one, during its development in the course of evolution, would not necessarily affect the development of the others. Once the core TOM complex had been established in the outer membrane, a possible scenario provides for the TIM23 and TIM22 complexes being established to take over from bacterial protein translocase(s) the roles of protein translocation through the inner membrane and protein insertion into the inner membrane.

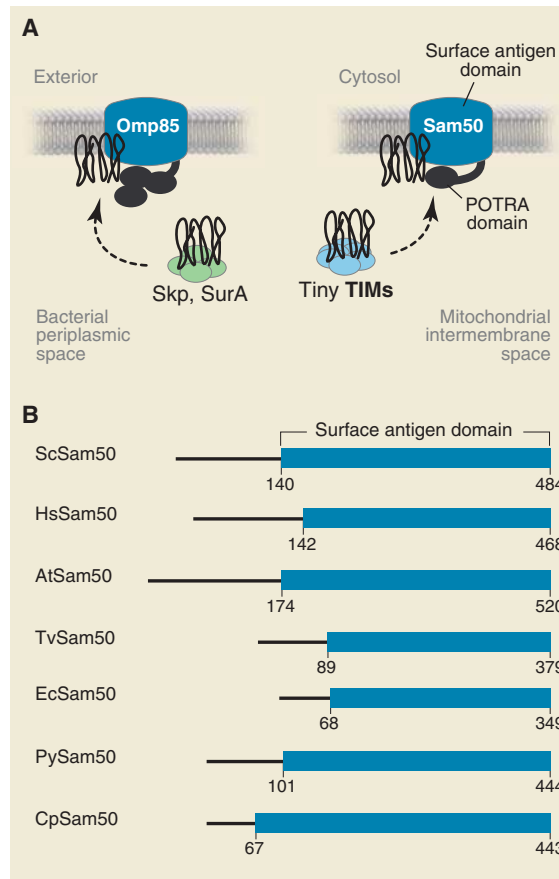


Fig. 4. Sam50 is found in all eukaryotes. **(A)** Omp85 is a protein in bacteria that mediates outer membrane assembly. It has an N-terminal periplasmic domain composed of multiple POTRA repeats and a C-terminal surface-antigen domain integrated into the outer membrane. Bacterial precursor proteins are presented to Omp85 by the molecular chaperones Skp and SurA. The mitochondrial protein Sam50 is a member of the Omp85 protein family, with a shortened POTRA domain in the mitochondrial intermembrane space. Mitochondrial precursor proteins are presented to Sam50 by the tiny TIM molecular chaperones. **(B)** A hidden Markov model built from animal, fungal, and plant Sam50 sequences (22) was used to identify homologs in the recently sequenced genome data of various protist species (table S1).

TIM23 complex through an association with Tim44 and Pam18, and the presence of the mitochondrial translocase in hydrogenosomes is further evidence for the common ancestry of these organelles.

Conclusion

Mitochondria are archetypal to eukaryotic cells. Although some anaerobic unicellular eukary-

Intriguingly, because the core subunits of the TIM23 complex (Tim23 and Tim17) and the TIM22 complex (Tim22) are all related to each other, one of these machines might represent a sophistication of the other, ancestral form (39).

Through looking further afield into the genomes of more and more classes of eukaryotes, it now appears that the molecular machines that drive protein import into mitochondria are of modular design. Core modules representing the translocation channels for each machine are common to all eukaryotes. Additional modules have been added over time, being common only to particular eukaryotic lineages. This provides additional means to analyze the vexing questions in the evolution of eukaryotes. Evolutionary details of the machines also provide a means from which to decipher aspects of machine function, complementing details gained from biochemical studies on the machines of one or more model species. Some exciting questions are being raised from considerations of evolution: How do the highly conserved α -helical transmembrane segments of Tom22, Tom6, and Tom7 dock so tightly to the Tom40 β barrel? Can the highly conserved regions of some proteins, such as the transmembrane segments of the TOM complex, be used to understand the precise function of these proteins? Is the TIM22 complex derived from the TIM23 complex (or vice versa), and how did this occur? What is the nature of the relation between the chaperones of mitochondrial intermembrane space and those in the periplasm of Gram-negative bacteria? Why were bacterial inner membrane protein translocases replaced by TIM complexes? In each case, the questions on the protein import machinery in mitochondria mirror questions that can be addressed to other cellular machines. Future studies on bacterial and mitochondrial protein transport promise insight

into the precise structure and mechanisms of these many, incredible molecular machines.

References and Notes

1. L. Margulis, *Origin of Eukaryotic Cell* (Yale Univ. Press, New Haven, CT, 1970).
2. M. W. Gray, G. Burger, B. F. Lang, *Science* **283**, 1476 (1999).
3. T. Gabaldon, M. A. Huynen, *Science* **301**, 609 (2003).
4. T. M. Embley, W. Martin, *Nature* **440**, 623 (2006).
5. W. Neupert, M. Brunner, *Nat. Rev. Mol. Cell Biol.* **3**, 555 (2002).
6. P. Rehling, K. Brandner, N. Pfanner, *Nat. Rev. Mol. Cell Biol.* **5**, 519 (2004).
7. T. Endo, D. Kohda, *Biochim. Biophys. Acta* **1592**, 3 (2002).
8. C. Meisinger *et al.*, **21**, 2337 (2001).
9. C. M. Koehler, *Annu. Rev. Cell Dev. Biol.* **20**, 309 (2004).
10. J. M. Herrmann, W. Neupert, *Curr. Opin. Microbiol.* **3**, 210 (2000).
11. A. J. Perry, T. Lithgow, *Curr. Biol.* **15**, R423 (2005).
12. P. Rehling *et al.*, *Science* **299**, 1747 (2003).
13. M. Meinecke *et al.*, *Science* **312**, 1523 (2006).
14. A. Chacinska *et al.*, *Cell* **120**, 817 (2005).
15. D. Mokranjac, D. Popov-Celeketic, K. Hell, W. Neupert, *J. Biol. Chem.* **280**, 23437 (2005).
16. B. F. Lang *et al.*, *Nature* **387**, 493 (1997).
17. Organelle Genome Database, University of Montreal, <http://megasun.bch.umontreal.ca/gobase/gobase.html>.
18. O. Gakh, P. Cavadini, G. Isaya, *Biochim. Biophys. Acta* **1592**, 63 (2002).
19. A. Kuhn, R. Stuart, R. Henry, R. E. Dalbey, *Trends Cell Biol.* **13**, 510 (2003).
20. W. R. Boorstein, T. Ziegelhoffer, E. A. Craig, *J. Mol. Evol.* **38**, 1 (1994).
21. S. A. Paschen *et al.*, *Nature* **426**, 862 (2003).
22. I. Gentle, K. Gabriel, P. Beech, R. Waller, T. Lithgow, *J. Cell Biol.* **164**, 19 (2004).
23. V. Kozjak *et al.*, *J. Biol. Chem.* **278**, 48520 (2003).
24. N. Wiedemann *et al.*, *Nature* **424**, 565 (2003).
25. S. A. Paschen, W. Neupert, D. Rapaport, *Trends Biochem. Sci.* **30**, 575 (2005).
26. N. Pfanner, N. Wiedemann, C. Meisinger, T. Lithgow, *Nat. Struct. Mol. Biol.* **11**, 1044 (2004).
27. A. D. Humphries *et al.*, *J. Biol. Chem.* **280**, 11535 (2005).
28. I. P. Korndorfer, M. K. Dommel, A. Skerra, *Nat. Struct. Mol. Biol.* **11**, 1015 (2004).
29. T. A. Walton, M. C. Sousa, *Mol. Cell* **15**, 367 (2004).
30. C. T. Webb, M. A. Gorman, M. Lazarou, M. T. Ryan, J. M. Gulbis, *Mol. Cell* **21**, 123 (2006).
31. N. Wiedemann, N. Pfanner, A. Chacinska, *Mol. Cell* **21**, 145 (2006).
32. C. Meisinger *et al.*, *Dev. Cell* **7**, 61 (2004).
33. D. Ishikawa, H. Yamamoto, Y. Tamura, K. Moritoh, T. Endo, *J. Cell Biol.* **166**, 621 (2004).
34. T. Waizenegger, S. Schmitt, J. Zivkovic, W. Neupert, D. Rapaport, *EMBO Rep.* **6**, 57 (2005).
35. K. Hofmann, *Brief. Bioinform.* **1**, 167 (2000).
36. A. Bateman *et al.*, *Nucleic Acids Res.* **32**, D138 (2004).
37. I. E. Gentle, L. Burri, T. Lithgow, *Mol. Microbiol.* **58**, 1216 (2005).
38. D. Macasev *et al.*, *Mol. Biol. Evol.* **21**, 1557 (2004).
39. J. M. Herrmann, *Trends Microbiol.* **11**, 74 (2003).
40. M. F. Bauer *et al.*, *FEBS Lett.* **464**, 41 (1999).
41. J. Rassow, P. J. Dekker, S. van Wilpe, M. Meijer, J. Soll, *J. Mol. Biol.* **286**, 105 (1999).
42. R. Lucattini, V. A. Likic, T. Lithgow, *Mol. Biol. Evol.* **21**, 652 (2004).
43. N. C. Chan, V. A. Likic, R. Waller, T. D. Mulhern, T. Lithgow, *J. Mol. Biol.* **358**, 1010 (2006).
44. V. A. Likic *et al.*, *J. Mol. Biol.* **347**, 81 (2005).
45. Y. Abe *et al.*, *Cell* **100**, 551 (2000).
46. A. J. Perry, J. M. Hulett, V. A. Likic, T. Lithgow, P. R. Gooley, *Curr. Biol.* **16**, 221 (2006).
47. W. Werhahn *et al.*, *Plant Physiol.* **125**, 943 (2001).
48. P. Dolezal *et al.*, *Proc. Natl. Acad. Sci. U.S.A.* **102**, 10924 (2005).
49. P. Bozner, *J. Parasitol.* **83**, 224 (1997).
50. A. Regoes *et al.*, *J. Biol. Chem.* **280**, 30557 (2005).
51. T. Hausler, Y. D. Stierhof, J. Blattner, C. Clayton, *Eur. J. Cell Biol.* **73**, 240 (1997).
52. K. Romisch, *J. Cell Sci.* **112**, 4185 (1999).
53. W. K. Huh *et al.*, *Nature* **425**, 686 (2003).
54. A. Sickmann *et al.*, *Proc. Natl. Acad. Sci. U.S.A.* **100**, 13207 (2003).
55. M. Ott *et al.*, *EMBO J.* **25**, 1603 (2006).
56. A. E. Frazier *et al.*, *J. Cell Biol.* **172**, 553 (2006).
57. The project was supported by an award from the Melbourne Research Grants Scheme from University of Melbourne (to V.L. and T.L.), the Grant Agency of the Czech Republic (to J.T.), and a project grant from the Australian Research Council (to T.L.).

Supporting Online Material

www.sciencemag.org/cgi/content/full/313/5785/314/DC1

Table S1
References

10.1126/science.1127895

High-Resolution Three-Dimensional Imaging of Dislocations

J. S. Barnard,* J. Sharp, J. R. Tong, P. A. Midgley*

Dislocations and their interactions govern the properties of many materials, ranging from work hardening in metals to device pathology in semiconductor laser diodes. The geometry of a dislocation network reveals key information such as dominant slip mechanisms, dislocation loops, presence of locks, and stair-rod dislocations. Fifty years ago (1), transmission electron microscopy (TEM) enabled individual dislocations to be imaged and led to a far greater understanding of the relationship between the defect structure of materials and their mechanical and electronic properties. Conventional electron micrographs are, however, two-dimensional (2D) projections of three-dimensional (3D) structures, and even stereo microscopy cannot reveal the true 3D complexity of defect structures. Ludwig *et al.* (2) were the first to reconstruct a true 3D image of a dislocation network by using x-ray topography. However, dislocations separated by less than $\sim 10 \mu\text{m}$ are difficult to visualize and limit the resolvable dislocation density to 10^6 cm^{-2} . We describe an electron tomographic method that yields 3D reconstructions of dislocation networks with a spatial resolution three orders of magnitude better than previous work. We illustrate the method's success with a study of dislocations in a GaN epilayer, where dislocation densities of 10^{10} cm^{-2} are common (3).

Hetero-epitaxial films of Mg-doped, *p*-type α -GaN (wurtzite) were grown on sapphire, with the lattice mismatch resulting in dislocations threading through the film in the [0001] direction (3). During growth and subsequent rapid thermal annealing to activate the Mg dopants, partial delamination of the film led to near-surface cracks and associated dislocation networks. In TEM, weak-beam dark-field (WBDF) imaging (4) is able to resolve individual dislocations separated by only a few nm. A series of WBDF images, recorded about a single tilt axis, can be used for a 3D tomographic reconstruction of a dislocation

network if the diffraction conditions are kept constant throughout the tilt series. By ensuring the $\langle 11\bar{2}0 \rangle$ zone axis was parallel to the goniometer axis, we maintained a constant weak-beam condition along the entire tilt range. Images were recorded every 5° with the $11\bar{2}0$ reflection and setting the $33\bar{6}0$ reflection near the Bragg condition. More than 90% of the dislocations had a Burgers vector component parallel to $\langle 11\bar{2}0 \rangle$ and were therefore visible (5). Modified back-projection techniques were used to reconstruct the 3D dislocation network (6).

An oblique view of the reconstructed dislocation network is shown in Fig. 1, and an animated version is also available (movie S1). Although somewhat disturbed by a persistent "dust" arising from unwanted additional diffraction contrast (e.g., thickness fringes), the reconstruction shows the 3D structure of the dislocation network. Threading edge and mixed dislocations that bound small-angle grain boundaries of individual domains (labeled as D in Fig. 1) have a slight oscillatory appearance caused by

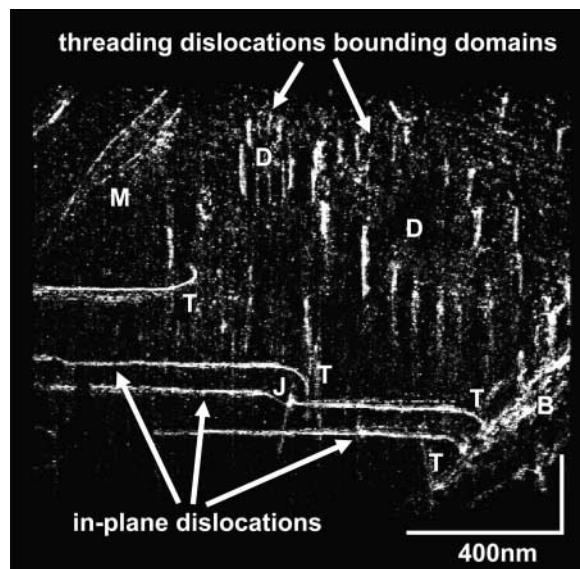


Fig. 1. An oblique view of a WBDF tomogram of a GaN film showing walls of threading dislocations surrounding domains (D), a dislocation bundle (B) associated with a crack, and threading dislocations that turn over at T to become in-plane dislocations and terminate at the specimen surface. Each turn over T occurs at a different height in the film, and one has interacted with a threading dislocation, causing a jog (J). Dislocations of mixed character (M) are also visible.

dynamical diffraction effects associated with dislocations inclined to the beam. In-plane dislocations are very clear owing to their near-constant visibility throughout the tilt series, but dense dislocation bundles (labeled as B), associated with the crack tip, are not resolved. These dislocations are spaced $\sim 10 \text{ nm}$ apart, thus establishing a resolvable dislocation density of $\sim 10^{12} \text{ cm}^{-2}$. The 3D reconstruction shows that the in-plane dislocations are caused by threading dislocations turning over (T) and gliding in response to the stress field of the dislocation bundle. The reconstruction also shows that the in-plane dislocations have parallel but not identical slip planes. A jog of an in-plane dislocation by a threading dislocation is also seen (J). Unannealed films did not show dislocation turn over and glide, suggesting that this mechanism requires thermal activation.

Three-dimensional reconstructions afford new perspectives on dislocation geometry, for example, the measurement of minimum distances between dislocations, the dislocation curvature (and the balance of line tension by local stresses), and the angles subtended by dislocations at surfaces (free or interfacial), which allow investigation of surface-dislocation forces. WBDF dislocation tomography is applicable to all crystal systems, but variations in the diffraction condition through the tilt series and materials with large elastic anisotropy can lead to distorted reconstructions. We anticipate that WBDF tomography will be useful for many dislocation-related issues, such as providing key input for models of 3D dislocation dynamics, a better understanding of dislocation interactions (e.g., pile-ups, cross-slips, jog formations, and kinks), and the visualization of dislocations under indentations.

References and Notes

1. P. B. Hirsch, R. W. Horne, M. J. Whelan, *Philos. Mag.* **1**, 677 (1956).
2. W. Ludwig *et al.*, *J. Appl. Crystallogr.* **20**, 602 (2001).
3. F. A. Ponce, D. P. Bour, *Nature* **386**, 351 (1997).
4. D. J. H. Cockayne, I. L. F. Ray, M. J. Whelan, *Philos. Mag.* **20**, 1265 (1969).
5. Materials and methods are available as supporting material on Science Online.
6. P. A. Midgley, M. Weyland, *Ultramicroscopy* **96**, 413 (2003).
7. We acknowledge M. Kappers and C. J. Humphreys for the provision of the GaN sample. J.S.B. acknowledges Newnham College for financial support. P.A.M. thanks the Royal Academy of Engineering and the Leverhulme Trust for the award of a Senior Research Fellowship.

Supporting Online Material

www.sciencemag.org/cgi/content/full/313/5785/319/DC1
Materials and Methods
Movie S1

3 February 2006; accepted 10 May 2006
10.1126/science.1125783

Department of Materials Science and Metallurgy, University of Cambridge, Pembroke Street, Cambridge CB2 3QZ, UK.

*To whom correspondence should be addressed. E-mail: pam33@cam.ac.uk (P.A.M.); jsb43@cam.ac.uk (J.S.B.)

A Distinct Small RNA Pathway Silences Selfish Genetic Elements in the Germline

Vasily V. Vagin,^{1,2*} Alla Sigova,^{1*} Chengjian Li,¹ Hervé Seitz,¹ Vladimir Gvozdev,² Phillip D. Zamore^{1†}

In the *Drosophila* germline, repeat-associated small interfering RNAs (rasiRNAs) ensure genomic stability by silencing endogenous selfish genetic elements such as retrotransposons and repetitive sequences. Whereas small interfering RNAs (siRNAs) derive from both the sense and antisense strands of their double-stranded RNA precursors, rasiRNAs arise mainly from the antisense strand. rasiRNA production appears not to require Dicer-1, which makes microRNAs (miRNAs), or Dicer-2, which makes siRNAs, and rasiRNAs lack the 2',3' hydroxy termini characteristic of animal siRNA and miRNA. Unlike siRNAs and miRNAs, rasiRNAs function through the Piwi, rather than the Ago, Argonaute protein subfamily. Our data suggest that rasiRNAs protect the fly germline through a silencing mechanism distinct from both the miRNA and RNA interference pathways.

In plants and animals, RNA silencing pathways defend against viruses (1–3), regulate endogenous gene expression (4), and protect the genome against selfish genetic elements such as retrotransposons and repetitive sequences (5). Common to all RNA silencing pathways are RNAs 19 to 30 nucleotides (nt) long that specify the target RNAs to be repressed. In RNA interference (RNAi) (6), siRNAs are produced from long exogenous double-stranded RNA (dsRNA). In contrast, ~22-nt miRNAs are endonucleolytically processed from endogenous RNA polymerase II transcripts. Dicer ribonuclease III (RNase III) enzymes produce both siRNAs and miRNAs. In flies, Dicer-2 (Dcr-2) generates siRNAs, whereas the Dicer-1 (Dcr-1)–Loquacious (Loqs) complex produces miRNAs (7–11). After their production, small silencing RNAs bind Argonaute proteins to form the functional RNA silencing effector complexes believed to mediate all RNA silencing processes.

Phased sense and antisense siRNAs in vivo.

In *Drosophila*, processive dicing of long dsRNA and the accumulation of sense and antisense siRNAs without reference to the orientation of the target mRNA are hallmarks of RNAi in vitro (12, 13) and in vivo (Fig. 1). We prepared total small RNA from the heads of adult males expressing a dsRNA hairpin (fig. S1A) that silences the *white* gene via the RNAi pathway (14). *white* silencing requires Dcr-2 (7), R2D2 (9), and Ago2. siRNAs were detected with a microarray containing T_M (melting temperature)–normalized probes, 22 nt long, for all sense

and antisense siRNAs that theoretically can be produced by dicing the *white* exon 3 hairpin (Fig. 1A). Both sense and antisense *white* siRNAs were detected in wild-type flies but not in *dcr-2^{LS11fsX}* homozygous mutant flies. The Dcr-2–dependent siRNAs were produced with a periodicity of ~22 nt (Fig. 1B), consistent with the phased processing of the dsRNA hairpin from the end formed by the 6-nt loop predicted to remain after splicing of its intron-containing primary transcript (fig. S1B).

***Su(Ste)* rasiRNAs.** *Drosophila* repeat-associated small interfering RNAs (rasiRNAs) can be distinguished from siRNAs by their longer length, 24 to 29 nt (15, 16). rasiRNAs have been proposed to

be diced from long dsRNA triggers (5, 16), such as the ~50 copies of the bidirectionally transcribed *Suppressor of Stellate* [*Su(Ste)*] locus on the Y chromosome (17) (fig. S2B) that in testes silence the ~200 copies of the protein-coding gene *Stellate* (*Ste*) found on the X chromosome.

Microarray analysis of total small RNA isolated from fly testes revealed that *Su(Ste)* rasiRNAs detectably accumulate only from the antisense strand (Fig. 2A), with little or no phasing (fig. S2A). As expected, *Su(Ste)* rasiRNAs were not detected in testes from males lacking the *Su(Ste)* loci (*cry^Y*) (Fig. 2A). *Su(Ste)* rasiRNAs were also absent from *armitage* (*armi*) mutant testes (Fig. 2A), which fail to silence *Ste* and do not support RNAi in vitro (18). *armi* encodes a non-DEAD-box helicase (19) homologous to the *Arabidopsis thaliana* protein SDE3, which is required for RNA silencing triggered by transgenes and some viruses (20), and depletion by RNAi of the mammalian Armi homolog Mov10 blocks siRNA-directed RNAi in cultured human cells (21). Normal accumulation of *Su(Ste)* rasiRNA and robust *Ste* silencing also require the putative helicase Spindle-E (Spn-E), a member of the DEXH family of adenosine triphosphatases (ATPases) (16, 22) (Fig. 2B and fig. S2B).

The accumulation in vivo of only antisense rasiRNAs from *Su(Ste)* implies that sense *Su(Ste)* rasiRNAs either are not produced or are selectively destroyed. Either process would make *Ste* silencing mechanistically different from RNAi. In support of this view, mutations in the central components of the *Drosophila* RNAi pathway—*dcr-2*, *r2d2*, and *ago2*—did not diminish *Su(Ste)* rasiRNA accumulation (Fig. 2B). Deletion of the *Su(Ste)* silencing trigger (*cry^Y*) caused a factor

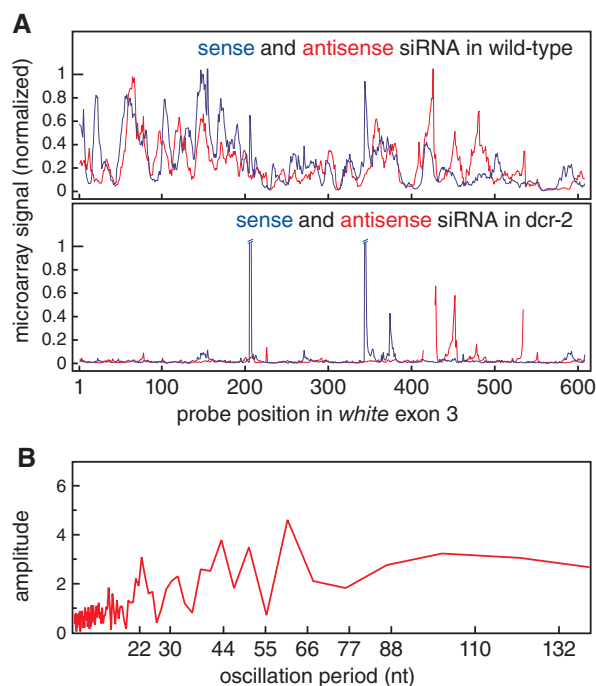


Fig. 1. Sense and antisense siRNAs accumulate during RNAi in vivo. (A) Microarray analysis of the siRNAs derived from the *white* exon 3 hairpin RNAi trigger. (B) Fourier transform analysis of the Dcr-2–dependent siRNAs in (A).

¹Department of Biochemistry and Molecular Pharmacology, University of Massachusetts Medical School, Worcester, MA 01605, USA. ²Department of Animal Molecular Genetics, Institute of Molecular Genetics, Moscow 123182, Russia.

*These authors contributed equally to this work.

†To whom correspondence should be addressed. E-mail: phillip.zamore@umassmed.edu

of ~65 increase in *Ste* mRNA (Fig. 3A), but null or strong hypomorphic mutations in the three key RNAi proteins did not (Fig. 3B).

Fly Argonaute proteins can be subdivided into the Ago (Ago1 and Ago2) and Piwi [Aubergine (Aub), Piwi, and Ago3] subfamilies. Unlike *ago1* and *ago2*, the *aub*, *piwi*, and *ago3* mRNAs are enriched in the germline (23–25). *Aub* is required for *Ste* silencing (16) and *Su(Ste)* rasiRNA accumulation (26). In *aub^{HN2}/aub^{QC42}* trans-heterozygous mutants, *Su(Ste)* rasiRNAs were not detected by microarray (fig. S2B) or Northern analysis (Fig. 2B), and *Su(Ste)*-triggered silencing of *Ste* mRNA was lost completely (Fig. 3B). Even *aub^{HN2}/+* heterozygotes accumulated less of the most abundant *Su(Ste)* rasiRNA than did the wild type (Fig. 2B). That the Ago subfamily protein Ago2 is not required for *Ste* silencing, whereas the Piwi subfamily protein Aub is essential for it, supports the view that *Ste* is silenced by a pathway distinct from RNAi. Intriguingly, *Su(Ste)* rasiRNAs hyperaccumulated in *piwi* mutant testes, where *Ste* is silenced normally (Figs. 2B and 3B and fig. S2B).

Mutations in *aub* also cause an increase in sense, but not antisense, *Su(Ste)* RNA (16); our results suggest that antisense *Su(Ste)* rasiRNAs can silence both *Ste* mRNA and sense *Su(Ste)* RNA, but that no *Su(Ste)* rasiRNAs exist that can target the antisense *Su(Ste)* transcript. Our finding that *Su(Ste)* rasiRNAs are predominantly or exclusively antisense is essentially in agreement with the results of small RNA cloning experiments, in which four of five *Su(Ste)* rasiRNAs sequenced were in the antisense orientation (15), but is at odds with earlier reports detecting both sense and antisense *Su(Ste)* rasiRNAs by non-quantitative Northern hybridization (16).

A third RNA silencing pathway in flies. Is germline RNA silencing of selfish genetic elements generally distinct from the RNAi and miRNA pathways? We examined the expression of a panel of germline-expressed selfish genetic elements—three long terminal repeat (LTR)-containing retrotransposons (*roo*, *mdg1*, and

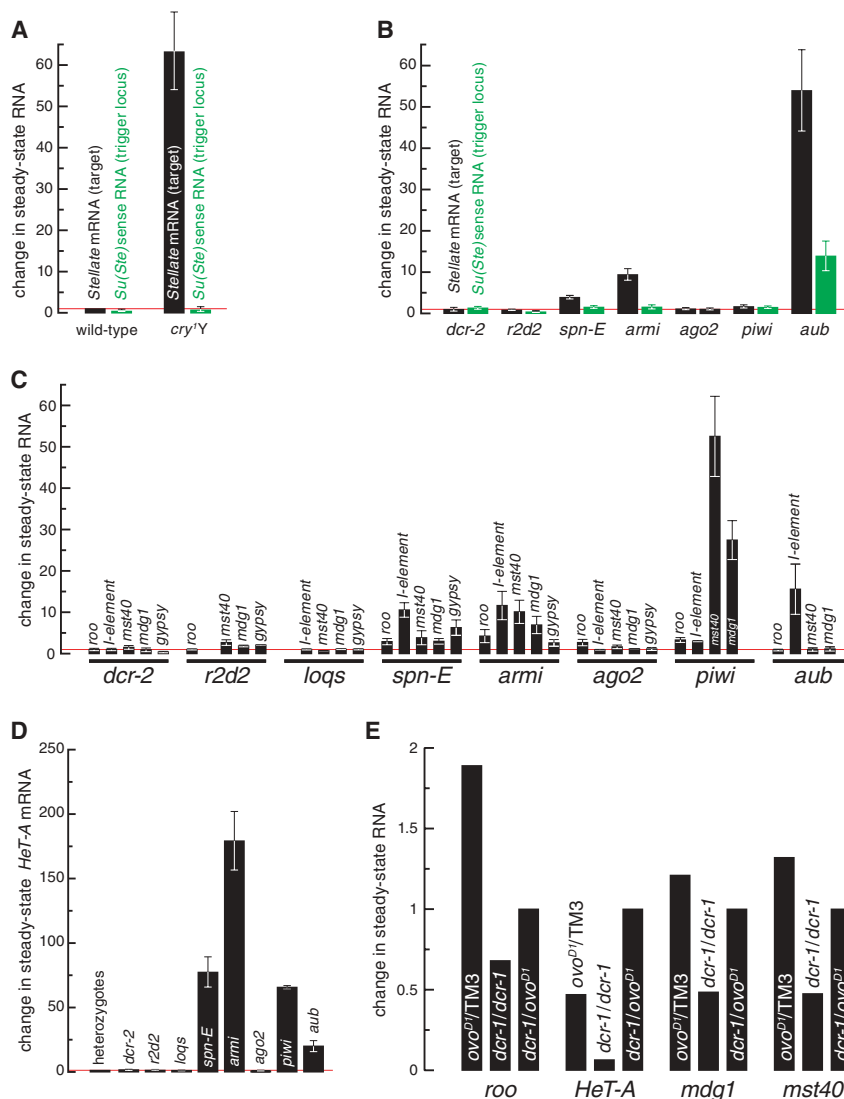


Fig. 3. (A to D) RNA expression from selfish genetic elements was measured in homozygous mutants relative to heterozygotes for *Ste* silencing in testes [(A) and (B)] and for the repeated locus *mst40*, the LTR retrotransposons *roo*, *mdg1*, and *gypsy*, and the non-LTR retrotransposons *I-element* and *HeT-A* in ovaries [(C) and (D)]. (E) RNA expression from selfish genetic elements in *dcr-1^{Q1147X}* null mutant clones generated by mitotic recombination in the ovary.

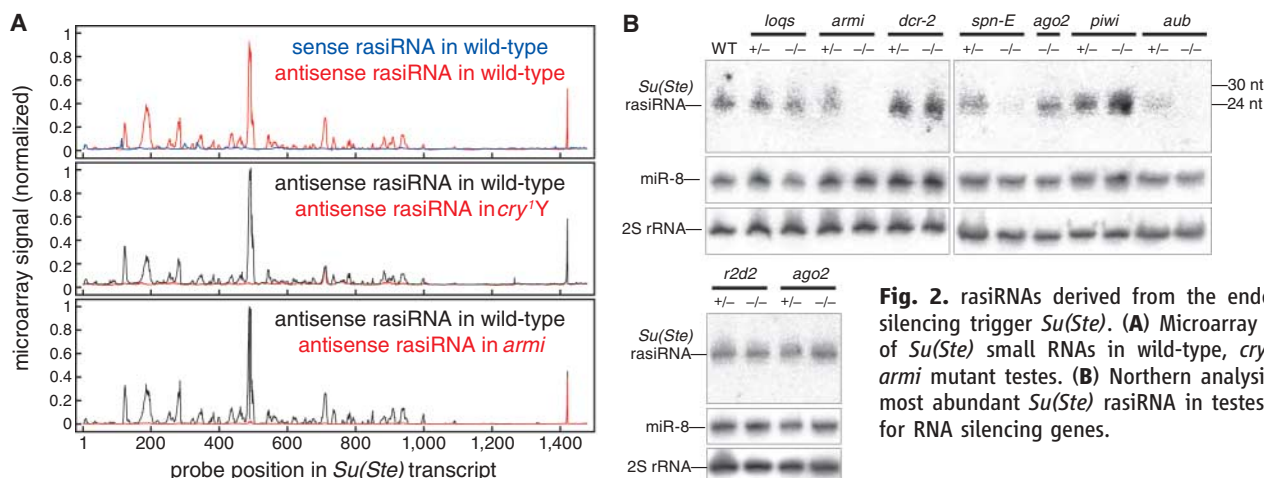


Fig. 2. rasiRNAs derived from the endogenous silencing trigger *Su(Ste)*. (A) Microarray analysis of *Su(Ste)* small RNAs in wild-type, *cry^{1Y}*, and *armi* mutant testes. (B) Northern analysis of the most abundant *Su(Ste)* rasiRNA in testes mutant for RNA silencing genes.

gypsy), two non-LTR retrotransposons (*I-element* and *HeT-A*, a component of the *Drosophila* telomere), and a repetitive locus (*mst40*)—in mutants defective for eight RNA silencing proteins. All selfish genetic elements tested behaved like *Ste*: Loss of the RNAi proteins Dcr-2, R2D2, or Ago2 had little or no effect on retrotransposon or repetitive element silencing (Fig. 3, C and D). Instead, silencing required the putative helicases Spn-E and Armi plus one or both of the Piwi subfamily Argonaute proteins, Aub and Piwi. Silencing did not require Loqs, the dsRNA-binding protein required to produce miRNAs (Fig. 3, C and D).

The null allele *dcr-1^{Q1147X}* is homozygous lethal, making it impossible to procure *dcr-1* mutant ovaries from *dcr-1^{Q1147X}/dcr-1^{Q1147X}* adult females (7). Therefore, we generated clones of *dcr-1^{Q1147X}/dcr-1^{Q1147X}* cells in the ovary by mitotic recombination in flies heterozygous for the dominant female-sterile mutation *ovo^{D1}* (27). We measured RNA levels, relative to *rp49* mRNA, for three retrotransposons (*roo*, *HeT-A*, and *mdg1*) and one repetitive sequence (*mst40*) in *dcr-1/dcr-1* recombinant ovary clones and in *ovo^{D1}/TM3* and *dcr-1/ovo^{D1}* nonrecombinant ovaries. The *ovo^{D1}* mutation blocks oogenesis at stage 4, after the onset of *HeT-A* (28, 29) and *roo* rasiRNA production. Retrotransposon or repetitive sequence transcript abundance was unaltered or decreased in *dcr-1/dcr-1* relative to *ovo^{D1}/TM3* and *dcr-1/ovo^{D1}* controls (Fig. 3E). We conclude that Dcr-1 is dispensable for silencing these selfish genetic elements in the *Drosophila* female germline.

roo is the most abundant LTR retrotransposon in flies. We analyzed *roo* silencing in the female germline with the use of microarrays con-

taining 30-nt probes, tiled at 5-nt resolution, for all ~18,000 possible *roo* rasiRNAs (Fig. 4, A and B); we corroborated the data at 1-nt resolution for those rasiRNAs derived from LTR sequences (fig. S3A). As observed for *Su(Ste)* but not for *white* RNAi, *roo* rasiRNAs were nonhomogeneously distributed along the *roo* sequence and accumulated primarily from the antisense strand (Fig. 4A and fig. S3A). In fact, the most abundant sense rasiRNA peak (asterisk in Fig. 4, A and B) corresponded to a set of probes containing 16 contiguous uracil residues, which suggests that these probes nonspecifically detected fragments of the mRNA polyadenylate [poly(A)] tail. Most of the remaining sense peaks were unaltered in *armi* mutant ovaries, in which *roo* expression is increased; this result implies that they do not contribute to *roo* silencing (Figs. 3C and 4A). We detected no phasing in the distribution of *roo* rasiRNAs (fig. S3B).

As for *Su(Ste)*, wild-type accumulation of antisense *roo* rasiRNA required the putative helicases Armi and Spn-E and the Piwi subfamily Argonaute proteins Piwi and Aub, but not the RNAi proteins Dcr-2, R2D2, and Ago2 (Fig. 4, B and C). Moreover, accumulation of *roo* rasiRNA was not measurably altered in *loqs¹⁰⁰⁷⁹¹*, an allele that strongly disrupts miRNA production in the female germline (Fig. 4C).

Are *roo* rasiRNAs not made by dicing?

Loss of Dcr-2 or Dcr-1 did not increase retrotransposon or repetitive element expression, which suggests that neither enzyme acts in rasiRNA-directed silencing. Moreover, loss of Dcr-2 had no detectable effect on *Su(Ste)* rasiRNA in testes or *roo* rasiRNA in ovaries (Figs. 2B and 4C). We measured the amount of *roo* rasiRNA and miR-311

in *dcr-1/dcr-1* ovary clones generated by mitotic recombination. Comparison of recombinant (*dcr-1/dcr-1*) and nonrecombinant (*ovo^{D1}/TM3* and *dcr-1/ovo^{D1}*) ovaries by Northern analysis revealed that *roo* rasiRNA accumulation was unperturbed by the null *dcr-1^{Q1147X}* mutation (Fig. 5A and fig. S4). Pre-miR-311 increased and miR-311 declined by a factor of ~3 in the *dcr-1/dcr-1* clones (Fig. 5B and fig. S4), consistent with about two-thirds of the tissue corresponding to mitotic *dcr-1/dcr-1* recombinant cells. Yet, although most of the tissue lacked *dcr-1* function, we observed improved, rather than diminished, silencing for the four selfish genetic elements examined (Fig. 3E). Moreover, the dsRNA-binding protein Loqs, which acts with Dcr-1 to produce miRNAs, was also dispensable for *roo* rasiRNA production and selfish genetic element silencing (Fig. 3, C and D, and Fig. 4C). Although we cannot exclude the possibility that *dcr-1* and *dcr-2* can fully substitute for each other in the production of rasiRNA in the ovary, previous biochemical evidence suggests that none of the three RNase III enzymes in flies—Dcr-1, Dcr-2, and Droscha—can cleave long dsRNA into small RNAs 24 to 30 nt long (10, 30, 31).

Animal siRNA and miRNA contain 5' phosphate and 2',3' hydroxy termini (32, 33). We used enzymatic and chemical probing to infer the terminal structure of *roo* and *Su(Ste)* rasiRNAs. RNA from ovaries or testes was treated with calf intestinal phosphatase (CIP) or CIP followed by polynucleotide kinase plus ATP. CIP treatment caused *roo* (Fig. 6A) and *Su(Ste)* (fig. S5) rasiRNA to migrate more slowly in polyacrylamide gel electrophoresis, consistent with the loss

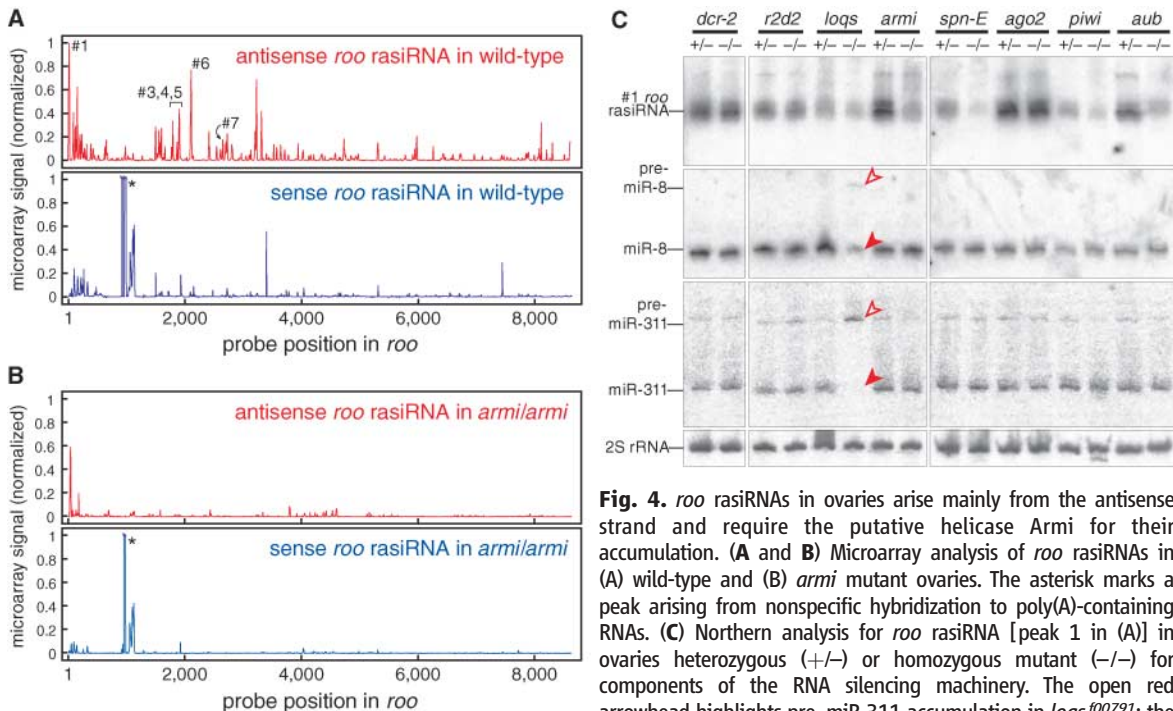


Fig. 4. *roo* rasiRNAs in ovaries arise mainly from the antisense strand and require the putative helicase Armi for their accumulation. (A and B) Microarray analysis of *roo* rasiRNAs in (A) wild-type and (B) *armi* mutant ovaries. The asterisk marks a peak arising from nonspecific hybridization to poly(A)-containing RNAs. (C) Northern analysis for *roo* rasiRNA [peak 1 in (A)] in ovaries heterozygous (+/-) or homozygous mutant (-/-) for components of the RNA silencing machinery. The open red arrowhead highlights pre-miR-311 accumulation in *loqs¹⁰⁰⁷⁹¹*; the solid red arrowhead highlights loss of mature miR-311. miR-311 is expressed predominantly in the germline.

of one or more terminal phosphate groups. Subsequent incubation with polynucleotide kinase and ATP restored the original gel mobility of the rasiRNAs, indicating that they contained a single 5' or 3' phosphate before CIP treatment. The *roo* rasiRNA served as a substrate for ligation of a 23-nt 5' RNA adapter by T4 RNA ligase, a process that requires a 5' phosphate; pretreatment with CIP blocked ligation (Fig. 6B), thus establishing that the monophosphate lies at the 5' end. The rasiRNA must also contain at least one terminal hydroxyl group, because it could be joined by T4 RNA ligase to a preadenylated 17-nt 3' RNA adapter (Fig. 6B). Notably, the 3' ligation reaction was less efficient for the *roo* rasiRNA than for a miRNA in the same reaction (22% versus 50% conversion to ligated product).

RNA from ovaries or testes was reacted with NaIO₄, then subjected to β-elimination, to determine whether the rasiRNA had either a single 2'

or 3' terminal hydroxy group or had terminal hydroxy groups at both the 2' and 3' positions, as do animal siRNA and miRNA. Only RNAs containing both 2' and 3' hydroxy groups react with NaIO₄; β-elimination shortens NaIO₄-reacted RNA by one nucleotide, leaving a 3' monophosphate terminus, which adds one negative charge. Consequently, NaIO₄-reacted, β-eliminated RNAs migrate faster in polyacrylamide gel electrophoresis than does the original unreacted RNA. Both *roo* (Fig. 6A) and *Su(Ste)* (fig. S5) rasiRNA lack either a 2' or a 3' hydroxyl group, because they failed to react with NaIO₄; miRNAs in the same samples reacted with NaIO₄. Together, our results show that rasiRNAs contain one modified and one unmodified hydroxyl. Because T4 RNA ligase can make both 3'-5' and 2'-5' bonds (34), we cannot currently determine the blocked position. Some plant small silencing RNAs contain a 2'-O-methyl modification at their 3' terminus (34).

Fig. 5. (A) Northern analysis of mitotic recombinant *dcr-1^{Q1147X}* homozygous mutant ovaries and nonrecombinant controls. *roo* rasiRNAs were detected with a mixture of five hybridization probes. Arrowheads are as in Fig. 4C. **(B)** Quantification of the data in (A), normalized to the 2S rRNA loading control.

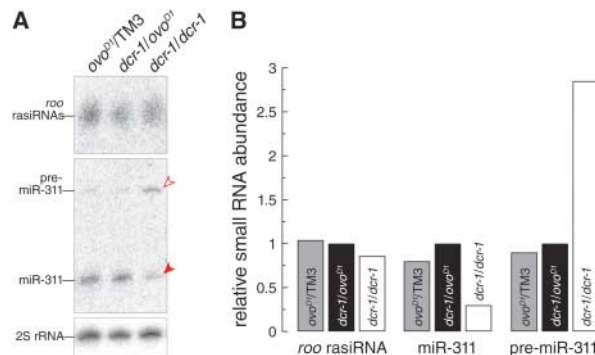
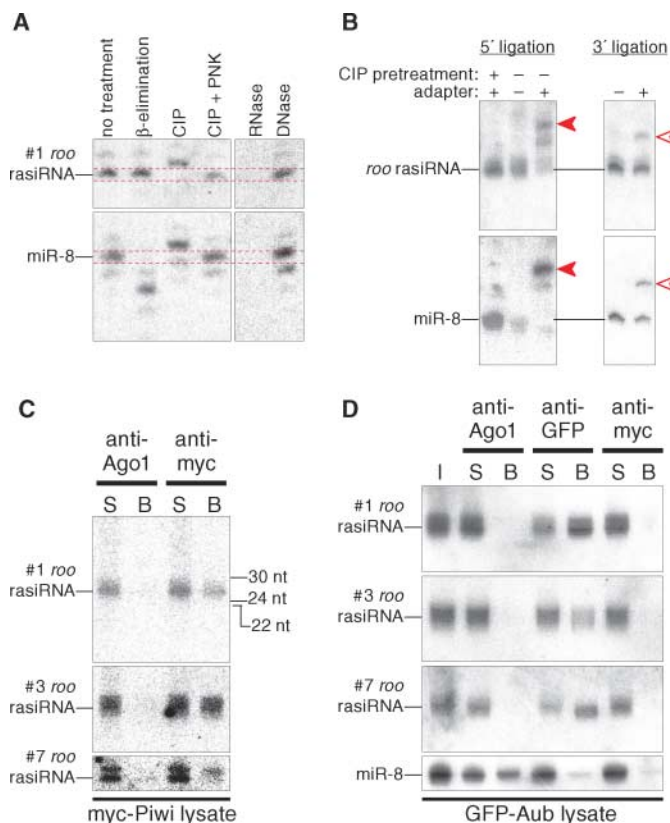


Fig. 6. *roo* rasiRNAs are modified at their 3' terminus and associate with Piwi subfamily Argonaute proteins. (A) Chemical and enzymatic probing of *roo* rasiRNA structure. *roo* rasiRNAs (peak 1 in Fig. 4A) were detected by Northern hybridization. The membrane was then stripped and reprobed for miR-8. **(B)** *roo* rasiRNAs can serve as a 3' or a 5' substrate for T4 RNA ligase. Solid arrowheads, 5' ligation products; open arrowheads, 3' ligation products. **(C and D)** *roo* rasiRNAs associate with myc-tagged Piwi (C) and GFP-tagged Aub protein (D), but not with Ago1. I, input; S, supernatant; B, bound.



rasiRNAs bind Piwi and Aub. *Drosophila* and mammalian siRNA and miRNA function through members of the Ago subfamily of Argonaute proteins, but *Su(Ste)* and *roo* rasiRNAs require at least one member of the Piwi subfamily for their function and accumulation. To determine whether *roo* rasiRNAs physically associate with Piwi and Aub, we prepared ovary lysate from wild-type flies or transgenic flies expressing either myc-tagged Piwi or green fluorescent protein (GFP)-tagged Aub protein (25, 35); immunoprecipitated them with monoclonal antibodies (mAbs) to myc, GFP, or Ago1; and then analyzed the supernatant and antibody-bound small RNAs by Northern blotting (Fig. 6, C and D, and fig. S6). We analyzed six different *roo* rasiRNAs. All were associated with Piwi but not with Ago1, the *Drosophila* Argonaute protein typically associated with miRNAs (36); miR-8 (Fig. 6D and fig. S6C), miR-311, and *bantam* immunoprecipitated with Ago1 mAb. No rasiRNAs immunoprecipitated with the myc mAb when we used lysate from flies lacking the myc-Piwi transgene (fig. S6B).

Although *aub* mutant ovaries silenced *roo* mRNA normally, they showed reduced accumulation of *roo* rasiRNA relative to *aub*/+ heterozygotes (Fig. 4C), which suggests that *roo* rasiRNAs associate with both Piwi and Aub. We analyzed the supernatant and antibody-bound small RNAs after GFP mAb immunoprecipitation of ovary lysate from GFP-Aub transgenic flies and flies lacking the transgene. *roo* rasiRNA was recovered only when the immunoprecipitation was performed with the GFP mAb in ovary lysate from GFP-Aub transgenic flies (Fig. 6D and fig. S6D). The simplest interpretation of our data is that *roo* rasiRNAs physically associate with both Piwi and Aub, although it remains possible that the *roo* rasiRNAs are loaded only into Piwi and that Aub associates with Piwi in a stable complex. The association of *roo* rasiRNA with both Piwi and Aub suggests that *piwi* and *aub* are partially redundant, as does the modest reduction in *roo* silencing—by a factor of 3.3 ± 0.6 (average \pm SD, $n = 3$)—in *piwi* but not in *aub* mutants (Fig. 3C). Alternatively, *roo* silencing might proceed through Piwi alone, but the two proteins could function in the same pathway to silence selfish genetic elements.

Our data suggest that in flies, rasiRNAs are produced by a mechanism that requires neither Dcr-1 nor Dcr-2, yet the patterns of rasiRNAs that direct *roo* and *Ste* silencing are as stereotyped as the distinctive siRNA population generated from the *white* hairpin by Dcr-2 (Fig. 1A) or the unique miRNA species made from each pre-miRNA by Dcr-1. A key challenge for the future will be to determine what enzyme makes rasiRNAs and what sequence or structural features of the unknown rasiRNA precursor lead to the accumulation of a stereotyped pattern of predominantly antisense rasiRNAs.

References and Notes

1. D. Galiana-Arnoux, C. Dostert, A. Schneemann, J. A. Hoffmann, J.-L. Imler, *Nat. Immunol.* **7**, 590 (2006).

2. X.-H. Wang *et al.*, *Science* **312**, 452 (2006); published online 22 March 2006 (10.1126/science.1125694).
3. R. A. Zambon, V. N. Vakharia, L. P. Wu, *Cell. Microbiol.* **8**, 880 (2006).
4. T. Du, P. D. Zamore, *Development* **132**, 4645 (2005).
5. A. I. Kalmykova, M. S. Klenov, V. A. Gvozdev, *Nucleic Acids Res.* **33**, 2052 (2005).
6. A. Fire *et al.*, *Nature* **391**, 806 (1998).
7. Y. S. Lee *et al.*, *Cell* **117**, 69 (2004).
8. N. T. Hoa, K. M. Keene, K. E. Olson, L. Zheng, *Insect Biochem. Mol. Biol.* **33**, 949 (2003).
9. K. Forstemann *et al.*, *PLoS Biol.* **3**, e236 (2005).
10. K. Saito, A. Ishizuka, H. Siomi, M. C. Siomi, *PLoS Biol.* **3**, e235 (2005).
11. F. Jiang *et al.*, *Genes Dev.* **19**, 1674 (2005).
12. D. S. Schwarz *et al.*, *Cell* **115**, 199 (2003).
13. P. D. Zamore, T. Tuschl, P. A. Sharp, D. P. Bartel, *Cell* **101**, 25 (2000).
14. Y. S. Lee, R. W. Carthew, *Methods* **30**, 322 (2003).
15. A. A. Aravin *et al.*, *Dev. Cell* **5**, 337 (2003).
16. A. A. Aravin *et al.*, *Curr. Biol.* **11**, 1017 (2001).
17. P. Tritto *et al.*, *Genetica* **117**, 247 (2003).
18. Y. Tomari *et al.*, *Cell* **116**, 831 (2004).
19. H. A. Cook, B. S. Koppetsch, J. Wu, W. E. Theurkauf, *Cell* **116**, 817 (2004).
20. T. Dalmay, R. Horsefield, T. H. Braunstein, D. C. Baulcombe, *EMBO J.* **20**, 2069 (2001).
21. G. Meister *et al.*, *Curr. Biol.* **15**, 2149 (2005).
22. W. Stapleton, S. Das, B. D. McKee, *Chromosoma* **110**, 228 (2001).
23. R. W. Williams, S. M. Rubin, *Proc. Natl. Acad. Sci. U.S.A.* **99**, 6889 (2002).
24. D. N. Cox *et al.*, *Genes Dev.* **12**, 3715 (1998).
25. A. N. Harris, P. M. Macdonald, *Development* **128**, 2823 (2001).
26. A. A. Aravin *et al.*, *Mol. Cell. Biol.* **24**, 6742 (2004).
27. I. Sahut-Barnola, D. Pauli, *Development* **126**, 1917 (1999).
28. V. V. Vagin *et al.*, *RNA Biol.* **1**, 54 (2004).
29. M. Savitsky, D. Kwon, P. Georgiev, A. Kalmykova, V. Gvozdev, *Genes Dev.* **20**, 345 (2006).
30. E. Bernstein, A. A. Caudy, S. M. Hammond, G. J. Hannon, *Nature* **409**, 363 (2001).
31. Q. Liu *et al.*, *Science* **301**, 1921 (2003).
32. S. M. Elbashir, W. Lendeckel, T. Tuschl, *Genes Dev.* **15**, 188 (2001).
33. G. Hutvagner *et al.*, *Science* **293**, 834 (2001); published online 12 July 2001 (10.1126/science.1062961).
34. Z. Yang, Y. W. Ebright, B. Yu, X. Chen, *Nucleic Acids Res.* **34**, 667 (2006).
35. D. N. Cox, A. Chao, H. Lin, *Development* **127**, 503 (2000).
36. K. Okamura, A. Ishizuka, H. Siomi, M. C. Siomi, *Genes Dev.* **18**, 1655 (2004).
37. We thank T. Du, M. Ghildiyal, and A. Boucher for assistance with fly husbandry, and J. Birchler, R. Carthew, F. Gao, R. Lehmann, H. Lin, P. MacDonald, M. Siomi, H. Siomi, D. Smith, E. Sontheimer, H. Ruohola-Baker, and M. Van Doren for fly stocks. P.D.Z. is a W.M. Keck Foundation Young Scholar in Medical Research. Supported in part by NIH grants GM62862 and GM65236 (P.D.Z.) and postdoctoral fellowships from the European Molecular Biology Organization (EMBO) and the Human Frontier Science Program (H.S.).

Supporting Online Material

www.sciencemag.org/cgi/content/full/1129333

Materials and Methods

Figs. S1 to S7

Table S1

References

1 May 2006; accepted 19 June 2006

Published online 29 June 2006;

10.1126/science.1129333

Include this information when citing this paper.

α -Synuclein Blocks ER-Golgi Traffic and Rab1 Rescues Neuron Loss in Parkinson's Models

Antony A. Cooper,^{1*} Aaron D. Gitler,^{2*} Anil Cashikar,^{2†} Cole M. Haynes,^{1§} Kathryn J. Hill,^{1†} Bhupinder Bhullar,^{2,3} Kangning Liu,^{4,5} Kexiang Xu,⁴ Katherine E. Strathearn,⁶ Fang Liu,⁶ Songsong Cao,⁷ Kim A. Caldwell,⁷ Guy A. Caldwell,⁷ Gerald Marsischky,³ Richard D. Kolodner,⁸ Joshua LaBaer,³ Jean-Christophe Rochet,⁶ Nancy M. Bonini,^{4,5} Susan Lindquist^{2,9||}

Alpha-synuclein (α Syn) misfolding is associated with several devastating neurodegenerative disorders, including Parkinson's disease (PD). In yeast cells and in neurons α Syn accumulation is cytotoxic, but little is known about its normal function or pathobiology. The earliest defect following α Syn expression in yeast was a block in endoplasmic reticulum (ER)-to-Golgi vesicular trafficking. In a genome-wide screen, the largest class of toxicity modifiers were proteins functioning at this same step, including the Rab guanosine triphosphatase Ypt1p, which associated with cytoplasmic α Syn inclusions. Elevated expression of Rab1, the mammalian *YPT1* homolog, protected against α Syn-induced dopaminergic neuron loss in animal models of PD. Thus, synucleinopathies may result from disruptions in basic cellular functions that interface with the unique biology of particular neurons to make them especially vulnerable.

Parkinson's disease (PD) is the second most common neurodegenerative disorder (1, 2). Accruing evidence points to a causative role for the presynaptic protein alpha-synuclein (α Syn) in PD pathogenesis. α Syn is a major constituent of Lewy Bodies—cellular inclusions that are the hallmark pathological feature of PD and other neurodegenerative disorders collectively referred to as synucleinopathies (3). Moreover, missense mutations in the α Syn gene (A53T, A30P, E46K) (4–6) and duplication or triplication of the locus cause PD (7–9). In mouse, rat, fly, and nematode models of PD, increased levels of α Syn lead to neurodegeneration (10–13). Elucidating the mechanisms underlying the cytotoxic effects of α Syn will be essential for the development of treatments to ameliorate or prevent the synucleinopathies.

Despite extensive study, little is known about α Syn's normal function or how α Syn contributes

to disease. Many cellular defects have been implicated in the etiology of synucleinopathies, including impairment of the ubiquitin-proteasome system, mitochondrial dysfunction, accumulation of lipid droplets, production of reactive oxygen species (ROS), and stress within the ER (14). A yeast PD model, with dosage sensitivity for α Syn expression, recapitulates many of these defects (15). But which are cause and which effect remain unclear. Here, two independent approaches, genetic and cell biological, converged to identify inhibition of ER-Golgi trafficking as a major component of synuclein-dependent toxicity.

α Syn accumulation causes ER stress. An increase in α Syn gene dosage in yeast from one copy (no growth defect) to two copies results in growth arrest and cell death (15) (Fig. 1A). To investigate the earliest defects caused by α Syn, we took advantage of the ability to rapidly and

synchronously induce its expression from a galactose-inducible promoter. A slight decline in viability was observed after 4 hours of induction, and 60% of cells lost colony-forming ability by 8 hours (Fig. 1, A and B). ER stress, measured by a reporter for the unfolded protein response, appeared earlier. Expression of wild-type α Syn (α Syn-WT) or disease-associated α Syn (α Syn-A53T) caused a fourfold increase in ER stress relative to control cells after 6 hours (Fig. 1C).

α Syn accumulation impairs degradation of selective ERAD substrates. ER stress typically results from the accumulation of misfolded proteins within the ER. Such malformed proteins are retrotranslocated from the ER to the cytoplasm for degradation by the proteasome through a process termed ERAD (endoplasmic reticulum associated degradation) (16). Misfolded cytosolic α Syn might impair the proteasome's capacity for protein degradation and so cause an accumulation of misfolded proteins in the ER and associated ER stress. To investigate this possi-

¹School of Biological Sciences, University of Missouri—Kansas City, Kansas City, MO 64110, USA. ²Whitehead Institute for Biomedical Research, Cambridge, MA 02142, USA. ³Harvard Institute of Proteomics, 320 Charles Street, Cambridge, MA 02141, USA. ⁴Department of Biology, University of Pennsylvania, Philadelphia, PA 19104, USA. ⁵Howard Hughes Medical Institute, Philadelphia, PA 19104, USA. ⁶Department of Medicinal Chemistry and Molecular Pharmacology, Purdue University, West Lafayette, IN 47907–2091, USA. ⁷Department of Biological Sciences, University of Alabama, Tuscaloosa, AL 35487, USA. ⁸Ludwig Institute for Cancer Research, University of California, San Diego, School of Medicine, La Jolla, CA 92093, USA. ⁹Howard Hughes Medical Institute, Massachusetts Institute of Technology, Cambridge, MA 02142, USA.

*These authors contributed equally to this work.

†Present address: Garvan Institute of Medical Research, Sydney, Australia.

‡Present address: Medical College of Georgia, Augusta, GA, USA.

§Present address: New York University, New York, NY, USA.

||To whom correspondence should be addressed. E-mail: lindquist_admin@wi.mit.edu

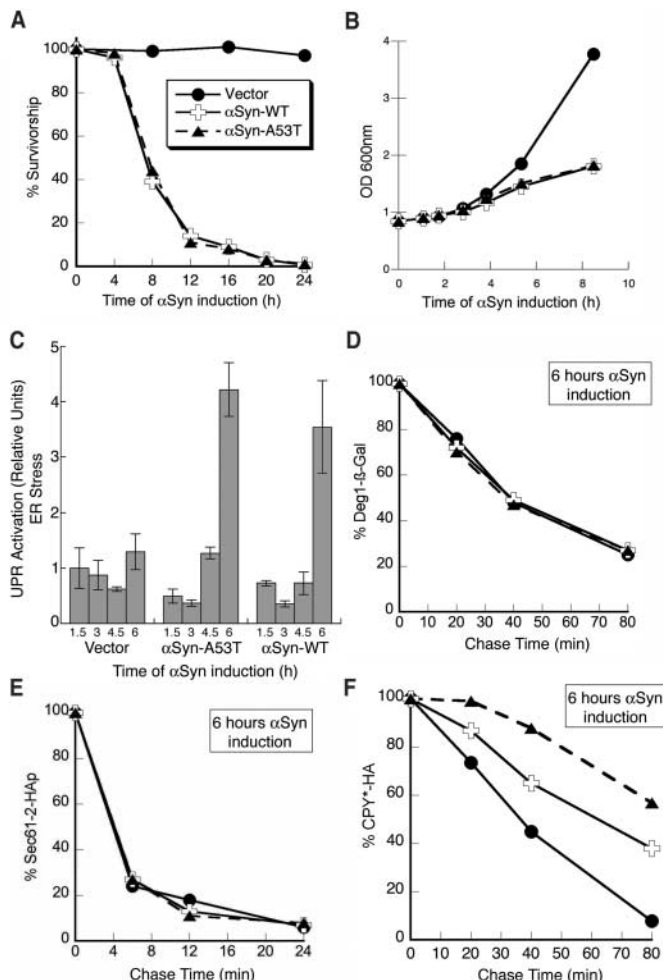
bility, we examined the degradation rate of a well-characterized cytosolic proteasome substrate, Deg1- β -Gal (17). Its rate of degradation was identical to that of control cells after 6 hours of α Syn expression (Fig. 1D). Thus, general proteasome activity was unaffected at a time when the level of an ER stress reporter was elevated fourfold (Fig. 1C) and a significant percentage of cells had lost viability (Fig. 1A).

A second cause of ER stress might be impairment of ERAD at a step before proteasome degradation. We therefore examined the degradation of two different misfolded proteins within the ER: (i) CPY*, a soluble misfolded substrate (18); and (ii) Sec61-2p, a misfolded membrane-spanning substrate (19). The degradation of Sec61-2p was unaffected (Fig. 1E), yet the turnover of CPY* was impaired in cells expressing α Syn-WT, and more so in cells expressing the disease-associated α Syn-A53T (Fig. 1F). Thus, paradoxically, toxic levels of α Syn inhibited the degradation of one ERAD substrate (CPY*) without perturbing the turnover of another (Sec61-2p).

α Syn accumulation inhibits ER-Golgi trafficking. A distinction between CPY* and

Sec61-2p is that CPY* degradation requires trafficking from the ER to the Golgi (20, 21). We investigated if α Syn affects vesicular trafficking between the ER and Golgi, by following two wild-type proteins that traffic through this pathway, correctly folded CPY and alkaline phosphatase (ALP). Their subcellular location is easily determined by compartment-specific glycosylations and proteolytic cleavages that alter the molecular mass of each protein in a well-characterized manner (22, 23). In cells expressing either α Syn-WT or α Syn-A53T, a pronounced defect in CPY (Fig. 2, A and B) and ALP (Fig. 2, C and D) trafficking was observed 3 hours after α Syn induction; by 4 hours their transport from the ER to the Golgi was almost completely blocked. For both CPY and ALP, expression of mutant α Syn-A53T (which causes early-onset PD in humans) caused a more rapid onset of the trafficking block than did α Syn-WT at equivalent levels of expression (Fig. 2, B and D). Notably, the earliest detectable impairment of growth (Fig. 1B) corresponded to the earliest detectable impairment in vesicular transport (Fig. 2, A and B) and preceded the onset of ER stress (Fig. 1C).

Fig. 1. Expression of α Syn causes cell death and ER stress and impairs ERAD. (A) Survivorship curve during α Syn induction. After induction of α Syn-WT, α Syn-A53T expression, or control cells (Vector), cells with an optical density at 600 nm (OD_{600nm}) of 1 were harvested and treated as described (24). Colony-forming units were determined and converted to relative percentages. (B) Growth curve during α Syn induction. After induction, the OD_{600nm} for each sample was measured at the indicated times. (C) Cells induced for expression of α Syn-WT, α Syn-A53T, or control cells (Vector) were harvested at the times indicated; the level of UPR activation was then determined and plotted as relative units of ER stress. The degradation rate of Deg1- β -Gal (D), Sec61-2p (E), and CPY* (F), after 6 hours of either α Syn-WT or α Syn-A53T expression, was determined by pulse-chase immunoprecipitation as described (24) and compared to that of control cells (Vector).



Genomewide overexpression screen identifies modifiers of α Syn toxicity. A genetic approach was employed to advance from determining the timing of affected cellular processes to identifying critical lethal lesions. We used an overexpression library in which individual yeast open reading frames (ORFs) were fully sequenced and placed, without protein tags, under the control of a galactose-inducible promoter. The 3000 randomly selected genes in this library, representing all functional classes, were individually transformed into a strain expressing α Syn-WT (Fig. 3). We used a strain with an intermediate level of α Syn expression (24), and thus an intermediate level of toxicity, enabling us to screen simultaneously for enhancers and suppressors. We identified 34 genes that suppressed and 20 genes that enhanced α Syn toxicity when overexpressed (table S1). One functional class enriched in our screen provided proof-of-principle for the effectiveness of the screen. This class included genes involved in carbohydrate metabolism or galactose-regulated gene expression specifically. Not surprisingly, these modifiers were not specific for α Syn toxicity; most were also recovered in a screen for suppressors of a galactose-regulated toxic huntingtin protein.

ER-Golgi vesicle trafficking genes modify α Syn toxicity. The largest and most effective class of suppressors, all highly specific for α Syn toxicity (fig. S1), were involved in vesicle-mediated membrane trafficking. Notably, all act at the same step of ER-to-Golgi trafficking or are known suppressors of defects in this step: the Rab guanosine triphosphatase (GTPase), Ypt1p; SNARE [soluble NSF (*N*-ethylmaleimide-sensitive factor) attachment protein receptor] protein, Ykt6p; Ubp3p and Bre5p, a ubiquitin protease and its cofactor required for deubiquitination of coat protein complex II (COPII) component Sec23p; and Erv29p, an ER-exit cargo receptor (table S1 and Fig. 3B). We also recovered Gyp8p as an enhancer of toxicity. *GYP8* encodes a Rab GTPase activating protein whose preferred substrate is Ypt1p. Thus, overexpression of genes promoting forward ER-Golgi transport suppresses α Syn toxicity, and those negatively regulating this step enhance toxicity.

A Ypt1-regulated step is particularly important. There are many Rab GTPases, which function at different points of the secretory pathway. Genes that encode other Rab proteins were present in the library but were not identified as α Syn suppressors. Because false-negatives are common in high-throughput screens, these Rabs were carefully and quantitatively retested. Whereas overexpression of Ypt1p rescued toxicity, six other Rab GTPases functioning at more distal points in vesicular trafficking (Ypt6p, Sec4p, Ypt31p, Ypt52p, Ypt53p, or Ypt35p) did not (Fig. 3C).

If inhibition of ER-Golgi trafficking is indeed a critical aspect of α Syn-induced toxicity, then ameliorating toxicity by Ypt1p overexpression should increase forward trafficking. Indeed,

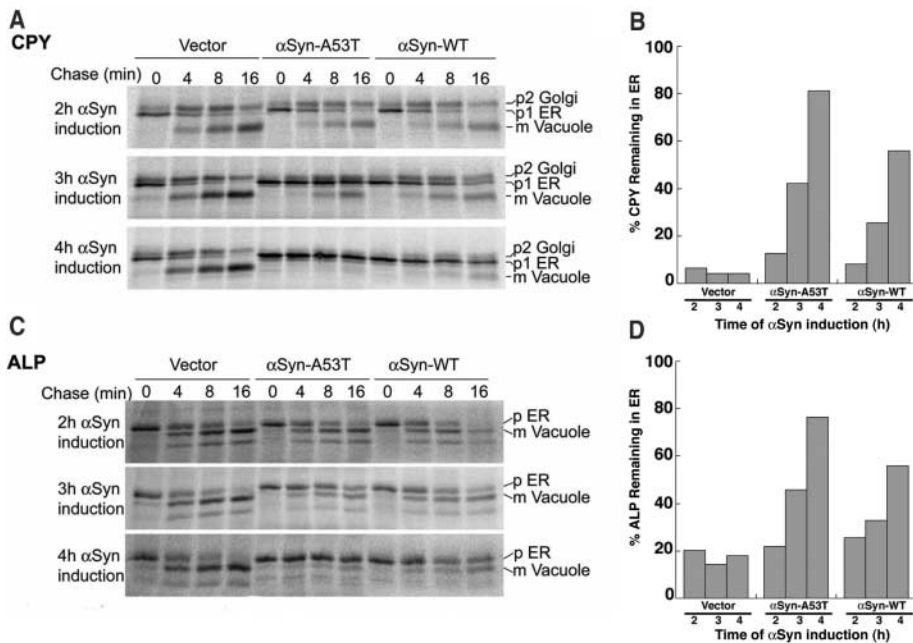
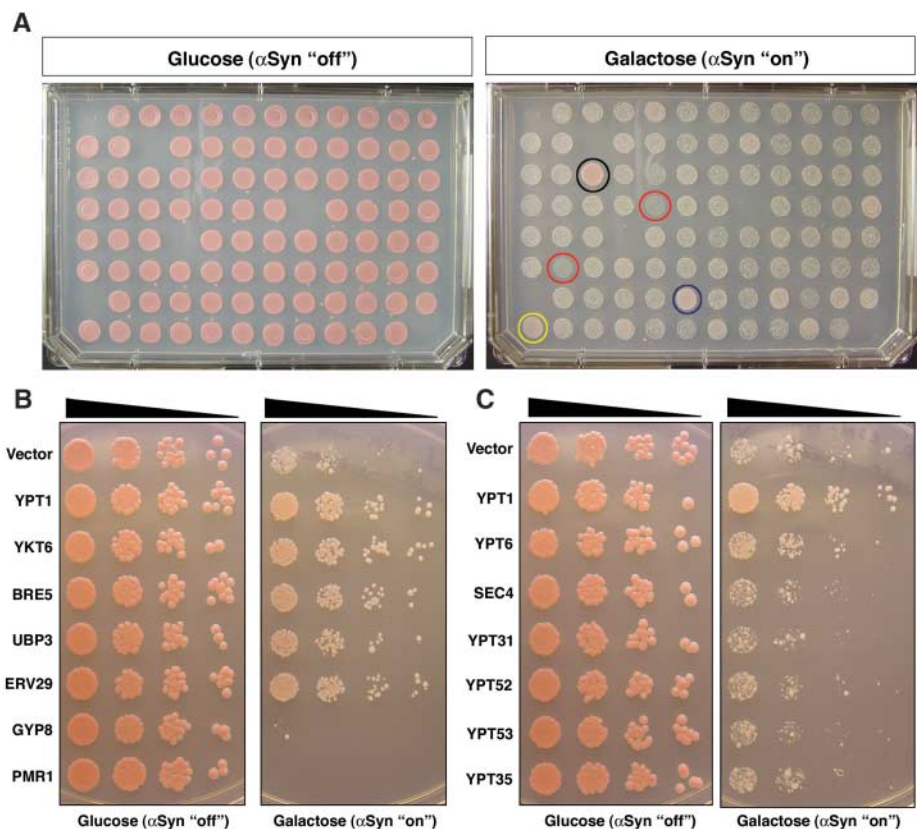


Fig. 2. α Syn accumulation causes a severe block in vesicular trafficking in the early secretory pathway. The trafficking of CPY (**A** and **B**) and ALP (**C** and **D**) was monitored in cells expressing α Syn-WT or α Syn-A53T at the times indicated by pulse-chase immunoprecipitation and compared to that of control cells (Vector). (**B**) Graphic representation of the amount of CPY remaining in the ER [p1/(p1 + p2 + mCPY)]. (**D**) Graphic representation of the amount of ALP remaining in the ER [p1/(p1 + p2 + mALP)]. For CPY, p1 is the ER form, p2 is the Golgi form, and m is the mature vacuolar form. For ALP, p is the ER form and m is the mature vacuolar form.

Fig. 3. Plasmid overexpression screen identifies ER-Golgi trafficking genes as modifiers of α Syn toxicity. (**A**) Representative plates from α Syn modifier screen (24). α Syn-expressing cells were transformed individually with each of 3000 random ORFs under the control of a galactose-inducible promoter. Transformants were grown on synthetic media containing either glucose (control, α Syn “off”) or galactose (to induce expression of α Syn and candidate ORFs, α Syn “on”). Examples of strong- and moderate-toxicity suppressors are shown as black and blue circles, respectively. Examples of enhancers of α Syn-induced toxicity are shown as red circles, and a false-positive that did not reproduce upon further analysis is shown as a yellow circle. (**B**) Spotting assay shows that overexpression of ER-Golgi trafficking genes *YPT1*, *YKT6*, *BRE5*, *UBP3*, and *ERV29* suppress α Syn-induced toxicity, whereas *GYP8* and *PMR1* overexpression enhances toxicity. (**C**) Suppression of toxicity is specific to the transport step facilitated by *YPT1*, because overexpression of other Rab GTPases has no effect on growth.



overexpression of Ypt1p markedly enhanced forward transport of CPY (Fig. 4, A and B). Overexpression of *GYP8*, a negative regulator of Ypt1p, exacerbated the trafficking defect (Fig. 4, A and B). A dominant-negative version of Ypt1p, a protein fusion that obviates the function of Ypt1p's C-terminal geranylgeranyl membrane anchor signal, enhanced α Syn toxicity. Defects in Ypt1p can be suppressed by *SLY1-20*, which encodes a dominant form of the ER-to-Golgi target (t)-SNARE associated protein Sly1p (25). In a corresponding manner, *SLY1-20* strongly suppressed both the α Syn-induced growth defect (fig. S2) and the CPY trafficking defect (Fig. 4, C and D). The ability of these specific suppressors and enhancer alleles to rescue or exacerbate trafficking defects, as well as to rescue or exacerbate α Syn toxicity, confirms that forward ER-to-Golgi vesicular transport is particularly sensitive to α Syn accumulation. Ypt1p frequently localized to α Syn cytoplasmic inclusions (Fig. 4E), suggesting that the cytotoxic form of α Syn may associate with transport vesicles as α Syn normally does with synaptic vesicles (26, 27).

Rescue of α Syn-induced dopaminergic neuron loss by Ypt1p/Rab1. Next we tested the ability of our strongest yeast suppressor to rescue α Syn-associated dopaminergic (DA) neuron loss in animal models of PD (10, 13). In *Drosophila*, the ability of Rab1 (the murine *YPT1* ortholog) to mitigate toxicity of α Syn-WT as well as of the disease-associated α Syn-

A53T was determined. Adult flies expressing α Syn, in the presence or absence of added Rab1, were aged, and DA neuron numbers were assessed in the dorsomedial (DM) cluster after immunostaining for tyrosine hydroxylase

(TH), which specifically identifies DA neurons. Consistent with previous studies (10), flies expressing α Syn-WT or α Syn-A53T alone exhibited DA neuron loss (Fig. 5, A to C). Coexpression of Rab1 was sufficient to

fully rescue this loss (Fig. 5, A to C; two independent transgenic lines). Rescue was specific to Rab1 because directed expression of the control protein β -galactosidase (β -Gal) has no effect on α Syn toxicity (10). Suppression of α Syn toxicity by Rab1 was at least as strong as that of the strongest suppressor previously identified in this system, the chaperone protein Hsp70 (10).

We also tested Rab1 in a *Caenorhabditis elegans* model (13). The dopamine transporter (DAT-1) gene promoter was used to direct expression of Rab1 along with α Syn in DA neurons. Expression of α Syn alone resulted in 60% of animals with reduced numbers of DA neurons at the 7-day stage compared to controls. Coexpression of Rab1 significantly rescued neurodegeneration in all three of the independent transgenic lines established (Fig. 5, D to F). Suppression by Rab1 was as strong as that seen with the strongest suppressor yet identified in this system, torsinA, an ER-associated protein with chaperone activity (13).

Finally, we tested the ability of Ypt1p/Rab1 to protect against α Syn toxicity in mammalian DA neurons. We produced lentiviruses expressing α Syn-A53T, Rab1, and a control protein, β -Gal. Primary cultures of rat midbrain neurons were transduced with viruses encoding α Syn-A53T, α Syn-A53T plus Rab1, or α Syn-A53T plus β -Gal (Fig. 5, G to I). The viability of DA neurons was assessed relative to the number of

Fig. 4. α Syn-induced cytotoxicity and vesicular trafficking defects are modified by ER-Golgi trafficking components. The trafficking of CPY in cells expressing α Syn-WT and harboring either galactose-inducible *GYP8* (A and B), galactose-inducible *YPT1* (A and B), or *SLY1-20* (C and D) was monitored by radiolabeling after 7 hours (C and D) or 8 hours (A and B) of induction and compared to trafficking in control cells (Vector). (B and D) Graphic representation of the amount of CPY remaining in the ER [p1/(p1 + p2 + mCPY)]. (E) Cells expressing α Syn-WT-GFP (green fluorescence protein) and HA (hemagglutinin)-Ypt1p were examined by fluorescence and indirect immunofluorescence microscopy after 6 hours of α Syn induction.

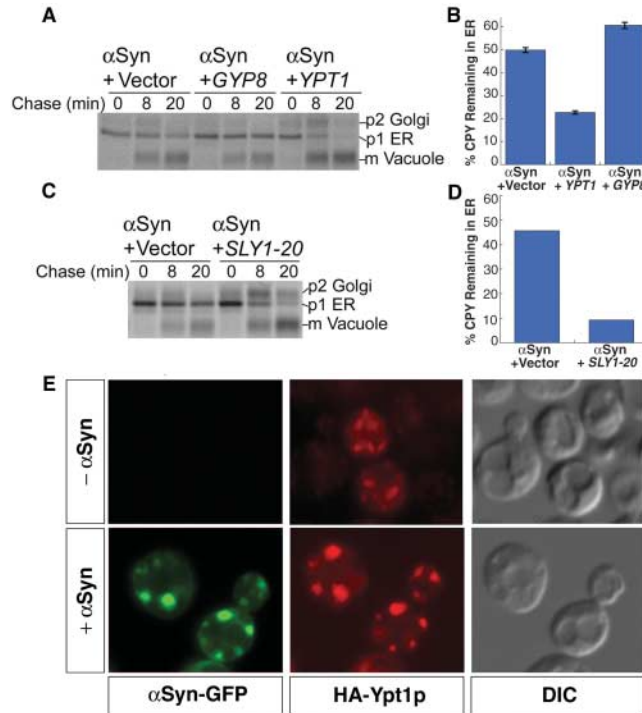
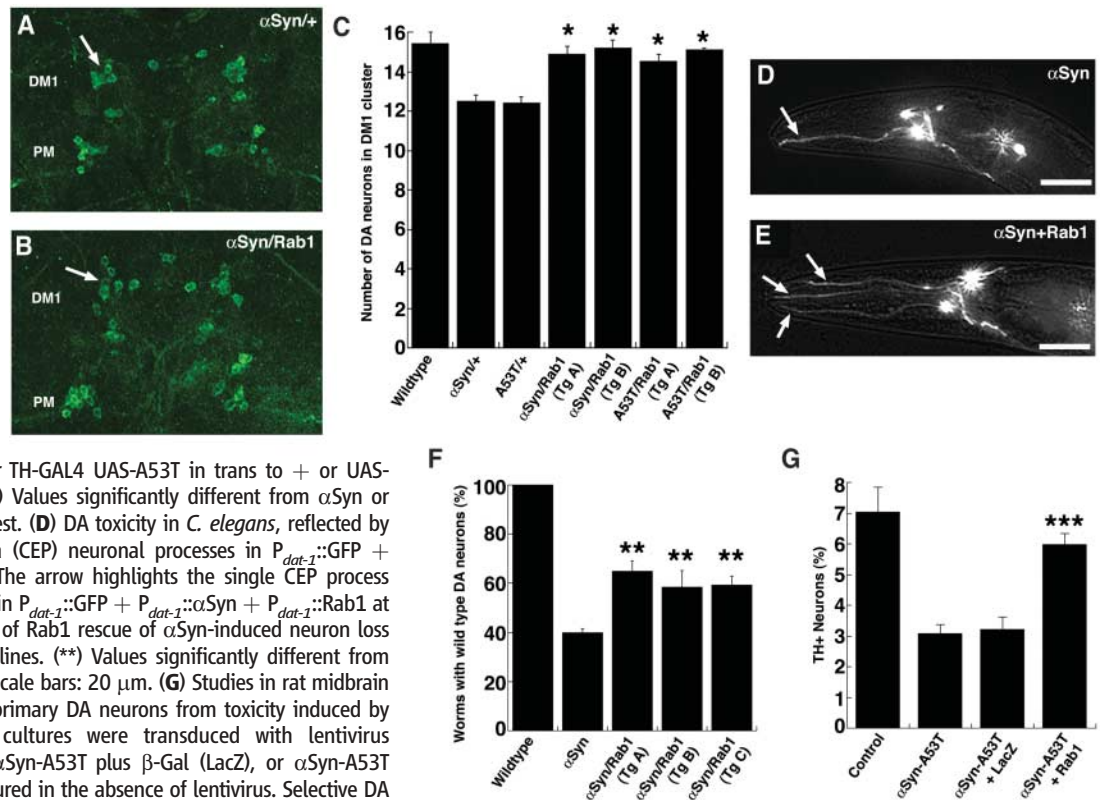


Fig. 5. Expression of Rab1 rescues DA neuron loss in animal models of PD. (A to C) Studies in *Drosophila*. (A and B) Aged fly brains immunostained for TH to highlight DA neurons; selective loss of TH immunostaining in the DM1 cluster is fully prevented by Rab1. Genotypes TH-GAL4 UAS- α Syn in trans to + or UAS-Rab1. (C) Quantitation of TH-positive neurons in DM1 cluster. Wild-type (α Syn) or mutant (A53T) α Syn causes loss of TH that is prevented by Rab1. Genotypes: TH-GAL4/+ (wildtype), TH-GAL4 UAS- α Syn or TH-GAL4 UAS-A53T in trans to + or UAS-Rab1 (two independent lines). (*) Values significantly different from α Syn or A53T, $P < 0.00001$, Student's t test. (D) DA toxicity in *C. elegans*, reflected by degeneration of cephalic sensilla (CEP) neuronal processes in $P_{dat-1}::GFP + P_{dat-1}::\alpha$ Syn at the 7-day stage. The arrow highlights the single CEP process remaining. (E) Intact DA neurons in $P_{dat-1}::GFP + P_{dat-1}::\alpha$ Syn + $P_{dat-1}::Rab1$ at the 7-day stage. (F) Quantitation of Rab1 rescue of α Syn-induced neuron loss in three independent transgenic lines. (**) Values significantly different from α Syn, $P < 0.05$, Student's t test. Scale bars: 20 μ m. (G) Studies in rat midbrain primary neurons. Rab1 protects primary DA neurons from toxicity induced by α Syn-A53T. Primary midbrain cultures were transduced with lentivirus encoding α Syn-A53T alone, or α Syn-A53T plus β -Gal (LacZ), or α Syn-A53T plus Rab1. Control cells were cultured in the absence of lentivirus. Selective DA cell death was evaluated immunocytochemically. Viability is expressed as the percentage of MAP2-positive neurons that were also TH-positive (three independent experiments, at least 100 cells counted per experiment for each condition). The data are presented as the mean \pm SD, $n = 3$ experiments; *** $P < 0.01$, analysis of variance with Newman-Keuls post-test.



primary DA neurons from toxicity induced by α Syn-A53T. Primary midbrain cultures were transduced with lentivirus encoding α Syn-A53T alone, or α Syn-A53T plus β -Gal (LacZ), or α Syn-A53T plus Rab1. Control cells were cultured in the absence of lentivirus. Selective DA cell death was evaluated immunocytochemically. Viability is expressed as the percentage of MAP2-positive neurons that were also TH-positive (three independent experiments, at least 100 cells counted per experiment for each condition). The data are presented as the mean \pm SD, $n = 3$ experiments; *** $P < 0.01$, analysis of variance with Newman-Keuls post-test.

total neurons by staining with antibodies specific for TH and the neuronal marker microtubule-associated protein 2 (MAP2). Cultures transduced with α Syn-A53T-encoding lentivirus had decreased numbers of DA neurons (~50% loss) relative to cultures infected with control virus. The selective toxicity of α Syn-A53T to the DA neurons was robustly attenuated by coexpression of Rab1. Thus, the ability of Ypt1p/Rab1 to protect from α Syn toxicity is conserved from yeast cells to DA neurons in animal models of PD.

Discussion. Inhibition of ER-Golgi trafficking by α Syn is a critical cellular lesion contributing to toxicity and cell loss. Moreover, increased Rab1 production is sufficient to protect against α Syn-associated DA neuron loss in animal models of PD.

Our current understanding of Rab function involves Ypt1p/Rab1 playing an essential role in the tethering and docking of the transport vesicle with the Golgi. α Syn likely inhibits this stage of ER-Golgi transport rather than vesicle generation at the ER: α Syn was not observed associated with the ER, and the trafficking-related modifiers act at this stage. The detrimental relation between α Syn and Rab1 is supported by the Golgi fragmentation that is caused by either a dominant mutant Rab1 or forced expression of α Syn (28, 29). A reduction in ER-Golgi transport caused by α Syn would result in an accumulation of proteins in the ER and produce ER stress, potentially accounting for the ER stress observed in PD disease models (30) and in yeast. A trafficking block associated with the Golgi would also explain the endocytosis defect we previously reported (15), because we observe a similar block in FM4-64 dye internalization in the temperature-sensitive *ypt1-3* strain in which a defect in endocytosis occurs secondarily to an ER-Golgi trafficking block.

Genes whose overproduction increases forward transport between ER and Golgi would allow cells to overcome the α Syn-induced transport block. Conversely, genes whose overproduction negatively regulates ER-Golgi trafficking exacerbate the transport block caused by α Syn. The results of our genetic screen in yeast are consistent with this scenario: Overexpression of Ypt1p and Ykt6p both likely increase forward transport by increasing the likelihood of membrane vesicles from the ER tethering to Golgi target membranes. Likewise, overexpression of the negative regulator of Ypt1p, Gyp8p, would inhibit this process. Increasing exit of vesicles from the ER would also improve forward transport. Accordingly, overexpression of a ubiquitin protease (Ubp3p) and its cofactor (Bre5p), which together function to deubiquitinate the COPII coat protein Sec23p, would promote vesicle exit from the ER (31).

Recent experiments demonstrated a previously unappreciated, normal function for α Syn (32). Increased expression of α Syn is sufficient to rescue a lethal neurodegenerative phenotype in

mice lacking cysteine-string protein α (CSP α). CSP α may thus act as a chaperone to assemble or maintain synaptic SNARE components in functional states over the many repeated SNARE assembly/disassembly cycles expected in neurons (32). Although α Syn does not appear to simply substitute for the lost CSP α chaperone role, it might act downstream or in a parallel pathway involving SNARE complex assembly. This might well include interactions with Rabs, tethering factors, or SNARE proteins, an intriguing aspect because our yeast screen identified both Ypt1p/Rab1 and Ykt6p, a vesicle (v)-SNARE that has been shown to interact genetically with Ypt1p, as potent suppressors. Our findings, that inappropriate α Syn accumulation is toxic owing to specific cellular defects involving an ensemble of proteins that function with SNAREs to mediate vesicle trafficking—coupled with the ability of Rab1 to protect against neurodegeneration in animal models of PD—suggest that toxic activities of α Syn may be related to its normal function.

α Syn is expressed throughout the brain, yet DA neurons are particularly sensitive in PD. Our work suggests that α Syn accumulation is likely to impede the early secretory pathway in many cell types, potentially helping to explain the non-DA lesions resulting from α Syn duplication or triplication (7–9). What, then, might render DA neurons particularly sensitive to an ER-Golgi transport block? Dopamine is inherently unstable and can oxidize to generate ROS, with enzymatic metabolism by monoamine oxidase producing H₂O₂ (33). Dopamine is synthesized in the cytosol and rapidly pumped by the vesicular monoamine transporter 2 (VMAT2) transporter into synaptic vesicles, where the low vesicular pH and the absence of monoamine oxidase limits dopamine breakdown. Defects in the early secretory pathway could cause a shortage of synaptic vesicles and reduce delivery of VMAT2 to the synapse. Both would impede dopamine loading and produce a rise in cytosolic dopamine concentration. The inhibition of vesicular trafficking by α Syn may affect dopamine-producing neurons more particularly, because neurotransmitters produced by other neurons are less toxic.

The ability of Rab1 to protect against α Syn-induced neuron loss in three independent animal models is strong evidence for a specific link between α Syn and ER-Golgi trafficking. Neurons express additional Rab GTPases not present in yeast, and some of these might be affected by α Syn in a similar manner. Notably, our yeast screen identified additional modifiers of α Syn toxicity, involved in cell stress responses, signaling, and metal-ion transport, suggesting that there may be further links between the pathobiology of α Syn in yeast and neuronal cells. Our work cross-validates several different model systems for the study of PD and establishes that simple model systems can be useful in the investigation of even complex neurodegenerative diseases.

References and Notes

1. M. Vila, S. Przedborski, *Nat. Med.* **10** (Suppl.), S58 (2004).
2. M. S. Forman, J. Q. Trojanowski, V. M. Lee, *Nat. Med.* **10**, 1055 (2004).
3. M. G. Spillantini, R. A. Crowther, R. Jakes, M. Hasegawa, M. Goedert, *Proc. Natl. Acad. Sci. U.S.A.* **95**, 6469 (1998).
4. M. H. Polymeropoulos et al., *Science* **276**, 2045 (1997).
5. R. Kruger et al., *Nat. Genet.* **18**, 106 (1998).
6. J. J. Zarranz et al., *Ann. Neurol.* **55**, 164 (2004).
7. A. B. Singleton et al., *Science* **302**, 841 (2003).
8. M. C. Chartier-Harlin et al., *Lancet* **364**, 1167 (2004).
9. P. Ibanez et al., *Lancet* **364**, 1169 (2004).
10. P. K. Auluck, H. Y. Chan, J. Q. Trojanowski, V. M. Lee, N. M. Bonini, *Science* **295**, 865 (2002).
11. C. Lo Bianco, J. L. Ridet, B. L. Schneider, N. Deglon, P. Aebischer, *Proc. Natl. Acad. Sci. U.S.A.* **99**, 10813 (2002).
12. E. Masliah et al., *Science* **287**, 1265 (2000).
13. S. Cao, C. C. Gelwix, K. A. Caldwell, G. A. Caldwell, *J. Neurosci.* **25**, 3801 (2005).
14. W. Dauer, S. Przedborski, *Neuron* **39**, 889 (2003).
15. T. F. Outeiro, S. Lindquist, *Science* **302**, 1772 (2003).
16. A. A. McCracken, J. L. Brodsky, *Bioessays* **25**, 868 (2003).
17. M. Hochstrasser, A. Varshavsky, *Cell* **61**, 697 (1990).
18. M. Knop, N. Hauser, D. H. Wolf, *Yeast* **12**, 1229 (1996).
19. T. Biederer, C. Volkwein, T. Sommer, *EMBO J.* **15**, 2069 (1996).
20. S. R. Caldwell, K. J. Hill, A. A. Cooper, *J. Biol. Chem.* **276**, 23296 (2001).
21. E. D. Spear, D. T. Ng, *Mol. Biol. Cell* **14**, 2756 (2003).
22. D. J. Klionsky, S. D. Emr, *EMBO J.* **8**, 2241 (1989).
23. T. Stevens, B. Esmon, R. Schekman, *Cell* **30**, 439 (1982).
24. Materials and methods are available as supporting material on Science Online.
25. R. Ossig, C. Dascher, H. H. Trepte, H. D. Schmitt, D. Gallwitz, *Mol. Cell. Biol.* **11**, 2980 (1991).
26. D. L. Fortin et al., *J. Neurosci.* **24**, 6715 (2004).
27. J. C. Rochet et al., *J. Mol. Neurosci.* **23**, 23 (2004).
28. B. S. Wilson et al., *J. Cell Biol.* **125**, 557 (1994).
29. N. Gosavi, H. J. Lee, J. S. Lee, S. Patel, S. J. Lee, *J. Biol. Chem.* **277**, 48984 (2002).
30. E. J. Ryu et al., *J. Neurosci.* **22**, 10690 (2002).
31. M. Cohen, F. Stutz, N. Belgareh, R. Haguenaer-Tsapis, C. Dargemont, *Nat. Cell Biol.* **5**, 661 (2003).
32. S. Chandra, G. Gallardo, R. Fernandez-Chacon, O. M. Schluter, T. C. Sudhof, *Cell* **123**, 383 (2005).
33. J. Lotharius et al., *J. Biol. Chem.* **277**, 38884 (2002).
34. We thank D. Eide, M. Hochstrasser, J. Warner, and R. Collins for plasmids. We are grateful to members of the Lindquist lab for helpful suggestions and comments on the manuscript, especially J. Shorter and B. Bevis for advice and encouragement and T. Outeiro for making the screening strain. A.D.G. is a Lilly Fellow of the Life Sciences Research Foundation. The YEASTFlex collection was supported by National Human Genome Research Institute grant R01-HG002923. This work was supported by NIH (A.A.C.; Udall Center, S.L.; J.-C.R.; G.A.C.), Missouri Alzheimer's Grant (A.A.C.), National Institute on Aging (N.M.B.), and the McKnight Fund for Neuroscience (S.L.). S.L. and N.M.B. are investigators of the Howard Hughes Medical Institute. S.L. is a founder and former member of the Board of Directors of, and has received consulting fees from, FoldRx Pharmaceuticals, a company that investigates drugs to treat protein-folding diseases. She holds a patent on modulators of α -synuclein toxicity; genes described in the patent are licensed to FoldRx Pharmaceuticals. She is also a member of the Board of Directors of Johnson & Johnson. A.A.C. and J.-C.R. have received consulting fees from FoldRx Pharmaceuticals, and J.-C. R. has received payment from FoldRx for testing drugs in his laboratory.

Supporting Online Material

www.sciencemag.org/cgi/content/full/1129462/DC1

Materials and Methods

Figs. S1 and S2

Table S1

References

2 May 2006; accepted 12 June 2006

Published online 22 June 2006;

10.1126/science.1129462

Include this information when citing this paper.

Low-Frequency Spin Dynamics in a Canted Antiferromagnet

Norio Kumada,^{1*} Koji Muraki,¹ Yoshiro Hirayama^{1,2,3}

Resistively detected nuclear spin relaxation measurements in closely separated two-dimensional electron systems reveal strong low-frequency electron-spin fluctuations in the quantum Hall regime. As the temperature is decreased, the spin fluctuations, manifested by a sharp enhancement of the nuclear spin-lattice relaxation rate $1/T_1$, continue to grow down to the lowest temperature of 66 millikelvin. The observed divergent behavior of $1/T_1$ signals a gapless spin excitation mode and is a hallmark of canted antiferromagnetic order. Our data demonstrate the realization of a two-dimensional system with planar broken symmetry, in which fluctuations do not freeze out when approaching the zero temperature limit.

The quasi-two-dimensional electron system (2DES) in semiconductor heterostructures has become an indispensable laboratory for studying various many-body phenomena in low dimensions. When a strong perpendicular magnetic field (B) is applied, the kinetic energy of the electrons is quenched by quantization into discrete Landau levels (LLs), and electron-electron interactions completely dominate the physics. When the LL filling factor $\nu = nh/eB$ —the ratio of the electron density (n) to the degeneracy of a single spin-resolved LL (eB/h)—matches an integer or a certain rational fraction, the 2DES exhibits the quantum Hall (QH) effect (I) characterized by quantized Hall resistance and vanishing longitudinal resistance (where h is Planck's constant and $-e$ is the charge on the electron). Recent theory (2, 3) and experiment (4–9) have revealed that, when two or more LLs with different spin or layer indices are brought close in energy near the Fermi level, the Coulomb interactions combined with the additional spin or layer degrees of freedom (the latter represented by pseudospin) lead to a broken-symmetry state with spin or pseudospin order, which can be viewed as a new class of ferromagnet (10).

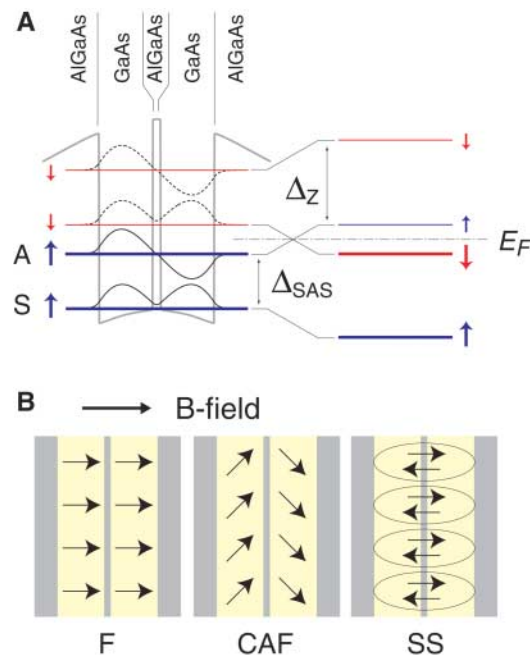
Unlike conventional ferromagnets or antiferromagnets, in which strong crystal fields exist to pin the magnetization along particular crystallographic directions, in QH ferromagnets the interactions with the host semiconductor crystal are almost entirely contained in the effective mass and effective g factor of electrons. The QH systems may then offer the opportunity to experimentally implement systems of certain symmetry that would otherwise have been hypothetical. Of fundamental interest is the case

when continuous symmetry is broken, where the magnetization emerges in one direction chosen out of infinitely degenerate equivalents. As the global rotation of the magnetization does not cost energy, there will be a low-energy collective excitation mode, called a Goldstone mode, whose energy goes to zero in the long-wavelength limit (11). This implies that the system no longer has any characteristic time scale in its long-wavelength behavior, which would lead to collective dynamics in which all particles participate.

We investigate low-frequency spin dynamics in a QH state with planar broken symmetry and present results indicative of its Goldstone mode. Specifically, we investigate a “bilayer” system of two closely separated 2DESs with

total filling factor $\nu_{\text{tot}} = 2$. In this system, intralayer spin interactions, interlayer pseudospin interactions, and a QH gap all play key roles in creating the Goldstone mode. Our results thus connect the physics of the QH systems with those of magnetism and pseudomagnetism. The interlayer interactions can be tuned by the energy gap Δ_{SAS} of the interlayer tunneling. When Δ_{SAS} is small, the $\nu_{\text{tot}} = 2$ ground state is a ferromagnetic (F) state, in which electron spins align ferromagnetically by intralayer interactions, with the spin direction fixed by weak Zeeman coupling to the magnetic field. A large value of Δ_{SAS} (or a large electric field across the two layers) favors antiparallel spin configurations (parallel pseudospin configurations), resulting in a spin-singlet (SS) ground state (Fig. 1A). Between these two states, the interplay of the intralayer and interlayer interactions and the Zeeman energy is believed to lead to a new state, the canted antiferromagnetic (CAF) state, in which spins have ferromagnetic correlation within each layer and antiferromagnetic correlation between the layers (Fig. 1B), as first predicted in (12) and further elaborated in (13–17). The CAF state breaks the spin rotational symmetry in the plane and thus has a gapless spin excitation mode (i.e., a Goldstone mode) even in a strong magnetic field (13, 14). Thus far, experimental data most indicative of the CAF state were given by inelastic light scattering (18, 19); the observed mode softening of the intersubband spin excitation pointed to a quantum phase transition to a new state. Transport (20, 21) and capacitance (22) measurements have also

Fig. 1. (A) Illustrations of the potential energy and the subband wave functions in a GaAs/AlGaAs double quantum well. The lowest Landau levels are split by the tunneling gap Δ_{SAS} into symmetric (S) and antisymmetric (A) states, which are further split into spin-up (blue) and spin-down (red) states by the Zeeman energy Δ_Z . At $\nu_{\text{tot}} = 2$, the lowest two levels below the Fermi level E_F are occupied, as shown by the thick blue lines in the left panel and by the blue and red lines in the right panel. When $\Delta_{\text{SAS}} < \Delta_Z$ (left panel), the ground state is spin-polarized (i.e., ferromagnetic) but undergoes a transition to the spin-unpolarized (i.e., spin-singlet) state upon increasing Δ_{SAS} (right panel). Note that the spin splitting is greatly enhanced by electron-electron interactions over its bare value, Δ_Z . **(B)** Spin configurations in the three possible ground states at $\nu_{\text{tot}} = 2$. Between the ferromagnetic (F) and spin-singlet (SS) states, the canted antiferromagnetic (CAF) state is expected to arise from the interplay among the intralayer and interlayer interactions and the Zeeman energy. In the CAF state, the spin direction in the two-dimensional plane is arbitrary, indicating broken symmetry.



¹NTT Basic Research Laboratories, NTT Corporation, 3-1 Morinosato-Wakamiya, Atsugi, Kanagawa 243-0198, Japan.

²SORST–Japan Science and Technology Agency, 4-1-8 Honmachi, Kawaguchi, Saitama 331-0012, Japan. ³Department of Physics, Tohoku University, Sendai 980-8578, Japan.

*To whom correspondence should be addressed. E-mail: kumada@will.brl.ntt.co.jp

revealed a phase transition. However, experimental evidence of the CAF ordering, or the predicted Goldstone mode, has not been observed to date.

We measure the nuclear spin-lattice relaxation rate $1/T_1$ of the GaAs crystal hosting the bilayer 2DES, which is proportional to the spectral density of transverse electron-spin fluctuations at the nuclear frequency (23, 24). As the Larmor frequency of nuclear spins is negligibly small relative to that of electron spins, $1/T_1$ is capable of probing electron-spin dynamics at very low frequencies that cannot be accessed by other means. We observe an enhancement of $1/T_1$ between the F and SS phases, revealing strong electron-spin fluctuations indicative of the CAF state. Furthermore, $1/T_1$ shows divergent behavior with decreasing temperature, highlighting the existence of the Goldstone mode.

Experiments were performed on double-quantum-well structures with GaAs quantum wells 20 nm in width. We investigated two samples: one with $\Delta_{\text{SAS}} = 8$ K and a tunnel barrier of $\text{Al}_{0.3}\text{Ga}_{0.7}\text{As}$ (thickness 3.1 nm), and the other with $\Delta_{\text{SAS}} = 3$ K and a tunnel barrier of AlAs (thickness 1.5 nm). The filling factors in the two layers were independently tuned by controlling the electron densities in the front and back layers (n_f and n_b) with the front- and back-gate biases while applying a constant magnetic field of 5.5 T perpendicular to the 2DES. We used current-pump and resistive-detection techniques (25–27) to measure $1/T_1$; this enabled sensitive and selective measurements of $1/T_1$ of those nuclei in contact with the 2DES.

The transitions between different $\nu_{\text{tot}} = 2$ ground states can be driven by changing the density imbalance $\delta n = n_f - n_b$ at a fixed total density $n_{\text{tot}} = n_f + n_b$ (16). The longitudinal resistance (R_{xx}) of the $\Delta_{\text{SAS}} = 3$ K sample measured as a function of the front- and back-gate biases clearly shows two distinct QH states along $\nu_{\text{tot}} = 2$ (Fig. 2B). The one at the balance point ($\delta n = 0$) is unstable against density imbalance and is therefore identified as the F state consisting of two single-layer $\nu = 1$ states (20). The other at large imbalance, which evolves continuously to the single-layer $\nu = 2$ QH state, is the SS state (28). The two phases are separated by a no-QH region with non-vanishing R_{xx} , as expected for a simple level-crossing picture (Fig. 1A). In contrast, in the sample with $\Delta_{\text{SAS}} = 8$ K, the two regions are connected continuously with the QH effect preserved (Fig. 2A). Because such a continuous evolution is not explained in a single-particle picture, the CAF state is expected to be formed in this region, supported by the larger Δ_{SAS} and hence by stronger interlayer antiferromagnetic coupling.

We investigated the nuclear spin relaxation over the relevant gate-voltage range (yellow boxes in Fig. 2, A and B). The experimental sequence consists of initial nuclear polarization

induced by current, followed by resistive detection of the nuclear relaxation after a given period of time τ (26, 27). The color plots in Fig. 2C represent the degrees of nuclear spin relaxation at several values of τ . In the $\Delta_{\text{SAS}} = 8$ K sample, two bright spots indicating extremely fast relaxation appear already at $\tau = 0.2$ s in the

region between the F and SS states (i.e., exactly where the CAF state is expected). In the sample with $\Delta_{\text{SAS}} = 3$ K, the relaxation becomes discernible only after $\tau = 1.0$ s in the region surrounding the F phase (Fig. 2D). Although similar features are also seen in the $\Delta_{\text{SAS}} = 8$ K sample (see the data for $\tau = 1.0$ and 10 s), the

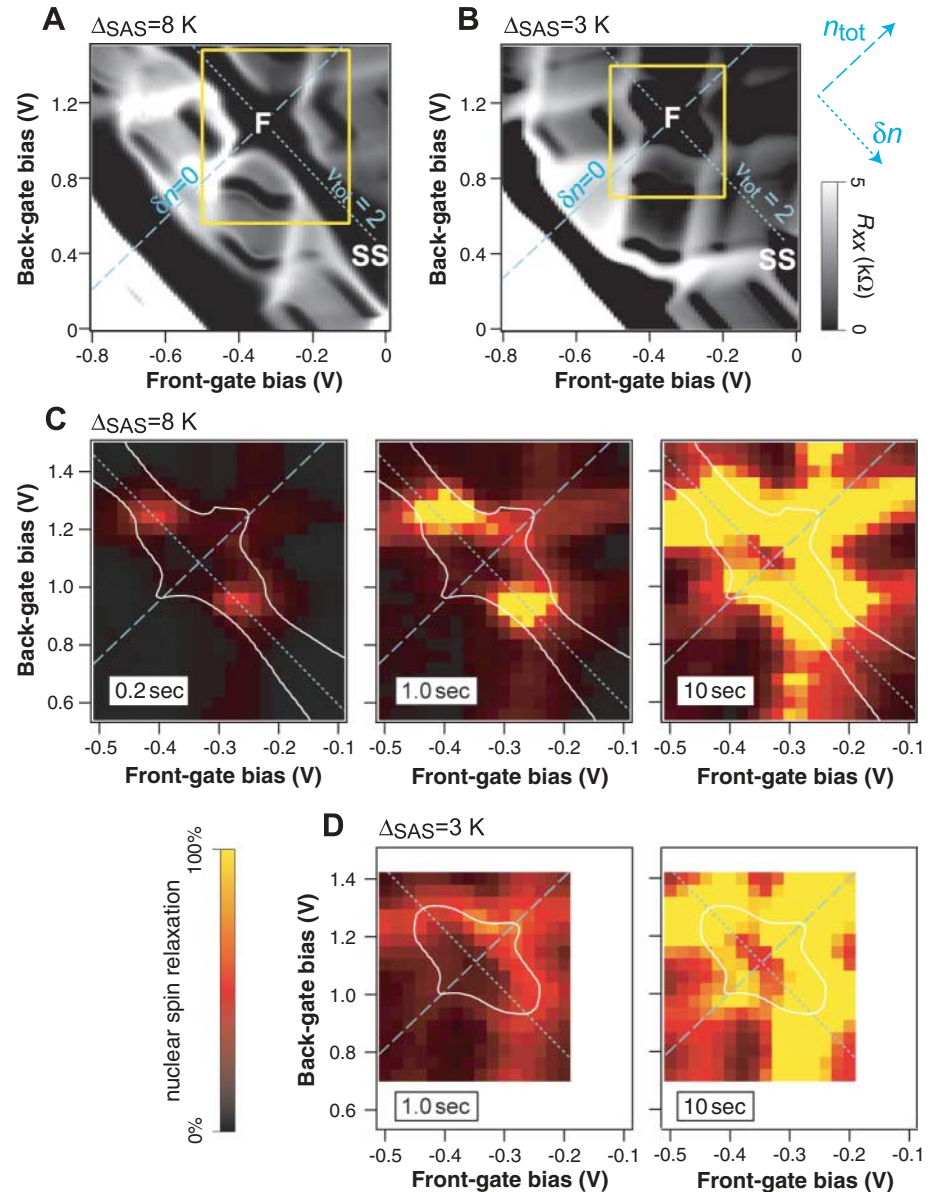


Fig. 2. (A and B) Grayscale plots of R_{xx} at 5.5 T as a function of the front- and back-gate biases for the samples with (A) $\Delta_{\text{SAS}} = 8$ K and (B) $\Delta_{\text{SAS}} = 3$ K. The front- and back-gate biases control the electron densities in the front and back layers (n_f and n_b), respectively, allowing for independent tuning of the total density $n_{\text{tot}} = n_f + n_b$ and the density imbalance $\delta n = n_f - n_b$ as shown by the blue arrows. Dashed lines represent the balance condition ($\delta n = 0$); dotted lines indicate the constant total filling factor of $\nu_{\text{tot}} = 2$. Quantum Hall (QH) states, where $R_{xx} \approx 0$, appear as black regions, with F and SS representing the ferromagnetic and spin-singlet states at $\nu_{\text{tot}} = 2$. Note that $n_b = 0$ on the horizontal axis, where the system becomes a single-layer 2DES. (C and D) Degrees of nuclear spin relaxation during a given period of time (0.2 to 10 s) for the samples with (C) $\Delta_{\text{SAS}} = 8$ K and (D) $\Delta_{\text{SAS}} = 3$ K. The data are shown in a color scale, where black and yellow correspond to no relaxation and complete relaxation (i.e., thermal equilibrium), respectively. For comparison with the R_{xx} data in (A) and (B), contours of the $\nu_{\text{tot}} = 2$ QH regions ($R_{xx} \approx 0.5$ kilohms) are shown as white solid lines. The gate-voltage ranges explored in (C) and (D) are shown by yellow lines in (A) and (B). Measurement temperature is 66 mK.

bright spots can be clearly distinguished by their extremely fast relaxation and the fact that they appear only at around $v_{\text{tot}} = 2$. The latter indicates that the bright spots reflect the properties of the $v_{\text{tot}} = 2$ QH ground state. On the other hand, the slower relaxation occurs only in the flanks of the QH region (Fig. 2, C and D), indicating that it reflects the properties of quasi-particles created in the QH liquid.

To identify the mechanisms responsible for the two types of nuclear relaxation, we measured the τ dependence of the relaxation and determined the nuclear spin-lattice relaxation rate $1/T_1$ (25–27). In Fig. 3, $1/T_1$ is measured along $v_{\text{tot}} = 2$ as a function of the normalized density imbalance between the two layers $\delta = \delta n/n_{\text{tot}}$. In the $\Delta_{\text{SAS}} = 8$ K sample (Fig. 3A), $1/T_1$ is sharply enhanced for $0.1 < |\delta| < 0.25$. The peak value reaches 5 s^{-1} , which is four orders of magnitude larger than typical values in a 2DES (29). The extremely rapid relaxation signals the development of low-frequency electron-spin fluctuations. We ascribe this to the spin correlation in the CAF state, which allows the spin directions in the plane to fluctuate without costing energy. In contrast to the marked change in $1/T_1$, R_{xx} is virtually vanishing for all values of δ (Fig. 3A). As the phase transitions among the F, CAF, and SS states are expected to be second order (12–17), it is reasonable that the QH effect is preserved across the phase boundaries, so that transport is insensitive to these transitions at low temperatures.

The results for the $\Delta_{\text{SAS}} = 3$ K sample (Fig. 3B), on the other hand, can be understood by noting that the F state consists of two $v = 1$ QH states and that, along $v_{\text{tot}} = 2$, the filling in each layer varies with δ as $v = 1 \pm \delta$. Indeed, if we read δ as $v - 1$ in Fig. 3B, both the $1/T_1$ and R_{xx} data resemble those of a single-layer 2DES around $v = 1$ (24–26). At both flanks of the $v =$

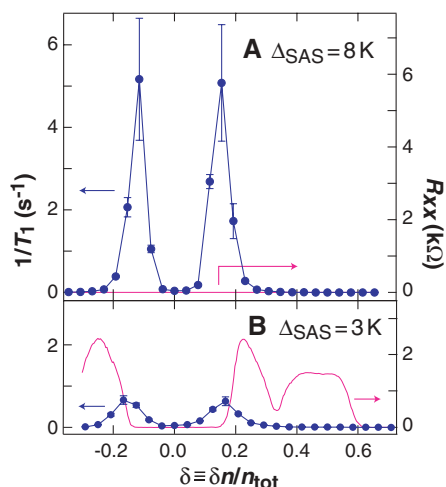


Fig. 3. (A and B) $1/T_1$ (blue circles) and R_{xx} (pink traces) at $v_{\text{tot}} = 2$ of the samples with (A) $\Delta_{\text{SAS}} = 8$ K and (B) $\Delta_{\text{SAS}} = 3$ K as a function of the normalized density imbalance $\delta \equiv \delta n/n_{\text{tot}}$. Temperature is 66 mK.

1 QH state, peaks in $1/T_1$ of the order of 0.1 s^{-1} are known to arise from low-frequency fluctuations associated with spin-textured quasi-particles called skyrmions (30, 31). We emphasize that the results for the $\Delta_{\text{SAS}} = 8$ K sample, where the QH effect is preserved (i.e., with R_{xx} vanishing) when $1/T_1$ peaks, cannot be explained by such single-layer $v = 1$ physics but can only be explained by bilayer $v_{\text{tot}} = 2$ physics, for which the CAF phase is predicted to be induced by density imbalance (16). The peak value of $1/T_1$ we observed for the CAF phase is yet another order of magnitude larger than that for skyrmions, indicating even stronger spin fluctuations.

Evidence for the gapless spin excitation mode, and hence of the CAF ordering, is given by the temperature dependence of $1/T_1$. Plots of $1/T_1$ versus δ for two different temperatures reveal three distinct regions distinguished by different temperature dependence (Fig. 4A). For $|\delta| > 0.25$, $1/T_1$ increases with temperature, consistent with the ground state being spin singlet, where nuclear spins relax through interactions with thermally activated quasi-particles. For $|\delta| < 0.1$, $1/T_1$ is almost independent of temperature (Fig.

4B), limited by spin-textured quasi-particles induced by disorder in the ferromagnetic ground state (32). Between these regions ($0.1 < |\delta| < 0.25$), $1/T_1$ increases with decreasing temperature. Such temperature dependence is unique and allows us to identify this phase, where $1/T_1$ continues to increase without saturation down to the lowest temperature of 66 mK (Fig. 4B). If the spin excitation has a gap, thermal fluctuations and thus $1/T_1$ would decrease as the temperature is reduced below the gap. Hence, the divergent behavior of $1/T_1$ at 66 mK is a hallmark of the gapless Goldstone mode associated with the CAF ordering. We emphasize that the thermal energy at 66 mK is much smaller than the electronic Zeeman energy, $\Delta_z = 1.6$ K at 5.5 T, or the charge excitation gap of the CAF state, $\Delta_{\text{CAF}} = 1.5$ K (at $\delta = 0.15$), obtained from the temperature dependence of R_{xx} (Fig. 4B, inset); this confirms that the QH state with a charge excitation gap and a finite Zeeman energy indeed has a gapless spin excitation mode.

To fully understand the low-temperature divergence of $1/T_1$, it is essential to note the dimensionality of the system; in two dimensions, the phase space for spin waves at low energies is large enough so that there is an infrared divergence in the number of excited magnons at any finite temperature (10). This causes strong low-frequency spin fluctuations, thereby enhancing $1/T_1$. As the temperature is increased, spin waves with higher energies are excited and the characteristic frequency of the spin fluctuation increases. As a result, the spectral density at the nuclear frequency decreases, hence $1/T_1$ decreases. We note that our observation is that of zero-frequency spin fluctuations of the Goldstone mode but not of its dispersion, which is predicted to be linear, reflecting the antiferromagnetic correlations (14). Detailed comparison of the temperature dependence of $1/T_1$ with theory would give information on the dispersion and may also shed light on other phases, such as the Bose glass phase predicted for this system (15).

The observation of the CAF ordering leads us to expect yet another class of phase transition, known as the Kosterlitz-Thouless (KT) transition (33), to take place at a certain critical temperature; the transition is expected for exactly the present system (13, 14), that is, a two-dimensional system with broken planar spin rotational symmetry. In such systems, vortex-like defects appear at finite temperatures, which are confined into pairs of zero net vorticity below a critical temperature T_{KT} , thus allowing for finite spin stiffness and hence the Goldstone mode. However, at T_{KT} , unbinding of vortices causes the spin stiffness to drop discontinuously to zero. Because $1/T_1$ reflects spin correlations, it should be capable of detecting the KT transition. Although our $1/T_1$ data show no criticality as naively expected, the saturation of $1/T_1$ at higher temperatures (>300 mK) may be a possible manifestation (Fig. 4B). This is not

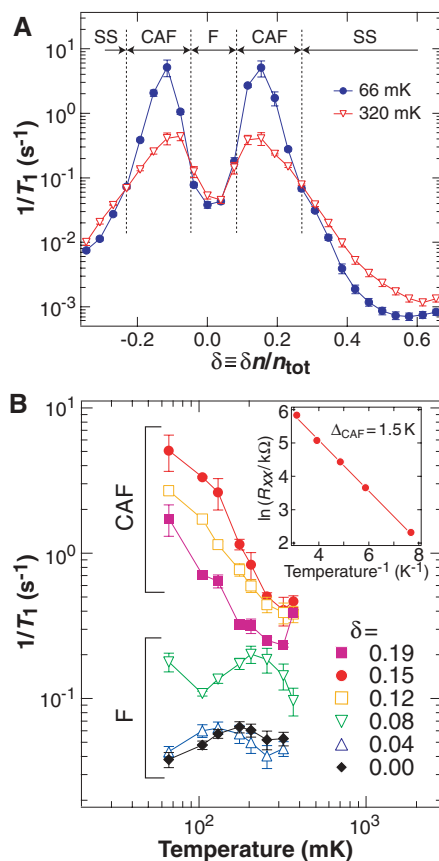


Fig. 4. (A) $1/T_1$ of the $\Delta_{\text{SAS}} = 8$ K sample at $v_{\text{tot}} = 2$ as a function of δ , taken at two different temperatures, 66 mK (solid blue circles) and 320 mK (open red triangles). (B) Temperature dependence of $1/T_1$ at $v_{\text{tot}} = 2$ for several values of δ . (Inset) Arrhenius plot of R_{xx} at $\delta = 0.15$, where $1/T_1$ becomes maximum.

inconsistent with the theoretical prediction of $T_{KT} = 1$ K (13, 14). Further investigations, not only experimental but also theoretical, are necessary to clarify this fundamental issue.

References and Notes

- K. von Klitzing, G. Dorda, M. Pepper, *Phys. Rev. Lett.* **45**, 494 (1980).
- S. L. Sondhi, A. Karlhede, S. A. Kivelson, E. H. Rezayi, *Phys. Rev. B* **47**, 16419 (1993).
- T. Jungwirth, A. H. MacDonald, *Phys. Rev. B* **63**, 035305 (2000).
- D. K. Maude *et al.*, *Phys. Rev. Lett.* **77**, 4604 (1996).
- V. Piazza *et al.*, *Nature* **402**, 638 (1999).
- J. Eom *et al.*, *Science* **289**, 2320 (2000).
- E. P. De Poortere, E. Tutuc, S. J. Papadakis, M. Shayegan, *Science* **290**, 1546 (2000).
- K. Muraki, T. Saku, Y. Hirayama, *Phys. Rev. Lett.* **87**, 196801 (2001).
- J. P. Eisenstein, A. H. MacDonald, *Nature* **432**, 691 (2004).
- S. M. Girvin, *Phys. Today* **53**, 39 (2000).
- P. W. Anderson, *Basic Concepts of Condensed Matter Physics* (Benjamin/Cummings, London, 1984).
- L. Zheng, R. J. Radtke, S. Das Sarma, *Phys. Rev. Lett.* **78**, 2453 (1997).
- S. Das Sarma, S. Sachdev, L. Zheng, *Phys. Rev. Lett.* **79**, 917 (1997).
- S. Das Sarma, S. Sachdev, L. Zheng, *Phys. Rev. B* **58**, 4672 (1998).
- E. Demler, S. Das Sarma, *Phys. Rev. Lett.* **82**, 3895 (1999).
- L. Brey, E. Demler, S. Das Sarma, *Phys. Rev. Lett.* **83**, 168 (1999).
- H. MacDonald, R. Rajaraman, T. Jungwirth, *Phys. Rev. B* **60**, 8817 (1999).
- V. Pellegrini *et al.*, *Phys. Rev. Lett.* **78**, 310 (1997).
- V. Pellegrini *et al.*, *Science* **281**, 799 (1998).
- A. Sawada *et al.*, *Phys. Rev. Lett.* **80**, 4534 (1998).
- A. Fukuda *et al.*, *Phys. Rev. B* **73**, 165304 (2006).
- V. S. Khrapai *et al.*, *Phys. Rev. Lett.* **84**, 725 (2000).
- T. Moriya, *J. Phys. Soc. Jpn.* **18**, 516 (1963).
- R. Tycko, S. E. Barrett, G. Dabbagh, L. N. Pfeiffer, K. W. West, *Science* **268**, 1460 (1995).
- K. Hashimoto, K. Muraki, T. Saku, Y. Hirayama, *Phys. Rev. Lett.* **88**, 176601 (2002).
- N. Kumada, K. Muraki, K. Hashimoto, Y. Hirayama, *Phys. Rev. Lett.* **94**, 096802 (2005).
- See supporting material on Science Online.
- N. Kumada *et al.*, *Phys. Rev. B* **69**, 155319 (2004).
- A. Berg, M. Dobers, R. R. Gerhardt, K. von Klitzing, *Phys. Rev. Lett.* **64**, 2563 (1990).
- R. Côté *et al.*, *Phys. Rev. Lett.* **78**, 4825 (1997).
- A skyrmion is a topological spin texture with a radial variation in the spin direction from down at the center to up at large distances (2, 4).
- Recently, $1/T_1$ increasing with decreasing temperature was reported for a single-layer system around $\nu = 1$, which was claimed to be evidence for skyrmion crystallization (34). We did not observe such behavior in our samples, probably because of the lower mobility.
- J. M. Kosterlitz, D. J. Thouless, *J. Phys. C* **6**, 1181 (1973).
- G. Gervais *et al.*, *Phys. Rev. Lett.* **94**, 196803 (2005).
- We thank T. Saku for growing the heterostructures used in this experiment, and Y. Tokura and K. Takashina for fruitful discussions.

Supporting Online Material

www.sciencemag.org/cgi/content/full/313/5785/329/DC1

Materials and Methods

Fig. S1

References

7 March 2006; accepted 24 May 2006

10.1126/science.1127094

Chemoselective Hydrogenation of Nitro Compounds with Supported Gold Catalysts

Avelino Corma* and Pedro Serna

The selective reduction of a nitro group when other reducing functions are present is a difficult process that often requires stoichiometric amounts of reducing agents or, if H_2 is used, the addition of soluble metals. Gold nanoparticles supported on TiO_2 or Fe_2O_3 catalyzed the chemoselective hydrogenation of functionalized nitroarenes with H_2 under mild reaction conditions that avoided the accumulation of hydroxylamines and their potential exothermic decomposition. These chemoselective hydrogenation gold catalysts also provide a previously unknown route for the synthesis of the industrially relevant cyclohexanone oxime from 1-nitro-1-cyclohexene.

Aromatic amines are generally produced by catalytic hydrogenation of nitro compounds. The reduction of simple nitro compounds is readily carried out with various commercial catalysts, but the selective reduction of a nitro group with H_2 , when other reducible groups are present in the same molecule, is more challenging. Functionalized anilines are industrially important intermediates for pharmaceuticals, polymers, herbicides, and other substances and fine chemicals (1, 2), so there is a strong incentive to develop chemoselective catalysts for the reduction of nitro groups.

Stoichiometric reducing agents such as sodium hydrosulfite (3), iron (2), tin (4), or zinc in ammonium hydroxide (5) have been successfully used to reduce aromatic nitro compounds containing olefinic bonds. However,

these processes are not environmentally sustainable. Cobalt and ruthenium sulfide catalysts can selectively convert nitro compounds into amines in the presence of olefinic groups (6), but the yields are rather low, and sulfur-containing by-products are also formed that strongly limit the usefulness of these catalysts. Other catalytic systems, such as iron complexes (7) or doped Raney nickel (8), are not for general use and entail important practical drawbacks regarding the difficulty for reuse. Transition metal catalysts simultaneously hydrogenate both the nitro and olefinic or carbonyl functions (9), but Siegrist *et al.* (10) and Blaser *et al.* (11) have indeed shown that a catalyst of Pt on C (Pt/C), modified by H_3PO_2 or other low valent phosphorous additives, together with soluble vanadium compounds can be highly selective in apolar solvents. However, Pt-Pb/ $CaCO_3$ catalysts, in the presence of $FeCl_2$ and tetramethylammonium chloride in solution, were shown to be adequate for polar solvents (10). Siegrist *et al.* and Blaser *et al.* have achieved excellent chemoselectivity in

apolar solvents by using the first catalyst and rather lower selectivity with the second type of catalyst and polar solvents. Although these catalytic systems are effective, catalyst preparation often remains critical, and the amount of the modifying agent must be precisely controlled (7). Moreover, the control of the Pt activity needed to improve the selectivity of the reaction produces an unavoidable accumulation of hydroxylamine intermediates, which makes the addition of soluble metal salts compulsory. Alternative heterogeneous catalysts for the chemoselective reduction of nitro groups that do not require soluble metal salts are highly desirable.

Noble metal catalysts can activate nitro groups as well as carbonyl and double bonds, leading to unselective reductions (9). The most common solution to the selectivity problem has been to modify the metal adsorption characteristics by means of surface modifiers. This approach has been taken in the case of carbonyl and double bond hydrogenation by modifying Pt with Sn (12) and CeO_2 (13, 14) or, as described above for nitro groups, by introducing different Pt modifiers. In our case, we have approached the problem by investigating an alternative metal catalyst that directly activates nitro groups preferentially to other competing functional groups.

Gold in the form of nanoparticles is an active redox catalyst for oxygen-containing hydrocarbons, such as alcohols and carbonyls, but does not interact with olefinic groups (15, 16). For reduction, gold can hydrogenate, although at different rates, alkenes, alkynes, imines, and carbonyls (19, 20) in the presence of H_2 . Gold exhibits some selectivity for the hydrogenation of C=O groups of α , β -unsaturated aldehydes, producing allyl-type unsaturated alcohols (21–23). Because Pt and Pd are not chemoselective catalysts for the reduction of nitro groups

Instituto de Tecnología Química, Universidad Politécnica de Valencia—Consejo Superior de Investigaciones Científicas, Avenida los Naranjos, s/n, 46022 Valencia, Spain.

*To whom correspondence should be addressed. E-mail: acorma@itq.upv.es

and because olefins and NO_2 adsorb differently on Pt and Pd than on Au (24), we explored gold as a potential chemoselective catalyst for the reduction of nitro compounds in the presence of other reducible functional groups.

Two supported gold catalysts [1.5 weight percent (wt %) Au/TiO₂ and 4.5 wt % Au/Fe₂O₃], as well as Pt-, Pd-, Au-Pt-, and Au-Pd-supported catalysts were used (25) for the hydrogenation of 3-nitrostyrene with H₂ under mild reaction conditions (9 bar, 120°C). The results (Table 1) show that neither the Pt, Pd, Au-Pd, nor Au-Pt catalysts were selective for this reaction. However, the two supported gold catalysts gave conversions >98% with 96% selectivity to 3-vinylaniline, whereas the residual product was 3-ethylaniline (26). The evolution of the reaction products when Au/TiO₂ and Au/Fe₂O₃ are used as catalysts for the hydrogenation of 3-nitrostyrene (Fig. 1) shows only traces of hydroxylamine styrene, azostyrene, and azoxystyrene. These low levels are desirable, because the accumulated hydroxylamines can undergo exothermic decomposition; their toxicity and ability to form colored condensation products lead to reductions in quality (11). Results (fig. S2) show that hydroxylamines derivatives are also avoided for multiple turnovers of the catalyst. Therefore, if the aryl hydroxylamine can be formed on the gold catalysts, it apparently reacts rapidly to give the corresponding aniline, as illustrated in schemes S1 and S2.

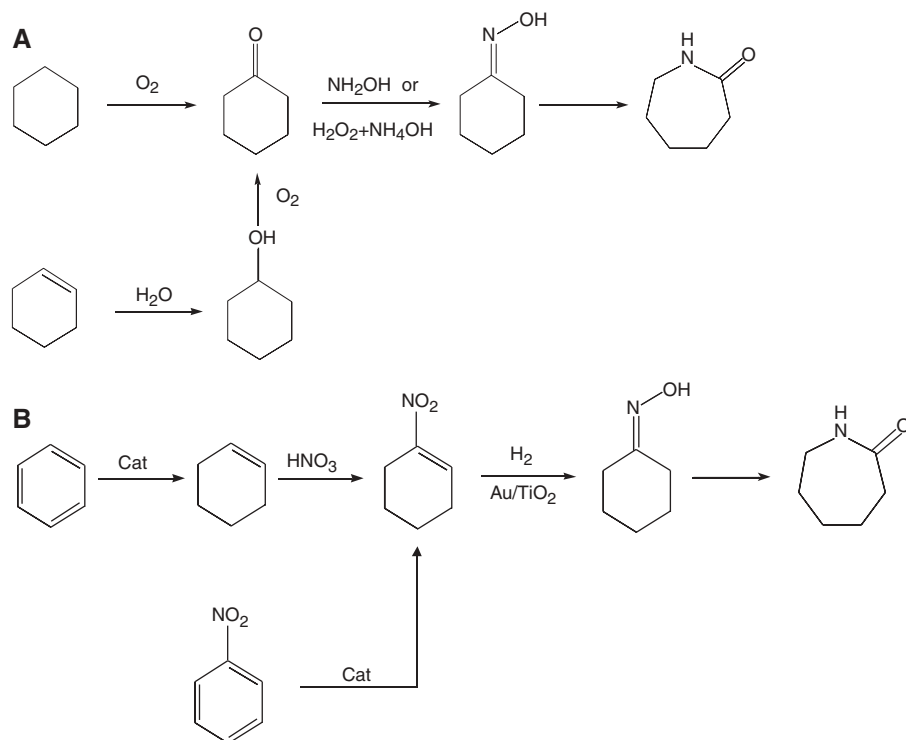
The chemoselectivity reduction of the nitro group in the presence of a carbonyl group has been studied through the hydrogenation of 4-nitrobenzaldehyde. Results (Table 1) show that Au/Fe₂O₃ is an active catalyst for the chemoselective reduction of the nitro group, giving the corresponding aminobenzaldehyde (table S3). In this case, we have detected relatively high amounts of the azoxy intermediate species as a reaction product, but its presence can be reduced below 4 wt % by using TiO₂ as support. The nitrogen mass balances were <90%, probably because of the well-known polymerization of the 4-aminobenzaldehyde, which yields heavier products. However, neither 4-nitrobenzyl alcohol, 4-aminobenzyl alcohol, nor decarboxylated products were detected when supported Au was used as a catalyst. However, when Pt and Pd were tested, the results (Table 1) show that, contrary to the case for Au, the reduction of the nitro group with hydrogen was not chemoselective and large amounts of the products with reduced carbonyl groups were formed (26).

Nitro groups can also be reduced selectively in the presence of nitriles with gold catalysts. Thus, 4-nitrobenzoxime was reduced to the corresponding amine with yields >96%, whereas much lower yields and selectivity (table S4) were obtained with Pt and Pd (Table 1).

Lastly, all of the noble metals studied were chemoselective for the hydrogenation of 4-nitrobenzamide. Nevertheless, the selectivity was still higher in the case of gold catalysts (Table 1).

Table 1. Catalytic results of the chemoselective hydrogenation of nitro groups of aryl compounds (italic type in table) in the presence of several functional groups and for cyclohexanone oxime from 1-nitro-1-cyclohexene. Gold catalysts show notably better behavior for reducing nitro groups without modifying double bonds and carbonyl, nitrile, or amide groups. Pressure (*P*) refers to initial pressure (not isobaric conditions). Conversion was determined by gas chromatography (GC) with the use of *o*-xylene as an internal standard. Products were identified by means of GC-mass spectrometry. *T*, temperature.

Catalysts	% Metal (Mol)	<i>T</i> (°C)	<i>P</i> (bar)	Time (hours)	Conversion (%)	Selectivity (%)
<i>3-Nitrostyrene</i>						
Au/TiO ₂	0.23	120	9	6.00	98.5	95.9
Au/Fe ₂ O ₃	0.39	130	12	9.50	95.2	95.1
Pd/C	0.11	120	9	0.03	99.0	0.0
Pt/C	0.12	120	9	0.03	96.7	2.9
Au-Pd/TiO ₂	0.20	120	9	0.03	99.5	0.0
Au-Pt/TiO ₂	0.31	120	9	0.02	93.0	1.8
<i>4-Nitrobenzaldehyde</i>						
Au/TiO ₂	1.14	100	10	1.25	99.0	96.8
Au/Fe ₂ O ₃	4.30	100	10	1.00	99.4	77.9
Pd/C	0.35	100	10	0.03	92.0	29.8
Pt/C	0.38	100	10	0.03	96.7	68.6
<i>4-Nitrobenzoxime</i>						
Au/TiO ₂	0.60	140	25	1.25	99.0	97.2
Au/Fe ₂ O ₃	1.13	140	25	2.00	99.4	97.1
Pd/C	0.60	140	25	0.42	99.6	79.5
Pt/C	0.60	140	25	0.42	99.4	55.8
<i>4-Nitrobenzamide</i>						
Au/TiO ₂	0.62	120	15	3.00	99.6	97.3
Au/Fe ₂ O ₃	1.86	120	15	2.00	76.6	98.2
Pd/C	1.30	120	15	0.02	99.1	95.2
Pt/C	0.70	120	15	0.02	99.0	94.3
<i>1-Nitro-1-cyclohexene</i>						
Au/TiO ₂	0.27	110	15	0.50	99.6	90.9
Pd/C	0.42	110	15	0.03	69.8	70.6
Pt/C	0.23	110	15	0.03	67.1	52.6



Scheme 1.

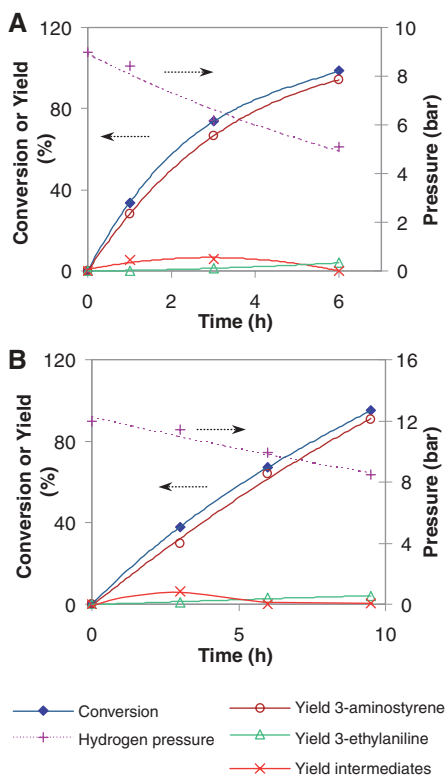


Fig. 1. Kinetic curves for 3-nitrostyrene hydrogenation with (A) Au/TiO₂ and (B) Au/Fe₂O₃ catalysts. Up to nearly 100% of conversion both catalytic systems provide selectivity >95%, avoiding the hydroxylamine accumulation problem (reaction conditions: for Au/TiO₂, 120°C, 9 bar, and 0.23 mol % of Au; for Au/Fe₂O₃, 130°C, 12 bar, and 0.39 mol % of Au). Arrows indicate that the hydrogen pressure curve is referred to the right y axis, and the remaining curves are referred to the left y axis.

Given the excellent chemoselectivity of gold for reducing nitro compounds, we explored this system as an alternative catalytic route for the production of cyclohexanone oxime, an important molecule in the production of ϵ -caprolactame. Cyclohexanone oxime is currently obtained via two different routes (Scheme 1A).

In these processes, hydroxylamine, which is a toxic and unstable product, has to be used or otherwise synthesized in situ by the Sumitomo and ENICHEM procedure. However, the high activity and selectivity of gold catalysts open the possibility for an alternative process that would involve the steps given in Scheme 1B. This process requires a catalyst that selectively hydrogenates 1-nitro-1-cyclohexene into cyclohexanone oxime. Whereas Pt and Pd produce low selectivity even at relatively low levels of conversions, selectivity >90% is achieved at practically 100% conversion with the gold catalysts (Table 1).

References and Notes

- R. S. Dowling, P. J. Kunkeler, H. van Bekkum, *Catal. Today* **37**, 121 (1997).
- M. Suchy, P. Winternitz, M. Zeller, World (WO) Patent 91/00278 (1991).
- F. Kovar, F. E. Armond, U.S. Patent 3,975,444 (1976).
- J. Butera, J. Bagli, WO Patent 91/09023 (1991).
- A. Burawoy, J. P. Critchley, *Tetrahedron* **5**, 340 (1959).
- R. Braden, H. Knupfer, S. Hartung, U.S. Patents 4,002,673 and 4,051,177 (1977).
- M. A. Narendra, O. P. Shivanand, D. R. Madhukar, WO Patent 2005.070.869 (2005).
- W. Gerhar *et al.*, U.S. Patent 6,395,934 (2002).
- P. N. Rylander, *Catalytic Hydrogenation in Organic Synthesis* (Academic Press, New York, 1979), p. 122.
- U. Siegrist, P. Baumeister, H.-U. Blaser, *Catalysis of Organic Reactions*, F. Herkes, Ed., vol. 75 of *Chemical Industries* (Dekker, New York, 1998).
- H.-U. Blaser, U. Siegrist, H. Steiner, in *Aromatic Nitro Compounds: Fine Chemicals through Heterogeneous*

- Catalysis*, R. A. Sheldon, H. van Bekkum, Eds. (Wiley-VCH, Weinheim, Germany, 2001), p. 389.
- E. Janin, *J. Catal.* **215**, 243 (2003).
- P. Concepción, A. Corma, J. Silvestre-Albero, *J. Am. Chem. Soc.* **126**, 5523 (2004).
- A. Sepulveda-Escribano, F. Coloma, F. Rodriguez-Reinoso, *J. Catal.* **178**, 649 (1998).
- A. Abad, P. Concepción, A. Corma, *Angew. Chem. Int. Ed. Engl.* **44**, 4066 (2005).
- A. Corma, M. E. Domine, *Chem. Commun.* **32**, 4042 (2005).
- S. Naito, M. Tanimoto, *J. Chem. Soc. Chem. Commun.* **12**, 832 (1988).
- S. A. Blankenship, A. Rokicki, J. A. Perkins, U.S. Patent 2003.232.719 (2003).
- C. Milone *et al.*, *J. Catal.* **236**, 80 (2005).
- C. González-Arellano, A. Corma, M. Iglesias, *Chem. Commun.* **15**, 3451 (2005).
- P. Claus, *Appl. Catal. Gen.* **291**, 222 (2005).
- J. E. Bailie, G. J. Hutchings, *Chem. Commun.* **21**, 2151 (1999).
- M. Ch. Daniel, D. Astruc, *Chem. Rev.* **104**, 293 (2004).
- X. Lu, X. Xu, N. Wang, *J. Phys. Chem. A* **103**, 10969 (1999).
- Materials and methods are available as supporting material on Science Online.
- Detailed product distributions with the different catalysts are given in tables S1 to S6.
- We thank the World Gold Council for supplying the gold catalysts that were used as well as for the corresponding transmission electron microscopy images and F. Sánchez, M. Iglesias, and C. González-Arellano for useful comments. This work was supported by Ministerio de Educación y Ciencia (grant MAT2003-07945-C02-01).

Supporting Online Material

www.sciencemag.org/cgi/content/full/313/5785/332/DC1
Materials and Methods
SOM Text
Figs. S1 to S3
Tables S1 to S6
Schemes S1 and S2
References

5 April 2006; accepted 7 June 2006
10.1126/science.1128383

A Dielectric Polymer with High Electric Energy Density and Fast Discharge Speed

Baojin Chu,^{1,2} Xin Zhou,³ Kailiang Ren,³ Bret Neese,^{1,2} Minren Lin,² Qing Wang,^{1,2} F. Bauer,⁴ Q. M. Zhang^{1,2,3*}

Dielectric polymers with high dipole density have the potential to achieve very high energy density, which is required in many modern electronics and electric systems. We demonstrate that a very high energy density with fast discharge speed and low loss can be obtained in defect-modified poly(vinylidene fluoride) polymers. This is achieved by combining nonpolar and polar molecular structural changes of the polymer with the proper dielectric constants, to avoid the electric displacement saturation at electric fields well below the breakdown field. The results indicate that a very high dielectric constant may not be desirable to reach a very high energy density.

Dielectric materials are used to control and store charges and electric energies and play a key role in modern electronics and electric power systems. As the requirements

grow for compact, low-cost electronic and electrical power systems, as well as for very high energy and power capacitive storage systems, the development of high power and energy density

dielectric materials becomes a major enabling technology (1–3). For example, high energy density dielectric capacitors would help to reduce the volume, weight, and cost of the electric power system in hybrid electric vehicles.

Among various dielectric materials, polymers are presently the material of choice for energy storage applications because of their relatively high energy density, high electric breakdown field (E_b), low dielectric loss, fast speed, low cost, and graceful failure (i.e., high reliability) (4–6). However, dielectric polymers that are currently used for high energy density capacitors show low (<3) dielectric constants (represented by K). Consequently, the high energy density in the dielectric polymers relies on the high E_b (>500 MV/m). In general, the

¹Materials Science and Engineering Department, ²Materials Research Institute, Pennsylvania State University, University Park, PA 16802, USA. ³Electrical Engineering Department, ⁴Institute Franco-Allemand de Recherches, 5 Rue du General Cassagnou, 68300 Saint-Louis, France.

*To whom correspondence should be addressed. E-mail: qxz1@psu.edu

energy density of a dielectric material (shaded area in Fig. 1A) is equal to the integral $U_e = \int E dD$, where E is the electric field and D is the electric displacement or charge density. Therefore, besides a high E_b , a high D value is another key factor in achieving a high energy density. Furthermore, with a proper K to avoid the electric displacement saturation (D_{sat}) at fields well below E_b (early polarization saturation), an even higher electric energy density can be achieved (Fig. 1B).

In high energy density dielectric polymers that are presently used, the level of D is low. For biaxially oriented polypropylene, which has the highest energy density ($\sim 4 \text{ J/cm}^3$) among the known polymers, D is below 0.012 C/m^2 under a field of 600 MV/m . Conversely, in polymers with high dipole density, D values higher than 0.1 C/m^2 can be achieved, providing the potential of reaching an order of magnitude increase in the energy density (7). One such polar-polymer system is poly(vinylidene fluoride) (PVDF) and its copolymer with trifluoroethylene (TrFE), which is the best known ferroelectric polymer and has been used widely in electro-mechanical sensors and actuators (7–10). We show that, by combining the reversible nonpolar and polar molecular structural changes to realize high D with proper (or matched) K values to avoid the early D -saturation, a very high energy density ($>17 \text{ J/cm}^3$) with fast discharge speed ($<1 \mu\text{s}$) and low dielectric loss can be obtained in defect-modified PVDF polymers.

A typical D - E loop for a P(VDF-TrFE) copolymer is shown (Fig. 2A). Owing to the high dipole density, the polymer displays a D_{sat} of $\sim 0.1 \text{ C/m}^2$. Alternatively, the large remnant polarization in the normal ferroelectric PVDF and its copolymer P(VDF-TrFE) renders a small energy density (shaded area in Fig. 2A). Therefore, besides possessing a high D value, a polymer should also have very small remnant polarization ($D \approx 0$ at zero E), allowing for a large change in D . From the molecular point of view, in the normal ferroelectric phase of PVDF and P(VDF-TrFE), the polymer chains are already in the all-trans conformation (fig. S1A), and an applied field along the original D direction can only induce small changes in D (curve from point A to point B in Fig. 2A), which then lead to low energy density (8, 9).

Recently, we demonstrated that by using defect modifications, the P(VDF-TrFE) copolymer at compositions below VDF/TrFE 70/30 mole percent (mol %) can be converted to a ferroelectric relaxor in which the remnant polarization is near zero and a large change in D can be obtained (11, 12). A D - E loop for a terpolymer of VDF-TrFE-chlorofluoroethylene (CFE) 58.3/34.2/7.5 mol % is presented in Fig. 2A (13, 14); CFE generates random defects in P(VDF-TrFE). Apparently, a much higher electric energy density can be achieved (upper shaded area in Fig. 2A). Integrating the

discharge D - E curve (fig. S2) yields the electric energy density of the terpolymer. The terpolymer exhibits an electric energy density higher than 9 J/cm^3 under 400 MV/m field (Fig. 2B), which is higher than known polymers and other dielectric capacitors (3, 4, 6).

The discharged energy density of the terpolymer (Fig. 2B) increases in an almost linear fashion with E . This relationship contrasts with that of the linear dielectric polymer, in which the electric energy density is proportional to the square of E : $U_e = \frac{1}{2} K \epsilon_0 E^2$, where ϵ_0 is the vacuum permittivity ($\epsilon_0 = 8.85 \times 10^{-12} \text{ F/m}$). Indeed, this is the effect of the early D -saturation in the terpolymer; the material reaches D -saturation at a field much lower than E_b , which reduces the energy density that can be stored in a dielectric material. As a quantitative estimation, we modeled the D -saturation as a reduction of the effective dielectric constant K_{eff} with the field (i.e., $U_e = \frac{1}{2} K_{\text{eff}} \epsilon_0 E^2$). The K_{eff} value was ~ 50 at low fields and decreased with E (Fig. 2B). At 400 MV/m , the terpolymer had a K_{eff} value of ~ 13 .

In this sense, a very high K at low E is not a desirable feature for a dielectric material to

achieve a very high electric energy density. Instead, a K that can maximize the electric energy density (curve II in Fig. 1B) is needed, even though that dielectric constant is lower than that of curve I. A piecewise response in D is used to approximate the real D - E response (Fig. 1B). This simple analysis illustrates the importance of a matched K to maximize the electric energy density.

In the relaxor ferroelectric polymer, the change in molecular conformation between the nonpolar and polar forms at room temperature is associated with the polar-glass transition process, which is accompanied by a broad and high K peak (11, 12, 15). Because the energy difference of PVDF homopolymer between the trans-gauche-trans-gauche' (TGTG') and all-trans conformations is very small, this may be used to generate a large change in D without the penalty of a high K at low E values (16, 17). The TGTG' and all-trans conformations as well as the associated α and β phases are illustrated in fig. S1. Recent simulations have shown that for the single molecular chain, a TGTG' conformation has a lower energy value compared with the all-trans conformation; however, in the crystal-

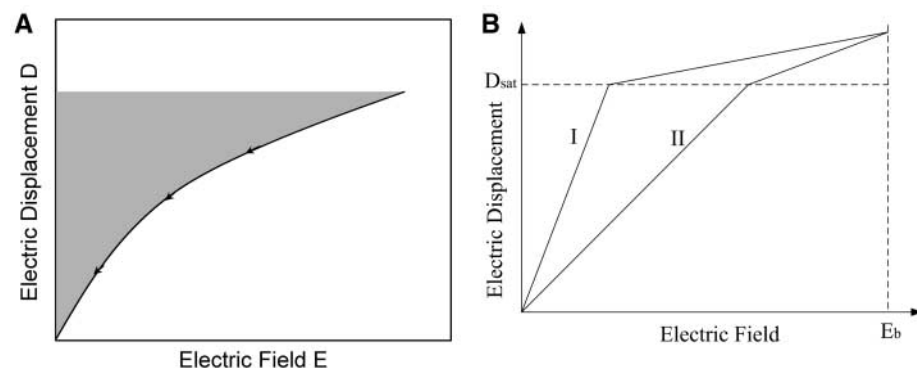


Fig. 1. (A) Schematic illustration of D and discharged energy density (shaded area) with E . Curve with arrows indicates energy release as the field is reduced. (B) Schematic illustration of the effect of K (the slope of D - E curve) on D_{sat} and energy density. The high K value of curve I leads to the early D -saturation and consequently to a lower energy density compared with that of curve II, despite its lower K value.

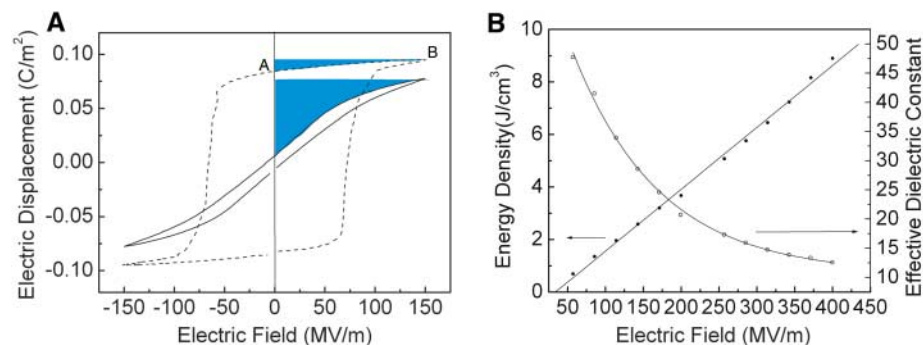


Fig. 2. (A) D - E loops for P(VDF-TrFE) 75/25 mol% (dotted lines) and P(VDF-TrFE-CFE) 58.3/34.2/7.5 mol% (solid lines) measured at 10 Hz. The shaded blue areas indicate the energy density. (B) The discharged energy density measured from the D - E loops and K_{eff} as a function of the field amplitude. The solid curves are drawn to guide eyes.

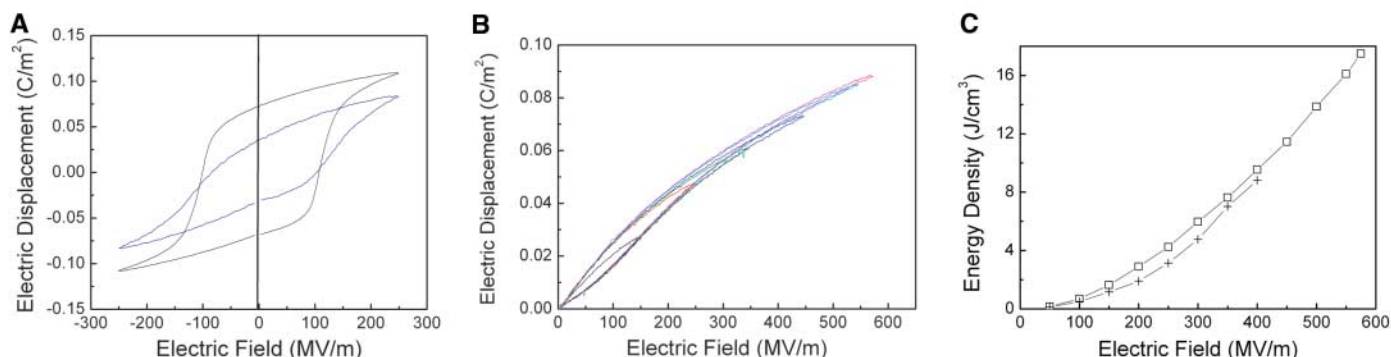


Fig. 3. (A) Comparison of the D - E loops of PVDF (black curves) and P(VDF-CTFE) 91/9 mol% (blue curves) measured at 10 Hz. P(VDF-CTFE) shows much lower remnant polarization even though the film was uniaxially stretched. (B) D - E loops measured under a unipolar E of 10 Hz for P(VDF-CTFE) 91/9 mol%. The different colored curves correspond to D - E loops

measured with different field amplitudes. The conduction contribution was subtracted. (C) The discharged energy density measured from D - E loops under unipolar fields. Open squares, uniaxially stretched films; +, unstretched films. The uniaxially stretched P(VDF-CTFE) films exhibit much higher E_b values compared with unstretched films.

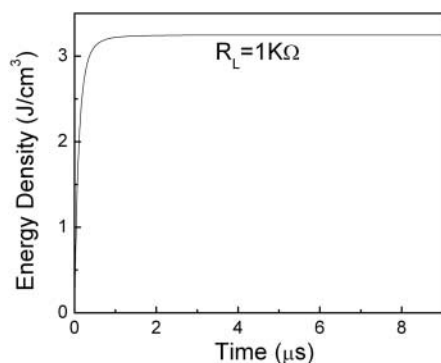


Fig. 4. Discharge energy density as a function of time measured from the direct discharge of the P(VDF-CTFE) polymer films to R_L of 1 kilohm. The E value is 253.5 MV/m.

line phase, the interchain coupling lowers the energy of the all-trans conformation with respect to the TGTG' conformation (17). Therefore, defects that expand the interchain lattice spacing may lower the energy of the TGTG' conformation and achieve a reversible change in conformations between the nonpolar and polar phases. This can also lead to a substantial change in D in the absence of a very high value of K at low E and the early D -saturation.

Based on these considerations, we examined random copolymers of VDF-chlorotrifluoroethylene (CTFE), in which the bulkier size of CTFE compared with VDF may expand the interchain space and distort the crystalline ordering (14). As previously observed for the PVDF homopolymer, the films prepared from the solution cast are in the α phase, whereas, after mechanical stretching, the films are converted to β phase, which is the thermodynamically lower energy phase for PVDF (16, 17). In contrast, both of the films [P(VDF-CTFE) 91/9 mol%, unstretched and uniaxially stretched] exhibited an x-ray pattern of mostly the α phase (fig. S3), indicating that the small amount of bulky CTFE stabilizes the TGTG' confor-

mations and the α phase. In addition, the D - E hysteresis loop, measured from the uniaxially stretched P(VDF-CTFE) 91/9 mol% films, also exhibited much smaller remnant polarization as compared with that of PVDF (Fig. 3A).

The discharged energy density from the films of P(VDF-CTFE) 91/9 mol% was measured by the use of the Sawyer-Tower circuit under unipolar E s of 10 Hz (Fig. 3B) (13, 14). The data indicate that P(VDF-CTFE) 91/9 mol% copolymer does not show D -saturation as seen in the terpolymers (fig. S2A). The discharged energy density as a function of E is presented in Fig. 3C, and the copolymer exhibited an energy density of more than 17 J/cm³ under a field of 575 MV/m. Furthermore, the discharged energy density increased with the square of E , which suggests that, by improving the film quality so that E_b can be further raised to >575 MV/m, a much higher energy density can be achieved ($U_e \propto E^2$). For instance, E_b in the Langmuir-Blodgett films of P(VDF-TrFE) copolymer has been shown to be higher than 1000 MV/m (18).

For many applications to energy storage capacitors, a fast discharge time is required (1, 5, 6). We measured the discharge speed of these copolymer films by using a specially designed, high-speed capacitor discharge circuit in which the discharged energy was measured from a load resistor (R_L) in series with the polymer capacitor (fig. S4). For P(VDF-CTFE) capacitor films of 0.16 nF (measured at low field and 1 kHz) discharging to a 1 kilohm load, the energy discharging time is well below 1 μ s (Fig. 4). As the R_L value changed from 1 to 100 kilohms, the discharge time increased by a factor of 100 (fig. S5). This finding indicates that the discharge time is controlled mainly by the capacitance of the film and external R_L and that the P(VDF-CTFE) copolymer capacitor can have very fast discharge time (<1 μ s). Indeed, the fitting to the voltage change $V(t)$ across the R_L yields the time constant that is nearly the same as that deduced from $R_L C$ (fig. S6), where C is the capacitance. Furthermore,

the discharged energy density does not change greatly when R_L is varied from 1 to 100 kilohms. These results show that the P(VDF-CTFE) copolymer capacitor possesses a low loss. Our demonstrated approach can also be applied to other polymers possessing high dipole density and high D to achieve ultra-high energy density with fast discharge time and low loss.

References and Notes

- H. S. Nalwa, Ed., *Handbook of Low and High Dielectric Constant Materials and Their Applications*, Vol. 2, (Academic Press, New York, 1999).
- Y. Cao, P. C. Irwin, K. Younsi, *IEEE Trans. Dielect. Elect. Insulation* **11**, 797 (2004).
- W. Sarjeant, J. Zirnheld, F. MacDougall, *IEEE Trans. Plasma Sci.* **26**, 1368 (1998).
- W. J. Sarjeant et al., in (1), chap. 9.
- J. H. Tortai, N. Bonifaci, A. Denat, *J. Appl. Phys.* **97**, 053304 (2005).
- M. Rabuffi, G. Picci, *IEEE Trans. Plasma Sci.* **30**, 1939 (2002).
- H. S. Nalwa, Ed., *Ferroelectric Polymers* (Marcel Dekker, New York, 1995).
- A. Lovinger, *Science* **220**, 1115 (1983).
- Q. M. Zhang, V. Bharti, G. Kavarnos, in *The Encyclopedia of Smart Materials*, Vol. 2, M. Schwartz, Ed. (Wiley, New York, 2002).
- T. T. Wang, J. M. Herbert, A. M. Glass, Eds., *The Applications of Ferroelectric Polymers* (Blackie, Glasgow, 1988).
- Q. M. Zhang, V. Bharti, X. Zhao, *Science* **280**, 2101 (1998).
- Q. M. Zhang, C. Huang, F. Xia, J. Su, in *Electroactive Polymer Actuators as Artificial Muscles*, Y. Bar-Cohen, Ed. (SPIE Press, Bellingham, WA, 2004), chap. 4.
- J. K. Sinha, *J. Sci. Instrum.* **42**, 696 (1965).
- Materials and methods are available as supporting material on Science Online.
- V. Bobnar et al., *Macromolecules* **36**, 4436 (2003).
- R. G. Kepler, in (7), chap. 3.
- H. Su, A. Strachan, W. Goddard III, *Phys. Rev.* **B70**, 064101 (2004).
- A. V. Bune et al., *Nature* **391**, 874 (1998).
- This work was supported by the Office of Naval Research under grant numbers N00014-05-1-0455 and N00014-05-1-0541. We thank 3M for supplying P(VDF-CTFE) and PVDF powders used in this investigation.

Supporting Online Material

www.sciencemag.org/cgi/content/full/313/5785/334/DC1
Materials and Methods
Figs. S1 to S6
References

23 March 2006; accepted 13 June 2006
10.1126/science.1127798

Cell-Directed Assembly of Lipid-Silica Nanostructures Providing Extended Cell Viability

Helen K. Baca,¹ Carlee Ashley,¹ Eric Carnes,¹ Deanna Lopez,¹ Jeb Flemming,² Darren Dunphy,² Seema Singh,² Zhu Chen,¹ Nanguo Liu,³ Hongyou Fan,² Gabriel P. López,¹ Susan M. Brozik,² Margaret Werner-Washburne,⁴ C. Jeffrey Brinker^{1,2,5*}

Amphiphilic phospholipids were used to direct the formation of biocompatible, uniform silica nanostructures in the presence of *Saccharomyces cerevisiae* and bacterial cell lines. The cell surfaces organize multilayered phospholipid vesicles that interface coherently with the silica host and help relieve drying stresses that develop with conventional templates. These host structures maintain cell accessibility, addressability, and viability in the absence of buffer or an external fluidic architecture. The cell surfaces are accessible and can be used to localize added proteins, plasmids, and nanocrystals. Prolonged cell viability combined with reporter protein expression enabled stand-alone cell-based sensing.

Living cells combine molecular recognition, amplification, and signal transduction in an extremely small “package,” making them ideally suited for miniaturized, stand-alone, environmental or physiological sensors. However, cellular integration into devices is problematic. Cells require functional bio/inorganic interfaces, benign synthesis conditions (1–3), and external fluidic support systems or immersion in buffer to avoid dehydration. Furthermore, as recently noted by Zhang (4), it is necessary to move beyond two-dimensional (2D) adhesion in dishes to 3D architectures that better represent the extracellular matrix, enabling cells to be surrounded by other cells, maintaining fluidic accessibility, and allowing development of 3D molecular or chemical gradients.

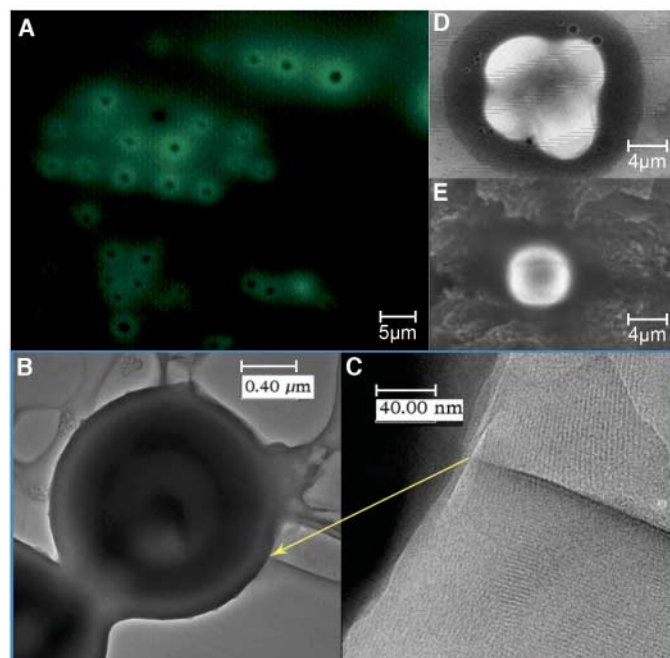
Although 3D cell immobilization in silica gels has been practiced for more than 15 years (5–12), shrinkage during drying creates stress in the silica network that causes cell lysis (13), and the nonuniform pore size leads to loss of fluidic connectivity (large pores dry out and isolate small water-filled pores). More specialized chemical vapor deposition and freeze-drying methods are effective in incorporating cells in silicate gels designed to avoid host-immune reactions or serve as bioreactors, but they also require maintenance in buffer or high humidity (14). Similar problems are encountered in other gel and polymer immobilization schemes, precluding their extended use under desiccating conditions. None of the approaches to date provide for bio/nano interfaces with 3D spatial control of structure and composition,

now recognized as important to the maintenance of natural cellular behavior patterns (15).

We have adapted our evaporation-induced self-assembly (EISA) approach (16) to incorporate cells in a uniform, biocompatible silica nanostructure, using standard unit operations like spin- or dip-coating, ink-jet printing, or molding [fig. S1 (17)]. In this case, the nanostructured host, composed of nanometer-scale channels with a narrow size distribution, prevents extensive drying and associated stresses (18, 19) and maintains 3D fluidic connectivity. The evaporation-driven immobilization procedures also allow facile cellular integration into devices.

Fig. 1. *S. cerevisiae* organize a lipid-rich shell that interfaces coherently with the surrounding nanostructured silica host.

(A) Confocal fluorescence image of immobilized cells with 1% substitution of the fluorescently labeled lipid analog, 1-hexanoyl-2-[6-[(7-nitro-2-1,3-benzoxadiazol-4-yl)amino]hexanoyl]-sn-glycero-3-phosphocholine (*diC₆PC-NBD*). Brighter areas indicate preferential concentration of lipid around cells compared to the surrounding lipid/silica host matrix. (B and C) TEM images of cell immobilized within nanostructured lipid/silica matrix by spin-coating directly on holey carbon-coated copper grid. (D and E) SEM of cells immobilized in silica host prepared with (D) and without (E) lipids. The dark region around the cells in (D) corresponds to an area of high carbon/phosphorus concentration consistent with the presence of lipids (fig S2). In (E), the dark region is a crevice. Cells are firmly immobilized only when the lipid interface is present. In the absence of lipid, cell washout occurs and film cracking is prevalent.



As we have shown using in situ grazing incidence small-angle x-ray scattering (GISAXS) (20), during EISA, solvent evaporation (typically water-ethanol) concentrates the dissolved silica and surfactant, which causes micelles to form and progressively assemble into 3D silica-surfactant mesophases. However, surfactants used to date in EISA, and more generally in templated mesoporous silicas (21), are detergent monomers that insert into cell membranes and lead to their solubilization, inducing rapid cell death. Thus, we replaced standard surfactants with phospholipids, which are integral components of the cell membrane. Through extensive GISAXS and cell-viability studies, we identified diacylphosphatidylcholines (*diC_nPC*), with zwitterionic head groups and short, double acyl tails ($n = 6$ to 10), as having minimal disruptive electrostatic interactions with cell membranes and as being water soluble with sufficiently small critical packing parameters g (22–24) to direct the formation of high-curvature 3D (hexagonal or cubic) lipid-silica mesophases. [For details on lipid-directed assembly of silica mesophases, see (17).]

Using *diC_nPC* as a structure-directing agent, we find that increasing *diC_nPC*/silica ratios cause the final silica mesostructure to progress from wormlike to hexagonal to cubic to lamellar phases in a manner similar to that reported by us previously for standard surfactants (25). However, the addition of stationary-phase *Saccharomyces cerevisiae* at concentrations >10 wt% markedly alters the lipid-silica self-assembly pathway in several respects. Laser-scanning confocal imaging

¹Department of Chemical and Nuclear Engineering, University of New Mexico, ²Sandia National Laboratories, Albuquerque, NM 87185, USA. ³Los Alamos National Laboratory, Chemistry Division, Los Alamos, NM 87545, USA. ⁴Department of Biology, ⁵Department of Molecular Genetics and Microbiology, University of New Mexico, Albuquerque, NM 87131, USA.

*To whom correspondence should be addressed. E-mail: cjbrink@sandia.gov

of systems prepared with 1% substitution of a fluorescently labeled lipid analog showed that, during EISA, cells rapidly organized around themselves a lipid-rich shell with nearly uniform

thickness of $\sim 2 \mu\text{m}$ (Fig. 1A). Elemental mapping indicated that this shell largely excludes silica (fig. S2) (17), and fluorescence recovery after photo-bleaching (FRAP) experiments show

that this lipid-rich region remains fluid for several hours after the EISA process. Corresponding FRAP experiments performed on the surrounding host matrix, where the lipid is confined within a partially solidified silica nanostructure, show no measurable fluorescence recovery.

Direct transmission electron microscopy (TEM) imaging and scanning electron microscopy (SEM) (Fig. 1, B to E) show that the lipid

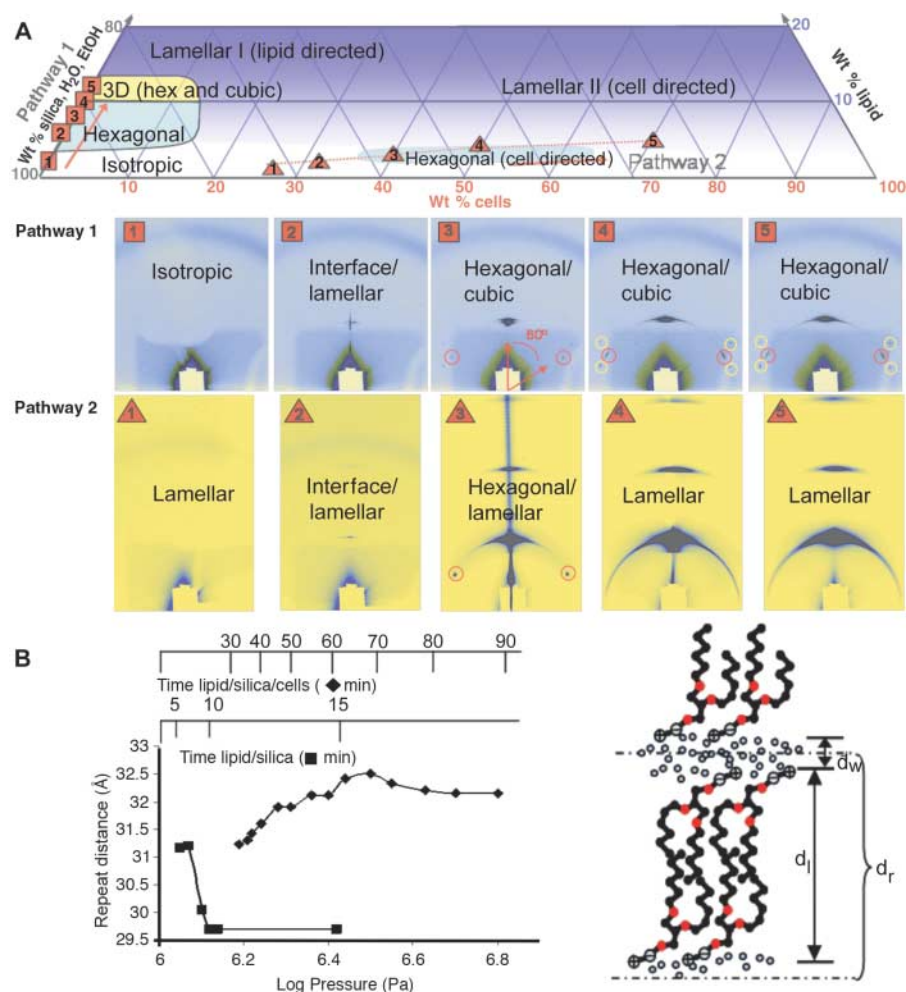


Fig. 2. Structural development in systems containing cells and cell surrogates. (A) Compositional space for lipid-directed (red squares, Pathway 1) and cell-directed assembly (red triangles, Pathway 2) with time-resolved GISAXS images showing structure development for the evolving systems. Films were cast remotely in a humidity-controlled chamber and probed in a horizontal geometry. Weight loss during solvent evaporation was measured to relate structural evolution to film composition. The evaporation-induced compositional trajectories are mapped onto a ternary diagram with vertices representing the weight percent of aqueous silica/solvent, lipid, and wet cells in the system. During lipid-directed assembly (Pathway 1), the film is initially isotropic (panel 1), with the first sign of order appearing as a Bragg reflection in the specular direction (panel 2), representing short-range lamellar ordering parallel to the substrate surface. This phase, which typically nucleates at the vapor/liquid interface, disappears as Bragg spots with sixfold symmetry appear, indicating the presence of a bulk 2D hexagonal phase (panel 3). The final phase is a mixture of 2D hexagonal and other 3D phases (panels 4 and 5). With cell-directed assembly (Pathway 2), the film is again initially isotropic (panel 1). A lamellar phase appears in panel 2 and persists throughout the self-assembly process (panels 3 to 5). The hexagonal phase in panel 3 disappears, and the end point is a global lamellar phase. (B) Progression of repeat distance for systems during EISA as a function of time and evolving osmotic pressure for lipid-silica (■) and lipid-silica-cell systems (◆). The repeat distance (d_r) is measured from in situ 2D GISAXS images with Bragg reflections in the specular direction. It includes the fluid interbilayer space (d_w) and the lipid bilayer (d_l) and is initially the same (31 Å) in the lamellar phase that forms first in both systems. We propose that with cells, the increase in repeat distance results from an increasing lipid bilayer thickness due to reduced interdigitation and lipid reorientation. Osmotic pressure Π is calculated from the concentration of all osmolytes [according to $\Pi = cRT$, where c is concentration ($\text{mol}\cdot\text{m}^{-3}$), R is the gas constant ($\text{J}\cdot\text{K}^{-1}\cdot\text{mol}^{-1}$), and T is temperature (K)] in the bulk solution, as determined from in situ gravimetric analysis of the evaporating system.

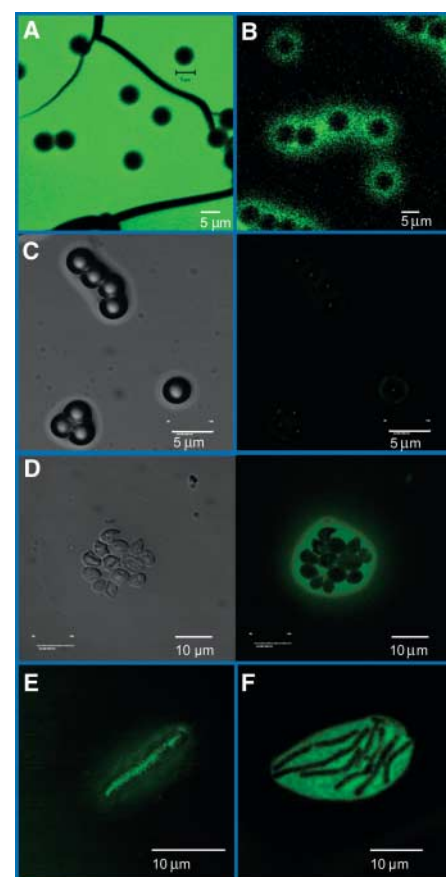


Fig. 3. Chemical gradient development during cell-directed assembly. (A) Fluorescently labeled lipid added with neutral latex beads (compare to Fig. 1A). Lipid is dispersed evenly throughout the sol, with no aggregation at the surface, consistent with the observation that uncharged beads have no influence on self-assembly. (B) Lipid aggregates inhomogeneously at the surface of charged beads, indicating that electrostatic interactions promote lipid accumulation. (C) Differential interference contrast (DIC) (left) and fluorescence images (right) of negatively charged beads with 2',7'-difluorofluorescein (Oregon Green 488) added during EISA. The DIC images locate the beads, whereas the fluorescence reports the local pH. The uniform low fluorescence corresponds to the pH observed for lipid/silica systems (D) far from the cells. (D) Lipid-silica system with *S. cerevisiae*. The bulk pH (dark area) is ~ 3 , whereas the local pH surrounding the cells is ~ 5 to 6. (E) Fluorescently labeled lipid aggregates at surface of *Bacillus subtilis*. (F) *B. subtilis* mediates local pH in a manner similar to that of *S. cerevisiae*.

shell maintains a coherent interface between the cell and the adjoining silica nanostructure that withstands drying and evacuation to 10^{-8} Pa during electron imaging while preserving cell viability (26). By comparison, *S. cerevisiae*-silica films prepared identically, but without lipid, develop macroscopic cavities (Fig. 1E) around the cells because of drying stresses. Such stresses are absent in the corresponding lipid-containing systems [see (17) and discussion below].

In addition to locally modifying their environments, *S. cerevisiae* globally alter the sequence of mesophase development during EISA. By performing in situ 2D GISAXS experiments on evaporating lipid-silica films with and without *S. cerevisiae* (17), we determined that a system that would ultimately form a 3D hexagonal/cubic mesophase prepared without yeast (Fig. 2A, pathway 1) evolves from an isotropic phase through intermediate lamellar and mixed lamellar/2D hexagonal mesophases to a final lamellar mesophase (Fig. 2A, pathway 2) when prepared with 27 wt% wet cells.

Although the mesophases are oriented with respect to the substrate surface in both cases, the repeat distances of the evolving mesophases differ markedly (Fig. 2B). With cells present, the *d*-spacing normal to the substrate increases throughout the course of EISA. This behavior is contrary to that observed generally in EISA (20) and specifically here in the system without cells, where dehydration and silica condensation cause a decrease in *d*-spacing.

These cellular influences on inorganic self-assembly can be contrasted with the situation when spherical colloidal particles are added to surfactant-silica systems—these particles have no influence on self-assembly (27). Unlike latex beads, cells are active colloids, where the cell wall is a dynamic structure, actively maintained by the living cell (28, 29) and capable of sensing and responding to its environment. We compared structural and chemical development in systems

containing yeast to surrogate systems in which cells were replaced with comparable volume fractions of uncharged or negatively charged latex beads. Confocal fluorescence images show that while cells accumulate a coherent lipid interface (Fig. 1A), no lipid aggregation occurs around the neutral bead surface (Fig. 3A). Lipid aggregation around negatively charged beads, although less homogeneous (Fig. 3B), implies that electrostatic interactions are responsible in part for forming the lipid-rich interface in cell-containing systems.

More pronounced are distinctions noted when probing local chemical effects. Fluorescence imaging of systems containing uncharged or negatively charged beads and an impermeant pH-sensitive dye shows that the film has a uniform pH of ~ 3 , attributed to the acidity of the silanol-terminated silica surface (Fig. 3C). In contrast, with cell-containing films, we observe a local pH of 5 to 6 at the cell surface that decreases to about 3 to 4, corresponding to the nanostructured silica matrix, at a distance of several micrometers (Fig. 3D). Time-resolved studies indicate that these very different pH conditions are maintained throughout the course of EISA.

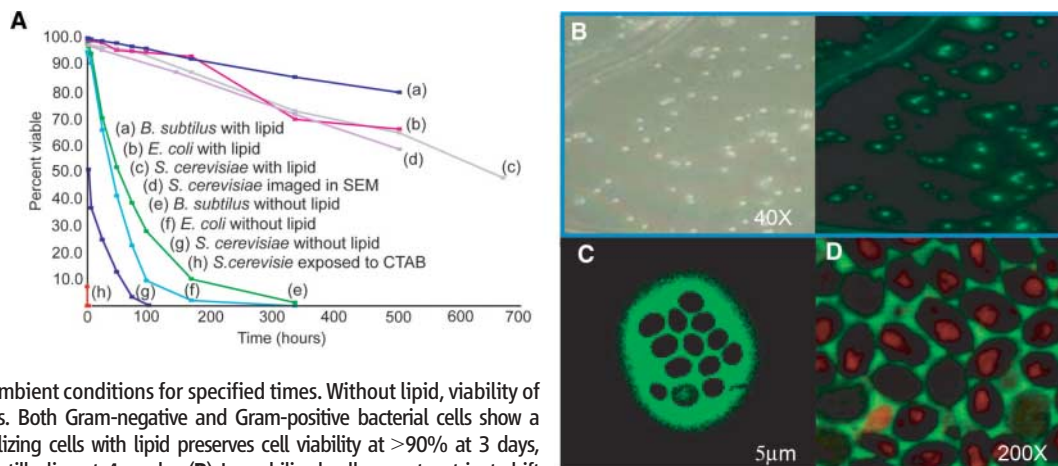
We rationalize the cell's influence on its local and global environments by considering its response to the evolving chemical and physical conditions of EISA. As solvent evaporates, the concentration of osmolytes in the system increases. Unlike latex beads, stationary-phase cells can release up to 35% of their cellular water volume (30) in response to a change in turgor pressure in the cell membrane, which would increase the volume of water in the surrounding lipid shell of ~ 2 - μm thickness by more than 60%. The resulting pH gradient that develops around the cell in turn affects both the local lipid interface and the host lipid/silica matrix.

The pH of ~ 5 in the immediate vicinity of the cell facilitates adsorption of a lipid layer on the cell surface; both $d1C_n$ PC and the cell wall are near their isoelectric points, where comple-

mentary interactions between dipoles on the lipid head group, and discrete positive and negative surface charges, will be enhanced (fig. S3) (17). Dipole-dipole interactions between head groups, and van der Waals interactions between alkane tails, promote the further aggregation of lipid bilayers into the ordered lamellar structure that appears rapidly in the sequence of GISAXS patterns (Fig. 2A). Far from the cells, a bulk 2D hexagonal phase develops on a longer time scale commensurate with that of the EISA process. This initial hexagonal phase (Fig. 2A, pathway 2, panel 3) is transient. During the later stages of EISA, it disappears through transformation to a lamellar mesophase with *d*-spacing corresponding to that of the lipid bilayers. Based on the coherent, seamless nature of the lipid-silica interface (Fig. 1), we suppose that the transformation initiates at this lipid interface because of charge matching with the high density of dipoles on the PC bilayers, and proceeds through the bulk system, giving the final global lamellar mesophase seen in Fig. 2A, pathway 2.

The pH gradient also determines the extent of silica incorporation in the lipid interface and the dimensional scale of the self-assembling lipid and silica nanostructures. The higher pH in the vicinity of the cell greatly enhances the silica condensation rate there and provides a kinetic barrier to diffusion of silica oligomers that effectively excludes silica from the immediate lipid-rich environment of the cell [see quantitative elemental analysis, fig. S2 (17)]. Based on combined in situ GISAXS and gravimetric analyses, we plot in Fig. 2B the measured repeat distance of the nanostructure as it varies with time and developing osmotic pressure during EISA. For lipid-silica systems without cells, EISA proceeds with a progressive reduction in *d*-spacing resulting from dehydration and silica condensation. However, for films containing cells, *d* increases both by expulsion of water

Fig. 4. (A) Viability of stationary-phase cells immobilized with and without lipid. Viability of *S. cerevisiae* is assessed with a two-color fluorescent probe that is incorporated into cellular intravacuolar structures by metabolically active cells. The dye undergoes an adenosine 5'-triphosphate-dependent change in fluorescence from green to red as it is transported from the cytosol to vacuoles. Bacterial cell viability is measured by means of a nucleic acid stain. Films are exposed to the buffered probe after aging at ambient conditions for specified times. Without lipid, viability of *S. cerevisiae* drops to 50% at 2 hours. Both Gram-negative and Gram-positive bacterial cells show a similar rapid drop in viability. Immobilizing cells with lipid preserves cell viability at $>90\%$ at 3 days, with more than 50% of *S. cerevisiae* still alive at 4 weeks. **(B)** Immobilized cells report nutrient shift through GFP expression after film-drying times of 24 hours. DIC image (left) identifies cell location, and fluorescence image (right) shows GFP expression by viable cells. **(C)** Optically labeled (2% NBD label) lipid-coated gold nanocrystals are concentrated at the cell surface after 6 hours while maintaining viability. **(D)** Lipid-coated CdSe nanocrystals are rapidly concentrated at the cell surface and internalized at 24 hours, as noted by red fluorescence from within cells. Labeled lipid (green, $d1C_6$ PC-NBD) concentrates around the cell.



from the cells, which helps maintain the interbilayer thickness (d_w in Fig. 2B), and through an increase in the bilayer thickness (d_l in Fig. 2B). d_l increases because the higher local pH deprotonates lipid head groups, which decreases their optimal surface area. To avoid water contact at the head group/hydrocarbon interface, lipid tails reorient toward configurations more normal to the interfacial planes (31, 32).

In addition to chemical stresses, we anticipated that the immobilized cells could sense and respond to mechanical stresses that arise during drying and condensation of the inorganic network (and are known to cause cell lysis in other immobilization schemes). However, as shown in fig. S4 (17), where we plot biaxial stress measured in situ using a cantilever beam, cell-directed assembly proceeds at a state of nearly zero stress, which likely accounts for its unusual biocompatibility (see discussion below). In comparison, without cells, and without cells and lipid, drying-induced shrinkage creates biaxial tensile stresses. This difference is attributed in part to the lamellar nanostructure that mechanically decouples each successive layer in the direction normal to the substrate surface. Stress may also be mitigated by the compensatory effects of water production and increased d -spacing resulting from the cell's response to hyperosmotic stress.

The cell-directed assembly process we describe creates a highly biocompatible environment for immobilized cells. Using live-dead viability probes, we determined the viability of cells maintained without buffer at ambient temperature and humidity. We compare results for cells immobilized by using cell-directed assembly to systems containing silica alone or silica plus a standard surfactant in Fig. 4A. Immobilized within silica alone, >50% of *S. cerevisiae* cells were dead within 2 hours, whereas exposure to a typical detergent resulted in immediate cell death. In comparison, >50% of the cells were viable after 4 weeks when immobilized in lipid-silica hosts. Even after SEM imaging, 60% of the cells were viable at 3 weeks.

The phospholipid interface contributes to this enhanced cell viability in several other ways. It minimizes cytotoxic electrostatic and hydrogen bonding interactions between the silica host and cell surface phospholipids (33). The zwitterionic PC head groups also avoid strong electrostatic binding interactions with the cell that are typical of positively charged surfactants, such as cetyltrimethylammonium bromide (CTAB), which immediately lyse the cell membrane (Fig. 4A). Wedge-shaped surfactants in general, including short-chained d_iC_n PCs, will distribute into the outer leaflet of the cell membrane, inducing tension and causing eventual destabilization (34). During cell-directed assembly, however, the immediate incorporation of lipids in a multilamellar mesophase reduces the concentration of monomers in the vicinity of the cell available for insertion. Finally, as confirmed by weight-loss

measurements and in situ attenuated total reflection Fourier transform infrared (ATR-FTIR) spectroscopy, the hygroscopic nature of the PC lipids and their organization into a uniform nanostructure serve to suppress overall water loss, allowing the cell to be maintained in a fluid, water-rich microenvironment.

We used *S. cerevisiae* as a model eukaryotic sensor based on reporter protein expression. Yeast cells were genetically modified with plasmids designed to express green fluorescent protein (GFP) regulated by the *GAL1* promoter (35) and immobilized by cell-directed assembly. Although previously reported induction of GFP expression in immobilized *Escherichia coli* required short film-drying times of 40 min or less to prevent cell inactivation (5, 13), we induced GFP expression in response to a glucose-to-galactose nutrient shift in films that were exposed to dry, ambient conditions for >24 hours (Fig. 4B). For samples provided to an external collaborator, GFP expression was induced in immobilized cells stored dry for >6 months at 4°C (36). Hyperspectral imaging (37) of GFP expression in immobilized cells confirmed the potential for use in array technologies and individual addressability of cells.

Variations in both cell surface characteristics and the cellular response to osmotic stress could cause the cell-directed assembly process to be cell-specific. However, Fig. 3, E and F, show that for Gram-positive bacterium *Bacillus subtilis*, both lipid aggregation and pH mediation occur in a manner similar to that for *S. cerevisiae*. In addition, Fig. 4A shows comparable levels of viability for *S. cerevisiae*, *B. subtilis*, and Gram-negative bacterium *E. coli*.

These scaffolds formed through cell-directed assembly also allow construction of hierarchical structures in which additional components are selectively localized at the cell surfaces (fig. S5). Confocal microscopy of systems containing fluorescently labeled bovine serum albumin, or the transmembrane protein bacteriorhodopsin (fig. S5) (17), demonstrate the selective incorporation of proteins in the naturally fluidic lipid environment surrounding *S. cerevisiae*. Retention of protein conformation, a challenge in localizing transmembrane proteins, may be assisted by modulation of interface fluidity and curvature through variation of lipid chain length and incorporation of fatty acids or cholesterol into the bilayers. For *E. coli* systems that incorporate plasmid vectors designed for GFP expression, plasmid localization at the cell interface enables highly efficient transformation and reporter protein expression (fig. S5) (17). Finally, Fig. 4, C and D, show immobilized cells prepared with lipid-stabilized Au or CdSe nanocrystals (38). The nanocrystals are rapidly organized at the cell surface and mainly internalized after 24 hours.

References and Notes

1. M. Tirrell, E. Kokkoli, M. Biesalski, *Surf. Sci.* **500**, 61 (2002).
2. R. Langer, D. A. Tirrell, *Nature* **428**, 487 (2004).

3. R. F. Service, *Science* **297**, 962 (2002).
4. S. G. Zhang, *Nat. Biotechnol.* **22**, 151 (2004).
5. J. R. Premkumar *et al.*, *Chem. Mater.* **14**, 2676 (2002).
6. E. Pope, *J. Sol-Gel Sci. Technol.* **4**, 225 (1995).
7. S. Y. Chia, J. Urano, F. Tamanoi, B. Dunn, J. I. Zink, *J. Am. Chem. Soc.* **122**, 6488 (2000).
8. N. Nassif *et al.*, *Nat. Mater.* **1**, 42 (2002).
9. A. Coiffier, T. Coradin, C. Roux, O. M. M. Bouvet, J. Livaige, *J. Mater. Chem.* **11**, 2039 (2001).
10. J. F. T. Conroy *et al.*, *J. Sol-Gel Sci. Technol.* **18**, 269 (2000).
11. I. Gill, A. Ballesteros, *J. Am. Chem. Soc.* **120**, 8587 (1998).
12. L. Inama, S. Dire, C. G. A. Cavazza, *J. Biotechnol.* **30**, 197 (1993).
13. M. L. Ferrer, L. Yuste, F. Rojo, F. del Monte, *Chem. Mater.* **15**, 3614 (2003).
14. H. Bottcher, U. Soltmann, M. Mertig, W. Pompe, *J. Mater. Chem.* **14**, 2176 (2004).
15. M. Stevens, *Science* **310**, 1135 (2005).
16. C. Brinker, Y. Lu, A. Sellinger, H. Fan, *Adv. Mater.* **11**, 579 (1999).
17. Materials, methods, and supporting material are available on Science Online.
18. Above several % relative humidity, hydrophilic channels <5 nm in diameter remain fully saturated.
19. A. P. Malanoski, F. van Swol, *Phys. Rev. E* **66**, 041602 (2002).
20. D. A. Doshi *et al.*, *J. Am. Chem. Soc.* **125**, 11646 (2003).
21. C. Kresge, M. Leonowicz, W. Roth, J. Vartuli, J. Beck, *Nature* **359**, 710 (1992).
22. The packing parameter $g = [v/(a-l)]$ describes the geometric packing of amphiphilic molecules as a function of their head-group area (a), hydrocarbon chain volume (v), and critical chain length (l) and predicts the structures they form. For double-chained lipids, the glycerol backbone extends in the direction of the head-group chain, displacing the relative length of the two acyl chains by about three methylene groups and requiring a correction in l of $\sim 4 \text{ \AA}$.
23. J. Israelachvili, *Intermolecular and Surface Forces* (Academic Press, San Diego, ed. 2, 1992).
24. J. H. Kleinschmidt, L. K. Tamm, *Biophys. J.* **83**, 994 (2002).
25. Y. F. Lu *et al.*, *Nature* **389**, 364 (1997).
26. For TEM imaging, lipid/silica/cell systems were spin-coated directly on a holey carbon-coated copper grid without fixative treatment for simultaneous visualization of cells and silica. Cell viability was assessed for cells exposed to 20 μA at 1 kV and 10^{-8} -Pa vacuum for 5 min during SEM imaging.
27. P. Yang *et al.*, *Science* **282**, 2244 (1998).
28. F. Klis, M. P. K. Hellingwerf, S. Brul, *FEMS Microbiol. Rev.* **26**, 239 (2002).
29. G. Smits, J. Kapteyn, H. van den Ende, F. Klis, *Curr. Opin. Microbiol.* **2**, 348 (1999).
30. I. M. deMaranon, P. A. Marechal, P. Gervais, *Biochem. Biophys. Res. Commun.* **227**, 519 (1996).
31. D. A. Doshi *et al.*, *J. Phys. Chem. B* **107**, 7683 (2003).
32. J. F. Nagle, S. Tristram-Nagle, *Biochim. Biophys. Acta Rev. Biomembr.* **1469**, 159 (2000).
33. N. Sahai, *J. Colloid Interface Sci.* **252**, 309 (2002).
34. H. Hauser, *Biochim. Biophys. Acta* **1508**, 164 (2000).
35. Yeast strains (mww966) with a 2 μ pYES2plasmid containing the *GAL1* promoter fused to the GFP coding sequence were used for reporter protein expression.
36. *S. cerevisiae* cells supplied by the Naik Lab (R. Naik, Air Force Research Laboratory, Wright Patterson AFB) were immobilized by cell-directed assembly and stored dry at 4°C. GFP expression was induced with a 60-min exposure to minimal media lacking arginine.
37. M. B. Sinclair, J. A. Timlin, D. M. Haaland, M. Werner-Washburne, *Appl. Opt.* **43**, 2079 (2004).
38. H. Y. Fan *et al.*, *Science* **304**, 567 (2004).
39. H.K.B. acknowledges support through the National Defense Science and Engineering Graduate Fellowship Program sponsored by the Air Force Office of Scientific Research (AFOSR). C.J.B. acknowledges support from AFOSR (FA9550-04-1-0087), the U.S. Department of Energy Basic Sciences Program, the Sandia National

Laboratories Laboratory Directed Research and Development program, the Army Research Office (DAAD 19-03-1-227), and the NIH Nanomedicine Center Program (#206-00139-06). We acknowledge P. Calvert for discussions of ink-jet printing. Images in this paper were generated in the University of New Mexico Cancer Center Fluorescence Microscopy Facility, supported as detailed at <http://kugrserver.health.unm.edu:16080/microscopy/>

facility.html. Use of the Advanced Photon Source was supported by the U.S. Department of Energy, Office of Science, Office of Basic Energy Sciences, under Contract No. W-31-109-ENG-38. Sandia is a multiprogram laboratory operated by Sandia Corporation, a Lockheed Martin Company, for the U.S. Department of Energy's National Nuclear Security Administration under Contract DE-AC04-94AL85000.

Supporting Online Material

www.sciencemag.org/cgi/content/full/313/5785/337/DC1
Materials and Methods
Figs. S1 to S5
References

23 February 2006; accepted 1 June 2006
10.1126/science.1126590

Mode Locking of Electron Spin Coherences in Singly Charged Quantum Dots

A. Grelich,¹ D. R. Yakovlev,^{1,2*} A. Shabaev,^{3,4} Al. L. Efros,^{3*} I. A. Yugova,^{1,5} R. Oulton,¹ V. Stavarache,⁶ D. Reuter,⁶ A. Wieck,⁶ M. Bayer^{1*}

The fast dephasing of electron spins in an ensemble of quantum dots is detrimental for applications in quantum information processing. We show here that dephasing can be overcome by using a periodic train of light pulses to synchronize the phases of the precessing spins, and we demonstrate this effect in an ensemble of singly charged (In,Ga)As/GaAs quantum dots. This mode locking leads to constructive interference of contributions to Faraday rotation and presents potential applications based on robust quantum coherence within an ensemble of dots.

Electron spins in ensembles of quantum dots (QDs) offer one possible pathway to implementing quantum information technologies in a solid-state environment (1–4). Unfortunately, inhomogeneities within an ensemble lead to the rapid loss of coherence among the phases of the spins, typically on the scale of nanoseconds (5–7). This is orders of magnitude shorter than the coherence time for a single QD, which can be as long as microseconds (8). Theoretically, the single-spin coherence time can be even longer, in principle up to twice the spin relaxation time (9), which is on the scale of milliseconds (10, 11). The fast dephasing in an ensemble is due to both spatial fluctuations in the nuclear magnetic fields (12, 13) and inhomogeneities in the electron g factor (3). These effects may be overcome by sophisticated spin-echo techniques (14), but a simple and robust technique for preserving spin coherence could ultimately enable many of the operations that are critical to the processing of quantum information, including initialization, manipulation, and read-out of a coherent spin state.

Here we report an optical technique based on time-resolved Faraday rotation (FR) measurements of the electron spin dynamics in an ensemble of QDs to recover the coherence time

of a single QD. A periodic train of circularly polarized light pulses from a mode-locked laser synchronizes the precession of the spins to the laser repetition rate, transferring the mode-locking into the spin system. This synchronization leads to constructive interference of the electron spin polarization in time. The interference also gives the possibility for all-optical coherent manipulation of spin ensembles: The electron spins can be clocked by two trains of pump pulses with a fixed temporal delay. After this pulse sequence, the QD ensemble shows multiple echo-like FR signals with a period equal to the pump pulse separation.

The experiments were performed on self-assembled (In,Ga)As/GaAs QDs prepared such that each dot contains on average a single electron (16) [Supporting Online Material (SOM) Text]. The full width at half maximum of the photoluminescence emission line is 15 meV (Fig. 1B). We used a mode-locked laser that emits pulses with 1.5-ps duration at a rate of 75.6 MHz, corresponding to a pulse separation of $T_R = 13.2$ ns. In the pump-probe FR with picosecond resolution, spin coherence is generated by a circularly polarized pump pulse, and this coherence is monitored through the precession of the spins about a magnetic field that is applied perpendicular to the structure growth axis (Fig. 1A). For this monitoring, a subsequent linearly polarized probe pulse is used; the beam polarization is rotated due to circular birefringence of the dots that is induced by the photogenerated spin polarization (SOM Text).

In Fig. 1C, FR signals of the QDs are shown as a function of delay between pump and probe at different magnetic fields B . At $B = 0$, a single, strongly damped oscillation is seen at positive delays after the pump pulse arrival at

time $t = 0$. This signal arises from light scattering by the spin-polarized photoinduced carriers, which together with the residual electron form a negatively charged exciton (trion). No signal is detected at negative delays ($t < 0$). In a magnetic field of 1 T, long-lived electron spin quantum beats appear at positive delays. From the weak decay of the FR signal with increasing delay, a spin dephasing time T_2^* of up to 2 ns can be estimated at low fields. Because this time is much longer than the 400-ps lifetime of the electron-hole pairs injected by the pump pulse (15), the beats are due to the spin precession of the residual electrons in the QDs with a frequency $\omega_e = g_e \mu_B B / \hbar$, where μ_B is the Bohr magneton and \hbar is Planck's constant divided by 2π . $|g_e| = 0.57$ is the electron g factor (16). For a magnetic field of 6 T, an additional modulation of the FR signal appears at short positive delays, whose decay during 400 ps matches the electron-hole lifetime. This modulation arises from interference of spin precessions of the residual electron and the photoexcited carriers (16).

The long-lived beats in the FR signal at positive delays are due to initialization of spin coherence of the residual QD electrons by the pump pulses that are resonant with the trion. If the electron spin precession is slow in the limit of weak or zero magnetic field such that $\omega_e \tau_r \ll 1$, where τ_r is the trion lifetime, then the coherence is nullified after trion recombination (16–18). In the opposite case of fast spin precession ($\omega_e \tau_r \gg 1$), the spin coherence is controlled by the pump pulse area (16). For that situation, Rabi-oscillations of the FR amplitude have been reported for the studied structures (16) for which the residual electron spin coherence reaches maximum for pulses with area π .

Under these conditions, strong spin quantum beats with a frequency corresponding to the electron precession are observed also at negative delays in a nonzero magnetic field. The amplitude of these quantum beats increases when approaching zero delay $t = 0$. Spin beats at negative delay have been reported for experimental situations in which the decay time exceeds the time interval between the pump pulses: $T_2^* \geq T_R$ (3). This is clearly not the case here, where the FR signal has fully vanished after 1.2 ns at $B = 6$ T, so that $T_2^* < T_R$.

The FR traces were analyzed for positive and negative delays by exponentially damped oscillatory functions. The magnetic field dependencies of the decay time T_2^* of the ensemble spin precession are given in Fig. 1D. The varia-

¹Experimentelle Physik II, Universität Dortmund, D-44221 Dortmund, Germany. ²A. F. Ioffe Physico-Technical Institute, 194021 St. Petersburg, Russia. ³Naval Research Laboratory, Washington, DC 20375, USA. ⁴School of Computational Sciences, George Mason University, Fairfax, VA 22030, USA. ⁵Institute of Physics, St. Petersburg State University, 198504, St. Petersburg, Russia. ⁶Angewandte Festkörperphysik, Ruhr-Universität Bochum, D-44780 Bochum, Germany.

*To whom correspondence should be addressed. E-mail: dmitri.yakovlev@physik.uni-dortmund.de (D.R.Y.); efros@dave.nrl.navy.mil (A.L.E.); manfred.bayer@physik.uni-dortmund.de (M.B.)

tions Δg_e of the electronic g factor in the ensemble are translated into variations of the precession frequency, $\gamma \equiv \Delta\omega_e = \sqrt{2}\Delta g_e \mu_B B/\hbar$, which becomes larger with increasing magnetic field. This is the dominant contribution to the enhanced dephasing with increasing field. From a fit to the T_2^* data that is proportional to B^{-1} (the solid line in Fig. 1D), we estimate the g factor dispersion to be $\Delta g_e \approx 0.005$, within the energy window of QDs excited by the laser. The coincidence of the dephasing times T_2^* for $t > 0$ and $t < 0$ gives us a clear hint that it is the same spin system—the residual electrons in the n-type doped QDs—which is responsible for the FR at positive and negative delays.

The negative delay precession can occur only if the coherence of the electron spin in each single dot prevails for much longer times than the time interval T_R between the laser pump pulses, in contrast with the ensemble spin dephasing. Therefore, the dependence of the FR amplitude at negative delay on the pump pulse repetition period may provide information on the spin coherence time of a single QD, T_2 . The corresponding data at $B = 6$ T measured for two pump densities differing by a factor of two are given in Fig. 1E. The repetition period T_R was increased from 13.2 ns up to 990 ns by means of a laser pulse picker. A significant FR signal can be measured even for the longest pulse interval of a microsecond, which is comparable to the recently measured electron coherence time T_2 in a gated single QD (8).

To understand why the single QD coherence time can be seen in an ensemble measurement, let us consider excitation of a single QD by a periodic π pulse train of circularly polarized light. The first impact of the pulse train is a synchronization of electron spin precession. For discussing this effect, we define the degree of spin synchronization by $P(\omega_e) = 2|S_z(\omega_e)|$. Here $S_z(\omega_e)$ is the z projection of the electron spin at the moment of pulse arrival. It was shown theoretically that if the pulse period T_R is equal to an integer number N times the electron spin precession period in transverse magnetic field $2\pi/\omega_e$, such a train of π pulses leads to almost 100% electron spin alignment along the direction of light propagation (17). As a result, the degree of spin synchronization reaches its largest value $P_\pi = \exp(-T_R/T_2)[2 - \exp(-T_R/T_2)]$, corresponding to almost 100% synchronization. This is because for excitation with a high repetition rate (as in experiment), $T_R \ll T_2$ so that $\exp(-T_R/T_2) \approx 1$.

An ensemble contains QDs whose precession frequencies fulfill the phase synchronization condition (PSC)

$$\omega_e = 2\pi N/T_R \equiv N\Omega \quad (1)$$

Generally, multiple QD subsets satisfy the condition Eq. 1 for different N within the whole ensemble. This is due to the wide distribution

of spin precession frequencies for the optically oriented electrons, γ , caused by the dispersion of g factors in Fig. 1B. This is illustrated by Fig. 2, where panel A sketches the precession for $N = K$ and $K + 1$, where K is a large integer, and panel B gives the spectrum of phase synchronized precession modes. The number of synchronized subsets ΔN can be estimated from the broadening of the electron spin precession frequencies by $\Delta N \sim \gamma/\Omega$. It increases linearly with magnetic field B and pulse period T_R . The spins in each subset precess between the pump pulses with frequency $N\Omega$, starting with an initial phase that is the same for all subsets. The spins' contribution to

the spin polarization of the ensemble at a time t after the pulse is given by $-0.5\cos(N\Omega t)$. As sketched in Fig. 2A, the sum of oscillating terms from all subsets leads to constructive interference of their contributions when the next pulse arrives. The rest of the QDs do not contribute to the average electron spin polarization $\bar{S}_z(t)$ at times $t \gg T_2^*$ due to dephasing. The average spin polarization can be written as $\bar{S}_z(t) = -0.5\Omega \sum_{N=-\infty}^{\infty} \cos(N\Omega t) \rho(N\Omega)$, where $\rho(\omega_e)$ is the density of the QD precession frequencies within the laser excitation profile. Assuming that this density has a Lorentzian shape (19) $\rho(\omega_e) = (\gamma/\pi)[1/(\{\omega_e - \bar{\omega}_e\}^2 + \gamma^2)]$, cen-

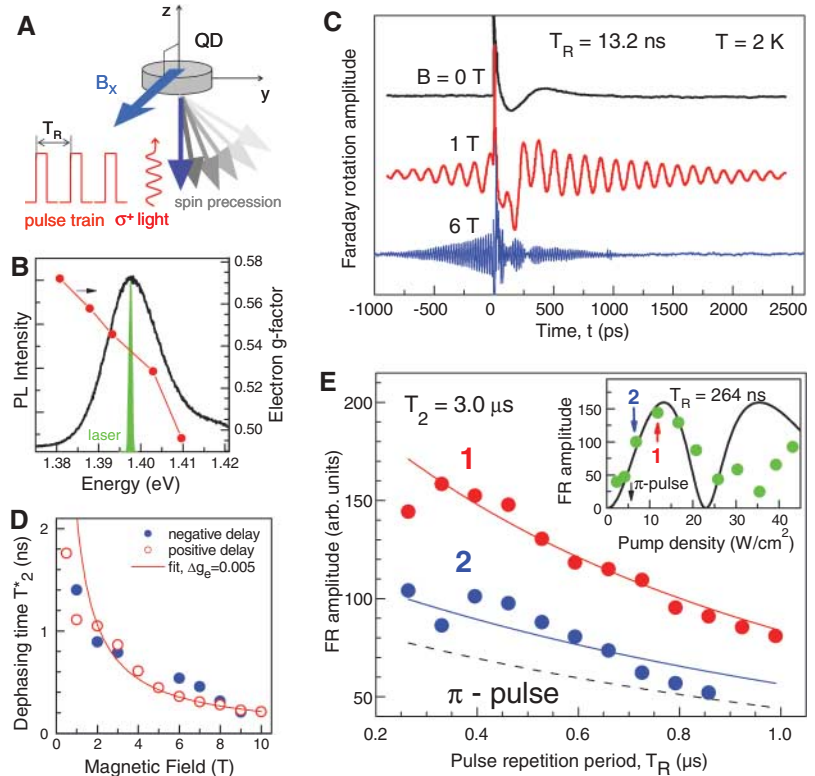


Fig. 1. (A) Geometry of experiment. The electron spin precession in a transverse magnetic field is excited by the train of short pulses of circularly polarized light. (B) Photoluminescence (PL) spectrum of the studied (In,Ga)As/GaAs dot ensemble measured at temperature $T = 2$ K. The spectrum of the pulsed laser with a spectral width of about 1 meV used for pumping and probing is shown by the green area. The symbols give the variation of the electron g factor across the inhomogeneously broadened emission spectrum (line is guide to the eye). (C) Pump-probe FR signal measured at different magnetic fields on singly charged (In,Ga)As/GaAs QDs. The pump power density is 60 W/cm 2 and the probe density is 20 W/cm 2 . For nonzero fields, distinct oscillations are seen at positive and negative delays due to Larmor precession of electron spins about the magnetic field. (D) Dephasing time T_2^* evaluated for positive (open circles) and negative (solid circles) delays as function of magnetic field. The solid line is a fit to the experimental data with a function $T_2^* \propto [\hbar\sqrt{2}]/(\Delta g_e \mu_B B)$ in order to evaluate $\Delta g_e \approx 0.005$. (E) FR amplitude at negative delay as function of time interval between pump pulses. The experimental data were measured at $B = 6$ T for two pump densities of 12 and 6 W/cm 2 shown in the inset by the red and blue arrows, respectively. The temperature $T = 6$ K. The solid lines show the theoretical dependencies described by Eq. B11, which contained as single fit parameter $T_2 = 3.0$ μ s. In the inset, the FR amplitude measured at $T_R = 264$ ns is shown as function of pump density. The solid line shows the theoretical dependence described by Eq. B11. The comparison of experiment and theory allows us to determine the pump density, which corresponds to the π pulse (shown by the black arrow). The theoretical dependence of the FR amplitude on T_R calculated for π pulse excitation is shown by the dashed line.

tered around the average frequency $\bar{\omega}_e$, we obtain

$$\bar{S}_z(t) \approx \frac{\beta \cosh\{\beta[1 - 2\text{mod}(t, T_R)]\} - \sinh\beta}{\beta \sinh\beta} \times \cos(\bar{\omega}_e t) \quad (2)$$

where $\beta = \gamma T_R/2$ and $\text{mod}(x, y) = x - y[x/y]$ is the modul function, with $[x/y]$ defined as integer division. The resulting time dependence of $\bar{S}_z(t)$ (Fig. 2A) explains the appearance of FR signal at negative delays.

π pulse excitation is not critical for the electron spin phase synchronization by the train of circularly polarized light pulses. Resonant pulses of arbitrary intensity create a coherent superposition of the trion and electron state in a QD (16), leading to a long-lived coherence of resident electron spins, because the coherence is not affected by the radiative decay of the trion component. Each pulse of σ^+ polarized light changes the electron spin projection along the light propagation direction by $\Delta S_z = -[1 - 2|S_z(t \rightarrow t_n)]W/2$, where $t_n = nT_R$ is the time of the n th pulse arrival and $W = \sin^2(\Theta/2)$, with Θ being the pulse area (16, 18). Consequently, a train of these pulses orients the electron spin opposite to the light propagation direction, and it also increases the degree of electron spin synchronization P . The application of pulses with $\Theta = \pi$ (corresponding to $W = 1$) leads to a 99% degree of electron spin synchronization after only a dozen pulses (17). However, if the electron spin coherence time is

long enough ($T_2 \gg T_R$), an extended train of pulses leads to a high degree of spin synchronization even for $\Theta \ll 1$ ($W \approx \Theta^2/4$). The general consideration of this problem in the SOM Text (Eq. B6) gives a degree of synchronization $P(\omega_e) = 2|S_z(\omega_e)|$

$$P(\omega_e) = \frac{(W/2T_R)(W/2T_R + 1/T_2)}{(W/2T_R + 1/T_2)^2 + (\omega_e - N\Omega)^2} \quad (3)$$

One sees the following: (i) A train of pulses synchronizes the spin precession of QD electrons with precession frequencies in a narrow range of width $W/2T_R + 1/T_2$ around the PSC. (ii) The electron spin synchronization still reaches 100% if $W/2T_R \gg 1/T_2$.

In case of $\Theta = \pi$, Eq. B7 gives the degree of the electron spin synchronization as

$$P_\pi(\omega_e) = \frac{e^{-T_R/T_2} |\cos(2\pi\omega_e/\Omega)|}{2 - e^{-T_R/T_2} \cos(2\pi\omega_e/\Omega)} \quad (4)$$

corresponding to the maximum degree of spin synchronization P_π for electrons matching the PSC. π pulses synchronize the electron spin precession in a broad range of frequencies with width $\sim \Omega$, which is about equal to the gap between neighboring PSC frequencies.

The effect of the pump density (namely of the pump area) on the distribution of the spin polarization synchronized by and with the pulse train at moment of the pulse arrival ($t = t_n$) for $\Theta = 0.4\pi, \pi$, and 1.6π is shown in Fig. 3, A to

C. Calculations were done for $T_R = 13.2$ ns (red) and 52.8 ns (blue). The density of the electron spin precession modes is shown by the black line, which gives the envelope of the spin polarization distribution. The quasi-discrete structure of the distribution created by the pulse train is the most important feature, which allows us to measure the long spin coherence time of a single QD on an ensemble. A continuous density of spin precession modes would always cause fast dephasing with a time inversely proportional to the total width of the frequency distribution: $T_2^* = \hbar/\gamma$. Only the gaps in the density of precession modes facilitate the constructive interference at negative delay times in Fig. 1C. These gaps are created by mode locking of the electron spins with the periodic laser emission.

The broadening of the quasi-discrete spectra around the PSC is significantly smaller than γ ; nevertheless, it leads to dephasing. The calculations in the SOM show that the dephasing rate of the QD ensemble can be written as $\Gamma + 1/T_2$, where the additional dephasing rate Γ depends on T_2 , W , and T_R as seen from Eq. B12. In the present limit of $T_R \ll T_2$, Eq. B12 gives $\Gamma \approx W/2T_R + 1/T_2$ and $\Gamma \approx \ln(2 + \sqrt{3})/T_R + 1/T_2$ for $W \ll 1$ and $W = 1$, respectively. Γ is obviously smaller for weak excitation pulses. These results are consistent with the fact that the dephasing is inversely proportional to the broadening of the phase-matched precession modes.

Figure 3D shows the decay of the normalized FR amplitudes as a function of pulse repetition time T_R and calculated using Eq. B11. The decay depends on the pulse area and is minimized for a π pulse. The decay rate for pulses with areas deviating from π are equal for $\Theta = \pi - \alpha$ and $\pi + \alpha$, where α is the deviation from a π pulse ($0 < \alpha < \pi$). We have fitted the experimental dependence of the FR amplitude on T_R (Fig. 1E) and its dependence on pump density (Fig. 1E, inset) by Eq. B11. The factor two difference in pumping intensities used for recording the data labeled 1 and 2 leads to a significant restriction of the T_2 value in Fig. 1E. The fit allows us to determine a pump density corresponding to the π pulse and a single quantum dot coherence time $T_2 = 3.0 \pm 0.3$ μ s, which is four orders of magnitude longer than the ensemble dephasing time $T_2^* = 0.4$ ns at $B = 6$ T.

The FR amplitude does not reach its largest value at π pulse pumping (Fig. 1E, inset). This is because the train of π pulses synchronizes the spin precession for a broad distribution of precession frequencies and not only for the ω_e satisfying the PSC. For example, in the QDs with $\omega_e = (N + 1/2)\Omega$, the spin synchronization degree is 1/3 (Eq. 4). However, the S_z projection of electron spin in these QDs is opposite to the one for QDs which satisfy the PSC ($\omega_e = N\Omega$) (Fig. 3B). This leads to cancellation effects in the total FR amplitude

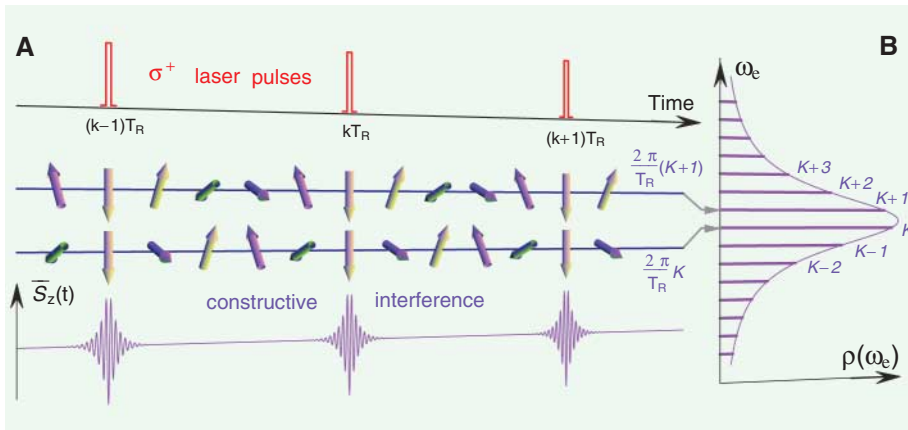


Fig. 2. (A) Phase synchronization of electron spin precession by a train of π pulses of circularly polarized light. The top panel shows the train of σ^+ polarized laser pulses with repetition period T_R . The train synchronizes the electron spin precession in QDs, where the precession frequency is a multiple of $(2\pi/T_R)$: $\omega_e = N(2\pi/T_R)$. In these QDs, the spins are aligned at the moment of the pulse arrival; each spin is opposite to the light propagation direction. The two middle panels show the phase synchronization for two spins with precession frequencies differing by $2\pi/T_R$: $N = K$ and $N = K + 1$ (K is a large integer). The bottom panel shows a time evolution of the average spin polarization $\bar{S}_z(t)$, resulting from a constructive interference of the phase synchronized QD subsets. **(B)** Spectrum of phase-synchronized electron spin precession modes enveloped by the density of precession frequencies $\rho(\omega_e)$ in a QD ensemble. Only those electron spins that are synchronized by the pulse train give a contribution to the spectrum, consisting of sharp peaks at the frequencies $\omega_e = N(2\pi/T_R)$ ($N = \dots, K - 1, K, K + 1, \dots$), which satisfy the phase synchronization condition Eq. 1.

of the QD ensemble. In contrast, one can see in Fig. 3C that pulses with an area $\Theta > \pi$ are not so efficient in synchronizing the electron

spin precession in QDs that do not satisfy the PSC. This diminishes the “negative” contribution of such QDs to the electron spin po-

larization and increases the FR amplitude. Generally, the rise of the excitation intensity from zero to π pulses increases the number of QDs contributing to the FR signal at negative delays.

After showing that a specific protocol for a laser pulse sequence can be used for selecting a subset of synchronized QDs with the single dot dephasing time, we turn to testing the degree of control that can be achieved by such sequences. For that purpose, each pump is split into two pulses with a fixed delay $T_D < T_R$ between them. The results of measurements for $T_D = 1.84$ ns are plotted in Fig. 4A. Both pumps were circularly copolarized and had the same intensities. When the QDs are exposed to only one of the two pumps (the two upper traces), the FR signals are identical except for a shift by T_D . The signal changes drastically under excitation by the two-pulse train (the lower trace). Around the arrival time of pump 1, the same FR response is observed as before in the one-pump experiment. Also around pump 2, qualitatively the same FR pattern is observed with considerably larger amplitude. Therefore the coherent response of the synchronized QD ensemble can be amplified by the second laser pulse. Even more remarkable are the echo-like responses showing up in the FR signal before the first and after the second pump pulse. They have a symmetric shape with the same decay and rise times T_2^* . The temporal separation between them is a multiple of T_D . These echo signals show no additional modulation of the FR traces as seen at positive delay times when the pump is applied. This is in agreement with the assignment of the modulation to the photogenerated carriers (16).

Apparently, the electron spins in the QD subensemble, which is synchronized with the laser repetition rate, have been clocked by introducing a second frequency, which is determined by the laser pulse separation. The clocking results in multiple echoes in the FR response. This behavior can be explained by our theoretical model: The echo-like signal has the same origin as the FR revival in the single-pump experiment, which is constructive interference of the FR amplitudes from QD subsets with phase-synchronized electron spin precession. We have calculated the distribution of electron spin polarization created by a train of π pulses in the two-pump experiment by using a technique similar to the one described in the SOM for the single pump experiment. The resultant time dependence of the FR signal reproduces the experimental echo signals well (Fig. 4B).

Phase synchronization of the electron spin precession modes in a QD ensemble by a laser pulse train reveals the long spin coherence time of a single dot. Two-pump experiments demon-

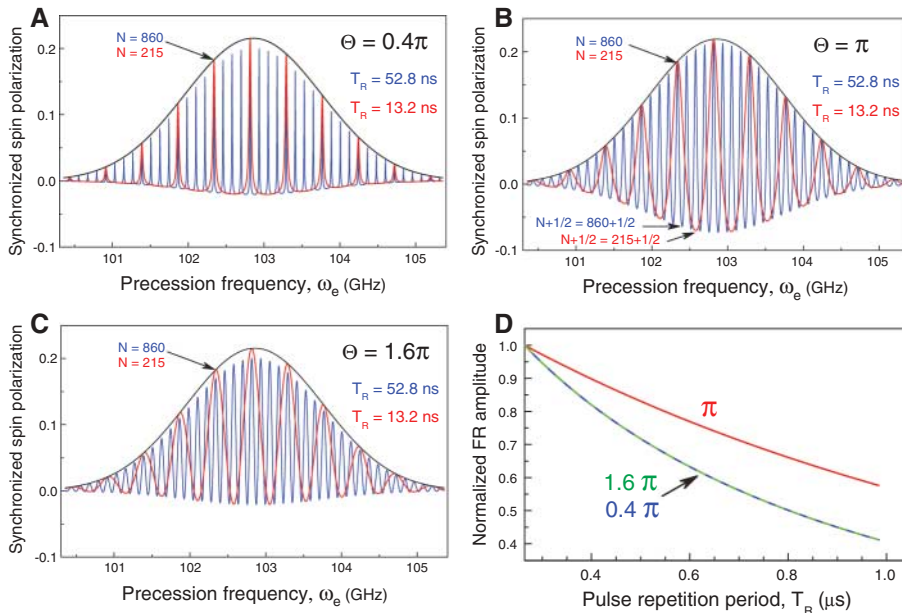
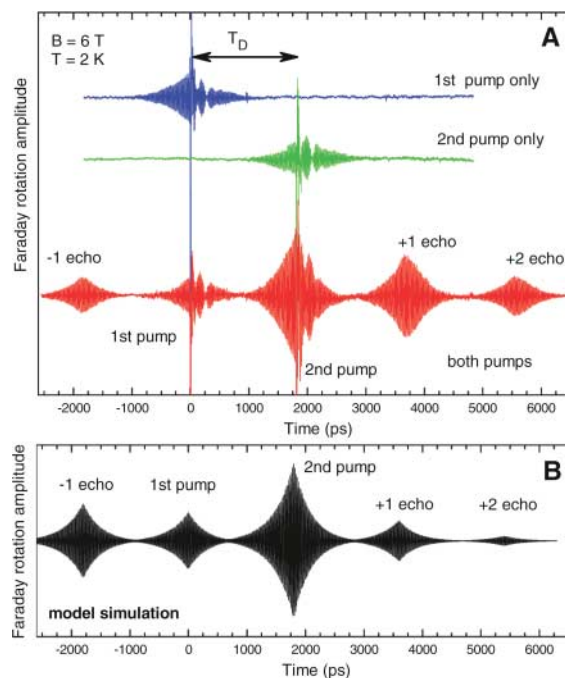


Fig. 3. (A to C) Spectra of phase-synchronized electron spin precession modes created by a train of circularly polarized pulses, $-\bar{S}_z(t_n)$, calculated for the pulse area $\Theta = 0.4\pi$, π , and 1.6π , respectively. The spectra have been calculated for two pump pulse repetition periods: $T_R = 13.2$ ns (red) and 52.8 ns (blue). At low pumping intensity (A), the pulse train synchronizes electron spin precession in a very narrow frequency range near the PSC: $\omega_e = N(2\pi/T_R)$. The π pulses (B) widen the range of synchronized precession frequencies. In addition, the electron spins with opposite polarization at frequencies between the PSC become significantly synchronized. The degree of synchronization for these spins decreases at $\Theta > \pi$ (C). (D) Negative delay FR amplitude dependence on pump pulse repetition period T_R calculated for the same three pulse areas. The amplitude is normalized to its value at $T_R = 264$ ns. The normalized FR amplitude shows the slowest decay for the π pulse excitation. The decay rates are equal for pulses with areas $\Theta = \pi - \alpha$ and $\Theta = \pi + \alpha$, where $\alpha < \pi$. All calculations have been done for a magnetic field of $B = 2$ T with $g_e = |0.57|$, $\Delta g_e = 0.005$, and $T_2 = 3.0$ μ s.

Fig. 4. Control of electron spin synchronization by two trains of pump pulses with $T_R = 13.2$ ns shifted in time by $T_D = 1.84$ ns. (A) Experimental FR measured for separate action of the 1st or the 2nd pump (the two upper curves) and for joint action of both pumps (the bottom curve). Pumps were copolarized (σ^+). The joint action of the two pumps leads to the echo-like responses before the first and after the second pump pulse. (B) Theoretical modeling of the spin echo-like signals in the two-pulse experiment. Parameters: $\Theta = \pi$ and $\gamma = 3.2$ GHz.



strate the opportunity to control the spin ensemble's coherent response by tailoring the desirable time response. The phase synchronization is "robust," because it allows one to exploit all advantages of working with a QD ensemble for "hardware" components in spintronics or quantum information: (i) a strong detection signal with relatively small noise can be recorded and (ii) changes of external parameters such as repetition rate and magnetic field strength can be accommodated in the PSC due to the broad distribution of electron spin precession frequencies in the ensemble and the large number of involved QDs.

References and Notes

- D. Loss, D. P. DiVincenzo, *Phys. Rev. A* **57**, 120 (1998).
- A. Imamoglu *et al.*, *Phys. Rev. Lett.* **83**, 4204 (1999).
- D. D. Awschalom, D. Loss, N. Samarth, Eds., *Semiconductor Spintronics and Quantum Computation* (Springer-Verlag, Heidelberg, 2002).
- S. A. Wolf *et al.*, *Science* **294**, 1488 (2001).
- M. V. Gurudev Dutt *et al.*, *Phys. Rev. Lett.* **94**, 227403 (2005).
- A. S. Bracker *et al.*, *Phys. Rev. Lett.* **94**, 047402 (2005).
- P.-F. Braun *et al.*, *Phys. Rev. Lett.* **94**, 116601 (2005).
- J. R. Petta *et al.*, *Science* **309**, 2180 (2005).
- W. A. Coish, D. Loss, *Phys. Rev. B* **70**, 195340 (2004).
- J. M. Elzerman *et al.*, *Nature* **430**, 431 (2004).
- M. Kroutvar *et al.*, *Nature* **432**, 81 (2004).
- I. A. Merkulov, Al. L. Efros, M. Rosen, *Phys. Rev. B* **65**, 205309 (2002).
- A. V. Khaetskii, D. Loss, L. Glazman, *Phys. Rev. Lett.* **88**, 186802 (2002).
- C. P. Slichter, *Principles of Magnetic Resonance* (Springer-Verlag, Berlin, 1996).
- A. Greilich *et al.*, *Phys. Rev. B* **73**, 045323 (2006).
- A. Greilich *et al.*, *Phys. Rev. Lett.* **96**, 227401 (2006).
- A. Shabaev, Al. L. Efros, D. Gammon, I. A. Merkulov, *Phys. Rev. B* **68**, 201305(R) (2003).
- T. A. Kennedy *et al.*, *Phys. Rev. B* **73**, 045307 (2006).
- We chose a Lorentzian profile for the QD precession frequencies in the consideration because it leads to the closed form for $\bar{S}_z(t)$ in Eq. 2. Generally, our numerical calculations do not show any qualitative or quantitative differences for either the Gaussian or the Lorentzian profiles as long as the distribution $\rho(\omega_e)$ is smoothly going to zero on the scale of its width.
- We are grateful to S. Erwin for his critical suggestions on the manuscript. This work was supported by the Bundesministerium für Bildung und Forschung program nanoquit, the Defense Advanced Research Projects Agency program QuIST, the Office of Naval Research, and the Deutsche Forschungsgemeinschaft (Forschergruppe Quantum Optics in Semiconductor Nanostructures). R. O. thanks the Alexander von Humboldt foundation.

Supporting Online Materials

www.sciencemag.org/cgi/content/full/313/5785/341/DC1

SOM Text

References

3 April 2006; accepted 14 June 2006

10.1126/science.1128215

Large Wind Shift on the Great Plains During the Medieval Warm Period

Venkatarmana Sridhar,^{1,2} David B. Loope,^{1*} James B. Swinehart,^{1,2} Joseph A. Mason,³ Robert J. Oglesby,^{1,2} Clinton M. Rowe¹

Spring-summer winds from the south move moist air from the Gulf of Mexico to the Great Plains. Rainfall in the growing season sustains prairie grasses that keep large dunes in the Nebraska Sand Hills immobile. Longitudinal dunes built during the Medieval Warm Period (800 to 1000 years before the present) record the last major period of sand mobility. These dunes are oriented NW-SE and are composed of cross-strata with bipolar dip directions. The trend and structure of the dunes record a drought that was initiated and sustained by a historically unprecedented shift of spring-summer atmospheric circulation over the Plains: Moist southerly flow was replaced by dry southwesterly flow.

Direct evidence of past changes in atmospheric circulation is largely absent from the geologic record. It is much easier to reconstruct indirect indicators of circulation such as vegetation, temperature, and precipitation. Episodically active dunes are an exception to this, however. Periods of dune activation and stabilization have frequently been used to infer alternating periods of drought and pluvial conditions, but few studies have fully exploited the orientation, morphology, and internal structures of dunes to reveal the wind regime under which they formed. We have used those features to explore paleowind regimes from the North American Great Plains.

In spring and early summer, strong southerly-to-southeasterly winds sweep over the Gulf of Mexico and transport moisture for growing-season rains to North America's core (1–3). Today, this moisture sustains the vegetation that stabilizes extensive dunefields on the Great Plains. A distinctive set of NW-SE-trending,

grass-stabilized longitudinal dunes occupies 7500 km² of central Nebraska (Fig. 1); these dunes formed only 800 to 1000 years ago, near the end of the Medieval Warm Period (MWP) (4, 5).

Annual precipitation ranges from 60 cm in the eastern Sand Hills to less than 43 cm in the west; ~50% comes in May, June, and July (1). During the 1930s and 1950s droughts, only isolated blowouts formed in the Sand Hills. Historical accounts indicate that some dune crests were grass-free at times during the 19th century (6). The large size of stabilized dunes and the dunefield's great extent indicate that the region is prone to droughts far more severe than those in the historical record (7). Optically stimulated luminescence (OSL) ages from deep within the largest dunes extend to 15,000 years before the present (yr B.P.), but shallow core and outcrop samples from dunes and adjacent wetlands indicate an episode of dune migration 800 to 1000 yr B.P., when aridity was widespread and persistent across western North America (8–16).

Many modern deserts contain morphologically distinct generations of dunes with different trends (17). If the internal structure and age of each generation are known, changes in regional winds can be reconstructed (18). The modern wind regime in the Sand Hills is dominated by

northerly winter winds associated with midlatitude cyclones and by southerly flow in spring and summer associated with anticyclonic return flow of moist air from the Gulf of Mexico.

Dunes orient themselves to maximize sand transport normal to their crests (19, 20). In bidirectional flows, transverse dunes form if the divergence angle between flows is less than 90° or close to 180°; oblique or longitudinal dunes (both with linear morphology) form if the angular difference is between 90° and 165° (19). Crests of longitudinal dunes lie within 15° of the resultant transport vector, crests of oblique dunes lie between 15° and 75°, and crests of transverse dunes lie between 75° and 90° (fig. S1) (19). Using wind data from six meteorological stations in and near the Nebraska Sand Hills (Fig. 1), we used the computer program Trend (19, 21) to calculate the trend and resultant sand-drift vectors of dunes that would form (if sand were free to move) at each site. Trends range from S70°W to S55°W (fig. S2). Angles between calculated dune trends and modern resultants range from 44° to 90° and show that modern winds would generate oblique and transverse dunes, both of which would migrate southeastward; internally, these dunes contain only southward-dipping cross-strata (Fig. 2).

Crests of Medieval dunes in the southeastern Sand Hills are oriented N65°W. These dunes are 12 to 15 m high and several km long, with 0.2-km spacing (fig. S3). Cross-strata have bimodal dip directions (both NE and SW; Fig. 2 and fig. S4), which is the key characteristic of longitudinal dunes (22). These structures indicate that the wind regime that shaped the dunes was not only bidirectional, but also that the two wind vectors were of nearly equal magnitude (Fig. 2). Elongate dunes commonly join to form "y junctions" that are trustworthy indicators of resultant sand-drift direction (23). Because y junctions in the southeastern Sand Hills open toward the WNW (fig. S3), the resultant sand-drift direction for the Medieval dunes was ESE (Fig. 2).

¹Department of Geosciences, University of Nebraska, Lincoln, NE 68588-0340, USA. ²School of Natural Resources, University of Nebraska, Lincoln, NE 68583-0758, USA. ³Department of Geography, University of Wisconsin, Madison, WI 53706, USA.

*To whom correspondence should be addressed. E-mail: dloope1@unl.edu

Hypothetical dunes that formed under the modern wind regime would thus be morphodynamically and structurally distinct from the ancient dunes, and the two would have crestal trends that diverge by 45° to 60°. These differences show that wind directions and relative strengths have changed markedly since the 800-year-old dunes were active. The northerly vector lay between 340° and 17.5°, and the southwesterly vector lay between 212.5° and 250° (Fig. 2). If the dominant fall-winter-early spring (September to April) portion of the modern wind regime is retained as the northerly vector (~345°), a relative strengthening (to become equal to the northerly vector) and a 70° westward shift of the modern spring-summer winds would produce a dune trend, resultant vector, and internal structure that fit those of the

Medieval dunes. A greater westward shift of the warm-season flow (regardless of wind strength) would reduce the divergence angle so that only transverse dunes form; a lesser shift would produce longitudinal dunes, but they would not produce NW-SE trends or y junctions opening to the WNW (Fig. 2). Analysis of the dunes shows only that the sand-transporting northerly and southwesterly winds were similar in sand-transporting potential during the MWP drought. Assuming little significant change in the September-to-April wind regime at that time, southwesterlies would have been considerably stronger than the present southerlies and southeasterlies. Such a westward shift would also greatly reduce the flow of moist air into the central Great Plains, thereby generating severe drought.

Southwesterly flow of dry air across Nebraska is common in spring and summer in the modern regime but at the 850-millibar level (~1200 m aloft) instead of at the surface (24). In spring and summer, strong heating of the land surface in the deserts of Mexico generates a deep, well-mixed layer of hot, dry air that moves to the northeast and eventually becomes elevated under the influence of the subtropical jet. Cooler, moister air from the Gulf of Mexico moves under the hot, dry air. The surface boundary between the moist air and the hot, dry air—the “dry line”—reaches as far north and east as the Sand Hills several times each year at present, and it helps trigger outbursts of strong storms when it does so. Although it is ill-defined in a climatological sense, the mean position of the dry line at present is probably in eastern Wyoming or western Nebraska, well west of the Sand Hills. Our work suggests that during the MWP, the mean position of the dry line moved much farther east, such that the Sand Hills were most often in the dry, hot air with greatly reduced precipitation.

Under present conditions, dunes on the Plains—including those in eastern Colorado, central Kansas, and western Nebraska—are very near their threshold for mobilization (6, 25–28). The dunes discussed here, however, lie within the easternmost (wettest) portion of the Nebraska Sand Hills, which is an area that would presumably be among the last to activate if only slight alterations of the modern hydrological conditions and wind regime were necessary for dune mobility. Previous studies of Great Plains drought, including the Dust Bowl of the 1930s, have emphasized the importance of synoptic feedbacks associated with depleted soil moisture (23–25, 29–31). We interpret the southwesterly

Fig. 1. Locations of weather stations and extent of Nebraska Sand Hills (light gray shading) and longitudinal dunes with NW-SE trends (dark gray shading). Wind data stations and periods of record are as follows: A, Ainsworth, 1973–2005; B, Brewster, 1973–1979 and 1996–2005; BB, Broken Bow, 1973–2005; NP, North Platte, 1973–2005; ON, O’Neill, 1984–1991 and 1995–2005; OR, Ord, 1981–2005. The inset map shows Nebraska’s position relative to the Rocky Mountains and Gulf of Mexico (G), modern winter winds (solid arrow), and modern spring-summer winds (dashed arrow).

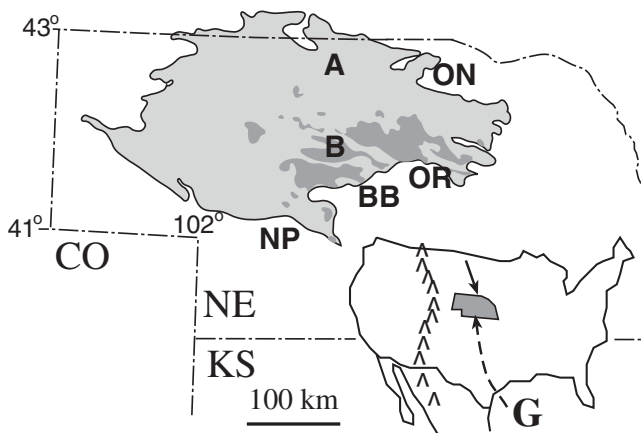
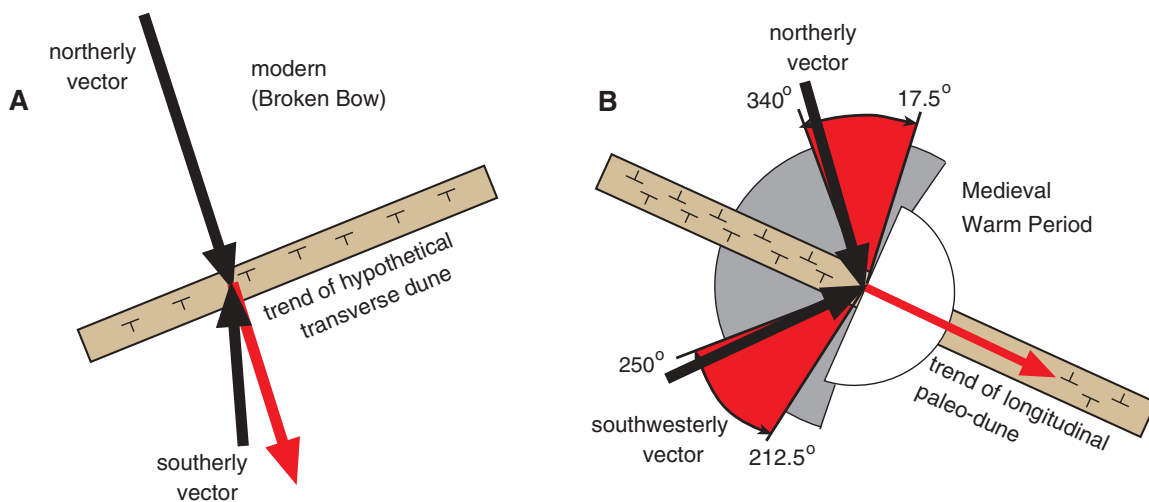


Fig. 2. Modern and Medieval sand-drift vectors (directions of sand movement caused by main sand-transporting winds; bold black arrows), resultants (directions of sand movement resulting from net effects of all winds; red arrows), and trends of dune crests. Dip symbols (“Ts”) show slope direction for sand layers (cross-strata) inside dunes and on downwind flanks. (A) Sand-drift vectors and resultant based on modern wind data from Broken Bow, Nebraska (simplified from fig. S2) and calculated trend of hypothetical dunes (19) (if sand were free to move). Migration of such dunes would generate sand cross-strata that would slope downward toward the SE. (B) Interpreted sand-drift vectors that generated NW-SE trend and bidirectional cross-strata (22) of Medieval longitudinal dunes. Y junctions (23) (fig. S2) indicate that the resultant is to ESE (not WNW), thereby excluding easterly vectors (180° white sector). Vectors diverging less than 90° and more than 165° (gray sectors) would have



generated transverse (not longitudinal) dunes (19, 20) (fig. S1C), thereby constraining the drift vectors to two 37.5° sectors (red). The trend of longitudinal dunes bisects two subequal sand-drift vectors (19, 22). If, for example, the modern northerly (September through April) wind vector (~345°) is retained from (A), the southerly (May to August) vector must be rotated ~70° westward and strengthened to generate both the orientation and internal structure of the ancient dunes.

flow recorded by the longitudinal dunes of the eastern Sand Hills to be one of those feedbacks. When soil moisture is low, diurnal surface heating is very strong, and the momentum from winds aloft can be transferred to the land surface. Dry, southwesterly surface winds across the eastern Sand Hills were greatly enhanced after wetlands were desiccated (5), grass cover was breached, and sandy soils were exposed to direct solar radiation.

We used National Centers for Environmental Prediction/National Center for Atmospheric Research (NCEP/NCAR) reanalysis data from 1949 to 2005 to determine if years of low precipitation corresponded with years when spring-summer surface flow was more westerly. Circulation composites for wet, dry, and normal years were constructed for May, June, and July. Although the Plains suffered severe droughts in the 1950s and 1970s, and experienced numerous dry (individual) years, the reanalyses do not show a westward wind shift. The NCEP/NCAR reanalysis is model-dependent and has coarse resolution, therefore surface winds can be suspect. Further, by considering only monthly means, strong winds capable of sand transport may not be well-represented. Therefore, daily and monthly wind data for individual stations in central and western Nebraska were also examined. Again, no consistent westward shift was found, indicating that modern droughts and the Medieval drought cannot be explained by the same mechanism. Droughts of the last 57 years were relatively short and due more to diminished moisture convergence than to diminished moisture transport. The dunes record a historically unprecedented large-scale shift of circulation that removed the source of moisture from the region during the growing season. Eastward or southward migration of the North Atlantic subtropical ridge of high pressure (the "Bermuda High") likely initiated the Medieval drought (32), allowing midlevel southwesterly flow to descend. The drought may then have been enhanced and prolonged by reduced soil moisture and related surface-heating effects.

The MWP was a time of warmth and aridity throughout much of the western United States (7, 8, 16); this suggests that the circulation change indicated by dune morphology is part of a larger climate anomaly (33). A switch in Pacific sea-surface temperature (SST) to a quasi-perennial "La Niña" state may be an important factor (33), because such an SST regime has been associated with drought throughout much of the western half of the United States (8). This concept may also help explain more pronounced episodes of aridity during the mid-Holocene, and it has seen recent support from climate modeling studies (34).

References and Notes

- D. A. Wilhite, K. G. Hubbard, in *An Atlas of the Sand Hills*, A. Bleed, C. Flowerday, Eds. (Univ. of Nebraska Conservation and Survey Division Resource Atlas, Lincoln, NE, vol. 5a, 1990), p. 17.
- D. B. Loope, J. B. Swinehart, J. P. Mason, *Bull. Geol. Soc. Am.* **107**, 396 (1995).
- D. B. Loope, J. B. Swinehart, *Great Plains Res.* **10**, 5 (2000).
- R. J. Goble, J. A. Mason, D. B. Loope, J. B. Swinehart, *Quat. Sci. Rev.* **23**, 1173 (2004).
- J. A. Mason, R. J. Goble, J. B. Swinehart, D. B. Loope, *Holocene* **14**, 209 (2004).
- D. R. Muhs, V. T. Holliday, *Quat. Res.* **43**, 198 (1995).
- C. A. Woodhouse, J. T. Overpeck, *Bull. Am. Meteorol. Soc.* **79**, 2693 (1998).
- E. R. Cook, C. A. Woodhouse, C. M. Eakin, D. M. Meko, D. W. Stahle, *Science* **306**, 1015 (2004).
- S. H. Millspaugh, C. Whitlock, P. J. Bartlein, *Geology* **28**, 211 (2000).
- J. A. Mohr, C. Whitlock, C. N. Skinner, *Holocene* **10**, 587 (2000).
- T. W. Swetnam, *Science* **262**, 885 (1993).
- S. Stine, *Nature* **369**, 546 (1994).
- K. R. Laird, S. C. Fritz, K. A. Maasch, B. F. Cumming, *Nature* **384**, 552 (1996).
- J. M. Daniels, J. C. Knox, *Holocene* **15**, 736 (2005).
- K. J. Brown *et al.*, *Proc. Natl. Acad. Sci. U.S.A.* **102**, 8865 (2005).
- T. J. Osburn, K. R. Briffa, *Science* **311**, 841 (2006).
- N. Lancaster, *Sedimentology* **39**, 631 (1992).
- N. Lancaster *et al.*, *Geology* **30**, 991 (2002).
- D. M. Rubin, H. Ikeda, *Sedimentology* **37**, 673 (1990).
- G. Kocurek, in *Sedimentary Environments: Processes, Facies and Stratigraphy*, H. G. Reading, Ed. (Blackwell, Oxford, ed. 3, 1996), pp. 125–153.
- S. G. Fryberger, in *A Study of Global Sand Seas*, E. D. McKee, Ed. (U.S. Geological Survey Professional Paper, vol. 10521979), p. 137.
- D. M. Rubin, R. E. Hunter, *Sedimentology* **32**, 147 (1985).
- D. S. G. Thomas, Z. *Geomorph.* **30**, 231 (1986).
- T. N. Carlson, *Mid-latitude Weather Systems* (HarperCollins, London, 1991), pp. 448–481.
- R. F. Madole, *Quat. Sci. Rev.* **14**, 155 (1995).
- A. F. Arbogast, *J. Arid Environ.* **34**, 403 (1996).
- R. F. Madole, *Geology* **22**, 483 (1994).
- D. R. Muhs, P. B. Maat, *J. Arid Environ.* **25**, 351 (1993).
- S. D. Schubert, M. J. Suarez, P. J. Pegion, R. D. Koster, J. T. Bacmeister, *Science* **303**, 1855 (2004).
- R. D. Koster, M. J. Suarez, M. Heiser, *J. Hydrometeorology* **1**, 26 (2000).
- S. D. Schubert, M. J. Suarez, P. J. Pegion, R. D. Koster, J. T. Bacmeister, *J. Clim.* **17**, 485 (2004).
- S. L. Forman, R. Oglesby, R. S. Webb, *Global Planet. Change* **29**, 1 (2001).
- R. S. Bradley, M. K. Hughes, H. F. Diaz, *Science* **302**, 404 (2003).
- S. Shin, P. D. Sardeshmukh, R. S. Webb, R. J. Oglesby, J. J. Barsugli, *J. Clim.* **19**, 2801 (2006).
- We thank D. Wedin, A. Houston, and K. Hubbard for helpful discussions and R. Goble and the Department of Geosciences for support of OSL dating. Our work is part of the Sand Hills Biocomplexity Project and was funded by NSF (grant nos. DEB 0322067 and BCS 0352683).

Supporting Online Material

www.sciencemag.org/cgi/content/full/313/5785/345/DC1
Figs. S1 to S4

19 April 2006; accepted 14 June 2006
10.1126/science.1128941

Receptor Activation Alters Inner Surface Potential During Phagocytosis

Tony Yeung,^{1,3} Mauricio Terebiznik,² Liming Yu,¹ John Silvius,⁴ Wasif M. Abidi,⁵ Mark Philips,⁵ Tim Levine,⁶ Andras Kapus,⁷ Sergio Grinstein^{1,3*}

The surface potential of biological membranes varies according to their lipid composition. We devised genetically encoded probes to assess surface potential in intact cells. These probes revealed marked, localized alterations in the charge of the inner surface of the plasma membrane of macrophages during the course of phagocytosis. Hydrolysis of phosphoinositides and displacement of phosphatidylserine accounted for the change in surface potential at the phagosomal cup. Signaling molecules such as K-Ras, Rac1, and c-Src that are targeted to the membrane by electrostatic interactions were rapidly released from membrane subdomains where the surface charge was altered by lipid remodeling during phagocytosis.

The plasma membrane of mammalian cells contains about 20 mol % of anionic lipids on the inner leaflet. The preferential accumulation of negative charges creates an electric field, estimated at 10⁵ V/cm, that strongly attracts cationic molecules, including peripheral membrane proteins (1). This electrostatic interaction has been best documented for the myristoylated

alanine-rich C kinase substrate (MARCKS), which interacts with the plasmalemma through a polycationic domain, in conjunction with a myristoyl anchor (2). The realization of this charge-dependent anchorage led to the postulation of an "electro-static switch" model (2), which predicts that the formation and stability of electrostatic associations can be regulated by changes in the charge of either the cationic protein complex or the anionic lipid layer.

Little is known about the regulation of the electrostatic potential of the plasmalemma. It is not clear whether the surface potential of the cytoplasmic leaflet undergoes regulated changes and, if so, whether such changes play a role in modulating the association of cationic proteins. This paucity of information is due to the absence of methods to monitor the surface potential of the inner membranes of intact cells.

¹Division of Cell Biology, ²Gastroenterology, Hepatology, and Nutrition Department, Hospital for Sick Children, Toronto, Ontario M5G 1X8, Canada. ³Institute of Medical Sciences, University of Toronto, Toronto, Ontario M5S 1A8, Canada. ⁴Department of Biochemistry, McGill University, Montreal, Quebec H3G 1Y6, Canada. ⁵Department of Medicine, New York University School of Medicine, New York, NY 10016, USA. ⁶Division of Cell Biology, University College, London EC1V 9EL, UK. ⁷St. Michael's Hospital Research Institute, Toronto, Ontario M5B 1W8, Canada.

*To whom correspondence should be addressed. E-mail: sga@sickkids.ca

Phagocytosis is associated with extensive remodeling of the plasma membrane lipids (3). Such lipid changes could potentially alter the overall charge of the plasmalemma and may therefore serve as an “electrostatic switch” to modulate the interaction with cationic ligands, which could in turn affect the phagocytic response. To investigate this possibility, we developed means to assess the electrostatic potential of the inner aspect of the plasma membrane in intact cells. We designed several polycationic fluorescent probes that are selectively targeted to the plasmalemma by virtue of its unique negative surface charge. One probe was modeled after the C terminus of K-Ras, which was shown to associate with the membrane in a charge-dependent manner (4). To ensure that the probe was not phosphorylated, we mutated all serine and threonine residues to alanine to create a second probe (K-pre, Fig. 1A). In a third probe, all lysines were substituted by arginines to avoid ubiquitination (R-pre, Fig. 1A).

An *in vitro* assay assessed the effect of surface potential on the affinity of R-pre for pure lipid bilayers (5). R-pre labeled with bimanane, a solvochromic dye, partitioned preferentially to liposomes containing anionic lipids (Fig. 1B). Inclusion of phosphatidylinositol 4,5-bisphosphate (PIP₂) or phosphatidylserine (PS), at concentrations resembling those in the plasmalemma, or phosphatidic acid (PA) increased the partition coefficient by factors of 10, 51, and 87, respectively, relative to liposomes containing only phosphatidylcholine (PC) with or without phosphatidylethanolamine (PE) (Fig. 1D). Moreover, progressive elevation of the ionic strength reduced the interaction of R-pre with anionic liposomes and minimized the affinity difference relative to uncharged liposomes (Fig. 1, C and D, and fig. S1B).

We next expressed a genetically encoded form of R-pre conjugated to red fluorescent protein (RFP) in RAW264.7 macrophages. R-pre-RFP associated almost exclusively with the inner aspect of the plasma membrane (Fig. 1E), as found for the tail of K-Ras (Fig. 1F) (6), as found for the tail of K-Ras (Fig. 1F) (6). We also used polybasic constructs containing an N-terminal myristoylated sequence (K-myristoyl and Nt-Src) or containing an amphiphilic helix (KR ϕ) instead of a farnesylation site (Fig. 1A) (6, 7). Like R-pre, KR ϕ partitions preferentially to anionic liposomes in an ionic strength-dependent manner (fig. S1, A and C). When expressed in macrophages, KR ϕ (Fig. 1E), K-myristoyl (Fig. 1E), and Nt-Src (fig. S5A) localized to the plasma membrane, which implies that the common feature of these constructs—namely their positive charge—was a primary determinant of their targeting. Accordingly, progressive elimination of cationic residues resulted in graded detachment of K-Ras tail–derived mutants from the plasmalemma (Fig. 1, F and G) (6).

Three approaches were used to show that the probes responded to changes in the elec-

tric field at the inner surface of the plasma membrane. First, cells were treated with an ionophore to elevate cytosolic calcium, which shields the surface charge of the membrane and induces PIP₂ hydrolysis through activation of phospholipase C (PLC). The extensive degradation of PIP₂ was verified with the use of PH-PLC δ -GFP, a green fluorescent protein (GFP)-tagged probe for this phosphoinositide (Fig. 2A). Calcium also activates the lipid scramblase, resulting in net translocation of PS to the outer leaflet (Fig. 2A). In parallel with the changes in anionic lipid composition and distribution, ionomycin induced a pronounced dissociation of R-pre, KR ϕ , and K-myristoyl from the inner surface of the membrane (Fig.

2A and movie S1). Redistribution of the probes was not due to wholesale remodeling or disruption of the membrane. This was established with the use of three different genetically encoded fluorescent markers retained at the plasma membrane by hydrophobic interactions: glycosylphosphatidylinositol (GPI)-linked GFP, a transmembrane chimeric protein (GT46), and a farnesylated and diacylated GFP termed Palm (fig. S1D). When coexpressed with the cationic probes, the distribution of these markers remained essentially unaltered after treatment with ionomycin (Fig. 2A), which confirmed the integrity of the plasmalemma. Quantitation of the effects of ionomycin on the distribution of the probes is shown in Fig. 2B.

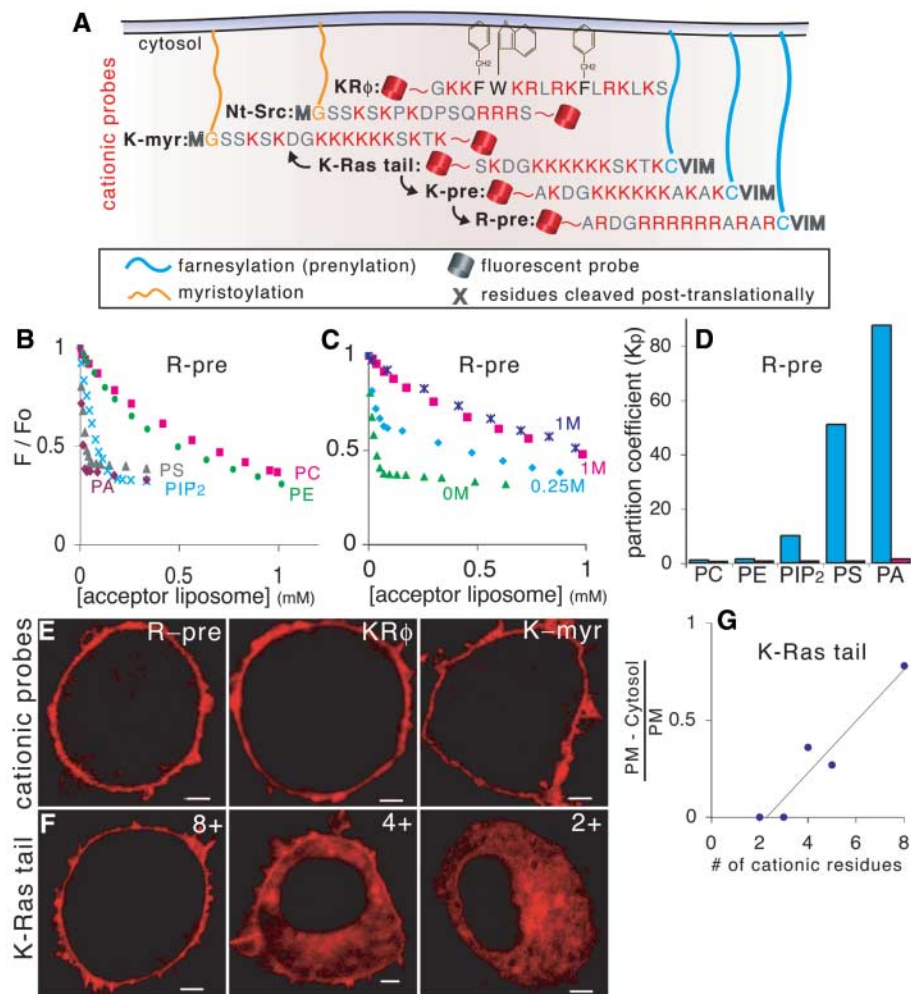


Fig. 1. Design and characterization of surface potential-sensitive probes. (A) Structure of surface potential-sensitive probes. Amino acid abbreviations: A, Ala; C, Cys; D, Asp; F, Phe; G, Gly; I, Ile; K, Lys; L, Leu; M, Met; P, Pro; Q, Gln; R, Arg; S, Ser; T, Thr; V, Val; W, Trp. (B) Transfer of R-pre from donor liposomes (100 mol % PC) to acceptor liposomes containing PC (98 mol %), PC/PE (78/20 mol %), PC/PS (78/20 mol %), PC/PA (78/20 mol %), or PC/PIP₂ (96/2 mol %). F/F₀, fluorescence intensity ratio. (C) Transfer of R-pre to PC (98 mol %; navy) or PC/PS (78/20 mol %; other colors) acceptor liposomes in medium supplemented with the indicated NaCl concentrations. (D) Partition coefficient (K_p ; relative to PC) of R-pre binding to liposomes containing PC (100 mol %), PE, PS, or PA (20 mol % each), or PIP₂ (2 mol %) in the presence (red) or absence (blue) of 1 M NaCl. (E) Macrophages transfected with R-pre, KR ϕ , or K-myristoyl. (F) Macrophages transfected with K-Ras tail containing +8, +4, and +2 charges. Scale bars, 2 μ m. (G) Effect of charge on the membrane/cytosol ratio of K-Ras tail variants.

An alternative means of reducing surface charge is to inhibit the ongoing formation of polyphosphoinositides by depleting cellular

adenosine triphosphate (ATP). Simultaneous impairment of glycolysis and mitochondrial respiration was accompanied by dissociation

of PH-PLC δ -GFP from the membrane, indicating loss of PIP₂ (Fig. 2A). All three cationic probes detached from the plasma membrane of ATP-depleted cells, whereas GPI-GFP, GT46, and Palm remained unaltered (Fig. 2, A and B).

Flipping of PS can be induced by the anesthetic dibucaine, as indicated by the marked increase in annexin-V binding (Fig. 2A). Loss of PS from the inner leaflet, together with the positive charges contributed by dibucaine itself, sufficed to displace R-pre, KR ϕ , and K-my ν from the membrane (Fig. 2A). Because the three probes responded similarly to all treatments, regardless of their mode of hydrophobic interaction with the membrane, we conclude that their dissociation occurred in response to changes in surface charge. These probes are therefore suitable for monitoring the surface potential of the inner aspect of the plasma membrane.

We next applied the cationic probes to study membrane remodeling during phagocytosis. Confocal imaging was used to monitor ingestion of immunoglobulin G–opsonized latex particles by macrophages expressing the surface potential probes. The hydrophobically anchored markers were used along with the cationic probes to control for remodeling caused by fusion and fission events. The cationic and hydrophobically anchored probes localized to the nascent phagocytic cup (Fig. 3A and fig. S2, B and C). Both probes were also present in pseudopods as they progressed along the sides of the particle, although the cationic probes were often partially depleted from the base

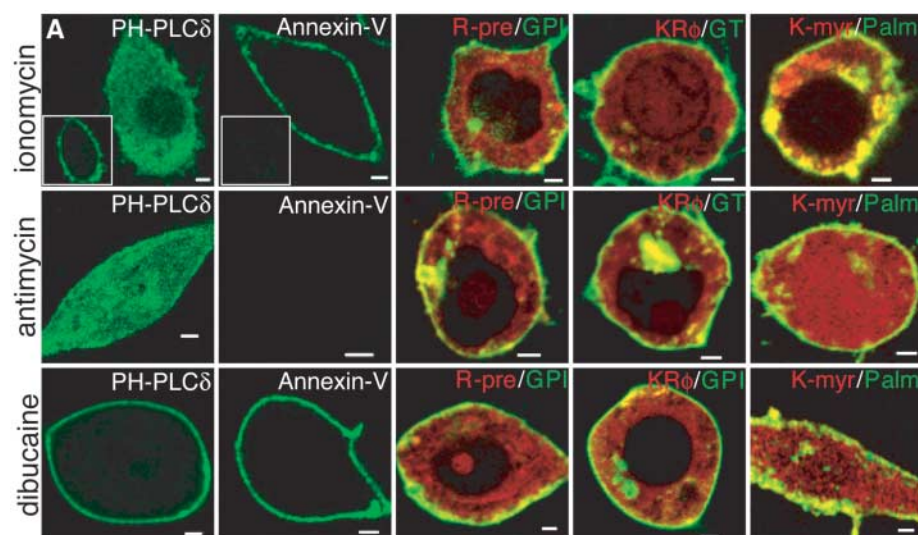


Fig. 2. Effect of manipulating surface potential on probe distribution. (A) Distribution of probes in cells treated with ionomycin (top), antimycin/deoxyglucose (middle), or dibucaine (bottom). Insets: cells before ionomycin. Scale bars, 2 μ m. (B) Quantification of effect of treatments on probe distribution (ratio of membrane fluorescence of probes specified). Data are means \pm SE ($n > 20$).

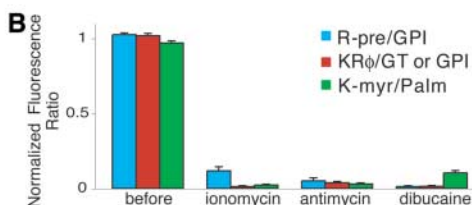
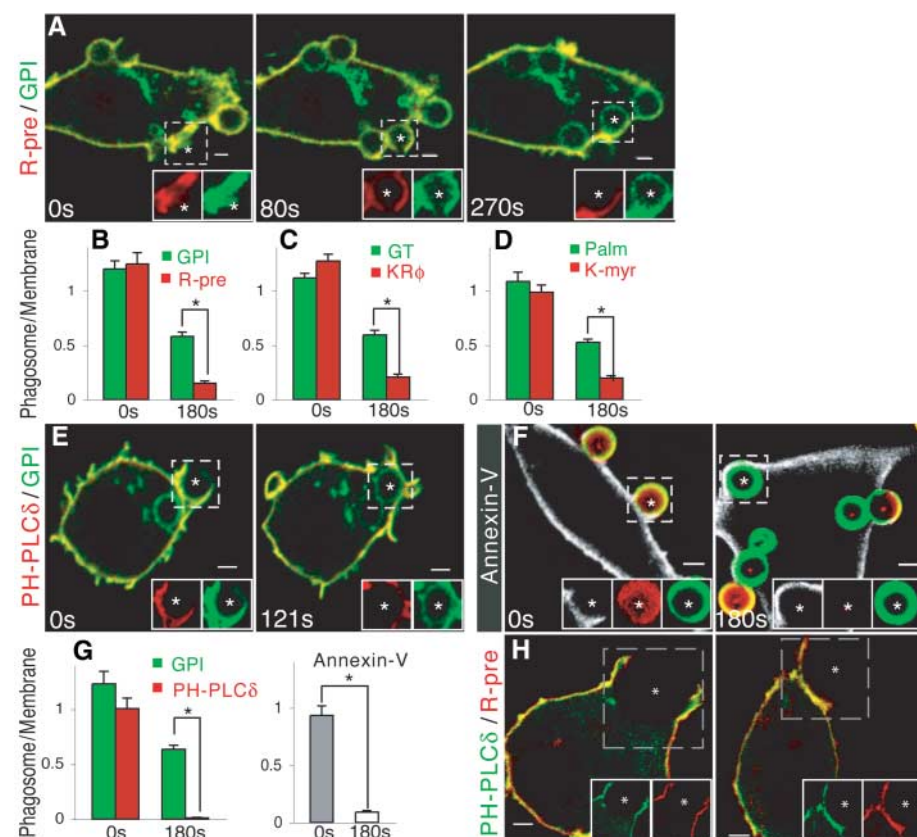


Fig. 3. Charge and lipid changes during phagocytosis. (A) Time course of R-pre/GPI-GFP redistribution. Asterisks indicate latex beads. (B to D) Fluorescence ratio of probes in phagosomal membrane/unengaged plasma membrane, calculated at onset of phagocytosis (0 s) and after 180 s. Data are means \pm SE ($n > 20$); * $P < 0.001$. (E) Redistribution of PH-PLC δ and GPI-GFP during phagocytosis. (F) Distribution of PS (white) during phagocytosis. Green, total beads; red, extracellular beads. (G) Fluorescence ratio of PH-PLC δ , GPI-GFP, or annexin-V in phagosomal membrane/unengaged plasma membrane. Data are means \pm SE ($n \geq 16$); * $P < 0.001$. (H) Distribution of R-pre (red) and PH-PLC δ (green) in absence (left) or presence (right) of LY294002. In (A), (E), and (H), insets show separately the fluorescence of RFP (red) and GFP (green) of the area boxed in the main panels. In (F), insets show (from left to right) PS, external beads, and total beads. Scale bars, 2 μ m.



of the cup at this intermediate stage (Fig. 3A and fig. S2, A to C). At more advanced stages of internalization, a further reduction of the cationic probes was observed, which was invariably followed by near-total depletion shortly after completion of particle engulfment (Fig. 3A; fig. S2, B and C; and movies S2 and S3). By contrast, a substantial fraction of the hydrophobically anchored probes remained associated with the phagosome even after internalization was completed (Fig. 3A and fig. S2, B and C). When calculated 3 min after initiation of phagocytosis, the phagosome-to-bulk (unengaged) plasma membrane ratios for R-pre (0.15 ± 0.02), KR ϕ (0.20 ± 0.03), and K-myr (0.20 ± 0.02) were significantly ($P < 0.001$) lower than those for GPI (0.58 ± 0.04), GT46 (0.59 ± 0.04), and Palm (0.52 ± 0.03) (Fig. 3, B to D). The depletion of the cationic probes was more profound than expected on the basis of remodeling, suggesting alterations in the surface potential of forming phagosomes.

We investigated whether changes in anionic lipid composition or distribution account for the alterations in surface potential of the phagosomal membrane. PIP₂ was markedly depleted from forming phagosomes (Fig. 3, E and G, and movie S4). Moreover, dissociation of the cationic probe (R-pre) could be prevented when the loss of PIP₂ was impaired (Fig. 3H).

Because PS contributes ~30% of the charge on the plasma membrane, its fate during phagocytosis was also studied. Annexin-V was used to monitor the distribution of PS at the onset of phagocytosis and 3 min thereafter. In nonpermeabilized cells, there was no discernible binding of annexin-V; this result implies that little PS is present on the outer monolayer before, during, or after phagocytosis. To gain access to PS in the inner leaflet, we fixed cells and gently permeabilized them with saponin. PS was clearly detectable at the base of nascent phagosomes but appeared greatly depleted from formed phagosomal vacuoles (Fig. 3, F and G). Similar results were obtained with a PS-specific antibody (fig. S4). Jointly, the metabolism of PS and phosphoinositides could account for the changes in surface potential during phagocytosis.

Could the change in surface potential have physiological consequences? Molecules attracted to the membrane by its negative potential are anticipated to dissociate, possibly altering signal transduction and cytoskeletal structure. The fact that certain members of the Ras superfamily (e.g., K-Ras, Rac1) contain a polybasic domain gives credence to this concept (8). K-Ras constitutively associates with the plasma membrane by both prenylation and a polycationic domain in its hypervariable region (Fig. 4A) (8). The importance of the positive charges in this region was validated by introduction of three negatively charged residues, which resulted in partial dissociation of the protein from the plasmalemma (Fig. 4A). Moreover, K-Ras responded to changes in surface potential induced by ionomycin, whereas H-Ras, which is dually palmitoy-

lated, was unaffected (Fig. 4A). As anticipated, H-Ras was retained in sealed phagosomes to an extent comparable to that of the GPI-anchored marker (Fig. 4, A and B). In sharp contrast, K-Ras was virtually absent from formed phagosomes (Fig. 4, A and B, and movie S6).

Like K-Ras, Rac1 also contains a polybasic domain (9). Recombinant prenylated Rac1 bound

preferentially to anionic (PS/PC-coated) beads relative to beads coated with PC only (Fig. 4C). Moreover, mutation of the cationic residues in the polybasic region to glutamine resulted in dissociation of constitutively active Rac1(Q61L) from the plasmalemma (Fig. 4D), and Rac1(Q61L) localization was sensitive to changes in surface potential, whereas a mutant with the polybasic

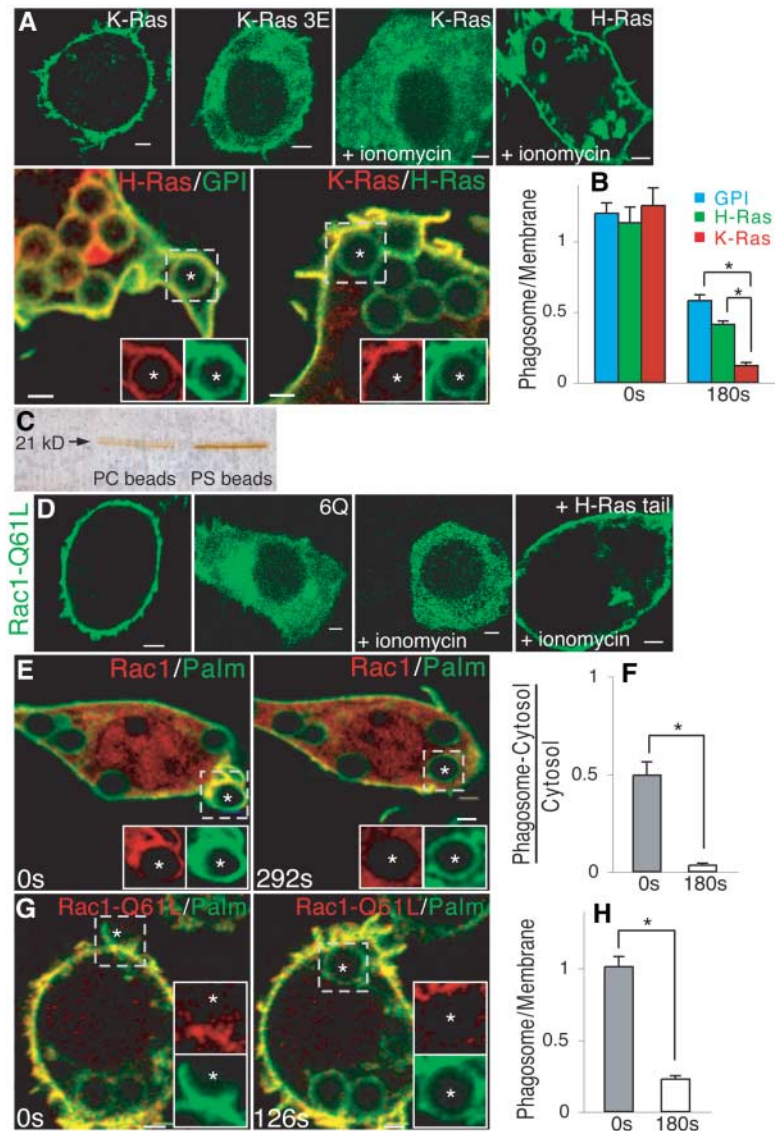


Fig. 4. Surface potential modulates guanosine triphosphatase localization. (A) Top: Distribution of full-length K-Ras, K-Ras-3E, and H-Ras before and after ionomycin treatment. K-Ras 3E is a mutant form of K-Ras with three additional negative charges (see fig. S6 for structure). Bottom: Distribution of H-Ras and GPI-GFP (left) or K-Ras and H-Ras (right) during phagocytosis. (B) Phagosome/bulk membrane ratio of GPI-GFP, H-Ras, or K-Ras at onset of phagocytosis (0 s) or after 180 s. Data are means \pm SE ($n > 20$); $*P < 0.01$. (C) Full-length prenylated Rac1 partitions preferentially (by a factor of 2.3 ± 0.7 ; $n = 8$) to beads coated with PC/PS (80/20 mol %) relative to beads coated with PC (100 mol %). (D) Distribution of Rac1(Q61L), Rac1(Q61L)-6Q, or Rac1(Q61L)-H-Ras tail before and after ionomycin treatment. From left to right: plain Rac1(Q61L); Rac1(Q61L)-6Q; plain Rac1(Q61L), treated with ionomycin; Rac1(Q61L)-H-Ras tail, treated with ionomycin [see fig. S6 for structures of Rac1(Q61L)-6Q and Rac1(Q61L)-H-Ras tail]. (E) Redistribution of Rac1 and Palm during phagocytosis. (F) Phagosome/cytosol ratio of wild-type Rac1 at 0 and 180 s. Data are means \pm SE ($n > 20$); $*P < 0.001$. (G) Redistribution of Rac1(Q61L) and Palm during phagocytosis. (H) Phagosome/membrane ratio of Rac1(Q61L) at 0 and 180 s. Data are means \pm SE ($n > 20$); $*P < 0.01$. Scale bars, 2 μ m.

domain substituted by the hydrophobic tail of H-Ras was not (Fig. 4D). Rac1 is of particular importance to Fc receptor-mediated phagocytosis and accumulates at the base of forming phagosomes, detaching rapidly upon sealing (Fig. 4, E and F, and fig. S7A) (10). Rac1(Q61L) also detached from sealing phagosomes with kinetics indistinguishable from those of wild-type Rac1 (Fig. 4, G and H, and movie S7). Because Rac1(Q61L) is constitutively bound to guanosine triphosphate (GTP), its dissociation from phagosomes was not due to nucleotide hydrolysis or cessation of nucleotide exchange. Instead, release was likely mediated by termination of its electrostatic association with the plasmalemma. Accordingly, the C-terminal tail of Rac1 containing the polybasic domain behaved similarly (fig. S7B).

Our data indicate that the surface potential of the inner leaflet of the membrane decreases locally during phagosome formation. The change is attributable primarily to depletion of PIP₂ and PS, but depletion of phosphatidylinositol 4-phosphate was also observed (fig. S3 and movie S5). Activation of inositol lipases, kinases, and phosphatases occurs during phagocytosis and bacterial invasion (3), readily accounting for the changes in PIP₂, PS

could be converted to PE by decarboxylation or could be externalized during phagocytosis by scramblases and/or efflux pumps.

Our results also indicate that the anchorage of important signaling molecules, including K-Ras and Rac1, can be modulated focally by localized changes in surface potential. Other proteins anchored electrostatically to the membrane, such as MARCKS, are equally susceptible to the charge alterations that accompany lipid remodeling. Indeed, we also obtained evidence for localized detachment of the tyrosine kinase c-Src (fig. S5, B and C).

The consequences of altered surface charge in other important biological phenomena must be considered. Activation of phosphoinositide metabolism, elevation in cytosolic calcium, and PS flipping occur after stimulation of multiple receptors and channels as well as during apoptosis. The effect of such responses on inner surface potential may be measurable with the use of approaches like the one described here. Cycles of membrane dissociation/reassociation may add a layer of functional control to complement the traditional biochemical mode of regulation of signaling proteins.

References and Notes

1. M. Olivetto, A. Arcangeli, M. Carla, E. Wanke, *Bioessays* **18**, 495 (1996).
2. S. McLaughlin, A. Aderem, *Trends Biochem. Sci.* **20**, 272 (1995).
3. R. J. Botelho, C. C. Scott, S. Grinstein, *Curr. Top. Microbiol. Immunol.* **282**, 1 (2004).
4. R. Leventis, J. R. Silvius, *Biochemistry* **37**, 7640 (1998).
5. See supporting material on Science Online.
6. M. O. Roy, R. Leventis, J. R. Silvius, *Biochemistry* **39**, 8298 (2000).
7. J. B. McCabe, L. G. Berthiaume, *Mol. Biol. Cell* **12**, 3601 (2001).
8. J. F. Hancock, H. Paterson, C. J. Marshall, *Cell* **63**, 133 (1990).
9. D. Michaelson *et al.*, *J. Cell Biol.* **152**, 111 (2001).
10. A. D. Hoppe, J. A. Swanson, *Mol. Biol. Cell* **15**, 3509 (2004).
11. We thank E. Pick for providing Rac1 and D. Russell for providing Nucleosil beads. Supported by the Canadian Institutes for Health Research and an NIH grant, by a Canadian Institutes of Health Research studentship (T.Y.), and by the Pitblado Chair in Cell Biology (S.G.).

Supporting Online Material

www.sciencemag.org/cgi/content/full/313/5785/347/DC1

Materials and Methods

Figs. S1 to S7

Movies S1 to S7

4 May 2006; accepted 5 June 2006

10.1126/science.1129551

Parallel Declines in Pollinators and Insect-Pollinated Plants in Britain and the Netherlands

J. C. Biesmeijer,^{1*} S. P. M. Roberts,² M. Reemer,³ R. Ohlemüller,⁴ M. Edwards,⁵ T. Peeters,^{3,6} A. P. Schaffers,⁷ S. G. Potts,² R. Kleukers,³ C. D. Thomas,⁴ J. Settele,⁸ W. E. Kunin¹

Despite widespread concern about declines in pollination services, little is known about the patterns of change in most pollinator assemblages. By studying bee and hoverfly assemblages in Britain and the Netherlands, we found evidence of declines (pre- versus post-1980) in local bee diversity in both countries; however, divergent trends were observed in hoverflies. Depending on the assemblage and location, pollinator declines were most frequent in habitat and flower specialists, in univoltine species, and/or in nonmigrants. In conjunction with this evidence, outcrossing plant species that are reliant on the declining pollinators have themselves declined relative to other plant species. Taken together, these findings strongly suggest a causal connection between local extinctions of functionally linked plant and pollinator species.

Anthropogenic changes in habitats and climates have resulted in substantial reductions in biodiversity among many vertebrate taxa (1), and evidence has been accumulating that insect biodiversity is at risk as well (2). Of particular concern is the possibility of community-level cascades of decline and extinction (3), whereby decline of some elements of the biota lead to the subsequent loss of other species that directly or indirectly rely upon them. Here we examine sets of pollinators and the plants that they pollinate to test (i) whether species that are linked to one another within communities show coincident declines and (ii) whether species with more links within communities are more robust to change because of

the availability of alternative links, if an interacting species is lost.

Any loss in biodiversity is a matter of public concern, but losses of pollinating insects may be particularly troubling because of the potential effects on plant reproduction. Many agricultural crops and natural plant populations are dependent on pollination and often on the services provided by wild, unmanaged, pollinator communities. Substantial concerns have been raised about the decline or loss of these services [(4) but see (5)], culminating in formal recognition within the Convention on Biological Diversity (6) in the São Paulo Declaration (7) and the International Initiative for the Conservation and Sustainable Use of Pollinators (8).

However, the evidence for such declines remains scanty (5).

To adequately demonstrate a decline in pollinator services, one would need to document (i) overall declines in pollinator density; and/or (ii) reductions in species diversity or substantial shifts in the species composition of pollinator communities, combined with changes in the distribution of traits represented in those communities (thus indicating that the loss of some pollinators has not been compensated by the rise of functionally equivalent species); and (iii) declines in either the reproductive success or abundance of plant species dependent on these pollinators. No suitable data are available to address overall pollinator density, but here we provide evidence for the remaining points, using data for bees, hoverflies, and plants from Britain and the Netherlands.

We compiled almost 1 million records for bee (all native species except the largely

¹Institute of Integrative and Comparative Biology and Earth and Biosphere Institute, University of Leeds, Leeds, LS2 9JT, UK. ²Centre for Agri-Environmental Research, University of Reading, Reading, RG6 6AR, UK. ³European Invertebrate Survey–Netherlands/National Museum of Natural History Naturalis, Postbus 9517, 2300 RA Leiden, Netherlands. ⁴Department of Biology, University of York, York, YO10 5YW, UK. ⁵Lea-side, Carron Lane, Midhurst, GU29 9LB, West Sussex, UK. ⁶Department of Animal Ecology, Bargeveen Foundation, Radboud University of Nijmegen, Postbox 9010, 6500 GL Nijmegen, Netherlands. ⁷Nature Conservation and Plant Ecology Group, Wageningen University and Research Centre, Bornesteeg 69, 6708 PD Wageningen, Netherlands. ⁸Umweltforschungszentrum—Centre for Environmental Research Leipzig-Halle, Community Ecology (Biozönoseforschung), Theodor-Lieser-Strasse 4, 06120 Halle, Germany.

*To whom correspondence should be addressed. E-mail: j.c.biesmeijer@leeds.ac.uk

domesticated honeybee *Apis mellifera*) and hoverfly observations for both countries from national entomological databases (9), focusing on areas with extensive sets of observations before and after 1980. We then applied rarefaction methods to compare species richness of focal areas over each period (10). This approach allows valid comparisons between time periods, despite unequal sample sizes and the incorporation of records collected by many recorders who used different collecting techniques over long time spans (10).

Bee diversity declined in large fractions of the 10 km by 10 km cells analyzed in both countries (Fig. 1). Bee richness was measured as the number of distinct species; significant decreases in richness were observed in 52% and ~67% of British and Dutch cells, respectively, as compared with richness increases in 10% and 4% of cells in the two countries (table S1). Shifts in hoverfly diversity were less consistent (Fig. 1), with no significant directional change in richness for the UK (increases in 25% and decreases in 33% of British cells); however, increases in hoverfly richness were reported in 34%, versus decreases in 17%, of Dutch cells (table S1).

These shifts in species richness reflect shifts in the distributions of many species in both groups. Our data set does not allow direct measurement of population densities of the species involved; nonetheless, shifts over time in the relative number of records for different species can be used as an indicator of their relative frequency and ubiquity (10). There has been an increase in the domination of the pollinator communities of both countries by a smaller number of species. For both taxa in both countries, about 30% fewer species account for half of the post-1980 records (percentages of fewer species: British bees, 29%; British hoverflies, 29%; Netherlands bees, 32%; Netherlands hoverflies, 36%). In Britain, the species that increased were disproportionately the ones that were already common before 1980; however, in the Netherlands, this was not the case (11).

The functional diversity of pollination networks contributes to the maintenance of diversity in plant communities (12), with different groups of pollinators being complementary in their pollination services and different groups of plants being complementary in their roles as food plants for pollinators. Consequently, a decline in pollinator diversity might have little effect on a community if the fluctuating species were functionally similar. However, the traits of increasing and declining species of solitary bees and hoverflies differ in consistent ways (Table 1). In both countries and in both groups, species with narrow habitat requirements have experienced greater relative declines. In solitary bees, oligolectic species (those using few flower taxa as food sources) have declined significantly in Britain, and long-tongued taxa have declined significantly in the Netherlands. Die-

tary specialization is important in hoverflies as well, with both adult and larval diets being strongly related to changes in hoverfly occurrence. Migratory hoverflies have fared better than nonmigratory species in both countries. In Britain, bee and hoverfly declines are greater among species with only a single generation per year; however, this pattern is not found in the Netherlands. The significant trends indicate that specialized species [i.e., in habitat and dietary requirements and, arguably, tongue length (12, 13)] and species characterized by slower development and lower mobility (those having fewer generations per year and being nonmigratory) tend to decline more than generalist, fast developing, and more mobile species.

Such shifts in pollinator traits suggest possible shifts in pollination services. Indeed, recent experiments have shown that the functional diversity of pollinators can affect diversity in plant communities (12). We know of no data that will allow us to assess directly whether rates of pollinator visitation or pollen deposition to flowers have shifted appreciably

in Britain or the Netherlands. We can, however, examine shifts in plant species distributions using floral inventories from both countries (10, 14, 15) to see whether shifts in plants are consistent with the observed shifts in pollinators. In Britain, obligately outcrossing plants reliant on insect pollinators were declining on average; species reliant on abiotic (wind or water mediated) pollination were increasing; and self-pollinating plant species showed an intermediate response (Table 2). In the Netherlands, changes were not significantly different among these three groups; however, given the observed decline in bees and increase in hoverflies in the Netherlands, divergent trends between bee-pollinated plants and other insect-pollinated plants may be expected there. After reexamining the data on the insect taxa reported as pollinators of outcrossing plants (15), we found that, on average in the Netherlands, plants that were exclusively pollinated by bees were declining, but plants pollinated by flies and other insects (including bees) were increasing. If the changes among bee-pollinated outcrossers, out-

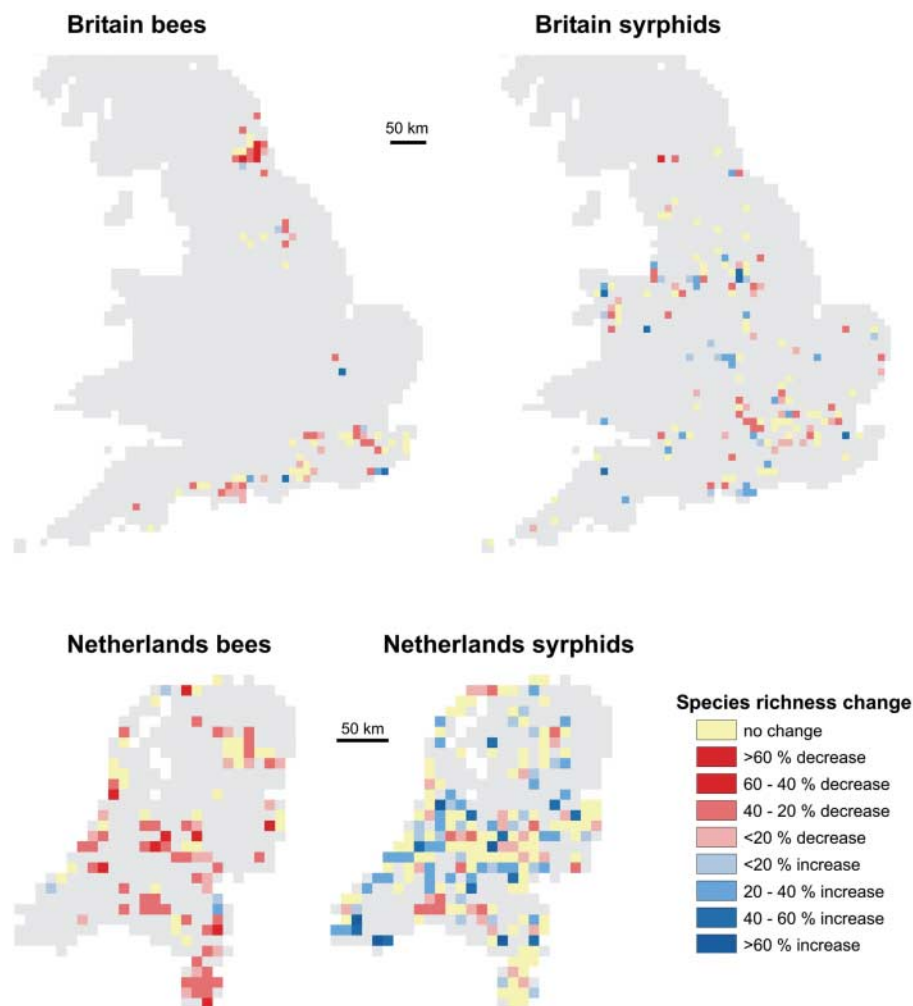


Fig. 1. Bee and hoverfly richness has changed in many of the 10 km by 10 km cells analyzed for Britain and the Netherlands. Some British cells contained adequate data only on eusocial or only on solitary bees (10). Changes in species richness were calculated from rarefaction analyses (10).

crossers with abiotic pollination, and predominantly self-pollinating plants are compared, the trends observed in the Netherlands mirror those for Britain: Bee-dependent plants have declined, abiotically pollinated plants have increased, and plants mainly relying on self-pollination have shown an intermediate response (Table 2).

We cannot tell from these data whether the decline of the plants precedes the loss of the

associated pollinators, whether the decline of the pollinators leads to the loss of reproductive function and then to the decline of the plants, or indeed whether the plants and their pollinators are both responding to some other factor. However, the results clearly show that linked elements in biological communities (i.e., specialist pollinators and the obligately outcrossed plants that they pollinate) are declining in tandem.

Furthermore, the difference between the two countries implies that there is probably a causal link, because it is the corresponding groups of plants and pollinators in both countries that are changing. The hypothesis that species that rely on a broader range of other species within a community are more robust in the face of change is supported by the following evidence: Pollinators that rely on few plants for their resources have declined the most, whereas generalists have prospered [compare with (16)]. Moreover, the decline of bees (specialized as pollinators) relative to hoverflies (having broader feeding habits) could be interpreted in this light.

Demonstrating that there are shifts in pollinator assemblages and associated changes in wild plant communities in two countries does not prove the existence of a global pollination crisis. Britain and the Netherlands are not only two of the countries with the best available data but also two of the most densely populated and anthropogenically modified landscapes on the planet. Few British habitats can be thought of as truly natural, and in the Netherlands the landscape is largely artificial. Nonetheless, it seems probable that shifts similar to those documented for these countries will be found in other parts of northwest Europe and, increasingly, in other regions (17). Documenting the geographical extent of the declines shown here is a priority for future research. It is also important to begin mechanistic studies of the causes of these declines, with habitat alteration (18), climate change (19–21), and agricultural chemical usage (18, 22) being potential key drivers of observed shifts (23).

Table 1. Trait-based patterns in pollinator declines. Proportions are based on species that showed significant change in the number of cells (*n*) in which they were reported during the two time periods (pre- and post-1980). Declining solitary bee and hoverfly species tend to be found more among the specialists (characterized by narrow habitat ranges, limited dietary choice, slower development, and greater residency) than among generalist species (characterized by wide habitat ranges, broader dietary choice, multiple generations per year, and greater tendency toward migration). Traits were assigned by using methodologies in (25) and (26). Bumblebees and honeybees were excluded from the analysis (10). Oligo, oligolectic; Poly, polylectic; Uni, univoltine; Multi, multivoltine; Macro, macroorganisms; Micro, microorganisms; Res, resident; Mig, migrant.

Trait	Britain		Netherlands					
	Trait category (proportion declining)		<i>P</i>	<i>n</i>	Trait category (proportion declining)		<i>P</i>	<i>n</i>
<i>Solitary bees</i>								
Habitat range	Narrow (0.90)	Wide (0.25)	0.0001	32	Narrow (0.83)	Wide (0.53)	0.090	29
Flower specificity	Oligo (0.86)	Poly (0.41)	0.034	34	Oligo (0.55)	Poly (0.76)	0.198	36
Tongue length	Long (0.70)	Short (0.41)	0.099	56	Long (1.00)	Short (0.51)	0.028	49
Generations	Uni (0.60)	Multi (0.14)	0.042	44	Uni (0.76)	Multi (0.55)	0.433	42
<i>Hoverflies</i>								
Habitat range	Narrow (0.96)	Wide (0.28)	0.0001	53	Narrow (0.52)	Wide (0.25)	0.025	67
Adult food	Narrow (0.63)	Wide (0.41)	0.095	60	Narrow (0.53)	Wide (0.16)	0.0001	86
Larval food	Macro (0.74)	Micro (0.43)	0.009	59	Macro (0.59)	Micro (0.20)	0.002	79
Generations	Uni (0.80)	Multi (0.29)	0.0001	50	Uni (0.43)	Multi (0.38)	0.63	88
Migration	Res (0.63)	Mig (0.20)	0.01	64	Res (0.46)	Mig (0.17)	0.025	88

Table 2. Mean relative change (±SE) in distribution of British (27) and Netherlands (28) plant species according to their main pollen vector (10). Insect-pollinated outcrossing plants in Britain and bee-pollinated outcrossing plants in the Netherlands have declined, whereas plants with abiotic pollination have increased. Plant breeding systems were derived by combining the ECOFLOR (29) and BIOLFLORE (30) databases (10). British data were tested with an analysis of variance and a post hoc Tukey test. Netherlands data were tested with a Kruskal-Wallis test and a post hoc multiple comparison test. Superscripts indicate group differences based on post hoc tests. *n*, number of plant species; NL, Netherlands.

	Obligatory outcrossing, insect pollinated	Obligatory outcrossing, wind or water pollinated	Predominantly self pollinating	<i>P</i>
Britain	-0.22 ± 0.06* (<i>n</i> = 75)	+0.18 ± 0.14†	-0.003 ± 0.70*†	0.009
Netherlands	+0.10 ± 0.08 (<i>n</i> = 182)	+0.18 ± 0.08	-0.08 ± 0.11	0.091
NL bee plants	-0.12 ± 0.13* (<i>n</i> = 42)	+0.18 ± 0.08†	-0.08 ± 0.11*†	0.036

References

1. S. L. Pimm, G. J. Russell, J. L. Gittleman, T. M. Brooks, *Science* **269**, 347 (1995).
2. J. A. Thomas *et al.*, *Science* **303**, 1879 (2004).
3. F. S. Chapin III *et al.*, *Science* **277**, 500 (1997).
4. S. Diaz *et al.*, in *Ecosystems and Human Well-Being: Current State and Trends, Volume 1*, R. Hassan, R. Scholes, N. Ash., Eds. (Island Press, Washington, DC, 2005), pp. 297–329.
5. J. Ghazoul, *Trends Ecol. Evol.* **20**, 367 (2005).
6. Convention on Biological Diversity (www.biodiv.org/default.shtml).
7. International Pollinators Initiative, the São Paulo Declaration on Pollinators (Brazilian Ministry of the Environment, 1999); (www.biodiv.org/doc/case-studies/agri/cs-agr-pollinator-rpt.pdf).
8. Agricultural Biodiversity—International Initiative for the Conservation and Sustainable Use of Pollinators (www.biodiv.org/programmes/areas/agro/pollinators.asp).
9. Dutch data on bees are held in the Apidae database of the European Invertebrate Survey—Netherlands (EIS-NL). Dutch data on hoverflies are held in the Syrphidae database of EIS-NL, the Dutch Youth Organisation for Nature Study, and the Dutch Entomological Society. British bee data were compiled by S.P.M.R., M.E., and J.C.B. from data of the UK Bees, Wasps, and Ants Recording Society. British hoverfly data were obtained from the National Biodiversity Network (www.searchnbn.net), largely based on the Hoverfly Recording Scheme.
10. Materials and methods are available as supporting material on *Science* Online.
11. Results of a Mann-Whitney test comparing pre-1980 cell totals for significantly declining versus significantly increasing species: British bees, *P* = 0.005; British

- hoverflies, $P < 0.0001$; Netherlands bees, $P = 0.07$ (the reverse trend); Netherlands hoverflies, $P = 0.10$.
12. C. Fontaine, I. Dajoz, J. Meriguet, M. Loreau, *PLoS Biol.* **4**, e1 (2006).
 13. M. Stang, P. G. L. Klinkhamer, E. Van der Meijden, *Oikos* **112**, 111 (2006).
 14. C. D. Preston, D. A. Pearman, T. D. Dines, *New Atlas of the British and Irish Flora: An Atlas of the Vascular Plants of Britain, Ireland, the Isle of Man, and the Channel Islands* (Oxford Univ. Press, Oxford, 2002).
 15. *Biobase 2003*, Centraal Bureau voor de Statistiek, Voorburg/Heerlen, The Netherlands (2003).
 16. J. Memmott, N. M. Waser, M. V. Price, *Proc. R. Soc. London Ser. B* **271**, 2605 (2004).
 17. J. Banaszak, Ed. *Changes in Fauna of Wild Bees in Europe* (Pedagogical University, Bydgoszcz, Poland, 1995).
 18. J. A. Foley *et al.*, *Science* **309**, 570 (2005).
 19. C. D. Thomas *et al.*, *Nature* **427**, 145 (2004).
 20. M. S. Warren *et al.*, *Nature* **414**, 65 (2001).
 21. C. Parmesan, G. Hoyle, *Nature* **421**, 37 (2003).
 22. P. G. Kevan, *Biol. Conserv.* **7**, 301 (1975).
 23. A Europe-wide assessment of the risks associated with pollinator loss and its drivers is currently being undertaken within the 6th European Union Framework Programme—Assessing Large-scale Environmental Risks for Biodiversity with Tested Methods project [GOCE-CT-2003-506675 (www.alarmpoint.net)], of which this study is a core element (24).
 24. J. Settele *et al.*, *GAIA* **14**, 69 (2005).
 25. S.P.M.R. compiled trait data of European bees from published sources (see www.alarmpoint.net).
 26. M. Speight, E. Castella, J.-P. Sarthou, C. Monteil, Eds., *Syrph the Net on CD, Issue 2. The Database of European Syrphidae* (Syrph the Net Publications, Dublin, 2004).
 27. Change indices from (14) were calculated from occupancy data in surveys conducted from 1930 to 1969 and from 1987 to 1999.
 28. Comparison of the number of 5 km by 5 km cells occupied in 1940 and 1990. Data from Biobase (15) were organized into frequency classes by A.P.S. (10).
 29. The Ecological Flora of the British Isles at the University of York (www.york.ac.uk/res/ecoflora/cfm/ecofl/index.cfm).
 30. S. Klotz, I. Kühn, W. Durka, Eds. *BIOLFLORE: A Database on Biological and Ecological Traits of the German Flora* (Bundesamt für Naturschutz, Bonn, 2002).

Supporting Online Material

www.sciencemag.org/cgi/content/full/313/5785/351/DC1

Materials and Methods

Figs. S1 and S2

Tables S1 and S2

References

24 March 2006; accepted 6 June 2006

10.1126/science.1127863

Crystal Structure of a Divalent Metal Ion Transporter CorA at 2.9 Angstrom Resolution

Said Eshaghi,^{1*}† Damian Niegowski,^{1,2*} Andreas Kohl,¹ Daniel Martinez Molina,^{1,2} Scott A. Lesley,³ Pär Nordlund^{1†}

CorA family members are ubiquitously distributed transporters of divalent metal cations and are considered to be the primary Mg^{2+} transporter of Bacteria and Archaea. We have determined a 2.9 angstrom resolution structure of CorA from *Thermotoga maritima* that reveals a pentameric cone-shaped protein. Two potential regulatory metal binding sites are found in the N-terminal domain that bind both Mg^{2+} and Co^{2+} . The structure of CorA supports an efflux system involving dehydration and rehydration of divalent metal ions potentially mediated by a ring of conserved aspartate residues at the cytoplasmic entrance and a carbonyl funnel at the periplasmic side of the pore.

Divalent metal cations are essential cofactors in many proteins. To provide cells with appropriate concentrations of divalent metal cations, highly regulated transporters and channels have evolved to translocate these ions across the hydrophobic membranes. CorA is one of the best studied families of divalent cation transporters (1–9). It is considered to be the primary Mg^{2+} transporter of both Bacteria and Archaea and is ubiquitously distributed (8). Sequence homologies between members of this family are most pronounced at the C termini; sequence conservation in the N termini is less significant (fig. S1). The overall sequence similarity between eukaryotes and prokaryotes is weak, except for the highly conserved Gly-Met-Asn (GMN) motif close to the C termini (10, 11). Never-

theless, some eukaryotic CorA family members show overlapping activities with the prokaryotic members that suggests functional, as well as structural, conservation (4, 10, 12, 13). Studies of CorA from *Salmonella typhimurium*, *Escherichia coli*, and the Archaeon *Methanococcus jannaschii* demonstrate that ions can be transported in both directions (1–3, 5, 8, 9).

Kehres and Maguire recently reported two classes of CorAs among Bacteria and Archaea (8). The second class, CorA-II, which differs from the extensively studied *S. typhimurium* and *E. coli* CorAs, was suggested to contain two transmembrane helices, with both termini in the cytosol. In the same report, the CorA-II proteins were suggested to be efflux systems. Moreover, a novel CorA-related protein, ZntB, was recently identified in *S. typhimurium* (14). ZntB was shown to be a Zn^{2+} efflux system with two predicted transmembrane helices and both termini facing the cytosol (15). This is in contrast with the predicted topology of *S. typhimurium* and *E. coli* CorA, with three transmembrane helices and the N terminus facing the periplasm.

Here, we report the crystal structure of a full-length CorA homolog from *Thermotoga maritima*, at 2.9 Å resolution. The recently

reported structure of a pentameric full-length CorA at 3.9 Å was used for molecular replacement, revealing two pentamers in the asymmetric unit (16). The structure has been refined to an R of 27.6% and an R_{free} of 29.5% with good stereochemistry (table S1).

The CorA structure reveals a pentamer with the shape of a cone (Fig. 1). The tip of the cone is formed by two transmembrane (TM) helical segments from each monomer and the large opening of the cone by the N-terminal region of CorA. The fold of the CorA monomer is composed of an N-terminal α/β domain with a central seven-stranded mixed β sheet lined by three small helices. Two long α helices cover one face of the α/β domain and form a bundle together with a giant α helix 7 constituted by ~70 residues. The C-terminal end of helix 7 constitutes the first transmembrane segments (residues 291 to 312). Following the large helix 7 is helix 8 (residues 327 to 349), which forms the second TM helix and packs in a ring around the TM segment of helix 7 (Fig. 1).

Thermotoga maritima CorA is most closely related to the class II CorA with both N- and C-terminal ends facing the cytosol and, therefore, is likely to be primarily involved in ion efflux. The localization of the N termini in the cytoplasm is also supported by the positive-inside rule (17) and the $N_{in}-C_{in}$ topology of “helical hairpin” structures (18). Sequence alignment of close homologs of *T. maritima* CorA and those of *S. typhimurium* CorA support the proposal for two distinct classes of CorA (fig. S1).

Our structure agrees in all general features with the structure determined by Lunin *et al.* (16) that was used for phasing. However, because of the higher resolution of 2.9 Å, our structure provides more details of functionally important regions, including potential regulatory metal binding sites beyond the metal in site 1 (M1) identified in the 3.9 Å structure. Two putative metal-binding sites are found at each interface between the N-terminal domains in the pentamer (Fig. 2). An anomalous difference map of Co^{2+} -soaked crystals shows that Co^{2+}

¹Division of Biophysics, Department of Medical Biochemistry and Biophysics, Karolinska Institute, SE-171 77 Stockholm, Sweden. ²Department of Biochemistry and Biophysics, Stockholm University, S-106 91 Stockholm, Sweden. ³Joint Center for Structural Genomics and Genomics Institute of the Novartis Research Foundation, San Diego, CA 92121, USA.

*These authors contributed equally to this work.

†To whom correspondence should be addressed. E-mail: Par.Nordlund@ki.se (P.N.); Said.Eshaghi@ki.se (S.E.)

can populate these sites, but in the native crystal they are most likely occupied by Mg^{2+} ions, because 100 mM of $MgCl_2$ was present during crystallization (19). Residues from two interacting N-terminal domains contribute a cluster of carboxylates to the interface region where the metal binds. M1 is closely coordinated by the side chains of two carboxylate residues, Asp⁸⁹ and Asp²⁵³. Because Mg^{2+} is most often hexacoordinated in biological systems (20–22), the M1 site is likely coordinated by three or four additional water molecules. Although these waters are not unambiguously defined at the

present resolution, the environment of the sites is constituted by an appropriate network of hydrogen-bonding residues, which can provide a second coordination sphere for these water molecules (residues Asn⁹², Gln⁹⁵, Glu¹⁰⁰, Asp²⁵⁶, and His²⁵⁷). The second metal site, M2, is found some 7 Å from M1, in a cavity surrounded by the main chain of Leu¹² and side chains of Glu⁸⁸, Asp¹⁷⁵, and Asp²⁵³. The distances from the bound cobalt to the surrounding potential protein ligands are greater than 3.5 Å, which is too long for direct coordination. It is possible that the metal ion binds in a fully

hydrated form and that water molecules mediate the metal coordination. The highly negative charge of the ligand sphere, including three carboxylates, implies that the site is well designed to accommodate highly charged cations.

In the region close to the metal-binding sites, a putative Cl^- ion is coordinated to the side chains of Arg¹⁵³ and Tyr¹⁶⁸, and the main chain of Ile¹⁶⁰. Both the metal at the M2 site and this chloride ion appear to be important in stabilizing the confirmation of the N-terminal residues 6 to 13.

A sequence alignment of prokaryotic CorAs reveals that the carboxylate residues coordinating M1 and M2, as well as Arg¹⁵³ coordinating the Cl^- ion, are conserved in all class II CorAs and to some extent in class I CorAs (with the exception of *M. jannaschii*, in which it seems to define a separate class), and these binding sites are therefore likely to be functionally important (fig. S1).

A symmetric five-fold ring of the N-terminal half of helix 7 from the five subunits, including the TM segment, forms the putative ion-transporting pore. The pore is narrowest at three rings formed by Met²⁹¹, Leu²⁹⁴, and Met³⁰², respectively. At the cytosolic side, the pore diameter rapidly increases around Asp²⁷⁷, which eventually leads to the funnel-shaped cavity formed by the N-terminal domain. At the periplasmic site, the pore remains narrow until Tyr³¹¹. No density is detected in the pore region

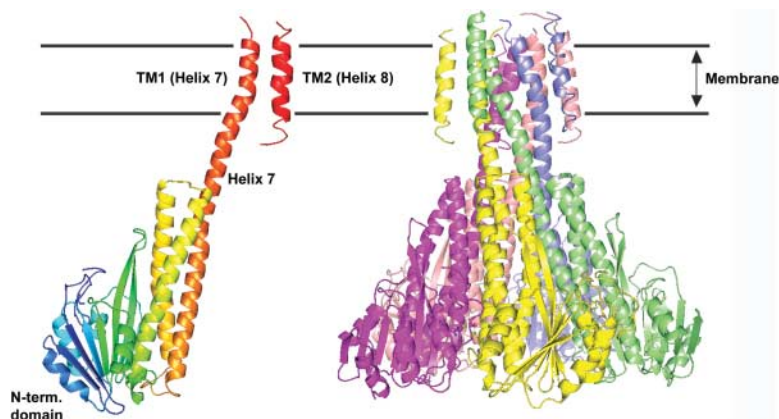


Fig. 1. Overall representation of the CorA. The position of the transmembrane region is indicated.

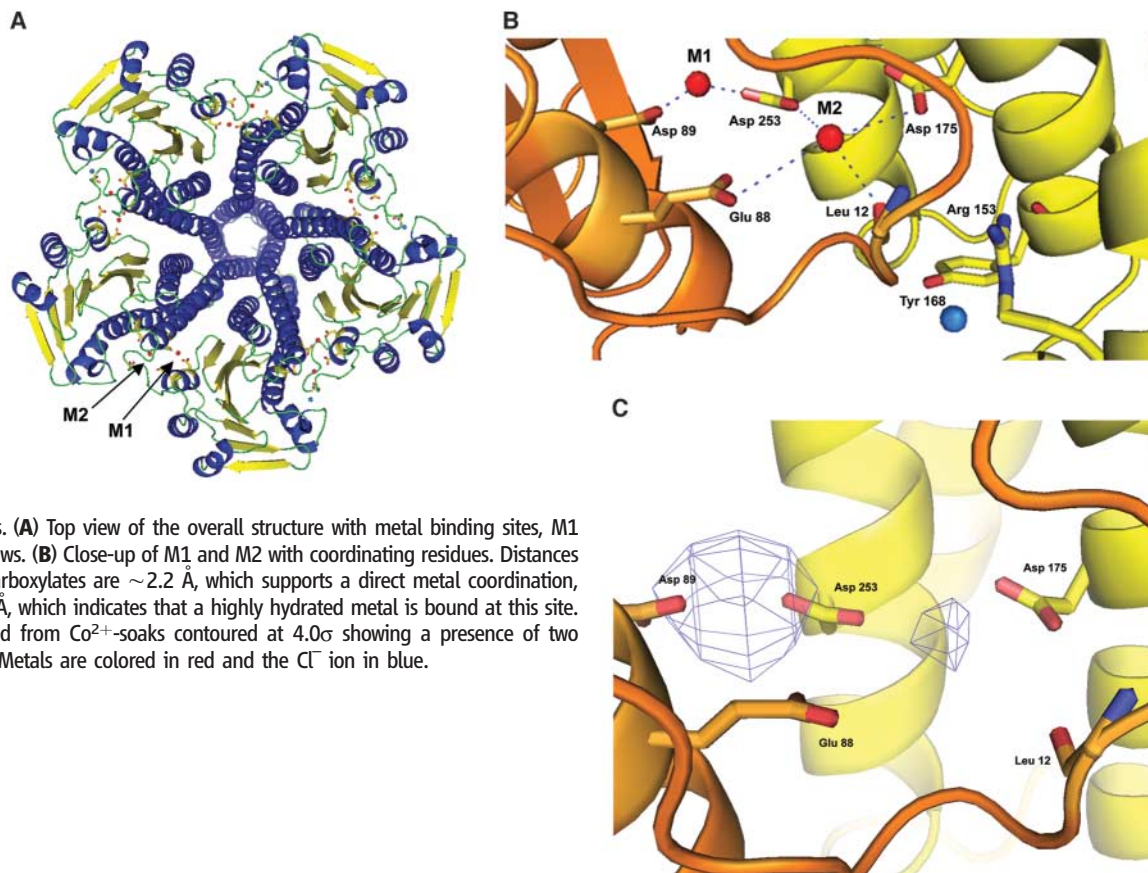


Fig. 2. Metal binding sites. **(A)** Top view of the overall structure with metal binding sites, M1 and M2, indicated with arrows. **(B)** Close-up of M1 and M2 with coordinating residues. Distances from M1 to surrounding carboxylates are ~ 2.2 Å, which supports a direct metal coordination, and for M2 are 3.6 to 4.7 Å, which indicates that a highly hydrated metal is bound at this site. **(C)** Anomalous map derived from Co^{2+} -soaks contoured at 4.0σ showing a presence of two Co^{2+} ions at M1 and M2. Metals are colored in red and the Cl^- ion in blue.

for bound water or metal ions. However, a significant residual density ($\sim 4.5\sigma$ in the $F_{\text{obs}} - F_{\text{calc}}$ maps) is found at the ring formed by the side chains of five symmetry-related Asp²⁷⁷ residues (Fig. 3) in one of the pentamers in the asymmetric unit. This density is asymmetrically located close to two of the five aspartates and is likely due to the binding of one or two metal ions, most probably Mg²⁺. Interestingly, Asp²⁷⁷ is highly conserved among class II CorAs (fig. S1). No similar density was reported in the 3.9 Å structure (16).

The conserved GMN sequence (residues 312 to 314) occurs just after the first TM segment on the periplasmic side. In one of the pentamers in the asymmetric unit, only residual density is present for the region Gly³¹² to Gly³²⁶, and the entrance of the pore is well exposed. In the other pentamer in the asymmetric unit, significant density is present for most of these loops, although an unambiguous placement of the side chains cannot be made. It appears, however, that this density covers the pore entrance, and therefore, the two pentamers represent two different forms, determined by the

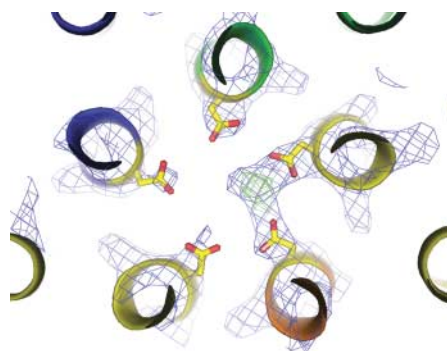
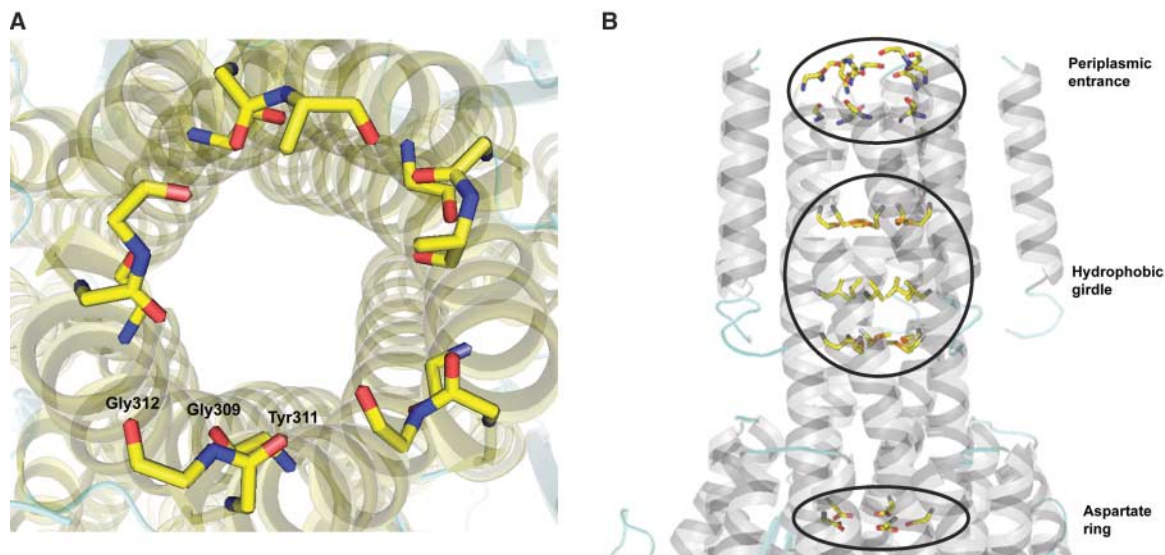


Fig. 3. Top view of Asp²⁷⁷ ring. Blue map, $2F_{\text{obs}} - F_{\text{calc}}$ contoured at 1σ ; green map, $F_{\text{obs}} - F_{\text{calc}}$ map contoured at 3σ showing extra density around Asp²⁷⁷ ring possibly from a bound Mg-ion.

Fig. 4. Charged periplasmic entrance to CorA pore. (A) Carbonyls from Gly³⁰⁹, Tyr³¹¹, and Gly³¹² pointing inward, possibly making dehydration interactions with incoming ion. (B) Side-view of the periplasmic entrance together with the Met²⁹¹, Leu²⁹⁴, and Met³⁰², which form a “hydrophobic girdle,” and the Asp²⁷⁷ ring.



loop structure that can toggle between an open and a more closed form. In the best-defined loops, the main-chain carbonyls of the Tyr-Gly-Met-Asn (YGMN) section are exposed into the central section of the periplasmic entrance of the pore. Furthermore, in the refined model, distortions are present in the last two turns of the TM segment of helix 7, resulting in the carbonyls of Gly³⁰⁹ also being exposed to the pore. These, together with the carbonyls of the conserved YGMN, make a polar strip well suited for interacting with cations (Fig. 4). The distortions of the TM segment persisted, although repeatedly regulated to standard helical positions during the refinement, and are well represented in the electron density. The cause of these distortions is Pro³⁰³, which breaks the regular hydrogen-bonding pattern in the middle of the helix. Note that Pro³⁰³ packs closely on to the side chain of Phe³⁰⁰ (fig. S2). These are the two residues most conserved in the pore region (fig. S1). However, whether this plays a structural and/or mechanistic role (e.g., as a hinge) is not clear from the present structure.

The structure of CorA reveals a TM pore that is different from pores seen in other cation channels (or transporters). The pore has several narrow regions and lacks appropriate polar groups for interacting with cations along more than two-thirds of its 60 Å length. The only polar groups exposed in the interior of the channel are Ser²⁸⁴, Thr²⁸⁷, and Thr³⁰⁵. However, these hydroxyl-containing side chains are not particularly well suited for cation interactions. In other gated cation channels, conformational realignment of the TM segments have led to an opening of a narrow region of the channel (23, 24). However, in all of these cases, this narrow region is only constituted by a smaller part of the pore, whereas most of the pore has an extensive cavity or selectivity filter preformed before the opening event. In contrast, in CorA, extensive, largely hydrophobic interac-

tions are made in the interior parts of the pore. This implies that gating, as well as transport, might work differently than in previously studied cation-transport systems. The high conservation of Asp²⁷⁷ in the bacterial CorA-II homologs, together with the localization of strong residual density at the Asp²⁷⁷ carboxylate ring at the entrance of the pore, implies that this residue is important for transport or regulation in CorAs. In the TolC transport system, an “aspartate ring” formed by the carboxylates of three aspartate residues was shown to determine selectivity, as well as to form a binding site for inhibitory cations (25, 26). It is possible that the “aspartate ring” of CorA plays a similar role. In addition, the aspartate ring in CorA might directly catalyze the essential events required for moving a divalent cation reversibly between the solvent and the low dielectric environment of the pore. These events could encompass dehydration through ligand-exchange reactions, but also, protonation or deprotonation events mediated by the clustered carboxylate residues to obtain an ion of appropriate charge.

The binding of two metals at sites M1 and M2 suggests that CorA transport is gated through regulation of these sites. Co²⁺ binds to these sites at a concentration one-fifth that of Mg²⁺, which suggests that cobalt might be a physiological relevant regulator and, therefore, also a transport substrate for *T. maritima* CorA. The primary effect of the binding of metals to the M1 and M2 sites appears to be in modulating the interactions between neighboring N-terminal domains. A metal-free protein is likely to have significantly reduced N-terminal domain interactions, because of the energetically unfavorable clustering of carboxylates when the metals are removed. The presence of two metal binding sites is intriguing and suggests that the regulatory mechanism might be more complex than in other gated channels, which are

normally regulated by two-state, on-off controls. The different coordination environments of the two ions, one directly coordinated to two carboxylates and the other likely coordinated as a hydrated ion, imply different binding kinetics and potentially allow a more refined mode of regulation. Alternatively, the presence of two metal binding sites could be a tool to allow more than one type of cation to regulate CorA. A broad substrate spectrum for divalent cation transporters is not unusual (8, 27). In the absence of a structure of the metal-free protein, the mechanism for the regulatory control has to remain speculative. However, it appears feasible that the realignment of the N-terminal domains due to metal release at the M1 and M2 sites could have direct effects on the orientation of helix 7. This could potentially affect conformations in the region of Asp²⁷⁷ ring, which would thereby regulate its function in the transport event, or potentially, its suitability as a binding site for inhibitory cations, in analogy with TolC. A different gating mechanism would be the opening of the hydrophobic girdle, as proposed for the acetylcholine receptor through a ligand-induced helical rotation (28). Because of the more extended hydrophobic interactions in CorA, we consider this to be less likely, but still a possibility.

The structure of CorA at 2.9 Å now provides a framework for addressing questions

related to regulatory metal sites, conformational changes in regulation and transport events, and the detailed mechanism for the control of hydration levels of the transported ions.

References and Notes

- S. P. Hmiel, M. D. Snavely, C. G. Miller, M. E. Maguire, *J. Bacteriol.* **168**, 1444 (1986).
- M. D. Snavely, J. B. Florer, C. G. Miller, M. E. Maguire, *J. Bacteriol.* **171**, 4761 (1989).
- R. L. Smith, J. L. Banks, M. D. Snavely, M. E. Maguire, *J. Biol. Chem.* **268**, 14071 (1993).
- R. L. Smith, E. Gottlieb, L. M. Kucharski, M. E. Maguire, *J. Bacteriol.* **180**, 2788 (1998).
- R. L. Smith *et al.*, *J. Biol. Chem.* **273**, 28663 (1998).
- M. A. Szegedy, M. E. Maguire, *J. Biol. Chem.* **274**, 36973 (1999).
- L. M. Kucharski, W. J. Lubbe, M. E. Maguire, *J. Biol. Chem.* **275**, 16767 (2000).
- D. G. Kehres, M. E. Maguire, *Biomaterials* **15**, 261 (2002).
- M. A. Warren *et al.*, *J. Bacteriol.* **186**, 4605 (2004).
- R. C. Gardner, *Curr. Opin. Plant Biol.* **6**, 263 (2003).
- V. Knoop, M. Groth-Malonek, M. Gebert, K. Eifler, K. Weyand, *Mol. Genet. Genomics* **274**, 205 (2005).
- D. M. Bui, J. Gregan, E. Jarosch, A. Ragnini, R. J. Schweyen, *J. Biol. Chem.* **274**, 20438 (1999).
- I. Schock *et al.*, *Plant J.* **24**, 489 (2000).
- A. J. Worlock, R. L. Smith, *J. Bacteriol.* **184**, 4369 (2002).
- A. M. Caldwell, R. L. Smith, *J. Bacteriol.* **185**, 374 (2003).
- V. V. Lunin *et al.*, *Nature* **440**, 833 (2006).
- G. von Heijne, *J. Mol. Biol.* **225**, 487 (1992).
- D. O. Daley *et al.*, *Science* **308**, 1321 (2005).
- Materials and methods and structure statistics are available as supporting material on *Science* online.
- H. Diebler, M. Eigen, G. Ilgenfritz, G. Maas, R. Winkler, *Pure Appl. Chem.* **20**, 93 (1969).
- R. B. Martin, *Met. Ions Biol. Syst.* **26**, 1 (1990).
- M. E. Maguire, J. A. Cowan, *Biomaterials* **15**, 203 (2002).
- D. A. Doyle, *Trends Neurosci.* **27**, 298 (2004).
- D. A. Doyle, *Eur. Biophys. J.* **33**, 175 (2004).
- C. Andersen, E. Koronakis, C. Hughes, V. Koronakis, *Mol. Microbiol.* **44**, 1131 (2002).
- M. K. Higgins *et al.*, *J. Mol. Biol.* **342**, 697 (2004).
- G. Grass *et al.*, *J. Bacteriol.* **187**, 1604 (2005).
- A. Miyazawa, Y. Fujiyoshi, N. Unwin, *Nature* **423**, 949 (2003).
- The authors thank A. Kreusch, H. Klock, M. DiDonato, and L. Columbus for their help with the cloning; K. Johnson, M. Moche, F. Schmitzberger, and A. Bakali for their help in data collection and processing; and A. Edwards and co-workers for providing with information on their structure. This work was supported by the Swedish Research Council, the European Union Integrated projects Structural Proteomics in Europe (SPINE) and the European Membrane Protein Consortium (E-MeP), the Knut and Alice Wallenberg Foundation, and the Göran Gustafsson Foundation. We are grateful for beam time and assistance at collection of synchrotron data at the European Synchrotron Radiation Facility (ESRF), the Swiss Light Source (SLS), and the Berlin Electron Storage Ring for Synchrotron Radiation BESSY (Berlin).

Supporting Online Material

www.sciencemag.org/cgi/content/full/313/5783/354/DC1
Materials and Methods
Figs. S1 and S2
Table S1
References and Notes
7 March 2006; accepted 1 June 2006
10.1126/science.1127121

Structure of the Vesicular Stomatitis Virus Nucleoprotein-RNA Complex

Todd J. Green, Xin Zhang, Gail W. Wertz,* Ming Luo†

Vesicular stomatitis virus is a negative-stranded RNA virus. Its nucleoprotein (N) binds the viral genomic RNA and is involved in multiple functions including transcription, replication, and assembly. We have determined a 2.9 angstrom structure of a complex containing 10 molecules of the N protein and 90 bases of RNA. The RNA is tightly sequestered in a cavity at the interface between two lobes of the N protein. This serves to protect the RNA in the absence of polynucleotide synthesis. For the RNA to be accessed, some conformational change in the N protein should be necessary.

The viral genomic RNA (vRNA) of negative-stranded RNA viruses (NSRVs), such as vesicular stomatitis virus (VSV), do not exist as naked RNAs but rather as a ribonucleoprotein (RNP) complex in which the RNA is encapsidated with the nucleocapsid (N) protein. The RNP, rather than the naked vRNA, is the active template for transcription and replication (1, 2). NSRVs include some of the most dangerous human pathogens, such as Ebola, rabies, avian influenza, and measles viruses.

VSV is an enveloped, nonsegmented NSRV that belongs to the family Rhabdoviridae. The 11,161-nucleotide (nt) genome of VSV comprises five genes, which are the nucleocapsid (N), the phosphoprotein (P), the matrix (M), the glycoprotein (G), and the large subunit of the polymerase (L) (3). The entire RNP of VSV contains an estimated 1258 molecules of the N protein, each of which is bound to nine bases of RNA (4). Chemical probing studies have indicated that the N protein primarily binds to the ribose-phosphate backbone of the RNA (5). The large polymerase subunit (L) and the phosphoprotein (P) are the two essential viral components in the polymerase (1, 6). Viral transcription and replication by VSV are distinct processes that are defined in part by the level of the N protein in the cell. The N protein is initially in complex with the P protein, which

prevents the concentration-dependent aggregation of N. This keeps the N protein in an encapsidation-competent form (7).

In addition to protection of the vRNA, the N protein complexed to RNA as the RNP has the structural role of forming the helical core of the assembled virion. The RNP in association with the matrix (M) protein condenses the vRNA into a compact bundle that is ready for packaging into the mature virus. Before being packaged into the progeny virion, the RNP exists in several states in the cell, including an undulating ribbon, a loosely coiled helix, and a tightly coiled helix that is usually found at the termini of the nucleocapsids (4, 8–10). The transition from the states observed in the cell to the helix observed in the intact virion is not well understood.

The inherent flexibility of the RNP has made it difficult to determine high-resolution structures by electron microscopy (EM) or x-ray crystallography. Recently, however, low-resolution EM reconstructions of ringlike structures composed of oligomeric N proteins in complex with RNA have been reported for rabies virus (11), influenza virus (12), and VSV (13). These structures showed that distinct N protein molecules are assembled on a single-strand RNA as parallel blocks. The RNA is bound in the center of the N protein ring.

We have previously reported the production of oligomers of a VSV N/P protein complex bound to RNA from an *Escherichia coli*

Department of Microbiology, School of Medicine, University of Alabama at Birmingham, 1025 18th Street South, Birmingham, AL 35294, USA.

*Present address: Department of Pathology, University of Virginia, MR5 Building Room 3051, Box 800904, 415 Lane Road, Charlottesville, VA 22908, USA.

†To whom correspondence should be addressed. E-mail: mingluo@uab.edu

expression system in which the N protein is concomitantly expressed with the P protein (14). After dissociation of the P protein, we obtained a single oligomeric species of the N protein that has a ringlike morphology and is bound to RNA (14). The size of the N-RNA complex was determined by size-exclusion chromatography and analytical ultracentrifugation analysis to be consistent with 10 copies of N molecules bound to a 90-nt strand of RNA (14). This N protein-RNA complex was crystallized, and diffraction data were collected (15).

The x-ray crystal structure of this VSV RNP-like complex (RLC) confirms the stoichiometry and reveals the details of RNA binding and protection by the N protein. The RNA is tightly bound in a cavity at the interface between two lobes in the N protein with nine nucleotides associated with each N molecule. The RNA adopts a unique conformation in which some of the bases are facing toward and others away from the N protein. The structure of the RLC also shows an extensive network of interactions between neighboring N molecules where each

monomer contacts three neighboring N protein molecules. The vRNA may need to be unsequestered from the N protein for transcription and replication.

The crystallographic asymmetric unit is composed of half of the ring (Fig. 1A). The second half is generated by the crystallographic two-fold on which the particle sits. Each monomer contains amino acid residues 2 to 422, a nine-nt strand of RNA, and three uranyl ions. The N protein has two lobes containing mainly α helices, which come together to form a cavity that accommodates the RNA (Fig. 1B). The structure commences with two short antiparallel β strands situated on an arm that extends downward to the core of the N-terminal lobe. The core of the N-terminal lobe consists of seven α helices and four β strands. The positions of the individual secondary-structure elements are described in the SOM Text and fig. S1. The C-terminal lobe begins at residue Ser²²⁰ and contains eight α helices. Between helices α 12 and α 13, a loop (Ser³⁴⁰-Val³⁷⁵) extends to interact with an adjacent molecule in the N protein ring. This extension rests upon the upper surface of the adjacent C-terminal lobe before eventually turning back, after residue Val³⁵⁰, toward its own C-terminal lobe. In three of the five N protein monomers, some residues on the extended loop, ranging from five to eight in each monomer, are disordered.

Functionally, the N protein has multiple roles with regard to its interaction with RNA. RNA is a structural element that contributes to the stability of the assembled nucleocapsid. In the N-RNA complex structure, a cavity about 10 Å wide and 20 Å deep is formed at the junction of the two lobes of the N protein to enclose the RNA (Fig. 2A, fig. S2). Of the nine RNA bases that contact the N protein,

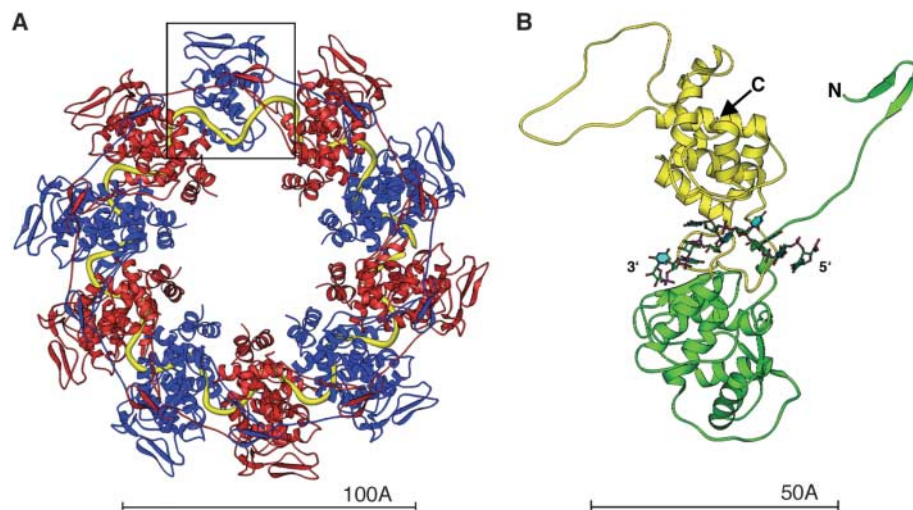
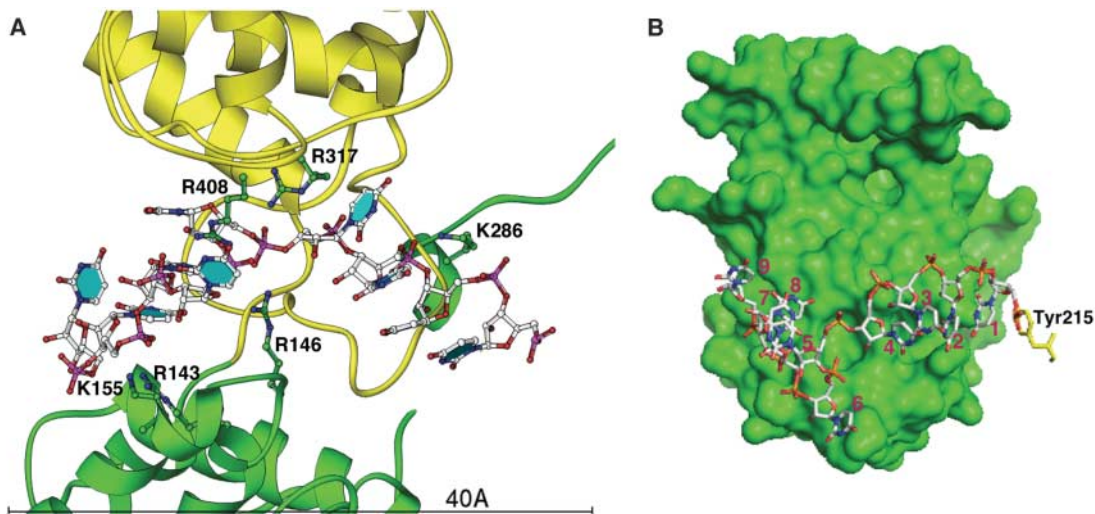


Fig. 1. The structure of the RNP complex of VSV. **(A)** Overall structure of the decamer of the N protein-RNA complex. The decamer has a near 10-fold rotational symmetry; alternating monomers within the ring are colored red and blue. The 90-nt strand RNA is represented by a yellow tube following along the ribose-phosphate backbone. The C-terminal lobe of the boxed monomer has been removed. **(B)** Ribbon representation of the N protein monomer bound with a 9-nt strand of RNA shown in ball-and-stick model. The N protein has two lobes, N-terminal and C-terminal, colored green and yellow, respectively. The view is from the inside of the ring looking out. Ribbon drawings throughout the manuscript were illustrated with Ribbons (17).

Fig. 2. The RNA binding cavity. **(A)** The side chains of positively charged residues that interact with the phosphate groups in the backbone of the single-stranded RNA are labeled and are shown in ball-and-stick representation. The nine nucleotides that bind to one monomer are shown in the same style, with the pyrimidine bases shaded in cyan. Lobe colors and orientation are as in Fig. 1B. **(B)** A top-view of RNA bases stacking in the two structural motifs. Bases are numbered 1 to 9 [right to left with respect to the view in (A), corresponding to the 5' to 3' direction]. Bases 1 to 4 along with Tyr²¹⁵ from a neighboring N molecule on the 5' end of the RNA stack to form a structural motif similar to a half duplex of RNA and are facing away from the interior of the protein cavity. Nucleotides 5, 6, and 8 also have a base-stacking ar-



angement but are rotated to face the inside of the protein. The N-terminal lobe is represented by the surface contour (green), whereas the C-terminal lobe is removed to reveal the RNA content. The image was generated with PyMOL (18).

bases 1 to 4 and base 6 point toward the solvent side of the cavity (Fig. 2, A and B), whereas bases 5, 7, and 8 face the protein interior. The final nucleotide, base 9, extends to join with nucleotide 1 from the adjacent N molecule. The overall structure of the RNA forms two individual quasi-helical structures (bases 1 to 4 and bases 5, 7, and 8) that are split by a bulge in the RNA at base 6. The bases have been modeled as the pyrimidine U. However, many of the bases have a density that is slightly larger, which suggests that the position could accommodate a purine base.

The interior of the N protein cavity is mainly hydrophobic, reflecting its role to accommodate the RNA bases from the second quasi-helix. However, the region that is occupied by the first quasi-helix displays many positively charged and polar residues that interact with the negatively charged RNA backbone (Fig. 2A). Residues whose side chains are involved in binding to the phosphate groups of the RNA are contributed by both lobes of the N protein. Residues from the N-terminal lobe include Arg¹⁴³, Arg¹⁴⁶, and Lys¹⁵⁵, whereas the C-terminal lobe donates residues Lys²⁸⁶, Arg³¹⁷, and Arg⁴⁰⁸ (Fig. 2A). A sequence alignment of several members of the family Rhabdoviridae shows that four of the six residues are conserved (Arg¹⁴³, Arg¹⁴⁶, Lys²⁸⁶,

and Arg⁴⁰⁸) and one (Arg³¹⁷) is only partially conserved (fig. S3). In addition, Arg²¹⁴ and Arg³¹², two residues that are found in the RNA binding cavity but that do not make contact with the RNA in VSV, are conserved among all six viruses. Arg³¹² is involved in stabilizing the N protein-to-N protein interaction. Arg²¹⁴ is adjacent to the RNA but is bonded to Asp¹⁹⁹ by a salt-bridge. Perhaps with some rearrangement of its side-chain rotamer, Arg²¹⁴ could be involved in RNA binding. Tyr²¹⁵, which stacks against nucleotide 1 of the RNA to extend the first quasi-helix (Fig. 2B), is conservatively substituted in five of the six viruses as an aromatic residue, Phe or Trp. Each of these residues could stack in a similar way to what is observed in the structure.

The assembled RNP is composed of more than 1200 copies of the N protein bound to the genomic RNA. In this polymeric state, the monomeric N protein must interact with adjacent N protein molecules to maintain the protective stability of the nucleocapsid. The most substantial interaction (1954 Å²) occurs at the side-to-side interface between the neighboring N protein molecules with three-fourths of the contact between the C-terminal lobes. This interface is primarily hydrophobic, but with a number of electrostatic and polar interactions. Between the neighboring C-terminal

lobes, the side chains of Tyr³²⁴ and Tyr⁴¹⁵ form a hydrophobic patch that interacts with the hydrophobic portion of the side chain of Arg³⁰⁹ from the neighboring C-terminal lobe. The positive charge of the Arg³⁰⁹ side chain is neutralized by the side chain of Glu⁴¹⁹ so that both side chains are buried in the hydrophobic interface. Between the N-terminal lobes, the hydrophobic interaction is mainly between a patch consisting of the side chain of Met¹⁶⁶ and part of Lys²⁰⁷, and a shallow pocket formed by the side chain of Val¹⁸⁴, part of Asn¹⁸⁷, and part of Asp¹⁸⁸ from the neighboring N-terminal lobe. There are three additional contacts made by the regions extended from the N monomer core that are clearly discernable in the RLC structure spanning four neighboring N molecules (labeled I, II, and III in Fig. 3). Each monomer has an extended N-terminal arm that interacts with the C-terminal lobe of the monomer to the left when viewed from the outside of the ring (I). The C-terminal lobe has an extended loop that interacts with the C-terminal lobe of the molecule to the right (II). Contact III is between the N-terminal arm of molecule 1 and the extended loop of molecule 2' (Fig. 3). The network of contacts among the four molecules would be repetitive throughout the N-RNA complex. Such a complexity implies that the orderly assembly of the N protein on the nascent RNA during replication requires the N protein to be delivered and correctly oriented in the replication site. New N molecules that are added to the growing RNP that contains the nascent vRNA must be kept in an RNA binding-competent conformation by chaperone factors such as the viral P protein before latching onto N molecules previously bound to the vRNA. Upon assembling on the nascent chain of newly synthesized RNA during replication, the N protein is tightly wrapped around the vRNA. The hinge between the two lobes of the N protein observed in the crystal structure may provide the necessary flexibility to allow the N protein to adopt alternative conformational states at different stages of RNP assembly. The sequestering of the RNA within the RLC structure is consistent with data showing that RNA bound to the N protein is resistant to ribonuclease as well as base-catalyzed hydrolysis (5, 14, 16).

The radius (80 Å) of the decameric N-RNA ring is substantially smaller than that (245 Å) of the RNP superhelix in the virus, as determined by EM (10). The N protein-vRNA complex in the RNP may be required to have considerable flexibility in order to act like a coil being wound up in the superhelical core. The hydrophobic interfaces between neighboring N molecules could tolerate rigid body rotations that may expand the RLC. Nucleotides 1 to 8 should be associated with the N protein as a rigid body during the structural changes, on the basis of their tight binding with the N protein. Nucleotide 9 and the hinge between the two lobes of the N protein may be the

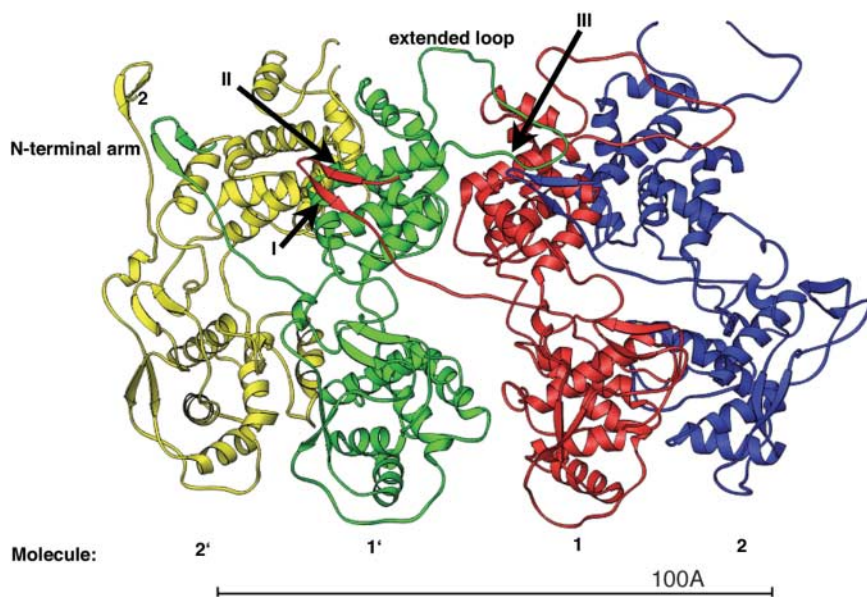


Fig. 3. Association of the N protein. Four N molecules of the N-RNA ring (colored yellow, green, red, and blue) are shown from the outside-in view. The C terminus is distal to the view and is not visible from this orientation. A single N protein monomer has unique contacts, labeled I, II, and III, with three other monomers within the ring in addition to the side-by-side contacts between the neighboring molecules. Each monomer has an N-terminal and C-terminal lobe (top and bottom, respectively). The molecule in red is designated as molecule 1, and the N molecules along the direction of 5'→3' of the vRNA in the RNP are sequentially labeled 2. The N molecules on the opposite side are labeled 1', 2', accordingly. The extended arm at the N terminus of the N-terminal lobe in molecule 1 makes contacts with the C-terminal lobe of molecule 1' at contact I. The C-terminal lobe has an extended loop that interacts with the C-terminal lobe of the molecule to the right (Contact II). Contact III is between the N-terminal arm of molecule 1 and the extended loop of molecule 2'. RNA is not displayed in this illustration.

points of notable rotation. We estimate that about 38.5 maneuvered N-RNA complex units are required to complete one round of the RNP structure with a radius of 245 Å.

The sequence of the vRNA in the RNP must be read by the polymerase complex during RNA synthesis. There are three possible mechanisms for copying the RNA sequence: (i) The vRNA is completely exposed in the RNP, so Watson-Crick base-pairing can occur without any change of the RNP structure. (ii) The vRNA is completely dissociated from the RNP, so it serves as a template like a naked RNA molecule. (iii) A pronounced structural change occurs in the RNP to allow the sequence of the vRNA to be read by the polymerase complex without disrupting the integrity of the RNP. The conformational arrangement of the RNA in the N protein as revealed by our structure suggests that Watson-Crick base-pairing could not occur when the N protein is closed on the vRNA. Bases in positions 5, 7, and 8 are completely shielded by the N protein such that their backbone conformation is held rigidly by the N protein, thus preventing the formation of an RNA duplex. The second possibility is also unlikely because the RNP remains intact after one round of RNA

synthesis and may be used as the template again. Thus, it is likely that the vRNA is temporarily dissociated from the N protein within the active polymerase complex.

References and Notes

1. S. U. Emerson, R. R. Wagner, *J. Virol.* **10**, 297 (1972).
2. S. Naito, A. Ishihama, *J. Biol. Chem.* **251**, 4307 (1976).
3. A. S. Huang, R. R. Wagner, *J. Mol. Biol.* **22**, 381 (1966).
4. D. Thomas *et al.*, *J. Virol.* **54**, 598 (1985).
5. F. Iseni, F. Baudin, D. Blondel, R. W. Ruigrok, *RNA* **6**, 270 (2000).
6. S. U. Emerson, Y. Yu, *J. Virol.* **15**, 1348 (1975).
7. M. Howard, G. Wertz, *J. Gen. Virol.* **70**, 2683 (1989).
8. A. F. Howatson, G. F. Whitmore, *Virology* **16**, 466 (1962).
9. R. M. McCombs, M. B. Melnick, J. P. Brunschwig, *J. Bacteriol.* **91**, 803 (1966).
10. T. Nakai, A. F. Howatson, *Virology* **35**, 268 (1968).
11. G. Schoehn, F. Iseni, M. Mavrikis, D. Blondel, R. W. Ruigrok, *J. Virol.* **75**, 490 (2001).
12. J. Martin-Benito *et al.*, *EMBO Rep.* **2**, 313 (2001).
13. Z. Chen, T. J. Green, M. Luo, H. Li, *Structure* **12**, 227 (2004).
14. T. J. Green *et al.*, *J. Virol.* **74**, 9515 (2000).
15. T. J. Green, M. Luo, *Acta Crystallogr. D* **62**, 498 (2006).
16. J. D. Keene, B. J. Thornton, S. U. Emerson, *Proc. Natl. Acad. Sci. U.S.A.* **78**, 6191 (1981).
17. M. Carson, *Methods Enzymol.* **277**, 493 (1997).
18. W. L. Delano, *The PyMOL User's Manual* (Delano Scientific, San Carlos, CA, 2002).
19. We thank L. Andrew Ball for critical reading of the manuscript before submission. We thank the staff of the South East Regional Collaborative Access Team (SER-CAT)

and Bio-CARS at the Advanced Photon Source, Argonne National Laboratory, for their assistance in data collection. Use of the Advanced Photon Source was supported by the U.S. Department of Energy, Office of Science, Office of Basic Energy Sciences, under Contract W-31-109-Eng-38. SER-CAT supporting institutions may be found at www.ser-cat.org/members.html. Portions of this research were carried out at the Stanford Synchrotron Radiation Laboratory (SSRL), a national user facility operated by Stanford University on behalf of the U.S. Department of Energy, Office of Basic Energy Sciences. The SSRL Structural Molecular Biology Program is supported by the U.S. Department of Energy, Office of Biological and Environmental Research, and by the NIH, National Center for Research Resources, Biomedical Technology Program, and the National Institute of General Medical Sciences. This work is supported in part by NIH grants AI050066 (to M.L.) and R37AI012464 (to G.W.W.). The atomic coordinates and reflection file have been deposited with the Research Collaboratory for Structural Bioinformatics Protein Data Bank. The access code for the coordinates is 2GIC.

Supporting Online Material

www.sciencemag.org/cgi/content/full/1126953/DC1
Materials and Methods
SOM Text
Figs. S1 to S3
Table S1
References

2 March 2006; accepted 5 June 2006

Published online 15 June 2006;

10.1126/science.1126953

Include this information when citing this paper.

Crystal Structure of the Rabies Virus Nucleoprotein-RNA Complex

Aurélien A. V. Albertini,^{1*} Amy K. Wernimont,^{2*} Tadeusz Muziol,² Raimond B. G. Ravelli,² Cedric R. Clapier,² Guy Schoehn,¹ Winfried Weissenhorn,^{2†} Rob W. H. Ruigrok¹

Negative-strand RNA viruses condense their genome into a helical nucleoprotein-RNA complex, the nucleocapsid, which is packed into virions and serves as a template for the RNA-dependent RNA polymerase complex. The crystal structure of a recombinant rabies virus nucleoprotein-RNA complex, organized in an undecameric ring, has been determined at 3.5 angstrom resolution. Polymerization of the nucleoprotein is achieved by domain exchange between protomers, with flexible hinges allowing nucleocapsid formation. The two core domains of the nucleoprotein clamp around the RNA at their interface and shield it from the environment. RNA sequestering by nucleoproteins is likely a common mechanism used by negative-strand RNA viruses to protect their genomes from the innate immune response directed against viral RNA in human host cells at certain stages of an infectious cycle.

Rabies virus, a member of the *Rhabdoviridae* family, is the causative agent of rabies, a fatal central nervous system disease (1), which constitutes a serious health problem in developing countries that lack effective vaccination programs (2). *Rhabdoviridae*, together with *Paramyxoviridae* (e.g., measles virus), *Filoviridae* (e.g., Ebola virus) and *Bornaviridae* (e.g., Borna disease virus),

are RNA-containing enveloped viruses that use nonsegmented negative sense RNA as their genome. The RNA is condensed by the nucleoprotein (N) into a helical nucleocapsid (NC) (3) and this N-RNA complex constitutes the essential template for replication by the RNA-dependent RNA polymerase complex (4). The polymerase complex selects for either transcription or replication and is composed of the enzymatic active L protein and the phosphoprotein P (5–7). Replication produces a full-length (+) copy of the viral RNA (vRNA), which is the specific target for encapsidation by N and serves as a template for (–) RNA replication. The switch from transcription to replication is in part regulated by the abundance of

free N in the cytoplasm (8). In order to understand the role of N-RNA complexes in the viral life cycle, we solved the crystal structure of a nucleoprotein oligomer from rabies virus complexed to a 99-nucleotide-long RNA segment.

Recombinant expression of most viral nucleoproteins from negative-strand RNA viruses leads to nonspecific host cell RNA encapsidation by N (9, 10), resulting in either helical or ring-like structures depending on the length of the RNA (10, 11). Rabies virus N expression in insect cells produced N-RNA rings containing 9, 10, 11, 12, or 13 copies of N as determined after purification (12). The undecameric ring produced the best diffracting crystals belonging to space group P2₁2₁2. The structure was solved by single anomalous dispersion (SAD) and refined to 3.5 Å resolution with an *R*-factor of 27.5 (*R*_{free} = 32.6) (table S1) (13). Two ~550-kDa large undecameric N-RNA rings pack head to head in the crystal asymmetric unit. Each ring has an outer diameter of 160 Å, an inner diameter of 60 Å, and a height of 74 Å (Fig. 1A). The N protomer consists of two main domains, which contact nine nucleotides of single-stranded RNA, as predicted (14), that are occluded in the center of the ring (Fig. 1, B, C, and D, and Fig. 2). The N-terminal core domain (NTD; residues 32 to 233) folds into a helical arrangement composed of 6 helices connected by large loops. The C-terminal core domain (CTD; residues 236 to 356 and 396 to 450) is composed of 11 helices joined by tighter loops (Figs. 1C and fig. S1). Two regions in N (NTD: 105 to 118 and CTD: 376 to 397) are

¹Institut de Virologie Moléculaire et Structurale, FRE 2854 Université Joseph Fourier-CNRS, ²European Molecular Biology Laboratory (EMBL), Boite Postale 181, 38042 Grenoble, France.

*These authors contributed equally to this work.

†To whom correspondence should be addressed. E-mail: weissen@embl-grenoble.fr

presumably flexible, because they are absent in the structure (Fig. 1C and fig. S1). In addition to the core domains, two smaller subdomains participate in domain exchange between protomers and stabilize polymerization (Figs. 1C and 3, A and B). Both the top (NTD) and bottom (CTD) domains act as “jaws” that clamp down onto the RNA strand and enclose it completely (Fig. 1D), an observation which is consistent with the fact that the RNA remains bound to N in CsCl gradients (15). The closest contact between the two jaws is between NTD residue N157 and CTD residue P435 (9 to 10 Å, depending on the protomer) (Fig. 1D). One likely reason for tight RNA sequestering is to prevent immune recognition. Tightly packaged RNA does not constitute a target for the innate immune system such as Toll-like receptors, which are present during transport of the nucleocapsid along the endosomal pathway into the cytoplasm to its replication site (16, 17) and is protected from exonuclease activities triggered by the interferon antiviral defense system (16, 18). In addition, complete genome protection could be crucial during transport of nucleocapsids to the site of virus assembly and budding.

The experimental electron density map showed continuous density representing the sugar-phosphate backbone and averaged densities for the bases indicating a 5′-3′ direction in clockwise orientation in the ring-structure (Figs. 1B and 2A). Although each N-RNA ring bound short random RNA from the expression host, differences between purines and pyrimidines could be discerned in the electron density map based on the angles and the sizes of the nucleotides, and they were modeled as either

adenine or cytosine (Fig. 2A). The RNA strand is twisted clockwise in an irregular left-handed helix along the inner perimeter of the ring within the continuous cleft made up by the NTD (top) and CTD (bottom) interface in the ring structure (Fig. 1B and fig. S2). For each protomer, the RNA strand is roughly split into two halves, which wrap around the NTD jaw; this arrangement provides most of the interactions and forces the RNA to bulge out at the tip of the NTD jaw (Figs. 1D and 2A). Each nucleotide makes polar contacts either via its phosphate group (seven out of nine phosphates are recognized), as predicted (19), or its ribose moiety (two out of nine are recognized), which is modeled in the C3′ *endo* sugar pucker conformation (Fig. 2, A and B). The first three bases point toward the solvent and stack onto each other and onto the last two bases of the preceding N protomer (M−1). Nucleotide 5 is involved in a kink that allows the base of nucleotide 4 to stack onto the bases from nucleotides 6 and 7 pointing toward the protein moiety, while its own base points away from the protein. The last two bases then point again away from the protein (Fig. 2, A and B). Most of the basic residues involved in RNA coordination are conserved between rabies virus and vesicular stomatitis virus (genus *Vesiculovirus*), indicating a conserved RNA coordination network (fig. S1).

There are no significant interactions between the NTDs within the ring structure (Fig. 1B). Their position is mainly determined by the connection to the CTD, the bound RNA, and extensive crystal contacts between NTDs of the two rings in the crystal asymmetric unit. In contrast, the CTDs share a large interaction

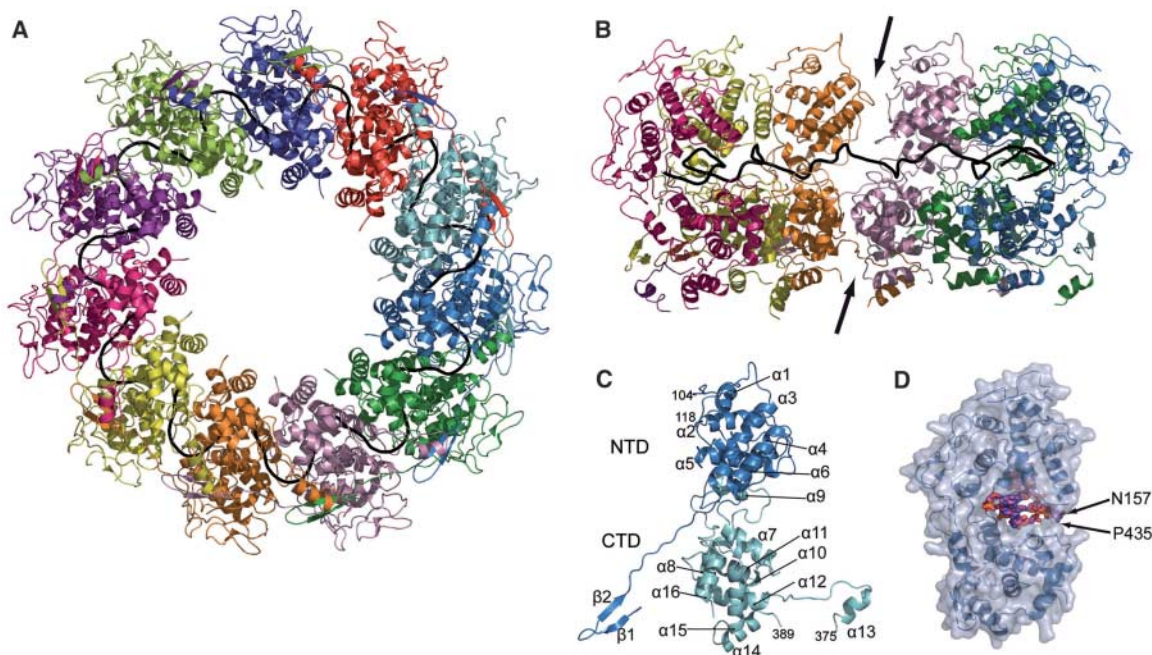
surface (2700 Å² total buried surface) (Fig. 1B) that is determined by hydrophobic and van der Waals contacts as well as multiple polar interactions (total of 15) involving many main chain contacts (total of nine contacts).

Two small subdomains emerge from NTD and CTD (Fig. 1C) and reach over to neighboring protomers, contacting them either clockwise (NTD; M+1) or counter clockwise (CTD; M−1) and so establish domain swapping (Fig. 3A). The extreme N terminus folds into a short β hairpin that nestles between the 3/10 helix η1 and helix 8 (fig. S1) of the CTD from M+1. The main contacts are made between the N11 and E266, as well as E20 and R254 in some monomers, in addition to hydrophobic interaction (V10, I22) (22). The β hairpin is followed by a stretch of residues (23 to 29) that are completely solvent exposed and constitute a potential hinge region between the subdomain and the core NTD, while Y28 and Y30 are used as anchor residues (Fig. 3B).

A second small subdomain emanates from the CTD as a coil region followed by helix 13 that reaches over to a neighboring protomer (M−1) in counterclockwise fashion (Fig. 3, A and B). The connection from helix 13 back to the core of the main CTD is disordered in all protomers (Fig. 1C). The CTD subdomain is much shorter and is firmly attached to the CTD by a hydrophobic core (F350, F349, F355), which is followed by a shorter potential hinge region (residues 351 to 356). The following loop region leading to helix 13 interacts with M−1 (R361 to E403; R357 to E403) and is in close contact with β strand 1 from M+1 (Fig. 3B).

Fig. 1. Overall structure of the N-RNA complex.

(A) Ribbon diagram of the 11-nucleotide oligomer N-RNA ring structure as viewed from the bottom. Each N protomer is colored differently. The RNA is shown as a black coil. (B) View of the inside of the ring structure; only six protomers are depicted in different colors with the NTD on the top and the CTD on the bottom. The path of the RNA is shown as a coil in a clockwise 5′ to 3′ orientation. The top arrow indicates that the NTDs do not interact with each other; the bottom arrow points toward the extensive interface between CTDs. (C) Ribbon diagram of the N protomer; the NTD is shown in dark blue and the CTD in light blue. The helical secondary structure elements are numbered consecutively. (D) Space-filling model of the N



protomer reveals that the RNA is completely clamped at the interface of the NTD and the CTD and thus is not accessible as a template for the polymerase.

The structural overlay of the C α atoms of the 11 protomers reveals that the two swapped domains and an NTD region present the highest level of flexibility (fig. S3); this supports the notion that the two subdomains could act as potential hinges and lead to lateral opening of the ring. This flexible domain linkage thus permits not only the formation of differently sized ring-like structures but also the assembly of the nucleocapsid that adopts a diameter of ~ 75 nm, containing ~ 53 protomers per helical turn (12).

The tight sequestering of the RNA suggests that the rabies virus genomic RNA has to

dissociate in order to become a template for the polymerase. However, simultaneously, the RNA must remain close to N, because the polymerase stays attached to N during its activity (4, 5). Although each protomer spans a distance of 22 Å between nucleotide ends (fig. S2), the nine nucleotides could be stretched out to a length of ~ 49 Å. Thus, a local dissociation of the RNA from one or several N protomers could provide sufficient space for binding of the polymerase complex (5) (fig. S4).

Phosphoprotein P links the polymerase complex to N and binding requires that S389 be

phosphorylated within a highly mobile region on the CTD of N (Fig. 1C and fig. S1) (21). This flexible region is disordered in the structure (Fig. 1C), but may become ordered upon P binding (22), as has been observed for the measles virus N-P interaction (23). P binding in the region of S389 (Fig. 3, A and B) may thus affect both subdomains including the hinge regions and could transfer a signal to the NTD, which would lead to the vertical opening of the NTD-CTD clamp, facilitating RNA exposure. The absence of any protein-protein contacts between NTDs (Fig. 1B) would facilitate a large NTD motion required for this process. In contrast, the CTD conformation is locked in by the large CTD-CTD interaction surface and by the tethering of the hinge loops. The latter interactions will thus maintain the contacts between the N protomers during the passage of the polymerase and the displacement of the RNA. Maintaining contact between N and RNA is required for rebinding of RNA and thus prevents the formation of double-stranded RNA during transcription and replication, which would otherwise require a helicase activity that is not encoded in the viral genome. Furthermore, an extensive production of double-stranded RNA would induce toll-like receptor 3 (TLR3) recognition and trigger immune reactions (16).

Even though N spontaneously associates with RNA in vivo in the absence of other viral proteins, a number of studies have shown that the 5' region of the viral genomic sequence regulates RNA packaging into a functional nucleocapsid (11, 24). Because the structure does not reveal any sequence specificity in RNA recognition, an alternative RNA-binding mechanism must exist. In the first protomer of the assembled nucleocapsid, the side extending the NTD hinge loop will be exposed and will not participate in polymerization (Fig. 1C); consequently, this region may provide a surface for sequence-specific RNA recognition. Conversely, at the 3' end of the packaged genome, the CTD hinge loop (Fig. 1C) may adopt a different conformation that may facilitate access of the polymerase to the 3' end,

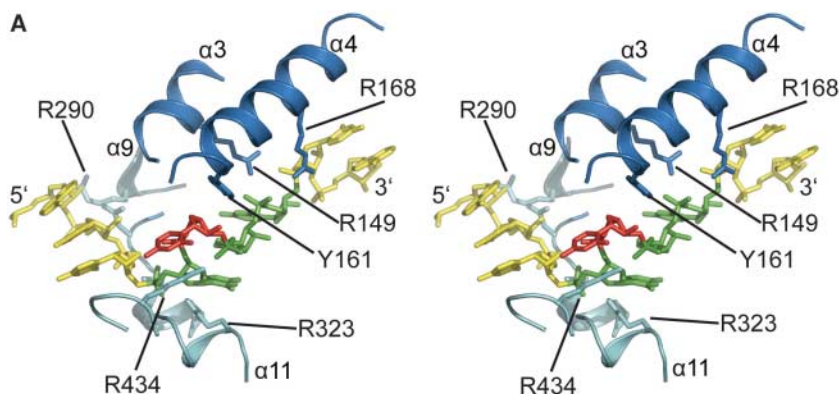
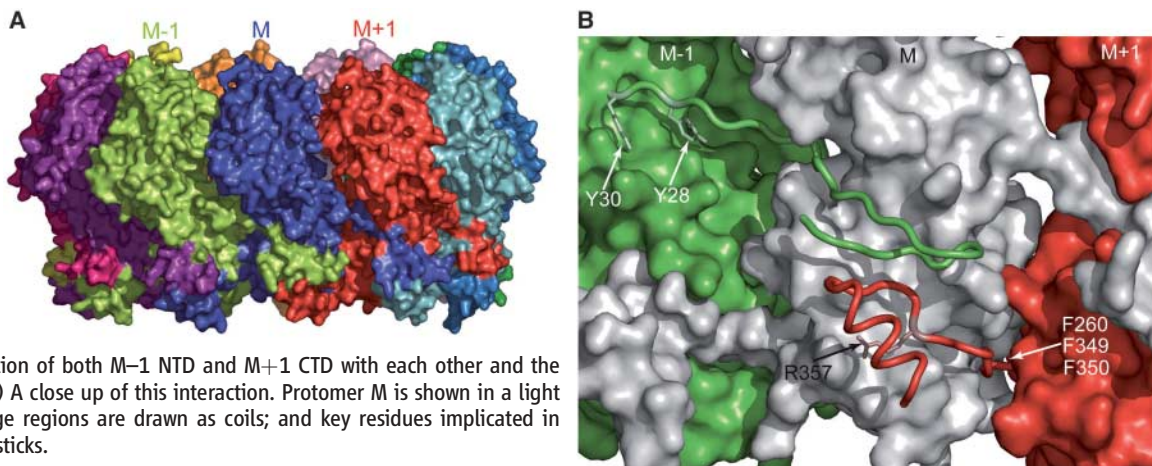


Fig. 2. Nucleoprotein-RNA interaction. **(A)** Stereo view of a close up of the interaction between N and the RNA. The RNA is shown as stick model and the protein moiety as a coil; the NTD is depicted in dark blue and the CTD in light blue. The nucleotides with bases facing the solvent are drawn in yellow and the bases facing the protein in green. The central nucleotide at the tip of the left-hand helical RNA segment is shown in red. Residues contacting the phosphates and ribose moieties are shown as sticks. **(B)** Schematic drawing highlighting the protein-RNA interactions with the phosphates and the ribose moieties. Color coding and orientations of the bases are the same as in (A). Most interactions are with the ribose-phosphate backbone.

Fig. 3. Two hinge regions stabilize polymerization of N. **(A)** Space-filling model of the N-RNA ring as viewed from the side. Each protomer is shown in a different color. This indicates that the NTD hinge from protomer M reaches over to M+1 and its CTD hinge reaches over to M-1. This arrangement leads to the interaction of both M-1 NTD and M+1 CTD with each other and the surface of protomer M. **(B)** A close up of this interaction. Protomer M is shown in a light gray for clarity; both hinge regions are drawn as coils; and key residues implicated in interaction are shown as sticks.



which is the start site for replication and transcription (25).

Electron micrographs of nucleocapsids from measles virus (*Paramyxoviridae*) and Marburg virus (*Filoviridae*), as well as an RNA-free crystal structure from the Borna virus (*Bornaviridae*) nucleoprotein, suggest that these nucleoproteins also adopt a two-domain structure (26, 27). This suggests that these enveloped viruses use an RNA-sequestering mechanism similar to that observed for the rabies virus N-RNA complex. The N-RNA polymer has thus evolved as the ideal template for the polymerase activity, which exposes the genomic RNA only temporarily to the host cell defense systems during replication. The tight sequestering of RNA observed in the crystal structure suggests further that the closed N-RNA conformation might be stabilized or frozen by small molecules, which could thus act as antiviral agents preventing rabies virus replication.

Note added in proof: This version of the manuscript is slightly changed relative to the version that was published *Science Express* on June 15. Improved refinement of the structure led to a better definition of the following regions, which have been changed accordingly: the N terminus, including the β hairpin leading to helix 1; Tyr¹⁶¹, Arg¹⁶⁸, and Arg⁴³⁴ contacting the RNA; as well as helices 13 to 16 of the C-terminal domain. None of

the changes made influences the overall conformation of the structure or any of the conclusions drawn from the structure.

References and Notes

1. B. Dietzschold, M. Schnell, H. Koprowski, *Curr. Top. Microbiol. Immunol.* **292**, 45 (2005).
2. D. L. Knobel *et al.*, *Bull. World Health Organ.* **83**, 360 (2005).
3. R. A. Lamb, D. Kolakofsky, in *Fields Virology*, D. M. Knipe and P. M. Howley, Eds. (Lippincott, Williams and Wilkins, Philadelphia, ed. 4, 2001), pp. 1305–1340.
4. H. Arnheiter, N. L. Davis, G. Wertz, M. Schubert, R. A. Lazzarini, *Cell* **41**, 259 (1985).
5. D. Kolakofsky, P. Le Mercier, F. Iseni, D. Garcin, *Virology* **318**, 463 (2004).
6. O. Poch, I. Sauvaget, M. Delarue, N. Tordo, *EMBO J.* **8**, 3867 (1989).
7. S. U. Emerson, M. Schubert, *Proc. Natl. Acad. Sci. U.S.A.* **84**, 5655 (1987).
8. D. Kolakofsky, *J. Virol.* **41**, 566 (1982).
9. D. Spohner, R. Drillien, P. M. Howley, *Virology* **232**, 260 (1997).
10. F. Iseni, A. Barge, F. Baudin, D. Blondel, R. W. Ruigrok, *J. Gen. Virol.* **79**, 2909 (1998).
11. B. M. Blumberg, C. Giorgi, D. Kolakofsky, *Cell* **32**, 559 (1983).
12. G. Schoehn, F. Iseni, M. Mavrikis, D. Blondel, R. W. Ruigrok, *J. Virol.* **75**, 490 (2001).
13. Supporting data are available on *Science Online*.
14. D. Thomas *et al.*, *J. Virol.* **54**, 598 (1985).
15. S. Lynch, D. Kolakofsky, *J. Virol.* **28**, 584 (1978).
16. S. Akira, S. Uematsu, O. Takeuchi, *Cell* **124**, 783 (2006).
17. I. Le Blanc *et al.*, *Nat. Cell Biol.* **7**, 653 (2005).
18. L. Espert *et al.*, *J. Biol. Chem.* **278**, 16151 (2003).
19. F. Iseni, F. Baudin, D. Blondel, R. W. Ruigrok, *RNA* **6**, 270 (2000).

20. Single-letter abbreviations for the amino acid residues are as follows: A, Ala; C, Cys; D, Asp; E, Glu; F, Phe; G, Gly; H, His; I, Ile; K, Lys; L, Leu; M, Met; N, Asn; P, Pro; Q, Gln; R, Arg; S, Ser; T, Thr; V, Val; W, Trp; and Y, Tyr.
21. B. Dietzschold *et al.*, *Virus Res.* **8**, 103 (1987).
22. H. Toriumi, A. Kawai, *Microbiol. Immunol.* **49**, 757 (2005).
23. S. Longhi *et al.*, *J. Biol. Chem.* **278**, 18638 (2003).
24. A. Kouznetsov, M. Buckle, N. Tordo, *J. Gen. Virol.* **79**, 1005 (1998).
25. S. U. Emerson, *Cell* **31**, 635 (1982).
26. G. Schoehn *et al.*, *J. Mol. Biol.* **339**, 301 (2004).
27. M. G. Rudolph *et al.*, *Structure* **11**, 1219 (2003).
28. We thank D. Kolakofsky (Geneva), Y. Gaudin, and D. Blondel (Gif-sur-Yvette), for many discussions and ideas; F. Iseni and M. Mavrikis for early contributions to the project; S. Cusack for discussions and comments on the text; and all members of the EMBL European Synchrotron Radiation Facility (ESRF) Joint Structural Biology Group (JSBG) for access to the ESRF beam lines. This work was supported by the EMBL (W.W.), the Deutsche Forschungsgemeinschaft SFB 593 (W.W.), the Université Joseph Fourier (R.W.H.R.), the CNRS (G.S.), an EMBO fellowship (C.R.C.), and a Ph.D. fellowship from the French Ministry for Education, Research, and Technology (A.A.V.A.). Coordinates have been deposited in the Protein Data Bank (accession code no. 2GTT).

Supporting Online Material

www.sciencemag.org/cgi/content/full/1125280/DC1

Materials and Methods

Figs. S1 to S4

Table S1

References

23 January 2006; accepted 17 May 2006

Published online 15 June 2006;

10.1126/science.1125280

Include this information when citing this paper.

Characterization of the piRNA Complex from Rat Testes

Nelson C. Lau,^{1*} Anita G. Seto,^{1*} Jinkuk Kim,^{2,3} Satomi Kuramochi-Miyagawa,⁴ Toru Nakano,⁴ David P. Bartel,^{3,5} Robert E. Kingston^{1†}

Small noncoding RNAs regulate processes essential for cell growth and development, including mRNA degradation, translational repression, and transcriptional gene silencing (TGS). During a search for candidate mammalian factors for TGS, we purified a complex that contains small RNAs and Piwi, the rat homolog to human Piwi. The RNAs, frequently 29 to 30 nucleotides in length, are called Piwi-interacting RNAs (piRNAs), 94% of which map to 100 defined (≤ 101 kb) genomic regions. Within these regions, the piRNAs generally distribute across only one genomic strand or distribute on two strands but in a divergent, nonoverlapping manner. Preparations of piRNA complex (piRC) contain rRecQ1, which is homologous to *qde-3* from *Neurospora*, a gene implicated in silencing pathways. Piwi has been genetically linked to TGS in flies, and slicer activity cofractionates with the purified complex. These results are consistent with a gene-silencing role for piRC in mammals.

Gene-silencing pathways guided by small RNAs, essential for maintaining proper cell growth and differentiation, operate at either the transcriptional or posttranscriptional level (1). Posttranscriptional gene silencing acts through mRNA destabilization or inhibition of mRNA translation (1), whereas TGS represses gene expression by altering chromatin conformation (2). Each pathway uses a core complex containing small RNA associated with a member of the Argonaute (Ago) protein family; however, the different mechanistic needs of each pathway

require differences in complex composition. Although RNA-mediated TGS has been studied in fission yeast and other eukaryotes (2–5), the mechanism of this process in mammals remains elusive.

To identify candidate complexes for TGS in mammals, we exploited the previous observations that TGS might use small RNAs longer than the 21- to 23-nucleotide (nt) microRNAs (miRNAs). In *Arabidopsis*, *Tetrahymena*, *Drosophila*, and zebrafish, RNAs that are 24 nt and longer have been associated with TGS and/or genomic repeats, which are often silenced (6–11).

In *Drosophila*, these repeat-associated small interfering RNAs (rasiRNAs) are enriched in the testis (6, 12). Therefore, we prepared extract from rat testes and fractionated it on an ion-exchange Q column, monitoring the small RNAs. A peak of small RNAs longer than a 22-nt marker eluted in mild salt conditions, which suggested the presence of a novel ribonucleoprotein complex (Fig. 1A).

To characterize the small RNAs, we sequenced cDNA libraries made from flowthrough and eluate fractions, obtaining 61,581 reads from the eluate that matched perfectly to the *Rattus norvegicus* genome (13). In contrast to the flowthrough RNAs, which were mostly miRNAs (69%), the eluate RNAs derived primarily from regions of the genome not previously thought to be expressed (Fig. 1A). Some eluate reads matched expressed sequence tags (EST) (11%),

¹Department of Molecular Biology, Massachusetts General Hospital, 185 Cambridge Street, Boston, MA 02114, USA.

²Harvard-MIT Division of Health Sciences and Technology, E18-435, 77 Massachusetts Avenue, Cambridge, MA 02139, USA. ³Howard Hughes Medical Institute and Whitehead Institute for Biomedical Research, 9 Cambridge Center, Cambridge, MA 02142, USA. ⁴Department of Molecular Cell Biology, Research Institute for Microbial Diseases, Osaka University, 3-1 Yamada-oka, Suita-shi, Osaka 565-0871, Japan. ⁵Department of Biology, Massachusetts Institute of Technology, Cambridge, MA 02139, USA.

*These authors contributed equally to this work.

†To whom correspondence should be addressed. E-mail: kingston@molbio.mgh.harvard.edu

but only a small fraction matched annotated mRNAs (< 1.1%). Some also matched repeats (20%), but when considering that ~40% of the

genome is annotated as repeats (13), the eluate reads were depleted in repeat sequences and thus, as a class, did not represent rasiRNAs.

The eluate RNAs were mostly 25 to 31 nt in length (Fig. 1A), and Northern blot analysis indicated a testis-specific expression pattern (Fig. 1B). Most eluate RNAs began with a 5' uridine (~84%), but no other sequence features or motifs were detected. A dominant subpopulation at 29 to 30 nt was observed (Fig. 1C); however, these 29- to 30-nt oligomers could not be distinguished from most of the remaining eluate reads by other criteria, including 5' nucleotide, genomic locus, and annotation. Thus, all the eluate RNAs that did not match annotated noncoding RNAs (miRNA, tRNA, rRNA, and snRNA) were considered together as representing a single newly identified class of small RNAs.

To understand potential functions for these RNAs, we purified the associated proteins. By monitoring the RNAs, we developed a five-step scheme to purify the native complex to near homogeneity (Fig. 2, A and B). Mass spectrometry of the purified complex identified the rat homologs to Piwi (Riwi) and the human RecQ1 protein (Fig. 2 and fig. S1). Western blotting confirmed the copurification of Riwi and rRecQ1 with the small RNAs (Fig. 2C, but see also independent purification described below). We designate RNAs found with rat Piwi to be Piwi-interacting RNAs (piRNAs) and the complex to be the piRNA complex (piRC).

To gain insight into the origins of piRNAs, we examined the genomic loci from which they presumably derived. About two-thirds of the piRNA sequences each perfectly matched a single locus, and in some cases that specific locus was matched by multiple reads (up to 149). For the remaining one-third of the reads, which each mapped to multiple loci

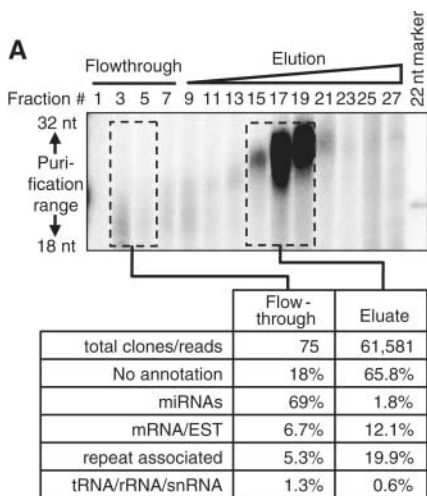
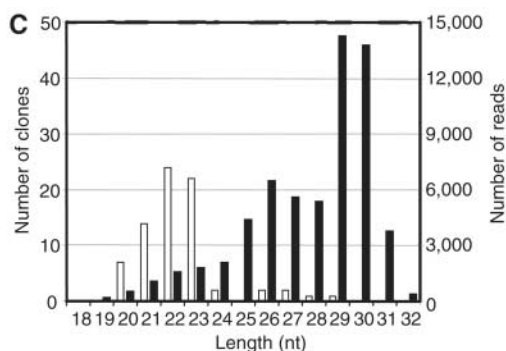
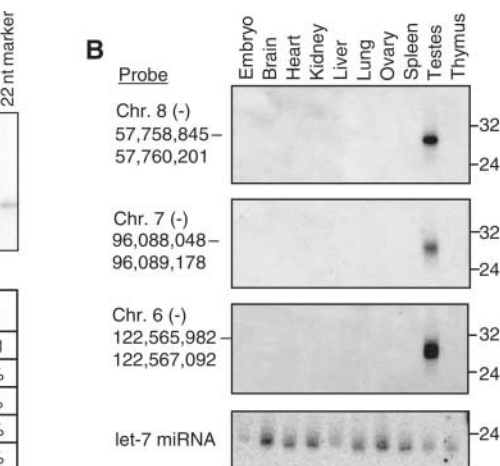


Fig. 1. Testes contain a longer class of small RNAs. (A) (Top) Rat testes extract was fractionated on a Q column (0.1 to 1 M potassium acetate gradient). RNA from fractions was end-labeled and resolved on a gel. (Bottom) Small RNAs from column fractions were gel-purified (dashed boxes), converted to cDNAs, and sequenced. (B) Rat tissue Northern blot hybridized with body-labeled RNA probes corresponding to small RNA sequences. The blot was stripped before reprobing for the indicated chromosomal regions or let-7 miRNA (loading control). Migration of RNA markers is indicated (right).



(C) Size distribution of small RNAs from flowthrough (white bars), and eluate (black bars). Y-axis scales are different for flowthrough RNAs (left) and eluate RNAs (right).

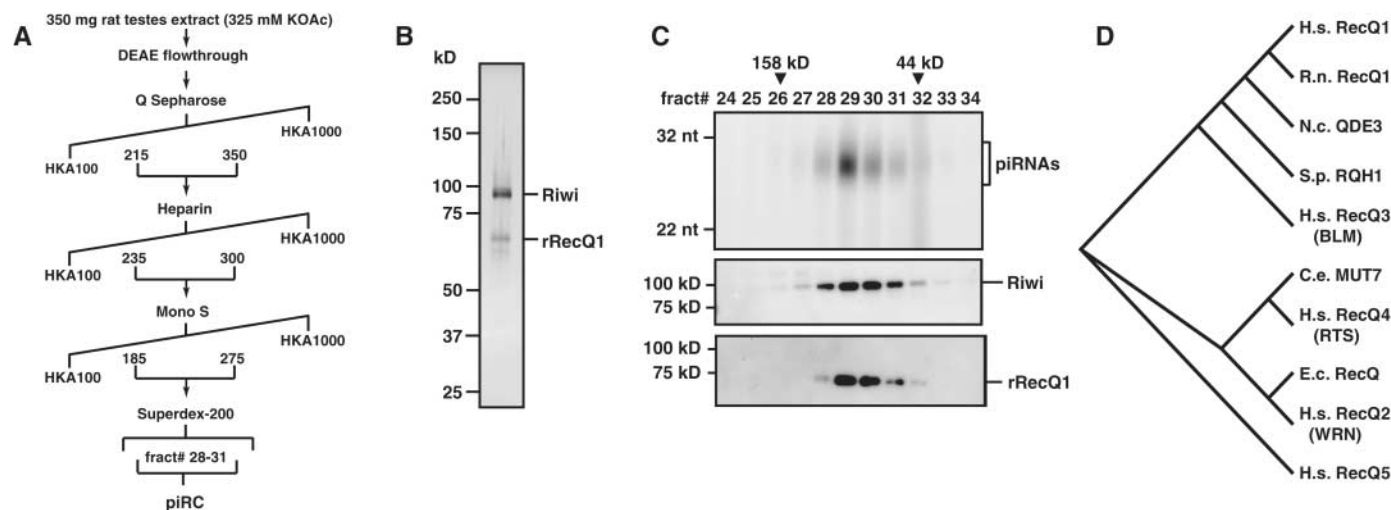


Fig. 2. Purification of a native small RNA-containing complex revealed Riwi and rRecQ1. (A) Schematic of piRC fractionation steps from rat testes extract. Numbers represent potassium acetate (KOAc) concentration (mM). (B) Proteins from the peak fraction of piRC (Superdex-200 column) were resolved on a gel and silver stained. Bands were excised and identified by mass spectrometry to be Riwi and rRecQ1 (See fig. S1). (C) Small RNAs, Riwi, and rRecQ copurify after five steps of chromatographic separation. Final Superdex-200 column fractions were assayed for the presence of small RNAs, Riwi, or rRecQ1. (Top) Small RNAs were end-labeled and resolved on a gel. (Middle and bottom) Western blots probed with antibodies to Miwi (mouse Piwi) and to hRecQ1. Elution profile of protein size markers from Superdex-200 column indicated above. (D) Phylogenetic profile of protein size markers from Superdex-200 column fractions was assayed for the presence of small RNAs, Riwi, or rRecQ1.

(D) Phylogenetic comparison of RecQ DNA helicase family members revealed *Neurospora* QDE-3 to be a close homolog to rRecQ1.

(up to 25,044 loci), we normalized the number of reads by the number of genomic hits and assigned this normalized hit count equally to all the loci; thus, a piRNA read with four perfect genomic hits contributed a

quarter of a count to each of its four loci. Counts were integrated into bins and plotted across each chromosome. The majority of counts (94%) fell into 100 genomic clusters that each contained at least 20 uniquely

mapping reads (table S1). As exemplified by four clusters on chromosome 20 (Fig. 3A) and illustrated for all 100 clusters (fig. S2), the clusters distributed across the genome; however, some chromosomes were underrepre-

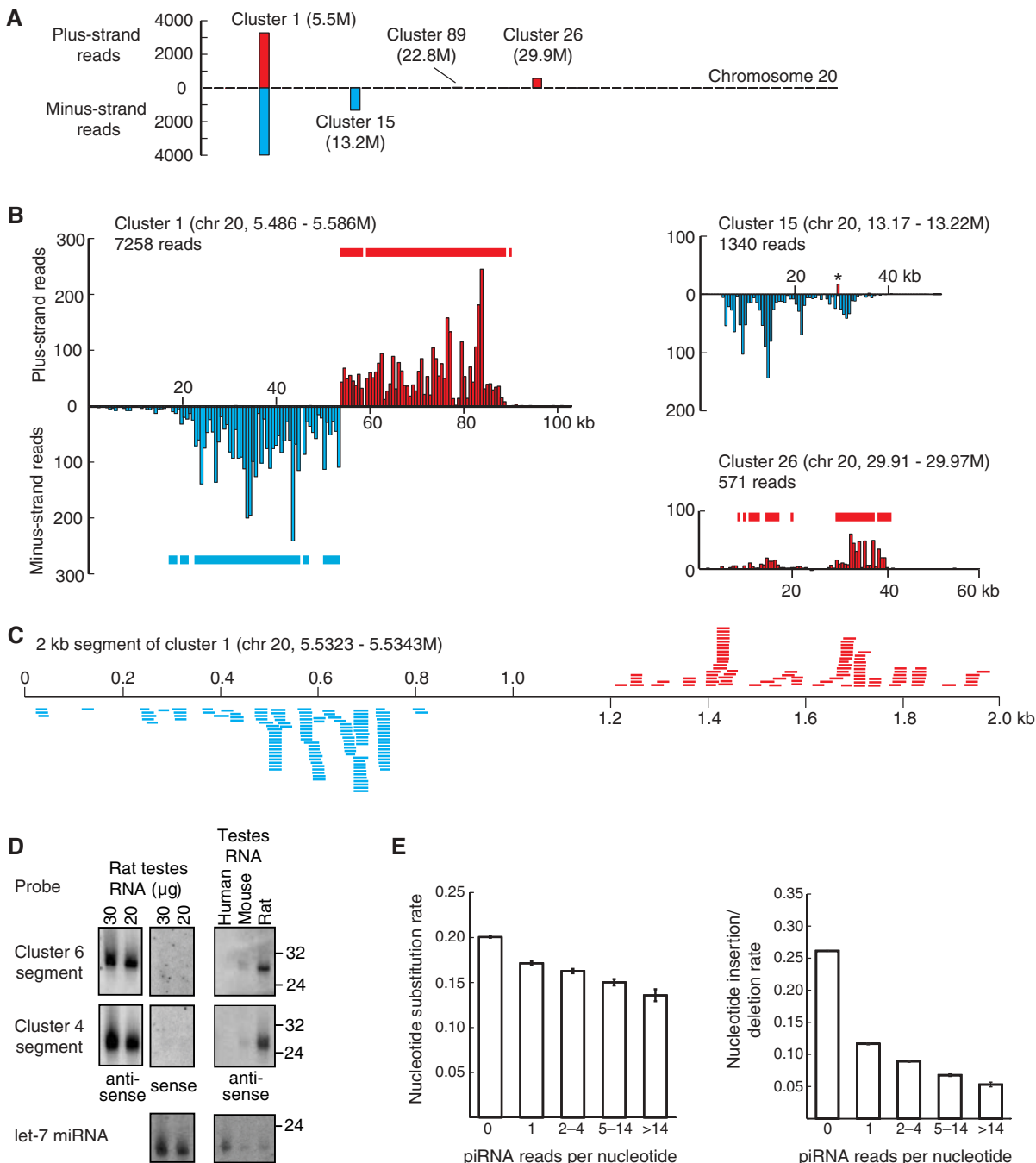


Fig. 3. Genomic characteristics of rat piRNAs. **(A)** Chromosomal view indicating the number of piRNA reads mapping to clusters on chromosome (chr) 20 [27]. **(B)** Medium-resolution view of clusters 1, 15, and 26. Horizontal bars above and below the histograms indicate regions orthologous to mouse regions that also produce piRNAs (indicated if the bin matches >2 uniquely mapping mouse piRNAs) (tables S1 and S3). An asterisk denotes a group of piRNAs from cluster 15 that perfectly mapped to more than one locus in the genome. **(C)** High-resolution view centered on the gap region that separates minus- and plus-strand piRNA hits in cluster 1. Horizontal bars represent individual piRNAs. **(D)** Northern blot analysis with probes

to the indicated clusters, testing strand-specific piRNA expression (left and middle) and cross-hybridization to mouse and human testes RNAs (right). Migration of RNA markers is indicated (far right). Blots were stripped and reprobed to let-7 miRNA (loading control). **(E)** piRNA conservation analysis. Orthologous rat and mouse clusters were identified, and rat residues were binned based on the number of matching rat piRNA reads. The estimated substitution rate per residue (left) and estimated insertion/deletion rate (right), comparing rat to mouse, was calculated for each bin. Error bars indicate 95% confidence intervals of the estimates (27).

sented in piRNA hits and clusters (fig. S2B). These clusters spanned 1 to 101 kb (table S1) and in aggregate made up less than 0.1% of the rat genome.

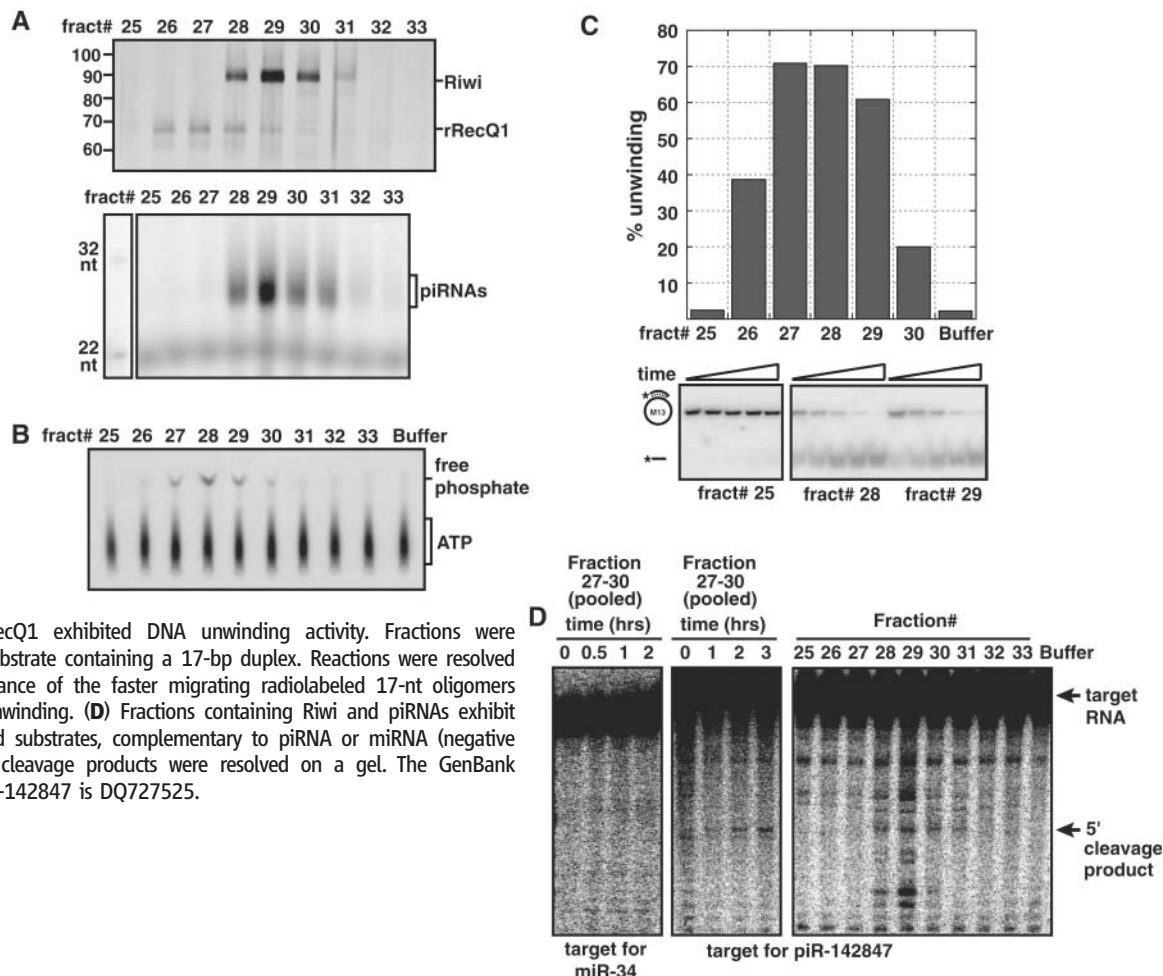
Known silencing RNAs (siRNAs and miRNAs) derive from double-stranded RNA precursors or foldback structures (1). In contrast, piRNAs of most clusters mapped exclusively to either the plus or minus genomic strand in irregular, sometimes overlapping, patterns, with no evidence of extensive foldback structures or double-stranded origins (Fig. 3B). Sixteen clusters, such as cluster 1 (Fig. 3, B and C), contained regions of minus- and plus-strand hits that were juxtaposed with each other but separated by a gap of ~100 to 800 base pairs (bps), an orientation that suggests divergent, bi-directional transcription, starting within the gap that separated the two distributions (table S1). Only two clusters had hits that suggested convergent or overlapping transcription (table S1, clusters 31 and 38). Northern blot analysis confirmed that piRNAs derived predominantly from one of the two genomic strands (Fig. 3D). Reverse transcription polymerase chain reaction results suggested that longer transcripts of the same polarity, perhaps piRNA precursors, also derived from these regions (fig. S3).

Analogous production of piRNAs from at least 94 clusters occurred in the mouse, as indicated by the analysis of 68,794 piRNA reads generated in the same manner as those of the rat (Fig. 3B, fig. S4, and tables S3 and S4). Most of the mouse clusters were homologous to rat clusters, with strikingly similar strand specificity and abundance profiles (Fig. 3B and tables S1 and S3). Nonetheless, their sequence conservation was low. Probes against rat clusters 4 and 6 hybridized only weakly to mouse piRNAs, as expected by the numerous point substitutions in the orthologous mouse piRNAs (Fig. 3D and fig. S5). Overall, the single-nucleotide substitution rate of the piRNA clusters was within the 15 to 20% expected for neutral residues (13). Nevertheless, residues represented by more reads had lower substitution and insertion/deletion rates, indicating detectable evolutionary pressure to conserve the sequence of the abundant piRNAs (Fig. 3E). We conclude that the production of piRNAs is highly conserved, but the sequence identities of the piRNAs are only weakly conserved. The weak conservation favors models in which piRNAs target the loci/transcripts that correspond to the same loci from which they derive.

We characterized two potential biochemical functions of piRC suggested by activities previously attributed to RecQ and Ago family members. Human RecQ1 is an adenosine triphosphate (ATP)-dependent DNA helicase (14). Both adenosine triphosphatase (ATPase) and DNA unwinding activities followed the rRecQ1 protein of piRC (Fig. 4, A and B, and fig. S6). Riwi contains the catalytic residues that other Ago proteins use for RNA-guided cleavage of target RNAs (15) (fig. S7A). Using a substrate complementary to a piRNA, we detected cleavage activity, peaking with fractions containing Riwi and piRNAs (Fig. 4D). However, it was not robust, perhaps because of the small representation of the cognate piRNA in the diverse population of piRNAs (<0.2%).

Our purification of piRC uncovered a novel class of small RNAs and identified as copurifying factors Riwi and rRecQ1, two proteins with intriguing functions genetically determined in other species. Piwi represents a subclade of the Ago family of proteins (16) and was first discovered to regulate germ stem cell maintenance in *Drosophila* (17). Subsequently, mammalian Piwi members were found to regulate germ cell maturation (18, 19). *Drosophila piwi* mutants are also defective in small

Fig. 4. piRC fractions contained ATP-dependent DNA helicase and slicer activities. **(A)** Visualization of proteins (top, silver stain) and end-labeled small RNAs (bottom) in fractions from final Superdex-200 column (independent purification from that shown in Fig. 2C). Size standards indicated on left. **(B)** Fractions containing rRecQ1 exhibit ATPase activity. Fractions were incubated with radiolabeled ATP. Free phosphate generated by ATPase activity was separated from unhydrolyzed ATP on thin-layer chromatography. **(C)** Fractions containing rRecQ1 exhibited DNA unwinding activity. Fractions were incubated with a DNA substrate containing a 17-bp duplex. Reactions were resolved on a native gel. Appearance of the faster migrating radiolabeled 17-nt oligomers indicated DNA duplex unwinding. **(D)** Fractions containing Riwi and piRNAs exhibit slicer activity. Cap-labeled substrates, complementary to piRNA or miRNA (negative control) sequences, and cleavage products were resolved on a gel. The GenBank accession number for piR-142847 is DQ727525.



RNA-dependent transgene and retrotransposon silencing (20, 21) and lose the inability to localize heterochromatic proteins, including the repressive Polycomb-group proteins (22, 23). *Tetrahymena* Piwi (*TIWI*) is needed for siRNA-mediated DNA elimination (24).

In *Neurospora*, a screen for mutants in quelling (gene silencing during vegetative growth) identified both QDE-2, an Ago-family protein, and QDE-3, a RecQ1 homolog (25, 26). When compared with RecQ homology in mammals and other organisms, *Neurospora* QDE-3 resided in the same clade as rRecQ1 (Fig. 2D and fig. S7B). rRecQ1 did not always precisely cofractionate with Riwi and the piRNAs during our final purification step (Fig. 4A). The lack of tight association of rRecQ1 might have reflected conditions specific to this step or might indicate that rRecQ1 is generally less tightly associated with piRNAs than is Riwi. Perhaps rRecQ1 is not critical for piRC function. However, the genetic links between the QDE-2 and QDE-3 silencing factors suggest that the biochemical association between Riwi and rRecQ1 has biological importance and, furthermore, implies a gene-silencing function for piRC. Addressing the functions of piRC and the biogenesis and localization of the piRNAs will be important

questions for elucidating the potential for piRC to regulate the genome.

References and Notes

- P. D. Zamore, B. Haley, *Science* **309**, 1519 (2005).
- M. A. Matzke, J. A. Birchler, *Nat. Rev. Genet.* **6**, 24 (2005).
- I. M. Hall *et al.*, *Science* **297**, 2232 (2002).
- A. Verdel *et al.*, *Science* **303**, 672 (2004).
- T. A. Volpe *et al.*, *Science* **297**, 1833 (2002).
- A. A. Aravin *et al.*, *Dev. Cell* **5**, 337 (2003).
- P. Y. Chen *et al.*, *Genes Dev.* **19**, 1288 (2005).
- A. Hamilton, O. Voynet, L. Chappell, D. Baulcombe, *EMBO J.* **21**, 4671 (2002).
- S. R. Lee, K. Collins, *Genes Dev.* **20**, 28 (2006).
- K. Mochizuki, M. A. Gorovsky, *Genes Dev.* **18**, 2068 (2004).
- D. Zilberman, X. Cao, S. E. Jacobsen, *Science* **299**, 716 (2003).
- A. A. Aravin *et al.*, *Mol. Cell. Biol.* **24**, 6742 (2004).
- R. A. Gibbs *et al.*, *Nature* **428**, 493 (2004).
- S. Cui *et al.*, *J. Biol. Chem.* **278**, 1424 (2003).
- F. V. Rivas *et al.*, *Nat. Struct. Mol. Biol.* **12**, 340 (2005).
- M. A. Carmell, Z. Xuan, M. Q. Zhang, G. J. Hannon, *Genes Dev.* **16**, 2733 (2002).
- D. N. Cox *et al.*, *Genes Dev.* **12**, 3715 (1998).
- W. Deng, H. Lin, *Dev. Cell* **2**, 819 (2002).
- S. Kuramochi-Miyagawa *et al.*, *Development* **131**, 839 (2004).
- A. I. Kalmykova, M. S. Klenov, V. A. Gvozdev, *Nucleic Acids Res.* **33**, 2052 (2005).
- M. Pal-Bhadra, U. Bhadra, J. A. Birchler, *Mol. Cell* **9**, 315 (2002).
- C. Grimaud *et al.*, *Cell* **124**, 957 (2006).
- M. Pal-Bhadra *et al.*, *Science* **303**, 669 (2004).
- K. Mochizuki, N. A. Fine, T. Fujisawa, M. A. Gorovsky, *Cell* **110**, 689 (2002).
- C. Catalanotto, G. Azzalin, G. Macino, C. Cogoni, *Genes Dev.* **16**, 790 (2002).
- C. Cogoni, G. Macino, *Science* **286**, 2342 (1999).
- Materials and methods are available as supporting material on Science Online.
- The order of listing of the first two authors is arbitrary. We thank N. Francis for initial work on this project; W. Johnston for technical assistance; L. Davidow, J. Morris, L. Lim, and J. Ruby for bioinformatics assistance; Z. Zhang and J. Goldman for performing preliminary assays; D. Schwarz for advice on slicer assays; and C. Woo, E. Troemel, J. Song, and S. Aigner for comments on the manuscript. Supported by Helen Hay Whitney (N.L.) and Damon Runyon (A.S.) postdoctoral fellowships, a Korea Foundation for Advanced Studies predoctoral fellowship (J.K.), and grants from NIH (D.B. and R.K.). D.B. is a Howard Hughes Medical Institute investigator.

Supporting Online Material

www.sciencemag.org/cgi/content/full/1130164/DC1

Materials and Methods

SOM Text

Figs. S1 to S7

Tables S1 to S6

18 May 2006; accepted 7 June 2006

Published online 15 June 2006;

10.1126/science.1130164

Include this information when citing this paper.

Aneuploidy and Isochromosome Formation in Drug-Resistant *Candida albicans*

Anna Selmecki,¹ Anja Forche,¹ Judith Berman^{1,2*}

Resistance to the limited number of available antifungal drugs is a serious problem in the treatment of *Candida albicans*. We found that aneuploidy in general and a specific segmental aneuploidy, consisting of an isochromosome composed of the two left arms of chromosome 5, were associated with azole resistance. The isochromosome forms around a single centromere flanked by an inverted repeat and was found as an independent chromosome or fused at the telomere to a full-length homolog of chromosome 5. Increases and decreases in drug resistance were strongly associated with gain and loss of this isochromosome, which bears genes expressing the enzyme in the ergosterol pathway targeted by azole drugs, efflux pumps, and a transcription factor that positively regulates a subset of efflux pump genes.

Candida albicans is the most prevalent human fungal pathogen and is especially problematic in immune-compromised individuals. Azoles are antifungal drugs used extensively in the therapy of *C. albicans* infections because they cause few side effects. Resistance to azoles arises during long-term low-level prophylactic treatment regimes (1). The evolution of azole-resistance can occur via

different pathways, e.g., increased activity of transcription factors that regulate drug pumps (2) or mutations in the ergosterol biosynthetic pathway (3), and may be facilitated by the heat shock protein Hsp90 (4). Although *C. albicans* does not have a complete sexual cycle, surveys of clinical strains suggest that it tolerates genome flexibility that generates a moderate level of selectable genetic diversity (5–11).

We adapted comparative genome hybridization (CGH) arrays for the analysis of gene copy number at all loci (10) for 70 azole-resistant and azole-sensitive strains from clinical and laboratory sources (table S1). We found 37 aneuploid chromosomes in 23 strains (Fig. 1A, black and

white bars). Aneuploidy was seven times as prevalent in fluconazole-resistant [Flu^R, minimum inhibitory concentration (MIC) \geq 4] (21 out of 42 strains) as in fluconazole-sensitive (Flu^S, MIC < 4) (2 out of 28 strains) isolates. Aneuploidy, primarily trisomy, was most prevalent on chr5 (15 events), which also exhibited a high level of segmental aneuploidy (8 events) (Fig. 1A, gray bars) (10).

All eight Flu^R strains with a chr5 segmental aneuploidy displayed distinctive features by CGH: increased gene copy number on the left arm of the chromosome; one or two copies of genes on the right arm of the chromosome; and, most strikingly, the breakpoint between the two arms was identical (Fig. 1B). This common breakpoint was located between open reading frames orf19.3161 and orf19.4219, which flank a gap between contigs 19.10170 and 19.10202 in the version 19 assembly of the genome sequence. We sequenced the region between these two contigs (fig. S1) from strains carrying either one of the two chr5 homologs, which allowed us to distinguish alleles found in this partially heterozygous region of the genome. The sequence gap was within one arm of an inverted repeat flanking the binding site for Cse4p, the histone H3 variant that is necessary for centromere function (12) (Fig. 1B, diagram).

The combination of CGH data and Southern blot analysis revealed an isochromosome (two identical chromosome arms flanking a centromere) in the eight strains with extra copies of chr5L. An isochromosome composed of two chr5L arms should include a unique fragment,

¹Department of Genetics, Cell Biology, and Development, ²Department of Microbiology, University of Minnesota, 6-160 Jackson Hall, 321 Church Street SE, Minneapolis, MN 55455, USA.

*To whom correspondence should be addressed. E-mail: jberman@umn.edu

spanning from one chr5L arm, through the inverted repeat and the centromere, to the other chr5L arm. This was verified by the presence of a unique ~10 thousand base pairs (kbp) Eco NI fragment (Fig. 2A) in all eight strains carrying the predicted isochromosome.

The predicted size of an independent chr5L isochromosome [i(5L)] is similar to that of a normal chr7. Consequently, ethidium bromide staining of whole-chromosome contour-clamped homogeneous electric field (CHEF) gels revealed no consistent changes in the karyotypes of most strains (Fig. 2B). Many strains had two separable chr5 homologs, likely due to differences in major repeat sequence (MRS) length in the two sister chromosomes (13), that were detected with probes from chr5L and chr5R (Fig. 2, C and D). Probes from chr5L, but not from chr5R, revealed an ~945-kbp band (twice the size of one chr5L arm) in six of the strains (Fig. 2C, lanes 2, 3, 4, 9, and 12). In these strains, the ~945-kbp band was not digested by the restriction enzyme Sfi I (Fig. 2, E to H), which cuts only within the MRS on the right arm of chr5 (14) (Fig. 2J).

Two other strains with chr5 segmental aneuploidy contained a larger band (~2.2 Mbp) that hybridized to probes from both chr5L and chr5R (Fig. 2, C and D, lanes 5 and 11) and only one chr5 homolog of normal

size. Southern analysis of Sac I-digested DNA confirmed the presence of a novel, telomere-associated band in strain YJB8738 (Fig. 2I), suggesting that an isochromosome is attached to a full-length copy of chr5, by means of the left telomere (Fig. 2L). In this case, one of the centromeres must have been inactivated, either by a breakage and healing event (15) or by silencing of one of the centromeres (16).

Several genes on chr5L potentially have a role in Flu^R, including *ERG11*, which encodes lanosterol-14 α -demethylase, the target of fluconazole (17), and *TAC1*, which encodes a transcription factor that up-regulates expression of adenosine triphosphate (ATP)-binding cassette (ABC) transporter genes on chr3 (18). In addition, there are genes encoding predicted efflux pumps: orf19.4144, which encodes an ABC transporter, and orf19.1942, which encodes a predicted multidrug resistance (MDR) transporter. Analysis of expression profiles confirmed that expression of most genes on chr5L were increased relative to expression of genes on chr5R in a strain carrying i(5L) (Fig. 1C), which may account for the increased Flu^R of these strains. Thus, as in *Saccharomyces cerevisiae*, chromosome copy number increases are associated with corresponding increases in expression of genes across the aneuploid region (19).

During a period of drug treatment, reversible resistance often develops such that when selection is relaxed, in vivo or in vitro, resistance levels can drop (20–22). The acquisition of unstable “hetero-resistance” has been documented in clinical isolates from a patient treated with azole antifungals (21). Strain YJB8638 (Fig. 3A) was the initial Flu^S isolate; strain YJB9185 was the isolate most resistant to fluconazole acquired from the same patient (Fig. 3B). This was an unstable strain that lost resistance when cultured in vitro in the absence of drug (22). The i(5L) aneuploidy was not present in the initial Flu^S isolate (Fig. 3A); appeared in the resistant strain (Fig. 3B); and subsequently was lost in YJB9517, a strain with significantly reduced Flu^R derived from YJB9185 in the absence of drug selection (Fig. 3C). All YJB9185-derived strains with dramatic reductions in Flu^R lost the segmental aneuploidy, whereas all strains that maintained high Flu^R also retained the segmental aneuploidy (table S3). YJB9185 and its derivatives are homozygous for a hyperactive allele of *TAC1* (2), which may account for the residual Flu^R of YJB9517 relative to that of YJB8638 (Fig. 3). We cannot rule out an additional contribution from the short segmental monosomy on chr1 that appeared in YJB9185 and was retained in YJB9517 (Fig. 3).

Strain YJB8736, which evolved Flu^R in vitro, grew significantly better in the presence of fluconazole and significantly worse in the absence of fluconazole than the progenitor strain, which did not carry i(5L) (23). Under fluconazole selection, i(5L) was maintained through more than 165 generations in this strain (23, 24), which indicated that i(5L) can confer a growth advantage in the presence of azoles and can be maintained in the presence of drug and that its loss is accompanied by a decrease in Flu^R.

We have detected aneuploidies, primarily trisomies, for all *C. albicans* chromosomes (Fig. 1A) (10). This may reflect nondisjunction events like those that return tetraploids to a state where most, but not all, chromosomes are in the diploid state (8). Until now the i(5L) aneuploidy had not been detected because i(5L) migrates in CHEF gels with chr7, and the attached i(5L) migrates close to chr2.

Increased levels of gene expression from chr5L required for ergosterol biosynthesis and drug efflux pump activity are likely to contribute to drug resistance or tolerance. These genes do not occur on i(5R), and interestingly, aneuploidies involving this arm are not associated with drug resistance. It is noteworthy that the only sequence shared by the i(5L) and i(5R) isochromosomes, which thus delimits the chr5 centromere, is a 9.5-kbp region containing the unique sequence flanked by the inverted repeat (Fig. 1D). Consistent with the idea that replication forks pause at centromere sequences (25), we suggest that the centromere region of chr5 may be a fragile site where breaks occur and are healed more frequently.

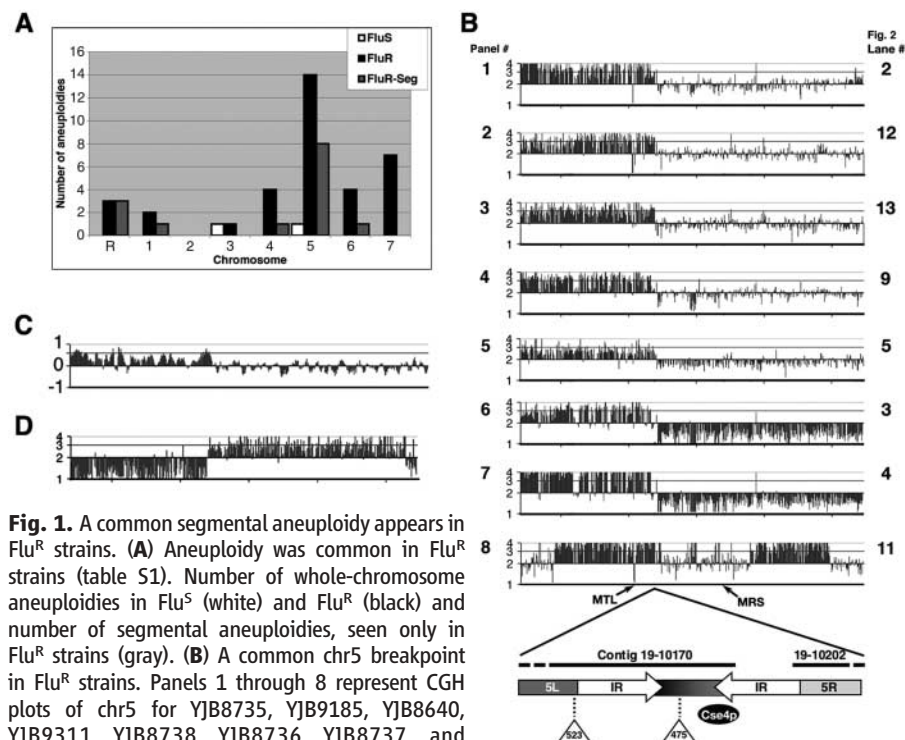


Fig. 1. A common segmental aneuploidy appears in Flu^R strains. (A) Aneuploidy was common in Flu^R strains (table S1). Number of whole-chromosome aneuploidies in Flu^S (white) and Flu^R (black) and number of segmental aneuploidies, seen only in Flu^R strains (gray). (B) A common chr5 breakpoint in Flu^R strains. Panels 1 through 8 represent CGH plots of chr5 for YJB8735, YJB9185, YJB8640, YJB9311, YJB8738, YJB8736, YJB8737, and YJB9180. The y axis plots gene copy number calculated from log₂ values. Two shorter segmental aneuploidies are seen in panel 8. Diagram illustrates the fine structure of the breakpoint including the *Cse4p* site and the two insertions found on one homolog. IR, inverted repeat; MTL, mating type-like. (C) Increased gene copy number correlated with increased gene expression. Transcript profile data (mean log₂ values) for strain YJB9311 (26) were plotted by using a running average over five ORFs. (D) CGH data of chr5 from a Flu^S strain reveals an i(5R) with the same breakpoint as strains with i(5L).

C. albicans is an organism in which isochromosome formation has been found to occur in response to antifungal drug selection. Because

i(5L) provides a selective growth advantage under drug conditions, *C. albicans* should provide a useful model system for studying the mechanisms

that generate isochromosomes (and, in some cases, telomere-telomere attachments). Reagents that reduce chromosome breakage and/or recombination events resulting in isochromosome formation could be useful companions to current azole antifungal treatments.

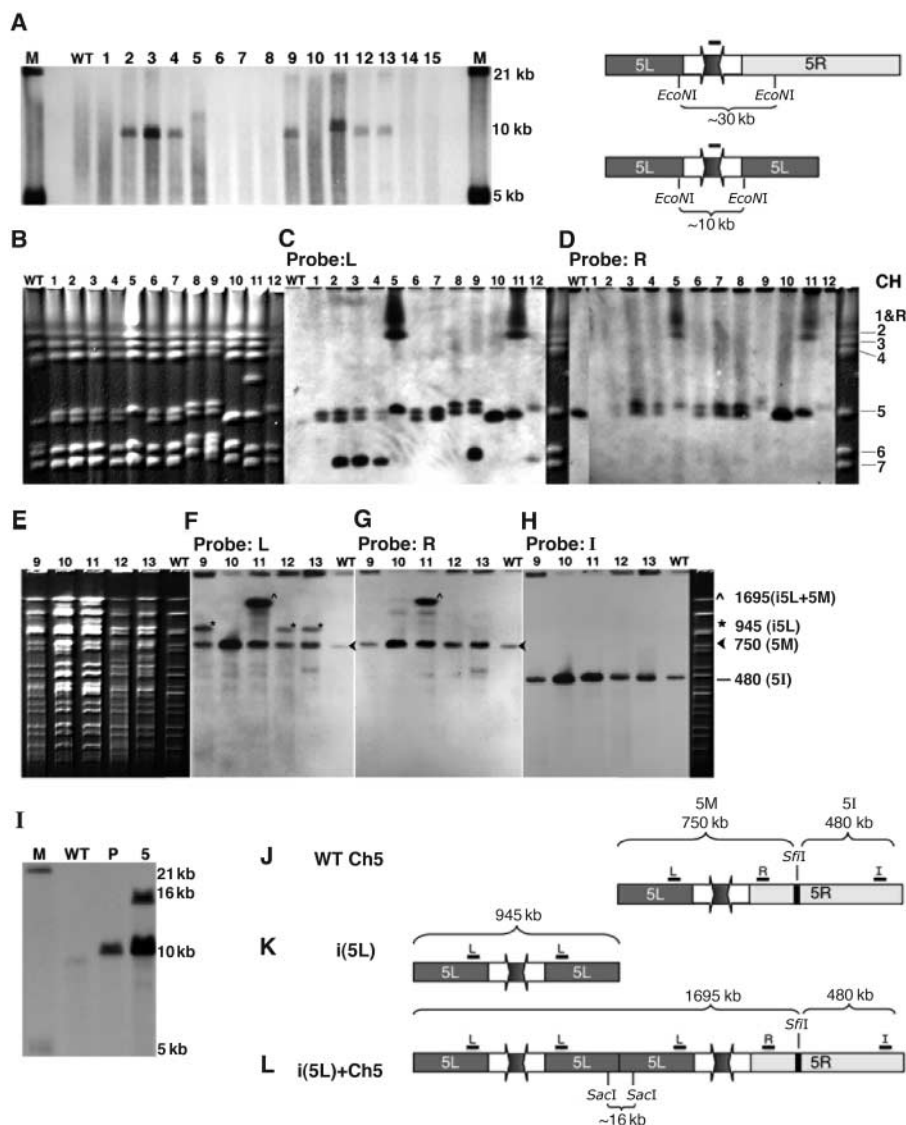


Fig. 2. The segmental aneuploidies on chr5 reflect isochromosome structures. (A) All strains from Fig. 1B contain a unique restriction fragment that spans the Cse4p binding site (lanes 2 to 5, 9, and 11 to 13). Southern blot of EcoNI-digested genomic DNA probed with Cse4p binding site sequence (black bar) detects an ~10-kbp fragment diagnostic of i(5L) structure. Differences in the size of this fragment are due to polymorphic insertion sequences (Fig. 1B). WT: wild type (SC5314), lanes 1 to 15: YJB8734, YJB8735, YJB8736, YJB8737, YJB8738, YJB8739, YJB8740, YJB9309, YJB9311, YJB9175, YJB9180, YJB9185, YJB8640, YJB9613, and YJB8638. Lane designations are identical for all other parts of this figure. (B to H) The isochromosome is either independent or attached to a homolog of chr5. Whole-chromosome CHEF gels stained with ethidium bromide (B), blotted, and probed with chr5L (C) or chr5R (D) reveal an independent isochromosome (lanes 2 to 4, 9, and 12) or an attached isochromosome (lanes 5 and 11). SfiI digestion of whole chromosomes separated by CHEF and stained with ethidium bromide (E); blotted; and probed with chr5L (F), chr5R (G), and chr5I (H) probes [diagramed in (J, K, and L)] show that the independent isochromosome (lanes 9, 12, and 13) does not contain an SfiI site. SfiI digestion of the attached isochromosome (lane 11) releases fragments expected if i(5L) were attached to the left arm of whole chr5. (I) The attached isochromosome includes a telomere-telomere junction. Southern blot analysis of SacI-digested genomic DNA probed with a chr5L telomere-adjacent probe detected a 10-kbp telomere fragment in all wild-type (WT) and parental (P) strains and an additional larger fragment in YJB8738 (lane 5), as would be expected if two chr5L arms attached via telomere sequence (L). YJB9180 contains a complex attachment not including this SacI fragment. (J to L) Diagrams, including relevant restriction sites and probes: (J) normal chr5, (K) independent i(5L), and (L) attached i(5L). The centromere region (inverted repeat and central unique sequence) is not to scale.

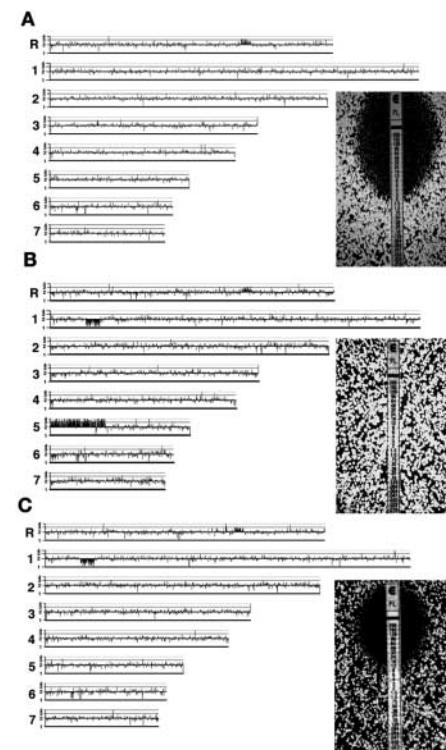


Fig. 3. Loss of i(5L) is associated with a dramatic decrease in Flu^R. Whole-genome CGH plots reveal, compared with (A), the gain (B) and loss (C) of i(5L) (left panels) and fluconazole-resistance by E-test assay (right panels) in isolates: (A) YJB8638, MIC = 2.0 μg/ml; YJB9185, (B) MIC > 256 μg/ml; (C) YJB9517, MIC = 8 μg/ml.

References and Notes

1. T. C. White, S. Holleman, F. Dy, L. F. Mirels, D. A. Stevens, *Antimicrob. Agents Chemother.* **46**, 1704 (2002).
2. A. T. Coste *et al.*, *Genetics* **172**, 2139 (2006).
3. J. B. Anderson *et al.*, *Genetics* **163**, 1287 (2003).
4. L. E. Cowen, S. Lindquist, *Science* **309**, 2185 (2005).
5. A. Forche, G. Schöniann, Y. Gräser, R. Vilgalys, T. G. Mitchell, *Fungal Genet. Biol.* **28**, 107 (1999).
6. G. Schonian *et al.*, *Mycoses* **36**, 171 (1993).
7. A. Tavanti *et al.*, *J. Clin. Microbiol.* **43**, 5601 (2005).
8. R. J. Bennett, A. D. Johnson, *EMBO J.* **22**, 2505 (2003).
9. G. Janbon, F. Sherman, E. Rustchenko, *Proc. Natl. Acad. Sci. U.S.A.* **95**, 5150 (1998).
10. A. Selmecki, S. Bergmann, J. Berman, *Mol. Microbiol.* **55**, 1553 (2005).
11. X. Chen, B. B. Magee, D. Dawson, P. T. Magee, C. A. Kumamoto, *Mol. Microbiol.* **51**, 551 (2004).
12. K. Sanyal, M. Baum, J. Carbon, *Proc. Natl. Acad. Sci. U.S.A.* **101**, 11374 (2004).
13. P. R. Lephart, H. Chibana, P. T. Magee, *Eukaryot. Cell* **4**, 733 (2005).
14. W. S. Chu, B. B. Magee, P. T. Magee, *J. Bacteriol.* **175**, 6637 (1993).
15. J. A. Fraser *et al.*, *Eukaryot. Cell* **4**, 401 (2005).
16. B. A. Sullivan, M. D. Blower, G. H. Karpen, *Nat. Rev. Genet.* **2**, 584 (2001).

17. T. C. White, *Antimicrob. Agents Chemother.* **41**, 1482 (1997).
 18. A. T. Coste, M. Karababa, F. Ischer, J. Bille, D. Sanglard, *Eukaryot. Cell* **3**, 1639 (2004).
 19. T. R. Hughes *et al.*, *Nat. Genet.* **25**, 333 (2000).
 20. H. M. Calvet, M. R. Yeaman, S. G. Filler, *Antimicrob. Agents Chemother.* **41**, 535 (1997).
 21. K. A. Marr, T. C. White, J. A. van Burik, R. A. Bowden, *Clin. Infect. Dis.* **25**, 908 (1997).
 22. K. A. Marr *et al.*, *Antimicrob. Agents Chemother.* **42**, 2584 (1998).
 23. L. E. Cowen, L. M. Kohn, J. B. Anderson, *J. Bacteriol.* **183**, 2971 (2001).
 24. L. E. Cowen *et al.*, *J. Bacteriol.* **182**, 1515 (2000).
 25. S. A. Greenfeder, C. S. Newlon, *Mol. Cell. Biol.* **12**, 4056 (1992).
26. M. Karababa, A. T. Coste, B. Rognon, J. Bille, D. Sanglard, *Antimicrob. Agents Chemother.* **48**, 3064 (2004).
 27. We thank J. Anderson, P. T. Magee, P. D. Rogers, D. Sanglard, and T. White for providing strains and M. Gerami-Nejad, M. McClellan, M. Carlson, and J. Borton for technical assistance. We thank A. Nantel, M. van het Hoog, and P. T. Magee for genome map information; S. Bergmann for Chromosome_Map programming; and N. Springer, D. Kirkpatrick, J. Strathern, M. Kupiec, M. Basrai, and D. Sanglard for helpful discussions and review of the manuscript. This work was supported by NIH R01 AI062427 to J.B., a Microbial and Plant Genomics Institute Integrative fellowship to A.S., and a microarray supplemental award DE10641-5 to M. Edgerton. Sequence analysis of chr5 is deposited in GenBank,

accession number DQ660981. The CGH array data are listed in GEO, the Gene Expression Omnibus, as series "CGH analysis of *Candida albicans* strains" with accession number GSE4995.

Supporting Online Material

www.sciencemag.org/cgi/content/full/313/5785/367/DC1
 Materials and Methods
 Fig. S1
 Tables S1 to S3
 References and Notes

3 April 2006; accepted 7 June 2006
 10.1126/science.1128242

Genome of Rice Cluster I Archaea—the Key Methane Producers in the Rice Rhizosphere

Christoph Erkel,¹ Michael Kube,² Richard Reinhardt,² Werner Liesack^{1*}

Rice fields are a global source of the greenhouse gas methane, which is produced by methanogenic archaea, and by methanogens of Rice Cluster I (RC-I) in particular. RC-I methanogens are not yet available in pure culture, and the mechanistic reasons for their prevalence in rice fields are unknown. We reconstructed a complete RC-I genome (3.18 megabases) using a metagenomic approach. Sequence analysis demonstrated an aerotolerant, H₂/CO₂-dependent lifestyle and enzymatic capacities for carbohydrate metabolism and assimilatory sulfate reduction, hitherto unknown among methanogens. These capacities and a unique set of antioxidant enzymes and DNA repair mechanisms as well as oxygen-insensitive enzymes provide RC-I with a selective advantage over other methanogens in its habitats, thereby explaining the prevalence of RC-I methanogens in the rice rhizosphere.

Rice fields contribute 10 to 25% of the global CH₄ emissions to the atmosphere (1). A large portion of the emitted CH₄ is produced by methanogenic archaea and released through the gas vascular system of the rice plant (2). This system enables oxygen to diffuse into the roots, leading to transient oxic conditions on the root surface and in the adjacent rhizosphere soil.

In a recent breakthrough, Rice Cluster I (RC-I) methanogens in the rice rhizosphere were found to be highly active and to play the key role in CH₄ production from plant-derived carbon (3). They were identified by cultivation-independent studies as the predominant methanogens in rice paddy soils of geographically diverse regions (4) and form a distinct clade within the phylogenetic radiation of *Methanosarcinales* and *Methanomicrobiales* (fig. S1). Given that up to 85% of the biogenic CH₄ is derived from photosynthesized carbon (5), RC-I is the methanogenic group responsible for microbial CH₄ emission from rice fields. Their

contribution to the global CH₄ budget is underscored by their ubiquitous occurrence in various other methanogenic environments (fig. S1).

Several attempts have been made to isolate RC-I representatives in pure culture (6, 7). Although isolation failed, one of these attempts with rice paddy soil as the inoculum resulted in the methanogenic consortium MRE50, in which RC-I methanogens constituted the only archaeal component (7). We generated a fosmid library from the MRE50 metagenome. The complete genome sequence of a single RC-I representative (RC-I_{MRE50}) was unambiguously reconstructed by end and shotgun sequencing of fosmid inserts with a 12-fold coverage (8). This homogeneous genome (one single-nucleotide polymorphism per 73,952 bases) (table S1) offers a means to elucidate the putative metabolic capacity of RC-I methanogens, which should thereby explain why they are able to outcompete other methanogenic groups in the rice rhizosphere.

The RC-I_{MRE50} genome is a circular chromosome of 3,179,916 base pairs (Fig. 1) with 3103 predicted coding sequences (Table 1). We deciphered general genotypic features (table S2) and metabolic capacities, some of which have been considered to be unique for either *Methanosarcina* spp. or obligately hydrogenotrophic methanogens (9).

The central energy metabolism of RC-I_{MRE50} is H₂/CO₂-dependent methanogenesis. In general, RC-I_{MRE50} appears to use the *Methanosarcina*-like set of enzymes for CO₂ reduction (table S3). The coding potential for a soluble and a membrane-bound hydrogenase, neither of which reduces coenzyme-F₄₂₀, is unique among methanogens. Because the membrane-bound hydrogenase contains cytochrome *b*, RC-I_{MRE50} is most likely capable of heme biosynthesis. Among methanogens, this trait has been hitherto attributed only to members of the *Methanosarcinales* (10). Similar to many obligately hydrogenotrophic methanogens but unlike *Methanosarcina* spp., RC-I_{MRE50} can use formate and formaldehyde for methanogenic growth (table S4). Consistent with a previous report on the inability of RC-I methanogens to grow methylo-trophically (6), the RC-I_{MRE50} genome encodes only an incomplete methanol-coenzyme M methyltransferase system (table S5). Similar to most obligately hydrogenotrophic methanogens, RC-I_{MRE50} harbors adenosine 5'-monophosphate-forming acetyl-coenzyme A (CoA) synthetase (ACS) for acetate assimilation (11) and the carbon monoxide dehydrogenase complex for acetyl-CoA biosynthesis from CO₂ (12) [table S6 and supporting online material (SOM) text]. In contrast to all other methanogens that use ACS for acetate activation, RC-I_{MRE50} solely encodes a membrane-bound pyrophosphatase (13) (table S7), which indicates that during acetate assimilation, RC-I_{MRE50} recovers a portion of the energy invested in acetate activation.

RC-I_{MRE50} appears to use the Embden-Meyerhof-Parnas (EMP) pathway for carbohydrate metabolism, thereby involving bacterial-type enzymes not yet identified in archaea (table S8). These include class II fructose-1,6-bisphosphate aldolase and family A adenosine 5'-triphosphate-phosphofructokinase (ATP-PFK) (table S9), the key regulator of the conventional EMP pathway. Both the overall sequence similarity to bacterial ATP-PFKs (65.8%) and the large number of conserved amino acid residues in the effector binding sites allow us to predict that the RC-I_{MRE50} ATP-PFK is allosterically regulated (fig. S2). By contrast, only nonregulated types of phosphofructokinases, including those depending on adenosine 5'-diphosphate (family C ADP-

¹Max-Planck-Institute for Terrestrial Microbiology, Karl-von-Frisch-Strasse, 35043 Marburg, Germany. ²Max-Planck-Institute for Molecular Genetics, Ihnestrasse 63, 14195 Berlin-Dahlem, Germany.

*To whom correspondence should be addressed. E-mail: liesack@mpi-marburg.mpg.de

PFK) (14, 15) or pyrophosphate (family A PPI-PFK) (16), and family B ATP-PFK (17), have been identified to date in archaea.

The pyruvate metabolism predicted for RC-I_{MRE50} includes ethanol production from acetaldehyde, acetoin production from acetolactate, and two mechanisms for acetyl-CoA formation from pyruvate (fig. S3 and tables S6 and S10). Besides oxygen-sensitive pyruvate-ferredoxin oxidoreductase typically found in methanogens (18), RC-I_{MRE50} encodes the pyruvate dehydrogenase (PDH) complex (PdhABCD), which might be expressed under oxic conditions. The PDH complex is typically found in aerobic and facultatively anaerobic microorganisms but is lacking in all other methanogens.

RC-I_{MRE50} most likely uses the glycolytic pathway to survive oxic periods (fig. S4 and SOM text). Energy for maintenance can be obtained during pyruvate and acetate production (19). Reducing equivalents generated from glucose and pyruvate oxidation can be regenerated by fermentation of pyruvate to ethanol (fig. S3). The allosteric control of the glycolytic pathway

by ATP-PFK should allow RC-I_{MRE50} to respond rapidly to changes in environmental redox states.

The biosynthetic pathways for all amino acids except glutamate appear to be complete in RC-I_{MRE50}. Glutamate is typically formed from 2-oxoglutarate, an intermediate synthesized by enzymes of the tricarboxylic acid cycle (20). RC-I_{MRE50} is not able to synthesize 2-oxoglutarate because it encodes only isocitrate dehydrogenase (CAJ36997) and fumarase (CAJ37197/CAJ37198). This finding suggests glutamate auxotrophy of RC-I_{MRE50} and is consistent with the identification of a candidate ABC-type glutamate import system (table S11). The ability of RC-I_{MRE50} to take up glutamate and to incorporate it into the methanogenic coenzyme F₄₃₀ was experimentally confirmed (fig. S5 and SOM text). Possible sources of glutamate are root exudates and/or decaying plant root material. Besides glutamate uptake, RC-I_{MRE50} possesses two additional mechanisms for nitrogen acquisition: ammonium assimilation (glutamine synthetase, glutamate synthase, and glutamate dehydro-

genase) and dinitrogen fixation (nitrogenase encoded by *nifH*_{1,2}*DKEN*) (table S11). These combined abilities provide RC-I_{MRE50} with metabolic flexibility in nitrogen acquisition.

We predict that sulfur assimilation by RC-I_{MRE50} occurs by means of reduction of sulfate to sulfide (table S12). To date, sulfate assimilation has only been reported for a single methanogen species, *Methanococcus thermolithotrophicus* (21). All methanogen genomes sequenced, except that of RC-I_{MRE50}, lack genes encoding sulfurylase and adenylyl-sulfate kinase. These methanogens therefore depend on sulfite, sulfide, or sulfur-containing amino acids as sulfur sources. The ability of RC-I_{MRE50} to use sulfate may be a beneficial adaptation to the rhizospheric environment, in which, owing to oxic conditions, sulfate concentrations exceed those of less-oxidized sulfur species.

The key to surviving and thriving in the rice rhizosphere is having enzymatic mechanisms to combat oxidative stress. The unique combination and multiple set of genes encoding anti-oxidant enzymes in RC-I_{MRE50} (Table 2 and

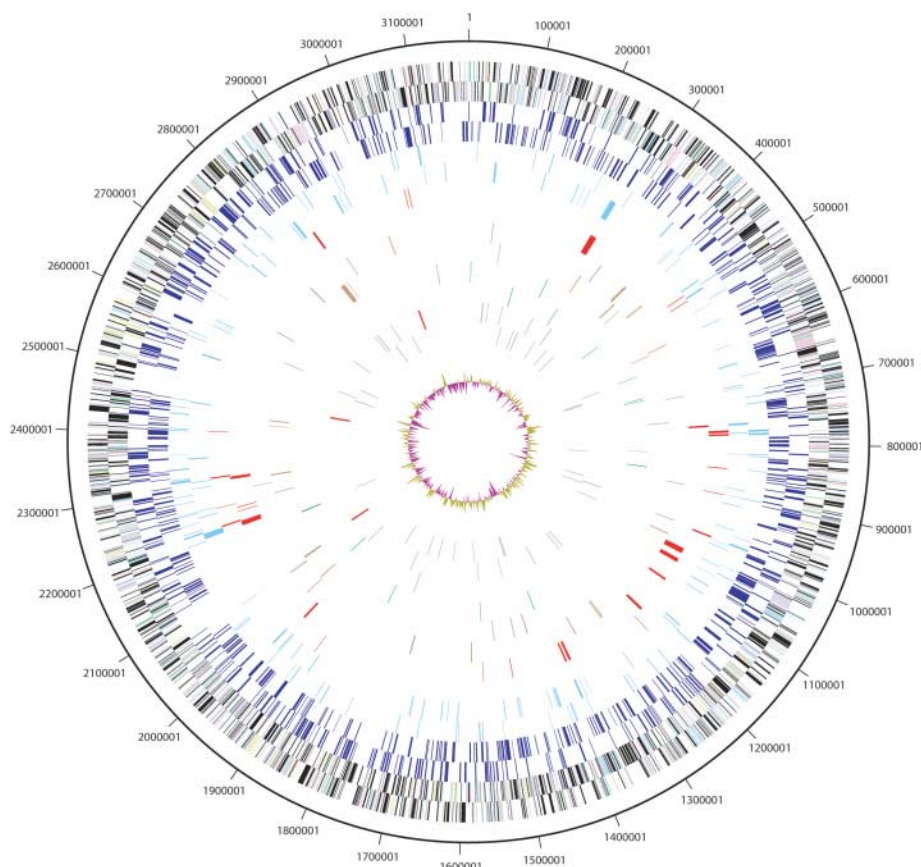


Fig. 1. Genomic organization of the RC-I_{MRE50} chromosome. Circular patterns (from outside to inside): 1 (outer circle), scale in base pairs of the chromosome; 2 (black with other colors), predicted coding sequences; 3 (dark blue), deduced amino acid sequences exhibiting top Blast Local Alignment Search Tool (BLASTP) hits to *Methanosarcina* spp.; 4 (light blue), coding sequences exhibiting top BLASTP hits to obligately hydrogenotrophic methanogens; 5 (red), coding sequences of energy metabolism and C₁ metabolism (methanogenesis); 6 (brown), coding sequences of C₂, C₃, and C₆ (acetate, pyruvate, and glucose) metabolism; 7 (green), coding sequences encoding antioxidant enzymes; 8, *rrm* operons (red), tRNAs (gray); and 9 (olive and pink), G+C skew.

Table 1. General characteristics of the RC-I_{MRE50} genome and top BLASTP hit distribution of deduced RC-I_{MRE50} amino acid sequences. tRNAs include three pseudo-tRNAs and five intron-containing tRNAs. *Methanosarcina* spp. include *M. mazei* Go1, *M. acetivorans* SC2, and *M. barkeri* fusaro. "Other *Methanosarcinales*" include *Methanococcoides burtonii*, *Methanolobus tindarius*, and *Methanosaeta concilii*. Obligately hydrogenotrophic methanogens include members of the *Methanobacteriales*, *Methanococcales*, and *Methanopyrales* (9).

Genome characteristics

Size (base pairs)	3,179,916
G+C content (mole %)	54.6
Coding (%)	84.7
Coding sequences	3103
Average size (base pairs)	868
G+C content (mole %)	56.4
Assigned function	1604
Conserved hypothetical	562
Predicted novel	937
Pseudogenes	18
Transposases	29
<i>rrn</i> operons (16S-23S-5S)	3
tRNAs	54

Top BLASTP hit distribution	Coding sequences	% of total
<i>Eucarya</i>	9	0.3
<i>Bacteria</i>	606	19.5
<i>Archaea</i>	1551	50.0
Methanogens	1203	38.8
<i>Methanosarcina</i> spp.	787	25.4
Other <i>Methanosarcinales</i>	240	7.7
Obligately hydrogenotrophic methanogens	176	5.5

Table 2. Antioxidant enzymes in RC-I_{MRE50} obligately hydrogenotrophic methanogens (OHM), *Methanosarcina* spp., and *Archaeoglobus fulgidus*. Catalases indicated are E (KatE, type I monofunctional clade II large subunit heme_a catalase), A (KatA, type I monofunctional clade III small subunit heme_b catalase), and G (KatG, type II bifunctional heme_b catalase/peroxidase). Gene copy number is given in parentheses. Types of superoxide dismutases indicated are C (SodC, Cu,Zn-containing periplasmic enzyme) and B (SodB, Fe-containing cytoplasmic enzyme). +, present; -, not present; +/-, mostly present; -/+, mostly not present.

Enzyme (gene)	RC-I _{MRE50}	OHM	<i>Methanosarcina</i> spp.	<i>A. fulgidus</i>
Catalase (<i>kat</i>)	E (1)	- / A (0-1)	A / G / E (1-2)	G (1)
Superoxide dismutase (<i>sod</i>)	C (1)	- / B (0-1)	B / C (1-2)	- (0)
1-Fe superoxide reductase (<i>sor</i>)	+ (1)	- / + (0-1)	+ (1)	+ (1)
2-Fe superoxide reductase, desulfoferrodoxin (<i>dfx</i>)	+ (1)	+ / - (1-0)	- (0)	+ (1)
Rubryerythrin (<i>rbr</i>)	+ (2)	+ / - (2-0)	+ (2)	+ (4)
Peroxiredoxin (<i>prx</i>)	+ (5)	+ / - (1-0)	+ (3)	+ (1)
F ₄₂₀ H ₂ oxidase (<i>fprA</i>)	+ (3)	+ / - (3-0)	+ (1-2)	+ (2)

table S13) indicate that RC-I methanogens are aerotolerant (fig. S6 and SOM text). The monofunctional large subunit heme catalase of RC-I_{MRE50} presents the most ancient and most robust type of all known catalases (22). RC-I_{MRE50} is the only organism known to encode three different superoxide anion scavengers. Exogenous superoxide anions are scavenged by a periplasmic Cu,Zn-dependent superoxide dismutase (SodC) (23) (fig. S7). Cu-containing enzymes are a typical characteristic of the aerobic world. Cytoplasmic superoxide anions are detoxified by two different types of superoxide reductase (SOR): rubredoxin-SOR and desulfoferrodoxin. SORs are considered the most important oxygen defense regulators in anaerobes (24), especially under strong oxygen exposure (23).

In the rice rhizosphere, RC-I methanogens compete for H₂/CO₂ with other hydrogenotrophic methanogens. Of these, *Methanosarcina* spp. that are able to grow on H₂/CO₂ might not be competitive because of their low affinity for hydrogen (25). Obligately hydrogenotrophic methanogens possess only a limited set of antioxidant enzymes (table S14). Thus, RC-I methanogens should have a competitive superiority over obligately hydrogenotrophic methanogens in the rice rhizosphere and other methanogenic environments with oxic episodes, such as boreal peatlands (26) and tropical soils (27) (fig. S1). Thriving in such environments also requires effective repair mechanisms for oxidative lesions of DNA (28). RC-I_{MRE50} encodes bacterial-type enzymatic systems not found in other methano-

gens. These systems are predicted to repair altered DNA bases [formamidopyrimidine-DNA glycosylase (MutM) and 3-methyladenine-DNA glycosylase (MPG)] and DNA double-strand breaks [Holliday junction resolvase (RuvABC)] (table S15).

The results of our analysis of the entire genome of RC-I_{MRE50} greatly enhance the understanding of the ecological role of RC-I methanogens and provide a genomic basis for their selective advantages and niche adaptation. The complete enzymatic equipment for an aerotolerant lifestyle is unique among methanogens and confers a competitive advantage over other obligately hydrogenotrophic methanogens. The mode of RC-I methanogens to acquire sulfur and nitrogen and to metabolize carbohydrates might also be beneficial for methanogenic life in the rice rhizosphere.

The genome data presented here could serve as a basis for the development of phylogenetic and functional gene probes for the detection and activity monitoring of RC-I methanogens in the environment. In the long-term, the increasing knowledge about RC-I methanogens might enable the development of promising strategies to mitigate global methane emission from rice fields by combating the metabolic activity of RC-I.

References and Notes

- H. U. Neue, *Bioscience* **43**, 466 (1993).
- I. Nouchi, S. Mariko, K. Aoki, *Plant Physiol.* **94**, 59 (1990).
- Y. Lu, R. Conrad, *Science* **309**, 1088 (2005).
- B. Ramakrishnan, T. Lueders, P. F. Dunfield, R. Conrad, M. W. Friedrich, *FEMS Microbiol. Ecol.* **37**, 175 (2001).

- A. Watanabe, T. Takeda, M. Kimura, *J. Geophys. Res.* **104**, 23623 (1999).
- M. V. Sizova, N. S. Panikov, T. P. Tourova, P. W. Flanagan, *FEMS Microbiol. Ecol.* **45**, 301 (2003).
- C. Erkel *et al.*, *FEMS Microbiol. Ecol.* **53**, 187 (2005).
- Materials and methods are available as supporting material on Science Online.
- The term "obligately hydrogenotrophic methanogens" is used for methanogens of the orders *Methanobacteriales*, *Methanococcales*, and *Methanopyrales* (there are no published genomes for *Methanomicrobiales*). These methanogens depend on hydrogen as the electron donor for methanogenesis.
- R. K. Thauer, *Microbiology* **144**, 2377 (1998).
- G. Oberlies, G. Fuchs, R. K. Thauer, *Arch. Microbiol.* **128**, 248 (1980).
- J. Shieh, W. B. Whitman, *J. Bacteriol.* **170**, 3072 (1988).
- S. Bäumer, S. Lentjes, G. Gottschalk, U. Deppenmeier, *Archaea* **1**, 1 (2002).
- J. E. Tuininga *et al.*, *J. Biol. Chem.* **274**, 21023 (1999).
- C. H. Verhees *et al.*, *J. Bacteriol.* **183**, 7145 (2001).
- B. Siebers, H.-P. Klenk, R. Hensel, *J. Bacteriol.* **180**, 2137 (1998).
- T. Hansen, P. Schönheit, *Arch. Microbiol.* **177**, 62 (2001).
- J. G. Zeikus, G. Fuchs, W. Kenealy, R. K. Thauer, *J. Bacteriol.* **132**, 604 (1977).
- T. Schäfer, M. Selig, P. Schönheit, *Arch. Microbiol.* **159**, 72 (1993).
- J. Shieh, W. B. Whitman, *J. Bacteriol.* **169**, 5327 (1987).
- L. Daniels, N. Belay, B. S. Rajagopal, *Appl. Environ. Microbiol.* **51**, 703 (1986).
- P. Chelikani, I. Fita, P. C. Loewen, *Cell. Mol. Life Sci.* **61**, 192 (2004).
- M. Fournier *et al.*, *J. Bacteriol.* **185**, 71 (2003).
- F. E. Jenney Jr., M. F. J. M. Verhagen, X. Cui, M. W. W. Adams, *Science* **286**, 306 (1999).
- Y. H. Lu, T. Lueders, M. W. Friedrich, R. Conrad, *Environ. Microbiol.* **7**, 326 (2005).
- P. E. Galland, H. Juottonen, H. Fritze, K. Yrjälä, *Microb. Ecol.* **49**, 209 (2005).
- S. E. Donovan, K. J. Purdy, M. D. Kane, P. Eggleton, *Appl. Environ. Microbiol.* **70**, 3884 (2004).
- B. Dimple, L. Harrison, *Annu. Rev. Biochem.* **63**, 915 (1994).
- The RC-I_{MRE50} genome sequence has been deposited in the GenBank, European Molecular Biology Laboratory, and DNA Data Bank of Japan nucleotide sequence databases under the accession number AM114193. Financed in parts by the Max Planck Society and the German Federal Ministry of Education and Research (contract 031U213A). We thank S. Fleissner, S. Patzak, J. Kahnt, H. Kuhl, J. Thiel, and I. Müller for technical support; P. Ricke and A. Beck for informatics support; R. Conrad, R. K. Thauer, and R. Hedderich for critical reading of the manuscript and expert advice; and K. A. Brune for editing the manuscript.

Supporting Online Material

www.sciencemag.org/cgi/content/full/313/5785/370/DC1
Materials and Methods
SOM Text
Figs. S1 to S7
Tables S1 to S15

6 March 2006; accepted 5 June 2006
10.1126/science.1127062